Investigations of Zinc Oxide and Carbon Nanostructures

A Thesis

Submitted for the Degree of

DOCTOR OF PHILOSOPHY

BY

LEELA SRINIVAS PANCHAKARLA

Chemistry and Physics of Materials Unit

Jawaharlal Nehru Centre for Advanced Scientific Research

(A Deemed University)

Bangalore – 560 064 (INDIA)

February 2011

Dedicated

To

My Parents

&

Teachers

DECLARATION

I hereby declare that the matter embodied in this thesis entitled **"Investigations of Zinc Oxide and Carbon Nanostructures"** is the result of investigations carried out by me under the supervision of Prof. C. N. R. Rao, FRS at the Chemistry and Physics of Materials Unit, Jawaharlal Nehru Centre for Advanced Scientific Research, Bangalore, India and that it has not been submitted elsewhere for the award of any degree or diploma.

In keeping with the general practice in reporting scientific observations, due acknowledgements have been made whenever the work described is based on the findings of other investigators.

February, 2011

Bangalore

Leela Srinivas Panchakarla

CERTIFICATE

I hereby certify that the matter embodied in this thesis entitled **"Investigations of Zinc Oxide and Carbon Nanostructures"** has been carried out by Mr. Leela Srinivas Panchakarla, at the Chemistry and Physics of Materials Unit, Jawaharlal Nehru Centre for Advanced Scientific Research, Bangalore, India under my supervision and that it has not been submitted elsewhere for the award of any degree or diploma.

_____

Prof. C. N. R. Rao, FRS

(Research Supervisor)

Acknowledgements

I am extremely grateful to ***Prof. C. N. R. Rao, FRS*** *for suggesting the interesting research problems, invaluable guidance and constant encouragement. He has been a constant source of inspiration for me. I greatly admire his enthusiasm towards science. I express my hearty gratitude to him for giving me an opportunity to work under his guidance.*

I would like to express my sincere thanks to Dr. A. Govindaraj who has helped me a great deal in carrying out the various experiments.

I am thankful to Basavaraj, Usha, Anil, Vasu, Selvi, Karthik, Amit (IISc), Srinath, Srinivas and srinivasa Rao for their help with the various characterization techniques. I am thankful to Dr. A. Sundaresan for magnetic measurement facility and Prof. G. U. Kulkarni and Prof. S. M. Shivaprasad for XPS facility. I am thankful to INI centre's Convenor Prof. K. Chattopadhyay, IISc for TEM facility.

I thank the past and present chairmen of CPMU, Prof. C. N. R. Rao and Prof. G. U. Kulkarni for providing all the facilities and a nice atmosphere in the department.

I am thankful to the faculty members of JNC and IISc for their courses. In particular, I would like to thank Prof. G. U. Kulkarni, Prof. Swapan Pati, Prof. Umesh V Waghmare, Prof. Chandrabhas Narayana, Prof. K. S. Narayan, Prof. M. Eswaramoorthy, and Prof. A. Sundaresan from JNC and Prof. S. Ranganathan from IISc.

I thank Bhat, Gomathi and Neenu for their help in the Raman measurements, Bhuvana and Jitesh for their help in the XPS measurements, Vengadesh, Pranab,

Madhu and Nitesh for their help in the magnetic measurements and Srinivasraju forhis help in FORTRAN calculations. I would like to thank Dr. Ujjal Gautam for CL amd FE measurements of ZnO nanobullets. I would like to thank Dr. U. A. Palnitkar, Prof. Joag and Ranjit for FE measurements on graphene samples. I thank Dr. Prashant kumar for his help in laser experiments.

I would like to thank all my lab members Drs. Vivek, Chandu, Kalyani, Bhat,Tiru, Gomathi, Rakesh, Claudy, Sahu, Kanishka, Late, Subrahmanyam, Neenu,Sandeep, Basanth, Matte, Anupama, Barun, Urmi, Kalyan, Manu, Sundarayya,Prashant, Joshi, Shashi, Gopal, Ajmala, Moses, Manju, Bello for their fruitful discussions, help and co-operation.

I am thankful to all academic, administrative, office, computer lab and work shop members for their help.

I would like to thank Mrs. Rao and Mr. Sanjay for their love and care towards me.

I would like to thank Mr. M. M. V. Y. Swamy, lecturer, who has been giving me constant encouragement and suggestions in my life.

I would like to thank CSIR for fellowship.

I would like to thank all my teachers, classmates, collaborators and friends.

Special thanks to my friends Anji, Uday, Phani, Rakesh, Lakshmi, Mouli, Kiran, Pavan, majhi, Ramesh, Prashant, KKR, manu, Gomathi, Neenu, Sandeep, Basanth, Reji, Saiki, kalyan, Vijay, Claudy, Raju, Shipra, Madhu, Pranab, Srinivasraj, Anil, Malik, and also thank all my sports friends.

Finally, I would like to express by deepest regards to my parents, brother and sister for their love, patience, understanding and motivation.

Preface

"Nano"-science and technology boom, *the fourth industrial revolution*, has aroused new excitement in scientists all over the world. Nanomaterials are thought to play an important role in everyday life of human beings because of their potential applications in diverse fields. A great deal of research is being focused on synthesis, modification and properties of nanomaterials in order to understand them better.

The thesis contains 7 chapters of which chapter 1 gives a brief overview of nanomaterials.

Chapter 2 is divided into six parts. The first three parts deal with the novel synthesis of nanoparticles, nanorods and thin films of ZnO by simple chemical routes, whereas the fourth part deals with the synthesis of N-doped ZnO nanobullets by the solvothermal method. Field emission and generation of white light from ZnO nanostructures are presented in the fifth and sixth parts of this chapter respectively.

Chapter 3 deals with surface ferromagnetism universally exhibited by metal oxide nanostructures. Here, we present a combined study of magnetic and photoluminescence properties of nanoparticles of ZnO, ZrO_2 and MgO annealed at different temperatures, and therefore are of different sizes. Magnetization and intensity of the PL band due to defects vary parallely in all these nanomaterials. Adsorption of ethanol decreases the magnetization and the PL band intensity of ZnO nanoparticles while UV irradiation has the opposite effect.

Chapter 4 describes the synthesis and spectroscopic characterization of nitrogen- and boron-doped double-walled carbon nanotubes (DWNTs). It also presents methods of functionalization of DWNTs.

Chapter 5 deals with the synthesis, characterization, properties and applications of nitrogen- and boron-doped few layer graphene. This chapter is divided into three parts. The first part deals with the synthesis and characterization of boron- and nitrogen-doped graphene, whereas the second and third parts are discussed with field emission as well as sensor properties of doped-graphenes.

Synthesis and characterization of graphene nanoribbons are discussed in chapter 6. In chapter 7, carbon nanostructures and graphite-coated metal nanostructures obtained by the pyrolysis of ruthenocene and ruthenocene-ferrocene mixtures are discussed.

Contents

Chapter-1

A Brief Overview of Nanomaterials

1.1 Introduction

Since the development of the two-cylinder steam engine by James Watt in the 1760s, human-kind has experienced three industrial revolutions [1]. The first industrial revolution, as represented by the appearance of Watt's steam engine, employed various machines to replace human work. The second industrial revolution began at the end of the 19th century and was earmarked by the discovery of the internal combustion engine and electric generator [2], which led to the increased usage of electrical appliances, automobiles, and petroleum products. The construction of the first computer in the 1940s led to the third industrial revolution, which was followed by the rapid development of information technology [2].

Although many of these inventions and developments provide numerous benefits, they also pose new and sometimes unforeseeable risks. For example, the emergence of internal combustion engineering led to the wide-spread accessibility of electric power for lighting, home appliances, industrial machines, automobiles, and aero crafts. However, it has also contributed to the levels of air pollution and accelerated global warming. With rapid increase in population, the consumption of natural resources,

environmental pollution, and information overflow, the turn of the last century witnessed the birth of nanotechnology. The demand for miniaturized with multifunctional systems has been a driving force for the development of nanotechnology, *the fourth industrial revolution.*

Owing to the fascinating size-dependent properties of nanophase materials [3], the recent development of nanoscience and nanotechnology has opened up novel fundamental and applied frontiers in materials science and engineering. The idea of nanotechnolgy was first introduced by *Nobel laureate Richard Feynman* [4] in 1959 at the annual meeting of the American Physical Society at the California Institute of Technology (Caltech). In his classic talk entitled: *"There is plenty of room at the bottom"*, Feynman stated, "The principles of physics, as far as I can see, do not speak against the possibility of maneuvering things atom by atom". In a while, Notio Taniguchi from the Tokyo Science University first defined the nanotechnology as: (a) the creation of useful materials, devices, and systems through the control matter at the nanometer (10^{-9} m) length scale and (b) the exploitation of new properties and phenomena developed at that scale [5]. Eric Drexler published the first scientific paper on nanotechnology in 1981 [6], a former student of Dr. Feynman at Caltech. Drexler's [7] idea of molecular manufacturing was followed by his book entitled: *Engines of Creation—The Coming Era of Nanotechnology* published in 1986. In this classic nanotechnology book, Drexler anticipated the atom-stacking mechanism to produce machines smaller than a living cell and also presented some

probable applications of nanotechnology. Although Drexler's publications have motivated researchers in the field of nanotechnology, the major breakthrough in nanotechnology occurred in 1981 when Binnig and Rohrer [8] at IBM Zurich invented the scanning tunneling microscope (STM), the first tool to generate real space images of surfaces with atomic resolution. This innovation opened up the important new field of nanotechnology and was recognized by the 1986 Nobel Prize in Physics, along with the inventor of the electron microscope.

1.2 Size and surface effects

Changes in the size-dependent properties can be observed in nanomaterials as the wave-like properties of electrons inside matter and atomic interactions are influenced by the size of materials at the nanometer scale [3]. Confinement of the de Broglie wavelength of charge carriers inside nanomaterials could also lead to new phenomena, such as the quantization effect [3]. When a gold nugget is converted into nanoparticles, for example, the color of the gold particles is changed to black. As the size decreases, the ratio of the surface atoms increases. These high energy surface atoms are very reactive. Due to the high surface-to-volume ratio associated with nanometer-sized materials, a tremendous improvement in chemical properties is also achievable through a reduction in size [3]. This is why platinum nanoparticles can be used as efficient catalysts for many reactions whereas platinum bulk sheets are sufficiently inert as electrodes in

electrochemistry. By creating nanostructures, therefore, new materials and advanced devices of desirable properties and functions can be developed for numerous applications

Nanostructures can be defined as systems in which; at least one dimension is less than 100 nm; that is, reducing 1, 2 or 3 dimensions (D) of a bulk material to the nanometer scale produces nanometer thick 2D layers, 1D nanowires, or 0D nanoclusters, respectively. A schematic illustration, showing the density of states versus energy for nanostructures of various dimensions, is given in Fig. 1.1.

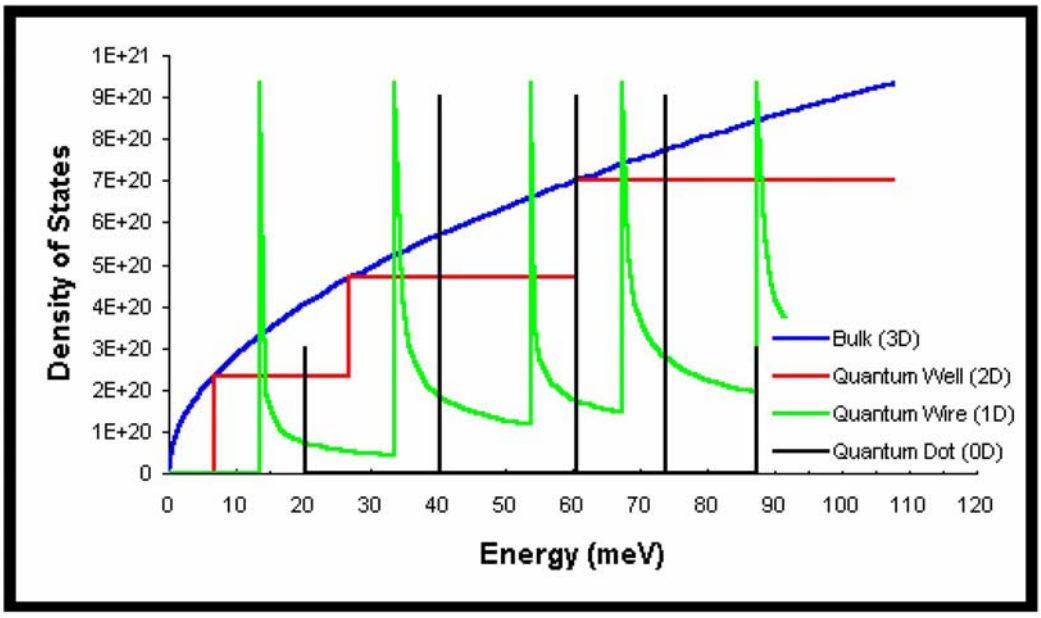

Fig. 1.1. Density of states for bulk (blue), quantum well (red), quantum wire (green) and quantum dot (black)

The density of states changes remarkably with dimension. For 2D nanostructures it is a step function with steps occurring at the energy of each quantized level. In the case of 1D nanostructure, van Hove singularities are observed. For 0D nanostructures, the density of states shows

quantization at particular energy levels. The quantum confinement of electrons by the potential walls of nanomaterials can provide one of the most powerful means to control the electrical, optical, magnetic, and thermoelectric properties of a solid-state functional material. Suitable control of these properties of nanomaterials can lead to new stream of science as well as new devices and technologies, the underlying theme of nanotechnology [9].

1.3 Zero-dimensional (0D) nanostructures

Nanocrystals are aggregates of a few hundred or even tens of thousands of atoms that combine into a crystalline form of matter known as a “cluster”. Typically a few nanometers in diameter, nanocrystals are larger than molecules but smaller than bulk solids and therefore frequently exhibit physical and chemical properties somewhere in between. Nanocrystals possess high surface area, with a large fraction of its atoms on the surface. Their properties can vary considerably with size. By precisely controlling a nanocrystal’s size and surface, its electronic, magnetic, and optical properties can be changed. Due to the confinement of electron wave function to the physical dimensions of the particles in small nanocrystals, electron energy levels are discrete, unlike in the bulk where it is continuous. This phenomenon is called quantum confinement [10]. Therefore, nanocrystals are also known as quantum dots. The nanocrystals can be discretely charged with electrons having characteristic charging energies. The electronic

absorption spectrum of metal nanocrystals in the visible region is dominated by the plasmon band and the surface plasmon excitations impart characteristic colors to the metal sols. In semiconductor nanocrystals, exciton peaks dominate the absorption [11, 12] The absorption band can be systematically varied by changing the size of the semiconductor nanocrystals. Semiconductor nanocrystals also exhibit interesting luminescent properties as well [13, 14]. For e.g., the emission from mono-disperse semiconductor nanocrystals such as CdSe is intense, narrow and can be brought about by excitation in a broad range of wavelengths [14]. The emission can be controlled by controlling the surface structure and the size of the nanocrystals.

1.3.1 Synthetic strategies

Modern materials science is characterized by a close interplay between physics and chemistry. This is especially true for nanomaterials. On the one hand, are the top-down methods which rely on continuous breakup of a piece of bulk matter while on the other are the bottom-up methods that build up nanomaterials from their constituent atoms. The top-down and bottom-up approaches can also be considered to be physical and chemical methods, respectively.

Physical methods

Most physical methods involve the evaporation of a solid material to form a supersaturated vapor from which homogenous nucleation of

nanoparticles occurs. In these methods, the size of the particles is controlled by temporarily inactivating the source of evaporation, or by slowing the rate by temporarily inactivating the source of evaporation, or by slowing the rate by introducing gas molecules to collide with the particles. Some of the physical methods to prepare nanocrystals are arc dischare, ion sputtering, laser ablation, spray pyrolysis, etc [10].

Chemical methods

Chemical methods have emerged to be indispensable for synthesizing nanocrystals of various types of materials. These methods are generally carried out under mild conditions and are relatively straight forward. Any chemical reaction resulting in a sol consists of three steps: seeding, particle growth and growth termination by capping. An important process that occurs during the growth of a colloid is Ostwald ripening. Ostwald ripening is a growth mechanism whereby smaller particles dissolve releasing monomers or ions for consumption by larger particles, the driving force being the lower solubility of large particles. Ostwald ripening limits the ultimate size distribution obtainable to about 15% of the particle diameter when the growth occurs under equilibrium conditions [10].

(a) Metal nanocrystals by reduction

Metal nanocrystals can be obtained by reducing the corresponding soluble metal salts and by terminating the growth with appropriate

surfactants or ions. A variety of reducing agents are used to reduce metals salts to get nanocrystals of metals. Some of them are (1) borohydride reduction [15], (2) citrate reduction

Fig. 1.2 Michael Faraday's gold colloids

[16], (3) alcohol reduction [17] and (4) reduction using alkylaluminates (AlR_3, R=C_1-C_8) [18]. In 17th century Farady prepared gold nanoparticles in lab by reducing gold salt. He termed them as "divided metal", which giving rise to a brilliant rose colour, as shown in Fig. 1.2.

(b) Solvothermal Synthesis

The Solvothermal method provides a means of using solvents at temperatures well above their boiling points, by carrying out the reaction in a sealed vessel. The pressure generated in the vessel due to the solvent vapors elevates the boiling point of the solvent. Typically, solvothermal methods make use of solvents such as ethanol, toluene and water. These are widely used to synthesize zeolites, inorganic open-framework structures and other solid materials. Due to the high pressures employed, one often obtains high-pressure phases of the materials. In the past few years, solvothermal synthesis has emerged to become the chosen method to synthesize

nanocrystals [19, 20]. Solvothermal methods are ideally suited for the synthesis of nanocrystals of metal chalcogenides and halides, rather than metal nanocrystals.

(c) Photochemical synthesis

Photochemical synthesis of nanoparticles can be carried out by the light induced decomposition of a metal complex or the reduction of metal salts by photogenerated reducing agents such as solvated electrons. The former is called photolysis and the latter radiolysis. The formation of photographic images on AgBr film is a familiar photolysis reaction. Metals such as Au, Cd and Tl, have been obtained by photolysis [21, 22]

(d) Arrested precipitation

Nanocrystals can be obtained from solutions that precipitate the bulk matter under conditions unfavorable for the growth of particulates in the precipitate. For example, the precipitation of metals salts by chalcogens can be arrested by employing a high pH. To prepare nanocrystals of CdS, CdSe, CdTe, HgSe, HgTe and CdHgTe, typically, a solution containing the metal salt (perchlorate) and the capping agent is treated with NaOH to raise the pH, degassed by bubbling inert gas (to prevent the oxidation of chalcogen source) followed by the introduction of the chalcogen in the form of Na_2S, NaHSe, etc under inert conditions [10].

(e) Liquid-liquid interface

Nanocrystals and films of metals, semi-conductors and oxides can be produced by reactions taking place at the interface of two liquids such as toluene and water [10]. In this method, a suitable organic derivative of the metal taken in the organic layer reacts at the interface with the appropriate reagent present in the aqueous layer to yield the desired product. For example, by reacting $Au(PPh_3)Cl$ in toluene with THPC in water, nanocrystals of Au can be obtained at the interface of two liquids.

1.3.2 Properties of nanocrystals and their applications

Colloidal semiconductor nanocrystals [23, 24] combine the physical and chemical properties of molecules with the optoelectronic properties of semiconductors. Their colour is highly controllable, a direct consequence of quantum confinement on the electronic states. Such nanocrystals find applications in optoelectronic systems such as light emitting diodes and photovoltaic cells, or as components of future nanoelectronic devices [25, 26]. The ability to control the electron occupation (especially in n-type or p-type nanocrystals) is important for tailoring the electrical and optical properties.

Shim and Sionnest [27] have reported the fabrication of n-type nanocrystals using an electron transfer approach commonly employed in the field of conducting organic polymers. Pellets of monodisperse nanocrystals have been used for electrical transport measurements [28, 29]. An insulator-

metal transition has been reported for Au and Ag nanocrystals by Aslam et al. [29].

Studies on both electrical and optical properties of single semiconductor nanocrystals have been carried out [30-33]. All these studies have shown that a single excess charge on a nanocrystal can greatly influence its properties. Klein et al. [34] have reported the fabrication of a single-electron transistor from a

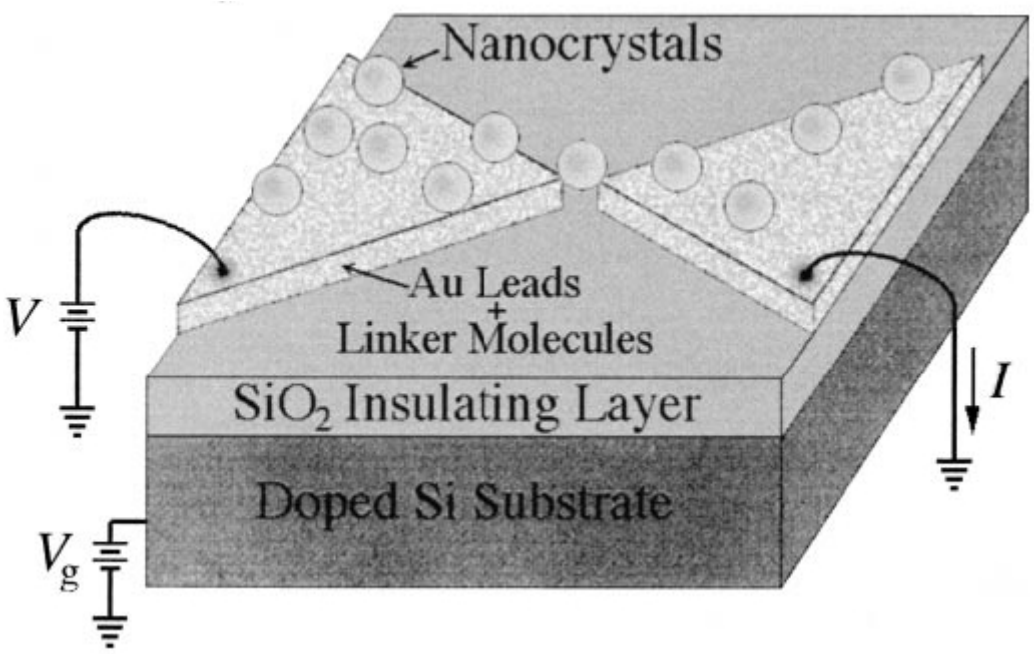

Fig. 1.3. Diagram of a single-electron transistor.

colloidal nanocrystal of CdSe. In Fig. 1.3 is given a diagram of their device. This device structure actually enables the number of charge carriers on the nanocrystal to be tuned directly, and in turn the measurement of energy required for the addition of successive charge carriers. Such measurements are invaluable in understanding the energy-level spectra of small electronic systems.

The optical properties of a super lattice of semiconductor nanocrystals are different from those of the individual nanocrystals due to their interparticle interactions [35]. The absorption spectra of nanocrystals get broadened and red-shifted when in a close-packed association, and have been attributed to the interparticle dipolar interactions [36]. Gaponenko and co-workers have shown that the optical properties of an ensemble of small CdSe nanocrystals are similar to those of bulk CdSe due to the complete delocalization of the electronic states of individual nanocrystals [37].

1.4 One-dimensional nanostructures

One-dimensional (1D) nanostructures have attracted much attention as well-defined building blocks to fabricate nanoscale electronic, and optoelectronic devices [9, 38-41]. The formation of various 1D semiconductor nanostructures is believed to be of importance in tailoring the optical, electronic, electrical, magnetic, and chemical properties of 1D nanostructures. In comparison to the zero-dimensional nanostructures (0D), the one-dimensional nanostructures pose as better model systems for investigating the dependence of electronic transport, optical and mechanical properties on the size confinement and dimensionality [9]. They also represent critical components in various nanoscale devices. The synthesis of nanowires with controlled composition, size, purity and crystallinity is no easy task and requires a proper understanding of the nucleation and growth process at the nanometer regime [42]. Many nanolithographic techniques

[43], such as proximal-probe patterning [44], electron-beam [45] or focused ion-beam writing [46], etc, have been employed for the synthesis of nanowires and other 1D nanostrctures. Since these physical methods are generally slow and costly, researchers have been investigating chemical routes towards the synthesis of 1D nanostructures [41, 47]. The common chemical methods include solution and vapor based methods.

1.4.1 Synthesis of nanowires

Crystallization is the essence of one-dimensional nanostructure formation [48]. When the concentration of the building blocks (atoms, ions or molecules) of a solid becomes sufficiently high, homogenous nucleation takes place, leading to the formation of small nuclei or clusters. Subsequently, larger clusters are formed from these small clusters, which serve as seeds. The formation of a perfect crystal requires a reversible pathway between the building blocks on the solid surface and those in a fluid phase (vapor, solution or melt). These conditions allow the building blocks to easily adopt correct positions in developing the long-range ordered, crystalline lattice. Also, to attain homogeneous composition and uniform morphology, the building blocks have to be supplied at a well-controlled rate.

Vapor-phase growth of nanowires

Vapor-phase synthesis is the most extensively investigated approach to the formation of 1D nanostructures such as whiskers, nanowires and nanorods, due to its simplicity and accessibility. This vapor-phase growth

was first observed in the formation of Hg nanofibers by Volmer and Estermann in 1921, when Hg vapor was condensed on a glass surface cooled below the melting point of mercury [49]. An important factor which determines the morphology of the product here is the level of supersaturation. A low supersaturation is required for whisker growth whereas a medium supersaturation leads to bulk growth. At high supersaturation, powders are formed by homogeneous nucleation in the vapor-phase. The two main mechanisms involved in the growth of nanowires in the vapor-phase are (a) vapor-solid and (b) vapor-liquid-solid mechanism.

(a) Vapor-liquid-solid growth

The most extensively studied among the vapor-phase methods is the vapor-liquid-solid (VLS) method. This mechanism was proposed by Wagner in 1960's during his studies on the growth of single-crystalline whiskers of Si and of the metals Pt, Ag, Pd, Cu and Ni [50]. This process has been employed for the synthesis of nanowires of many semiconducting materials such as Si [51], Ge [52, 53], ZnO [54], CdS [55], etc. According to this mechanism, a liquid alloy acts as the nucleation site for the formation of the nanowires. First, the gaseous reactant undergoes dissolution into the nanosized liquid droplets of an impurity metal catalyst, and forms a liquid alloy at a temperature higher than the eutectic point. Since the liquid surface has a large accommodation coefficient, it becomes the preferred deposition site for

the incoming vapors of the reactant material. After the liquid becomes supersaturated with vapor, the nanowire growth occurs by precipitation at

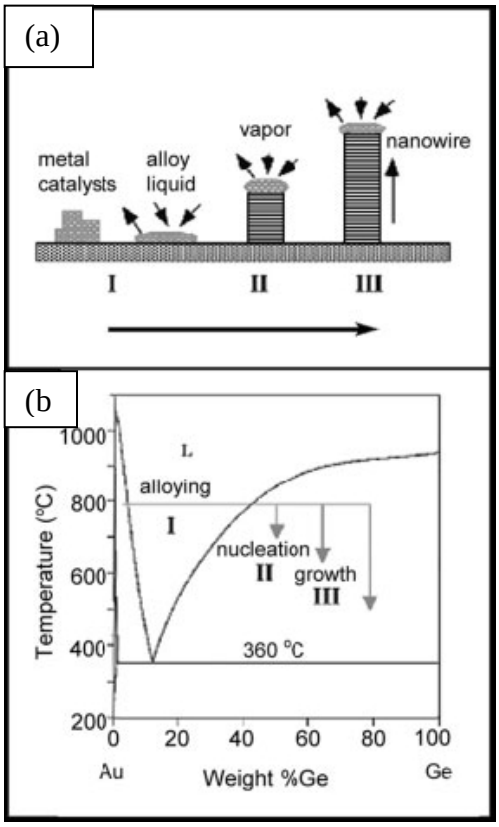

Fig. 1.4: (a) Schematic illustration of VLS nanowire growth mechanism including three stages: (I) alloying (II) nucleation, and (III) axial growth. (b) Binary phase diagram of Au-Ge system.

the liquid-solid interface. The different steps involved in the VLS growth are illustrated schematically in Fig. 1.4 (a).

The selection of a proper metal impurity for the VLS growth is an important criterion. The equilibrium phase diagram helps in the prediction of the catalyst materials to be used, as well as the reaction conditions for the growth of the nanowires. As an example, the Fig. 1.4 (b) shows the binary

phase diagram of the Au-Ge system. Diameter of the nanowires formed by the VLS method is determined by the size of the catalyst particles, which act as soft templates to limit the lateral growth of an individual nanowire. Thus, this method helps in the synthesis of uniform-sized nanowires; and also patterned nanowires through the patterned deposition of catalyst particles.

(b) Vapor-solid growth

Apart from the VLS mechanism, 1D nanostructures have also been grown via the classcal vapor-solid (VS) mechanism [56]. In a typical vapor-solid process, the vapor-species is first generated by physical evaporation, chemical reduction, and other kinds of gaseous reactions. These species are subsequently transported and condensed onto the surface of a solid substrate placed in a cooler zone. A large number of single-crystalline metal oxide nanowires have been grown via this mechanism. Due to the presence of trace

amounts of oxygen in reaction systems, majority of the products reported are oxides. Thus, nanowires of oxides of Zn, Mg, Ga, In, Si etc have been synthesized by this method [41]. Apart from nanowires, this process has been adopted for the growth of nanobelts also which are single-crystalline [57].

Carbothermal method

Another very useful and versatile chemical method employed for the synthesis of nanowires is the carbothermal method. Nanowires of a number

of oxides such as MgO, ZnO, SnO_2, Ga_2O_3, nitrides such as Si_3N_4, AlN and carbides, such as SiC have been synthesized by this method [58-60]. In a typical carbothermal method a carbon source is heated with a metal oxide in a flowing gas. The carbon sources generally used are activated carbon or charcoal (which are easily oxidized on heating in air) and carbon nanotubes or graphite (which are more stable to oxidation on heating). First, carbon reduces the metal oxide to give a suboxide. The suboxide when heated in the presence of either O_2, N_2/NH_3 or C, gives rise to oxide, nitride or carbide nanowires respectively. In this method, the flow rate of the gas is an important factor, which determines the morphology of the final products.

$$\text{Metal oxide} + C \longrightarrow \text{Metal suboxide} + CO$$

$$\text{Metal suboxide} + O_2 \longrightarrow \text{Metal oxide nanowires}$$

$$\text{Metal suboxide} + NH_3 \longrightarrow \text{Metal nitride nanowires}$$

Solution-based growth of nanowires

The other set of chemical methods adopted for the synthesis of inorganic nanowires is solution-based. This synthetic strategy involves mainly reactions that are confined and directed by templates or by the use of appropriate capping agents. In the template-based technique, the template serves as a scaffold against which other kinds of materials, with morphologies complimentary to that of the template, are generated.

The channels of the templates are filled using a solution route, sol-gel technique or an electrochemical route to produce nanowires. After the reaction, the nanowires could be released from the templates by selectively removing the template from the host matrix. Nanowires of various inorganic materials such as SnO_2, ZnO, Ag, Pt, etc, electronically conducting polymers: polypyrrole and polyaniline, and carbon nanotubules, have been prepared using anodic aluminum oxide membranes (AAMs) [61]. Apart from AAMs and polymer membranes, mesoporous silica have also been used as templates for the synthesis of polymer and inorganic nanowires. Mesophase structures self-assembled from surfactants provide another class of versatile templates for the synthesis of nanowires in large amounts. Carbon nanotubes (CNTs) have been used as templates for the synthesis of inorganic nanowires. By coating CNTs with oxide gels and then burning off the carbon, nanowires of a variety of metal oxides including ZrO_2 [62], SiO_2 [63] and MoO_2 [64] have been prepared.

Apart from the template-based methods, non-template methods, making use of the anisotropic bonding in the crystallographic structures, have also been adopted for the synthesis of inorganic nanowires of Se, Te, molybdenum chalcogenides and polysulfur nitride (SN_x) [65-68].

1.4.2 Properties of nanowires and their applications

Nanowires show very distinct electric, optical, and thermal properties due to their large surface area and possible quantum confinement, when

compared with their bulk counterparts. The thermal stability of nanowires is of critical importance for their implementation as building blocks in nanoscale electronic and photonic devices. It is well documented that the melting point of a solid material will be greatly reduced when it is processed as nanostructures [69]. In their investigations on the melting and recrystallization of Ge nanowires encapsulated by carbon-sheaths, Yang and co-workers [70, 71] observed the melting point to be inversely proportional to the diameter of the nanowire.

Once the diameter of a nanowire has been reduced below a critical value, size-confinement plays an important role in determining its energy levels. Absorption edge of Si nanowires was found to be considerably blue-shifted when compared with the indirect band gap of bulk Si (~1.1 eV), observed by Korgel et al. [72]. They also observed sharp, discrete features in the absorption spectra and relatively strong band-edge photoluminescence, arising due to quantum confinement effects with additional contributions from the surface states. Lieber and co-workers have shown anisotropy in PL (photoluminescence) intensities in single InP nanowires in directions parallel and perpendicular to the axis of the nanowire [73].

Nanowires and nanotubes are ideal building blocks for nanoscale electronics and optoelectronics. Nanowires of semiconducting elements such as Si and Ge, as well as those of ZnO, InP, GaN, CdS, etc have been studied extensively, towards their applications in nanotechnology. These nanowires

have been assembled into nanometric scale devices including FETs, LEDs, p-n junction diodes, logic gates and sensors.

1.4.3 Carbon nanotubes

With the revolutionary discoveries of the C_{60} molecule [74] and carbon nanotubes [75], carbon nanomaterials have become the building block of the entire field of nanotechnology. Exhibiting interesting electronic, mechanical and structural properties; Carbon nanotubes (CNTs) are extremely promising for applications in materials science, engineering and medicinal chemistry. CNTs consist of graphitic sheets, which have been rolled up into a cylindrical shape. The length of CNTs goes up to hundreds of micrometers and their diameters range from 1-50 nm.

Carbon has long been known to exist in three forms: amorphous carbon, graphite, and diamond [76]. Depending on how the carbon atoms are arranged, their properties vary. For example, the most common form of carbon, graphite, is soft, black, and stable. In graphite, the carbon atoms are located at the corners of regular and fused hexagons arranged in parallel layers and its density is 2.26 g/cm^3. However, diamond is hard and transparent due to its regular repetitive pattern, where each carbon atom is bound to four other carbon atoms and its density of 3.51 g/cm^3 is greater than that of graphite. The Noble-Prize-winning discovery of buckminsterfullerene created an entirely new branch of carbon chemistry. The subsequent discovery of carbon nanotubes by Iijima [75] opened up a

new era in materials science and nanotechnology [77-79]. Nanodiamonds and nanographenes are the most recent additions to members of the carbon family.

Fullerenes were discovered by Kroto et al. [74] in 1985 while investigating the nature of carbon present in interstellar space. The coordination at every carbon atom in fullerenes is not planar, but slightly pyramidalized, with some sp^3 character present in the essentially sp^2 carbons. The key feature is the presence of five-membered rings, which provide the curvature necessary for forming a closed-cage structure. C_{60} having truncated icosahedral structure formed by 12 pentagonal rings and 20 hexagonal rings. Carbon nanotubes are concentric graphitic cylinders closed at either end due to the presence of five-membered rings. Nanotubes can be multi-walled with a central tubule of nanometric diameter surrounded by graphitic layers separated by ~3.4 Å. Unlike the multi-walled nanotubes (MWNTs), in single-walled nanotubes (SWNTs), there is only the tubule and no graphitic layers. Whereas, Double-walled carbon nanotubes (DWNTs) occupy a position between MWNTs and SWNTs, consist of two concentric cylinders of rolled graphemes, a smallest MWNT. A transmission electron microscope (TEM) image of a MWNT is shown in Fig. 1.5 (a). In this nanotube, graphite layers surround the central tubule. Fig. 1.5 (b) shows the structure of a double-walled nanotube formed by two concentric graphitic cylinders. A single-walled nanotube can be visualized by cutting C_{60} along the center and spacing apart the hemispherical corannulene end-caps by a

cylinder of graphite of the same diameter. Fig. 1.5 (c) shows the bundles of SWNTs. Carbon nanotubes are the only form of carbon with extended bonding and yet with no dangling bonds. Since carbon nanotubes are derived from fullerenes, they are referred to as tubular fullerenes or bucky tubes.

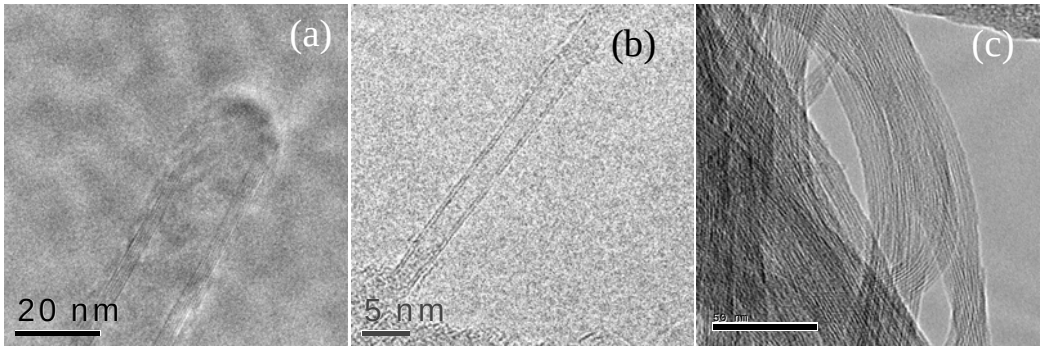

Fig. 1.5 shows TEM images of (a) multi-walled, (b) double-walled and (c) single-walled carbon nanotubes

Synthesis of carbon nanotubes

Ever since the discovery of the carbon nanotubes [75], several ways of preparing them have been explored. CNTs have been prepared by various methods e.g. electric arc discharge, laser evaporation and chemical vapor deposition. These methods are described in following sections.

(a) Electric-arc discharge

Carbon nanotubes (CNTs) are commonly prepared by striking an arc between graphite electrodes in an inert atmosphere (argon or helium), the process that also produces carbon soot containing fullerene molecules [74]. The carbon arc provides a convenient and traditional tool for generating the

high temperatures needed to vaporize carbon atoms into a plasma (>3000 ^{o}C) [80-82]. The yield of CNTs depends on the stability of the plasma formed between the electrodes, the current density, inert gas pressure and cooling of electrodes and chamber [80, 82]. For the MWNTs production, the conditions are optimized so that during the arc evaporation, the amount of soot production is minimized and 75% of the evaporated carbon from a pure graphite anode is made to deposit onto the facing graphite cathode surface. The optimized synthesis conditions 20-25 V, 50-100 Amp. d.c. (direct current) and the helium pressure maintained at 500 torr. Arc discharge is a simple process, and it is an excellent method to obtain structurally high quality CNTs.

In the arc discharge method, synthesis of MWNTs requires no catalyst, catalyst species are however, necessary for the growth of SWNTs. The first report on the production of SWNTs was by Ijima and Ichihashi [83]. These authors produced SWNTs material by arcing Fe-graphite electrode in a methane+argon atmosphere. A hole was made in the graphite anode, which was filled with a composite mixture of metal and graphite powders, while the cathode being pure graphite. The catalyst generally used to prepare isolated SWNTs include transition metals such as Fe, Co, Ni and rare earth metals such as Y and Gd [83-87], whereas composite catalyst such as Fe/Ni and Co/Ni have been used to synthesize ropes (bundles) of SWNTs [88]. In these experiments, the tubes exhibited an average diameter of 1.2 nm. Saito et al [89] compared SWNTs produced by using different catalysts and found that a

Co or a Fe/Ni bimetallic catalyst gives rise to tubes forming a highway-junction pattern. Ni catalyst yield long and thin tubes radially growing from the metal particles. High yield of SWNTs has been synthesized by d.c. arc discharge under low pressure of helium gas (100 torr) with a small amount of a mixture of Ni, Fe and graphite powders [90]. In addition, they introduced sulfur promoter to improve the yield, which gave rise to again the highest yield at low gas pressure.

(b) Laser vaporization

An efficient route for the synthesis of bundles of SWNTs with a narrow size distribution is the laser evaporation technique. In this method, a piece of graphite target is vaporized by laser irradiation under high temperature in an inert atmosphere. MWNTs were obtained when a pure graphite target was used [91]. The quality and yield of these products have been found to depend on the reaction temperature. The best quality is obtained at 1200 ^{o}C reaction temperature. At lower temperatures, the structure quality decreases and the CNTs start presenting many defects. As soon as small quantities (few percents or less) of transition metals (Ni, Co) playing the role of catalysts are incorporated into the graphite pellet, the yielded products undergo significant modifications and SWNTs are formed instead of MWNTs. The yield of SWNTs strongly depends on the type of the metal catalyst used and is seen to increase with furnace temperature, among other factors. A high yield with about 50% conversion of transition-metal/graphite composite rods to

SWNTs was reported in the condensing vapor in a heated flow tube (operating at 1200 ^{o}C) [92]. Depending on the metal catalyst used, the yield on the mono or bimetal catalysts are ordered as follows: Ni>Co>Pt>Cu or Nb and Co/Ni, Co/Pt>Ni/Pt>Co/Cu, respectively. A remarkably high nanotube yield of 50% on a Co/Ni run might have resulted from some uncertainty in the process of catalyst preparation and pretreatment [93].

Unfortunately, the laser technique is not economically advantageous because the process involves high-purity graphite rods, the laser powers required are high (in some cases two laser beams are required), and the amount of CNTs that can be produced per day is not as high as arc discharge method.

(c) Chemical vapor deposition

Chemical vapor deposition (CVD) is one of the most popular thin film deposition methods. CVD is very different from the other two common methods used for CNT production, namely electric arc discharge and laser vaporization [93, 94]. Arc discharge and laser vaporization can be classified as high temperature (>3000 °C) and short time reaction (μs-ms) techniques, whereas catalytic CVD is a medium temperature (500-1100 °C) and long time reaction (typically minutes to hours) technique. The main technological drawbacks with arc discharge and laser vaporization are that the CNTs are produced as stand alone on their own [95, 96]. The CNTs do not grow on a conventional or patterned substrate.

A major advantage of CVD is that the CNTs can be used directly without further purification unless the catalyst particle is required to be removed. In CVD method, CNTs are grown by decomposing an organic gas over a substrate covered with metal catalyst particles. Some CVD methods are reported, such as: thermal CVD, plasma enhanced CVD and catalytic pyrolysis of hydrocarbon.

A thermal CVD reactor is simple and inexpensive to construct and consists of a quartz tube enclosed in a furnace. The substrate material may be Si, mica, silica, quartz or alumina. The nature and yield of the deposit obtained in the reaction are controlled by varying different parameters such as the nature of the catalytic metals and their supports, the hydrocarbon sources, the gas flows, the reaction temperature, and the reaction time, etc. By selecting proper conditions, both the physical (e.g. length, shape, diameter) and chemical properties (e.g. defects, graphitization) of CNTs can be designed in advance. Most of the thermal CVD methods employed for the production of MWNTs use acetylene (C_2H_2) or ethylene (C_2H_4) gas as the carbon feedstock and Fe, Ni or Co nanoparticles as the catalyst. The growth temperature is typically in the range 500-900 ^{o}C. At these temperatures, the carbon atoms dissolve in the metal nanoparticles, which eventually become saturated. The carbon then precipitates to form CNTs, the diameters of which are determined by the sizes of the metal particles, which act as catalyst. When other elements (e.g. Cu, Cr, Mn) are used, only a negligible amount of CNTs is formed [97-99].

Plasma-enhanced chemical vapor deposition (PECVD) is a promising up-coming growth technique for the selective positioning and vertical alignment of CNTs. Vertical alignment is important in applications. This is very useful in field emitters, which are currently being considered for use in flat panel displays. The conventional wisdom in choosing plasma processing is that the precursor is dissociated by highly energetic electrons and as a result, the substrate temperature can be substantially lower than that in thermal CVD. The CNTs have been deposited from various plasma techniques such as hot filament PECVD, microwave PECVD, d.c. (glow discharge) PECVD, and inductively coupled PECVD and rf PECVD. It is clearly evident from these methods that PECVD is a high yield and controllable method of producing vertically aligned CNTs [100].

Catalytic pyrolysis of hydrocarbons is commonly used for the bulk production of CNTs by CVD. The main advantage of using this technique is that purification is not required to recover CNTs from the substrate. The simplest method is to inject catalyst nanoparticles (e.g. in the form of a colloidal/particle suspension or organometallic precursors with a carbon feedstock) directly into the CVD chamber. Organometallic compounds (e.g. metallocenes, iron pentacarbonyl and iron (II) phthalocyanine) are often used as precursors [101-107]. These precursors on heating sublime and form catalyst nanoparticles *in situ.* A double stage furnace is typically needed because of the different temperatures needed for organometallic sublimation and nanotube growth. In general, the sublimation of metallocenes offers little

control over the structural parameters of the nanotubes such as length and diameter. However, it has been shown that by varying the reactive concentration of the metallocene to carbon in the gas phase the average diameter of the structures may be changed [107, 108].

Chemically modified nanotubes

Doping with boron and nitrogen: Since the discovery of the carbon nanotubes, there has been interest in substituting carbon with other elements. Accordingly, boron-carbon (B-C), boron-carbon-nitrogen (B-C-N) and carbon-nitrogen (C-N) nanotubes have been prepared and characterized. Boron-substitution in the carbon nanotubes gives rise to p-type doping and nitrogen-doped carbon nanotubes correspond to n-type doping. Novel electron transport properties are expected of such doped nanotubes [109]. Boron-doped carbon nanotubes have been synthesized by carrying out the pyrolysis of mixtures of acetylene and diborane and characterized by employing microscopic and spectroscopic techniques [110]. B-C-N nanotubes have been prepared by striking an arc between a graphite anode filled with B-N and a pure graphite cathode in a helium atmosphere [111]. B-C-N nanotubes have also been obtained by laser ablation of a composite target containing B-N, carbon, Ni and Co at 1000 °C under flowing nitrogen [112]. Terrones et al. [113] pyrolyzed the addition compound $CH_3CN{:}BCl_3$ over Co powder at 1000°C to obtain B-C-N nanotubes. B-C-N as well as C-N nanotubes were prepared by Sen et al. [114] by the pyrolysis of appropriate

precursors. Pyrolysis of aza-aromatics such as pyridine over Co catalysts gives C-N nanotubes ($C_{33}N$ on average). Pyrolysis of the 1:1 addition compound of BH_3 with $(CH_3)_3N$ produces B-C-N nanotubes. Furthermore, considerable variability exists in the composition in any given batch of B-C, B-C-N or C-N nanotubes obtained by the pyrolysis of precursors.

Nath et al. [115] have obtained aligned carbon-nitrogen nanotube bundles by the pyrolysis of pyridine over sol-gel-derived iron/silica or cobalt/silica substrates. Employing anodic alumina, Sung et al. [116] synthesized the C-N nanotubes by electron cyclotron resonance CVD, using C_2H_2 and N_2. Suenaga et al. [117] carried out CVD of Ni-phthalocyanine to obtain aligned C-N nanotubes.

Characterization and Properties of Carbon Nanotubes

MWNTs can be conceived as multi-layered concentric cylinders of single graphitic (graphene) sheets. The diameter of the inner tube is of the order of a few nanometers while the outermost tubes could be as large as 10-30 nm. Helicity is introduced during the curling of a graphene sheet which is well-established by the electron diffraction studies. This suggests that the growth of the nanotubes occurs as in the spiral growth of crystals. Concentric cylinders in MWNTs are separated by about 3.45 Å, which is close to the separation between the (002) planes of graphite. CNTs being capped by dome-shaped hemispherical fullerene-type units don't have

dangling bonds at their tips as is generally expected of the graphitic cylinders.

SWNTs can be visualized by cutting the C_{60} structure across the middle and adding a graphite cylinder of the same diameter. Two types of non-chiral nanotubes occur in nature: armchair and zigzag. If C_{60} is bisected normal to a five-fold axis, an armchair tube is formed, and if it is bisected normal to a three-fold axis then a zigzag tube is formed. Apart from these, various chiral tubes can be formed with the screw axis along the axis of the tube. The models of the three types of nanotubes: zigzag, armchair and chiral nanotubes shown in Fig. 1.6.

A chiral angle θ and a chiral vector **C** is used to define a nanotube. Equation 1.1 below gives the value of **C** in terms of $\mathbf{a_1}$ and $\mathbf{a_2}$ which are unit vectors in a 2D graphene lattice and n and m are integers.

$$\mathbf{C} = n\mathbf{a_1}+m\mathbf{a_2} \quad \text{..... (1.1)}$$

Two crystallographically equivalent sites on a 2D graphene sheet are connected by the vector **C** and the chiral angle is the angle it makes with respect to the zigzag direction (Fig. 1.7). A tube is formed by rolling up the graphene sheet in such a way that the two points connected by the chiral vector coincide. Many number of chiral vectors can be envisaged in terms of pairs of inetegers (n,m), the limiting cases being $n = m \neq 0$ (armchair tube) and $n \neq 0$, $m=0$ (zigzag tube). For a nanotube defined by the index (n, m), the diameter, d, and the chiral angle, θ, are given in following equations 1.2 and 1.3, where $a=1.42\ (3)^{1/2}$ and $0 \leq \theta \leq 30°$.

$$D = a\,(m^2 + mn + n^2)^{1/2}/\pi \qquad \text{.....(1.2)}$$

$$\theta = \arctan\,(-\,(3)^{1/2}\,m)/2n + m) \qquad \text{.....(1.3)}$$

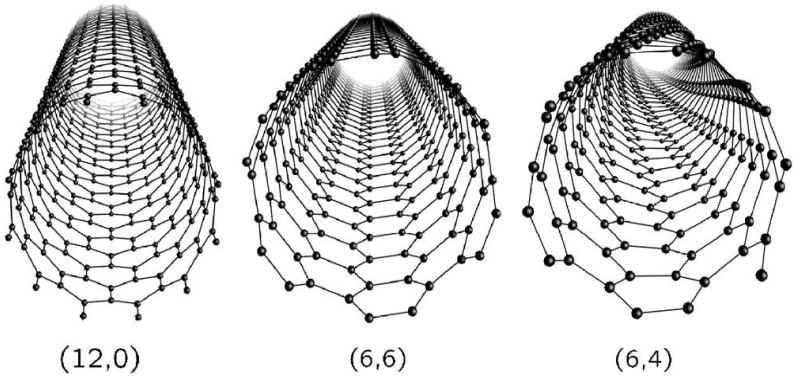

Fig. 1.6 atomic structures of (12, 0) zigzag, (6, 6) armchair and (6, 4) chiral nanotubes

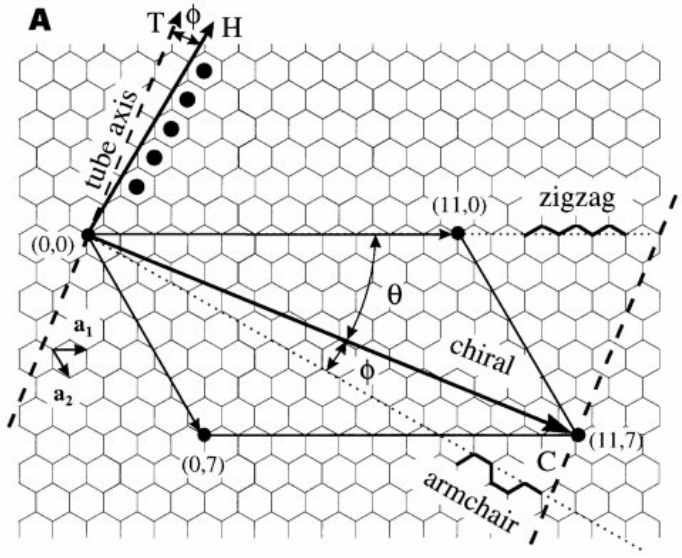

Fig. 1.7 The construction of a CNT from a single graphene sheet. By rolling up the sheet along the wrapping vector C, that is, such that the origin (0,0) coincides with point C, a nanotube indicated by indices (11, 7) is formed. Wrapping vectors along the dotted lines lead to tubes that are zigzag or armchair

Among the various characterization techniques, Raman spectroscopy, electron microscopy, diffraction techniques, UV-Vis spectroscopy are the most extensively used. The XRD pattern of MWNTs show only the (hk0) and the (001) reflections but no (hkl) reflections [118]. Lot of information regarding the structure of the nanotubes can be (and has already been) acquired from *Raman spectroscopy*. Using a zone-folding model, Jishi et al. [119] have calculated the Raman active phonon modes in the nanotubes. The main Raman features of the SWNTs includes radial breathing mode (RBM), the tangential G-band (derived from the graphite-like in-plane mode), the disorder-induced D-band, and its second-order harmonic, the 2 D-band (Fig. 1.8) [120]. The RBM is a bond-stretching out-of-plane phonon mode for which all the carbon atoms move coherently in the radial direction, and whose frequency ω_{RBM} is about 100–500 cm^{-1}. The RBM frequency is inversely proportional to the tube diameter and is expressed as $\omega_{RBM} = C/d_t$ *(*cm^{-1}*)* (*C* =248 cm^{-1} nm for isolated SWNTs on a SiO2 substrate). This dependence comes from the fact that the mass of all the carbon atoms along the circumferential direction is proportional to the diameter. It should be mentioned that several similar formulae have been proposed and a small correction to the formula comes from the effect of the substrate and from tube–tube interactions.

The G-band in carbon nanotubes occurring in the 1500– 1605 cm^{-1} range is basically derived from the Raman-allowed optical mode E_{2g} of 2D graphite by two zone folding the 2D graphene Brillouin zone into the 1D

nanotube Brillouin zone, noting that only modes with *A*, E_1, and E_2 symmetry are Raman active for single wall carbon nanotubes. The G-band is thus an intrinsic feature of carbon nanotubes that is closely related to vibrations in all sp^2 carbon materials. The most important aspect of the G-band is the characteristic Raman lineshape which differs in accordance with whether the nanotube is semiconducting or metallic, an intrinsic property of the nanotubes, allowing one to readily distinguish between metallic and semiconducting nanotubes [121].

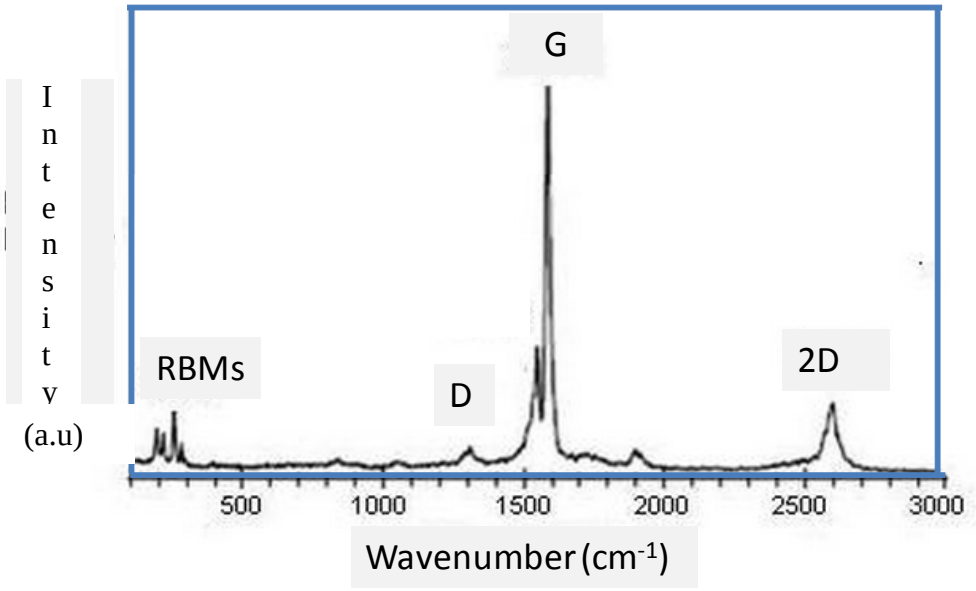

Fig. 1.8 Raman spectrum of HiPco SWNTs using a laser of wavelength of λ_{exc} = 633 nm. (from Ref. 120)

In fact, the G-band is the only band coming from a normal first order Raman scattering process. On the other hand, the 2D (~2600 cm^{-1}) and D (~1310 cm^{-1}) bands originate from a second-order process, involving two iTO

phonons near the K point for the 2D band or one iTO phonon and one defect in the case of the D-band. Since the 2D band is approximately twice the D band frequency authors prefer to call it the 2D band. Both the D and 2D bands exhibit a dispersive behavior since their frequencies in the Raman spectra change as a function of the energy of the incident laser.

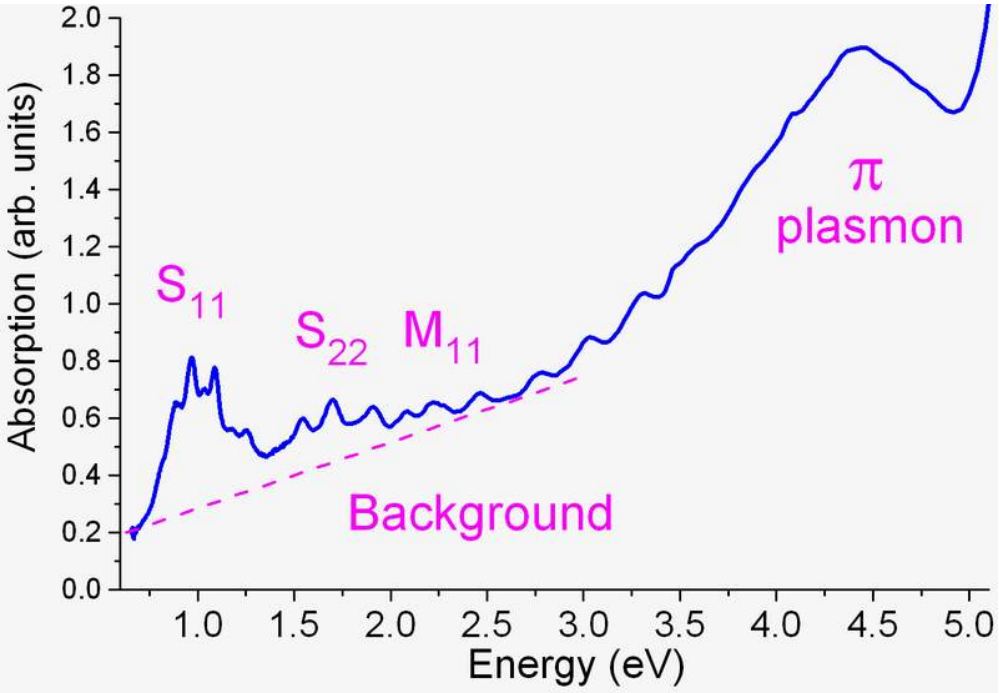

Fig. 1.9 Optical absorption spectrum of SWNTs

Optical absorption has also been used to study SWNTs. All spectroscopic processes in semiconducting and metallic SWNTs are attributed to transitions between corresponding van Hove singularities. The presence of energy gaps in induced by features such as doping, curvatures and bundling. A small energy gap at the Fermi level opens up in the case of metallic nanotubes due to the curvature of the graphene sheet. A tipical

optical spectrum of SWNTs is shown in Fig. 1.9. The near-infrared transitions designated at S_{11} and S_{22} arise from the inter-van Hove energy levels in semiconducting SWNTs while metallic SWNTs exhibit absorption bands (M_{11}) in the visible region.

Growth mechanisms

Several growth mechanisms are proposed for the formation of CNTs by the pyrolysis of hydrocarbons on the metal surfaces. The one suggested by Baker and Harris [122] has four steps in it. First step involves the decomposition of hydrocarbon on the metal surface to release hydrogen and carbon, which dissolves in the particle. In the second step, carbon diffuses through the metal particle and precipitates on the rear face to form the body of the filament. In step three, carbon forms a skin around the main filament body due the surface diffusion which helps in removing the carbon from the front face and hence keeps the active surface unblocked. Fourth step witnesses the overcoating and deactivation of the catalyst and subsequent termination of the tube growth. Oberlin et al. [123] proposed a mechanism in which bulk diffusion is insignificant and carbon is entirely transported around the particle by surface diffusion while Dai et al. [124] proposed a mechanism wherein carbon forms a hemispherical graphene cap on the catalyst particle and the nanotubes grow from such a yarmulke. An

important feature of this model is that it avoids dangling bonds at all stages of growth.

Apart from the above models, a number of growth models have also been proposed for the growth of MWNTs in the arc discharge method. Endo and Kroto [125] suggested that the tube formation process is a consequence of formation of fullerenes. Smalley, however pointed out that only the growth of outer layers is possible through such a mechanism. Iijima [126], on the other hand suggested that the termination of incomplete layers of carbon seen on the surface may arise because of the extension and thickening of the nanotubes by the growth of graphite islands on the surfaces of existing tubes. The nucleation of pentagons and heptagons on the open tube ends results in a change in the direction of the growing tube and some novel morphologies, including one where the tube turns around 180° during the growth, have been observed.

Applications of carbon nanotubes

The wide range of fascinating properties of carbon nanotubes provides attractive opportunities for potential technological applications [127, 128].

Carbon nanotubes can be used as electron sources for field-emission (FE) displays. Electrons can be easily emitted from CNT tips when a potential is applied between the CNT surface and an anode [129-136]. In particular, B-doped CNTs could exhibit enhanced field emission when compared to pristine CNTs. This phenomenon arises from the preferential

presence of B atoms at the nanotube tips, which results in an increased DOS close to the Fermi level.

Because of the high electrochemically accessible surface area of porous nanotube arrays, combined with their high electronic conductivity and useful mechanical properties, these materials are attractive as electrodes for devices that use electrochemical double-layer charge injection. Examples include supercapacitors, which have giant capacitances in comparison with those of ordinary dielectric-based capacitors, and electromechanical actuators that may eventually be used in robots [137-140].

SWNTs have also been grown directly onto atomic force microscope tips [141] to offer significant improvements in lateral AFM resolution, as compared with commercial silicon AFM tips. The resistance of SWNTs has also been found to be sensitive to various gases [142] implying sensor applications. It has been demonstrated by various groups [143, 144] that pure carbon SWNTs and MWNTs can be used to detect toxic gases and other species, because small concentrations are capable of producing large changes in the nanotubes conductance, shifting the Fermi level to the valence band, and generating hole-enhanced conductance. However, N-doped MWNTs have proved to be more efficient in this context.

SWNTs have nano-sized channels which can facilitate adsorption of liquids or gases. The adsorption properties of SWNTs with respect to methane, benzene and nitrogen have been studied [145]. The studies

indicate that SWNTs are good microporous materials with a total surface area above 400 m^2/g. The unique hexagonal packing of the SWNTs in the bundles offers ideal channels, thus allowing the realization of one-dimensional (1D) adsorbates.

1.5 Graphene

The mysterious two-dimensional form of carbon is named graphene, and it is probably the best-studied carbon allotrope theoretically. Graphene – planar, hexagonal arrangements of carbon atoms (Fig. 1.10) – is the starting point for all calculations on graphite, carbon nanotubes, and fullerenes[146, 147]. At the same time, Different attempts to synthesize these 2D atomic crystals have usually unsuccessful [148]. These difficulties are not surprising in light of the common belief that truly two-dimensional crystals cannot exist [149-152] (in contrast to the numerous, known *quasi*-two-dimensional systems). Moreover, during synthesis, any graphene nucleation sites will have very large perimeter-to-surface ratios, thus promoting collapse into other carbon allotropes.

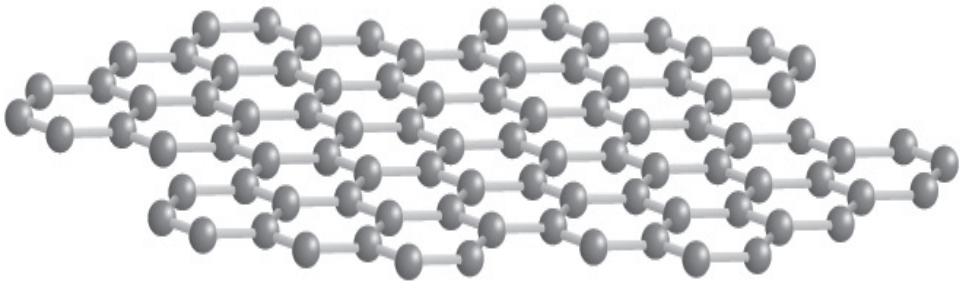

Fig. 1.10 Crystal structure of two-dimensional carbon allotrope (graphene)

A group of physicists from Manchester University, UK, led by Andre Geim and Kostya Novoselov, in 2004, used a very different approach to obtain graphene and lead a revolution in the field. The Nobel Prize in Physics 2010 was awarded jointly to Andre Geim and Konstantin Novoselov *"for groundbreaking experiments regarding the two-dimensional material graphene"*. They started with three-dimensional graphite and extracted a single sheet (a monolayer of atoms) using a technique called micromechanical cleavage [153, 154]. The researchers avoided all the issues with the stability of small crystallites, by using this top-down approach and starting with large, three-dimensional crystals. Furthermore, the same technique has been used by the group to obtain two-dimensional crystals of other materials [153], including boron nitride, some dichalcogenides, and the high-temperature superconductor Bi-Sr-Ca-Cu-O. This astonishing finding sends an important message: two-dimensional crystals do exist and they are stable under ambient conditions.

1.5.1 Electronic structure and unique properties

Single-layer graphene has two atoms per unit cell, giving rise to two conical points, K and K', per Brillouin zone where band crossing occurs (Fig. 1.11). Near these crossing points, the electron energy, E, is linearly dependent on the wave vector. As mentioned earlier, the charge carriers in single-layer graphene mimic relativistic particles and are described using the Dirac equation[155-157]. Although there is nothing relativistic about the electrons moving around the carbon atoms, their interaction with the

periodic potential of the honeycomb lattice of graphene gives rise to quasiparticles which are accurately described by the (2 + 1)-dimensional Dirac equation at low E, with an effective speed of light, $v_F \sim 10^6$ m s^{-1} [158]. The quasiparticles, called massless Dirac fermions, are electrons which have lost their rest mass m_0 (or can be considered as neutrinos that have acquired the electron charge e). The Dirac equation is a direct consequence of the crystal symmetry of single-layer graphene. Besides the linear dispersion of E with respect to the wave vector, the electron states of graphene near zero E (where the bands intersect) are composed of states belonging to different sublattices, whose relative contributions in the make-up of quasiparticles has to be taken into account. Because of the linear spectrum, quasiparticles in single-layer graphene are expected to behave differently from those in conventional metals or semiconductors, which exhibit a parabolic free electron-like dispersion relation.

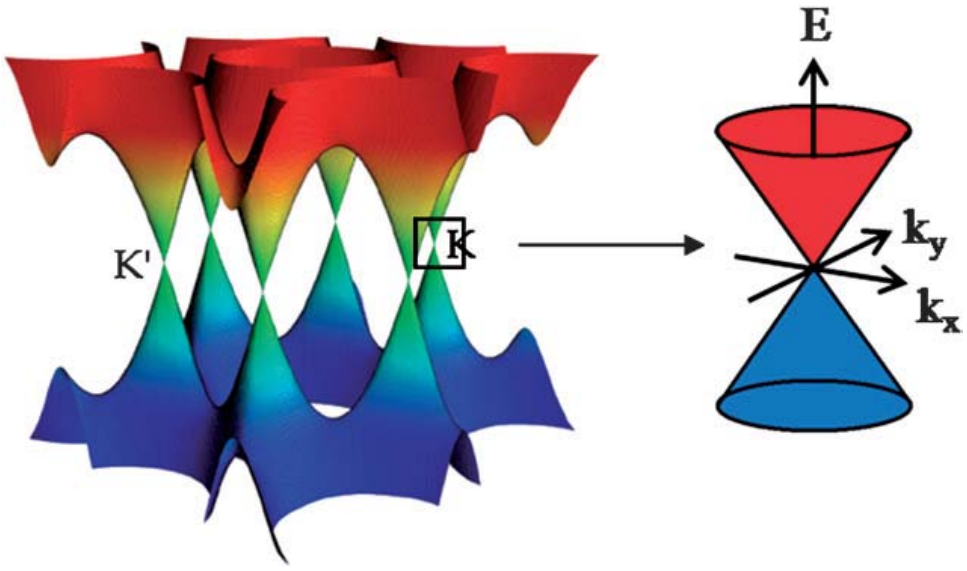

Fig. 1.11 Electronic band structure of single-layer graphene.

Single-layer graphene exhibits a strong ambipolar electric field effect such that charge carriers can be tuned continuously between electrons and holes in concentrations up to 10^{13} cm^{-2} and room-temperature mobilities of ~10,000 cm^2/V s can be induced by applying gate voltage [154]. Novoselov et al. [159] observed a half-integer quantum Hall effect (QHE) at low temperatures, where it shows an uninterrupted ladder of equidistant steps in Hall conductivity which persists through the neutrality (Dirac) point in single-layer graphene (Fig. 1.12). The sequence is shifted with respect to the standard QHE sequence by a factor of ½. The conductivity of graphene does not fall below a minimum value corresponding to a quantum unit of conductance even when the carrier concentration tends to zero [159]. A room-temperature half-integer QHE has also been observed in single-layer graphene [160]. An electrochemical resonator based on single-layer graphene has been fabricated by Bunch et al [161]. Micrometre-size sensors made from single-layer graphene are capable of detecting individual events when gas molecules such as NH_3, CO, H_2O and NO_2 attach to or detach from the surface [162]. The adsorbed molecules change the local carrier concentration leading to step-like changes in resistance. In the case of bi-layer graphene with two carbon layers, the nearest-neighbour tight-binding approximation predicts a gapless sate with parabolic bands touching at K and K' points, instead of conical bands [163]. Detailed considerations yield a small band overlap at larger energies. Bi-layer graphene can be treated as a gapless semiconductor [164]. The charge carriers have finite mass (massive Dirac

fermions). Bi-layer graphene exhibits an equally anomalous QHE [165]. The standard sequence of Hall plateaux has been observed, but the very first plateau at zero carrier concentration was missing (see inset of Fig. 1.12). This implies that bi-layer graphene remains metallic at the neutrality point [165]. A standard QHE with all the plateaux present can be recovered in bi-layer graphene by applying an electric field. The gate voltage changes the carrier concentration and induces an asymmetry between the two graphene layers, resulting in a semiconducting gap [166, 167]. Although graphene is supposed to be flat, ripples occur to eliminate the effect of thermal fluctuations.

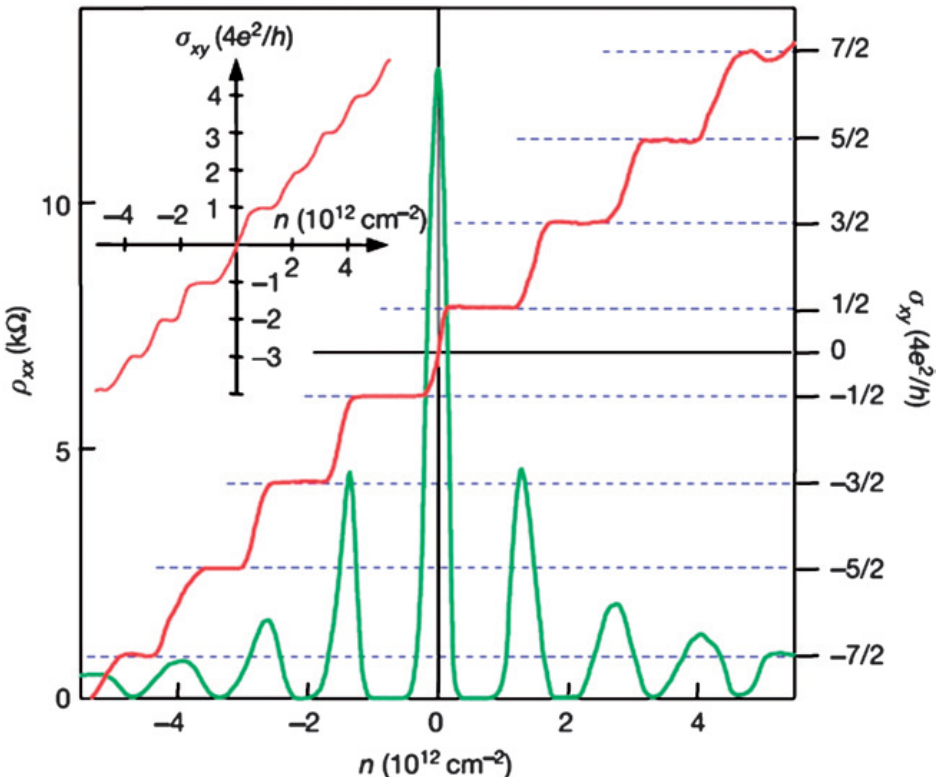

Fig. 1.12 Hall conductivity (σ_{xy}) and longitudinal resistivity (ρ_{xx}) of single-layer graphene as a function of carrier concentration at B = 14 T and T = 4K. Inset shows the Hall conductivity of bi-layer graphene. (from ref. 29).

1.5.2 Synthesis

Single- or few-layer graphene has been grown on metal substrates epitaxially by chemical vapour deposition of hydrocarbons [168] and by thermal decomposition of SiC [169]. Although, graphite flakes with 20-100 layers thick can be obtained easily by micromechanical cleavage of graphite, only recently Giem and co-workers [154] have successfully detected the presence of single-layer as well as bilayer graphene. The critical ingredient to their success was the observation that graphene becomes visible in an optical microscope if placed on top of a Si wafer with a carefully chosen thickness of SiO_2, owing to a feeble interference-like contrast with respect to an empty wafer. Even a small change in SiO_2 thickness (say only a 5% difference, 315 nm instead of the current standard of 300 nm) can make single-layer graphene completely invisible.

Several methods have been explored to prepare graphene in large quantities and they generally produce few-layer graphenes [170]. The methods are chemical vapor deposition of camphor [171] conversion of nanodiamond [172] and exfoliation of graphitic oxide [173] In the first method, camphor is pyrolysed over nickel nanoparticles at 770 ^oC in the presence of argon. The method to prepare DG involves annealing nanodiamond at 1650 ^oC or higher in an He atmosphere. In the product there is always some diamondlike particles admixed with graphene. The most popular method to prepare graphene is by the exfoliation of graphitic oxide. Graphitic oxide is prepared by reacting graphite with a mixture of

concentrated nitric acid and concentrated sulfuric acid with potassium chlorate at room temperature for 5 days [174]. Exfoliation is carried out by giving a sudden thermal shock to graphitic oxide in a long quartz tube at 1050 ^{o}C under an Ar atmosphere. Recently, an arc-discharge method involving evaporation of graphite electrodes in a hydrogen atmosphere has been found for preparing graphene flakes in our laboratory. The presence of H_2 during the arc-discharge process terminates the dangling carbon bonds with hydrogen and prevents the formation of closed structures, [175, 176] such as rolling of sheets into nanotubes and graphitic polyhedral particles. Using microwave plasma-enhanced CVD, under a flow of a methane/hydrogen mixture, micrometer-wide flakes consisting of few-layer graphene sheets (four to six atomic layers) have been prepared on quartz and silicon by the controlled recombination of carbon radicals in the microwave plasma [177].

1.5.3 Raman spectroscopy

Raman spectroscopy has proved to be an essential tool to characterize graphene [178-182]. Raman spectra of graphenes with increasing the number of layers (n = 1 to 19) along with HOPG (n = infinity) has been shown in Fig. 1.11 [178]. The strongest first order band at 1582 cm^{-1} is the G-band. The intensity of the G-band increases with the increasing numbers of layers. A shoulder around 1600 cm^{-1} on the G-band, designated as the G' band, appears in few-layer graphenes and this band is defect-related. Another first-

order band called the D-band (~1350 cm^{-1}) is inactive in single-layer graphene and is observed generally at the sample edges [178, 182]. The strongest second-order band is observed around 2700 cm^{-1} (2D band) [182]. Single-layer graphene can be distinguished from bi- and few-layer graphene by the width of the 2D band. The single 2D peak in single-layer graphene often splits into different peaks in bi- and few-layer graphenes. Raman spectra of graphenes are understood on the basis of the double-resonant Raman process involving phonons within the first Brillouin zone of graphite [182]. It is to be noted that though the 2D band is formally the overtone of the D band, the phonon-process and the phonon-electron interaction associated with them are different. The ratio of the intensities of the G and D bands, I_G/I_D is related to the in-plane crystallite size of few-layer graphene samples [181]. The ratio of intensities of the 2D and G bands is sensitive to hole or electron doping, as will be shown later. Changes in the Raman spectra due to changes in the number of layers (Fig. 1.13) or due to doping reflect the evolution of the electronic structure and electron–phonon interactions. Temperature-dependent Raman studies on single and bi-layer by Calizo et al [183] have enabled the determination of the temperature coefficient of the G band. It must be noted that the D and 2D bands cannot be used to determine the number of layers, but are useful to investigate electronic effects.

1.5.4 Doping

Tuning physicochemical properties by chemical modification of materials becomes necessary in many applications. One way of achieving this control is by elemental doping, a method effectively used in semiconductor silicon technology. For example, nitrogen atoms in silicon lock dislocations to increase mechanical strength [184, 185]. Effects of doping silicon with phosphorous and other elements with different oxidation states have been well documented. Chemical substitution brings about significant changes in carbon materials as well. In particular, substitution of boron or nitrogen in carbon nanostructures renders them p-type or n-type, respectively.

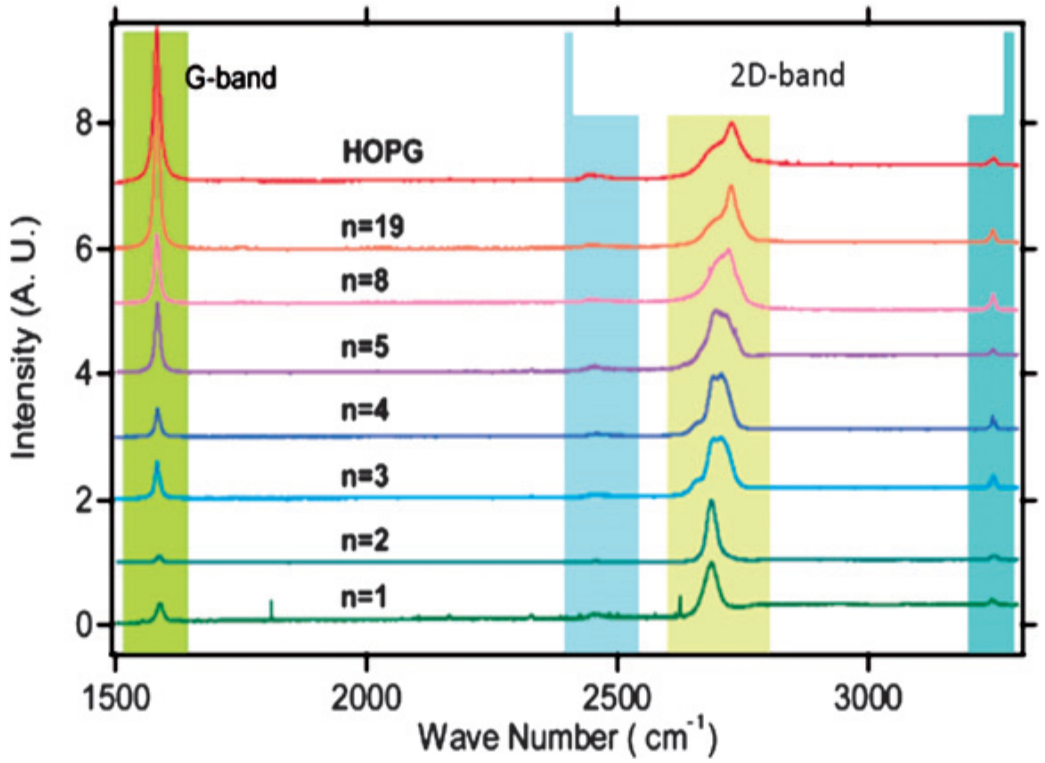

Fig. 1.13 Raman spectra of graphenes with increasing the number of layers (n = 1 to 19) along with HOPG (n = infinity). (Reproduced with permission from ref. 16a).

There are some methods to synthesize nitrogen doped graphene in the literature. N-doped graphene (up to 9 at.% N) has been prepared by a CVD process over Cu/Si substrate using CH_4 and NH_3 as the C and N sources, respectively [186]. N-doped reduced graphene oxide (GO) sheets up to 5% doping can be prepared through thermal annealing of GO in ammonia [187]. It is reported that graphene nanoribbons (GNRs) can be functionalized by nitrogen species by high-power electrical annealing in NH_3 [188].

Doping can be achieved by different ways. One of them is elemental doping which has been discussed above. Electrochemical method and molecular charge transfer also can be sued to dope graphene. It has been demonstrated recently that a top-gated single-layer graphene transistor is able to reach doping levels up to 5 x 10^{13} cm^{-2} by employing in-situ Raman measurements to monitor doping [189]. The G band stiffens and sharpens for both electron- and hole-doping, but the 2D band shows a different response to holes and electrons. The ratio of the intensities of the G and 2D bands shows a strong dependence on doping, making it a sensitive parameter to monitor doping. Electron-donor and -acceptor molecules also have marked effects on the electronic structure and properties of graphene [190, 191]. Thus, electron-donor molecules, such as aniline and tetrathiafulvalene (TTF), soften the Raman G band while electron-acceptor molecules, such as nitrobenzene and tetracyanoethylene (TCNE), stiffen the G band.

References

[1] J. Gribbin, The Scientists, Random House, New York, **2004**.

[2] T. Philbin, The 100 Greatest Inventions of All Time, Kensington Publishing Corp, New York, **2003**.

[3] A. N. Goldstein, Handbook of Nanophase Materials, New York, **1997**.

[4] R. P. Feynman, A lecture in engineering science, in California Institute of Technology, February, **1960**.

[5] L. Dai, Carbon nanotechnology, Elsevier, **2006**.

[6] E. K. Drexler *Proc. Natl. Acad. Sci. USA*. **1981**, 78, 5275.

[7] E. K. Drexler, Engines of Creation—The Coming Era of Nanotechnology, Anchor Press/Doubleday, Garden City, N.Y, **1986**.

[8] G. Binnig, H. Rohrer *Rev Mod. Phys.* **1987**, 59, 615.

[9] Y. Xia, P. Yang, Y. Sun, Y. Wu, B. Mayers, B. Gates, Y. Yin, F. Kim, H. Yan *Adv. Mater.* **2003**, 15, 353.

[10] G. U. Kulkarni, P. J. Thomas, C. N. R. Rao The Chemistry of Nanomaterials, p. 51, Wiley-VCH, Weinheim, , **2004**.

[11] T. Vossmeyer, L. Katsikas, M. Giersig, I. G. Popovic, K. Diener, A. Chemseddine, A. Eychmuller, H. Weller *J. Phys. Chem.* **1994**, 98, 7665.

[12] O. I. Micic, K. M. Jones, A. Cahill, A. J. Nozik *J. Phys. Chem. B.* **1998**, 102, 9791.

[13] M. Bruchez, M. Moronne, P. Gin, S. Weiss, A. P. Alivisatos *Science.* **1998**, 281, , 2013.

[14] X. S. Peng, G. W.Meng, X. F. Wang, Y. W. Wang, J. Zhang, L. D. Z. X. Liu *Chem. Mater.* **2002**, 14, , 4490.

[15] R. G. Nuzzo, D. L. Allara *J. Am. Chern. Soc.* **1983**, 105, 4481.

[16] A. Harriman, G. R. Millward, P. Nata, M. C. Richoux, J. M. Thomas *J. Phys. Chem.* . **1988**, 92, 1286.

[17] D. Mandler, I. Vlilner *J. Phys. Chem.* **1987**, 91, 3600.

[18] K. L. Tsai, J. L. Dai *Chem. Mater.* **1993**, 5, 540.

[19] S. H. Yu, J. Yang, Z. H. Han *J. Mater. Chem.* **1999**, 9, 1283.

[20] X. Chen, R Fan *Chem. Mater.* **2001**, 13, 802.

[21] M. Y. Han, L. Zhow, C. H. Quek , S. F. Y. Li, W. Huang *Chern. Phys. Lett.* **1998**, 287, 47.

[22] M. Marandi, N. Taghavinia, A. I. Zad, A. Iraji zad, S. M. Mahdavi *Nanotechnolgy*. **2005**, 16, 334.

[23] M. Nirmal , L. E. Brus *Acc. Chem. Res.* **1999**, 32, 407.

[24] A. P. Alivisatos *Science*. **1996**, 271, 933.

[25] V. L. Colvin, M. C. Schlamp, A. P. Alivisatos *Nature*. **1994**, 370, 354.

[26] B. O'Regan, M. Gratzel *Nature*. **1991**, 353, 737.

[27] M. Shim , P. Guyot-Sionnest *Nature*. **2000**, 407, 26.

[28] M. Brust, D. J. Schiffrin, D. Bethell, C. J. Kiely *Adv. Mater.* **1995**, 7, 795.

[29] M. Aslam, I. S. Mulla, K. Vijayamohanan *Appl. Phys. Lett.* **2001**, 79, 689.

[30] B. Alperson, S. Cohen, I. Rubinstein, G. Hodes *Phys. Rev. B.* **1995**, 53, 17017.

[31] D. L. Klein, P. L. McEuen, J. E. Bowen Katari, A. P. Alivisatos *Appl. Phys. Lett.* **1996**, 68, 2574.

[32] S. A. Blanton, A. Dehestani, P. C. Lin, P. Guyotsionnest *Chem.Phys. Lett.* **1994**, 229, 1994.

[33] S. A. Empedocles, D. J. Norris, M. G. Bawendi *Phys. Rev. Lett.* **1996**, 77, 3873.

[34] D. L. Klein, R. Roth, A. K. L. Lim, A. P. Alivisatos, P. L. McEuen *Nature*. **1997**, 389, 699.

[35] C. B. Murray, C. R. Kagan, M. G. Bawendi *Ann. Rev. Mater. Sci.* **2000**, 30, 545.

[36] M. V. Artemyev, U. Woggon, H. Jaschinski, L. I. Gurinovich, S. V. Gaponenko *J. Phys. Chem. B*. **1999**, 104, 11617.

[37] M. V. Artemyev, A. I. Bibik, L. I. Gurinovich, S. V. Gaponenko, U. Woggon *Phys. Rev. B.* **1999**, 60, 1504.

[38] X. Duan, Y. Huang, Y. Cui, J. Wang, C.M. Lieber *Nature*. **2001**, 409, 66.

[39] G. Y. Tseng, J. C. Ellenbogen *Science*. **2001**, 294, 1293.

[40] N.A. Melosh, A. Boukai, F. Diana, B. Gerardot, A. Badolato, P.M. Petroff , J.R. Heath *Science*. **2002**, 300, 112.

[41] C.N.R. Rao, F. L. Deepak, G. Gundiah, A. Govindaraj *Prog. Solid State Chem.* **2003**, 31, 5.

[42] A. Govindaraj, C. N. R. Rao, The Chemistry of Nanomaterials, Wiley-VCH, Weinheim, **2004**.

[43] F. Cerrina, C. Marrian *MRS Bull.* **1996**, 21, 56.

[44] S. Hong, J. Zhu, C. A. Mirkin *Science*. **1999**, 286, 523.

[45] S. Matsui, Y. Ochiai *Nanotechnology*. **1996**, 7, 247.

[46] J. M. Gibson *Phys. Today*. **1997**, 56.

[47] Y. Xia, J. A. Rogers, K. E. Paul, G. M. Whitesides *Chem. Rev.* **1999**, 99, 1823.

[48] E. I. Givargizov, Highly Anisotropic Crystals, Reidel, Dordrecht, The Netherlands, **1987**.

[49] M. Volmer , I. Estermann *Z. Phys.* **1921**, 7, 13.

[50] R. S. Wagner , W. C. Ellis *Appl. Phys. Lett.* **1964**, 4, 89.

[51] A. M. Morales , C. M. Lieber *Science*. **1998**, 279, 208.

[52] M.H. Huang, S. Mao, H. Feick, H. Yan, Y. Wu, H. Kind, E. Weber, R. Russo, P. Yang *Science*. **2001**, 292, 1897.

[53] Y. Wu , P. Yang *Chem. Mater.* **2000**, 12, 605.

[54] M. H. Huang, Y. Wu, H. Feick, N. Tran, E. Weber, P. Yang *Adv. Mater.* **2001**, 13, 113.

[55] Y. Wang, G. Meng, L. Zhang, C. Liang, J. Zhang *Chem. Mater.* **2002**, 14, 1773.

[56] R. S. Wagner, Wliey-Interscience, Whsiker Technology, New York, **1970**.

[57] Z. W. Pan, Z. R. Dai, Z. L. Wang *Science*. **2001**, 291, 1947.

[58] C. N. R. Rao, G. Gundiah, F. L. Deepak, A. Govindaraj, A. K.Cheetham *J. Mater. Chem.* **2004**, 14, 440.

[59] P. Yang , C. M. Lieber *J. Mater. Res.* **1997**, 12, 2981.

[60] P. Yang , C. M. Lieber *Science*. **1996**, 273, 1836.

[61] Huczko *Appl. Phys. A: Mater. Sci. Process*. **2000**, 70, 365.

[62] B. C. Satishkumar, A. Govindaraj, E. M. Vogl, L. Basumallick, C. N. R. Rao *J. Mater. Res.* **1997**, 12, 604.

[63] B. C. Satishkumar, A. Govindaraj, M. Nath, C. N. R. Rao , , *J. Mater. Chem.* **2000**, 10, 2115.

[64] C. N. R. Rao, B. C. Satishkumar, A. Govindaraj *Chem. Comm.* **1997**, 1581.

[65] J. Stejny, R. W. Trinder, J. Dlugosz *J. Mater. Sci.* **1981**, 16, 3161.

[66] B. Mayers, Y. Xia *J. Mater. Chem.* **2002**, 12, 1875.

[67] B. Gates, B. Mayers, B. Cattle *Adv. Funct. Mater.* **2002**, 12, 219.

[68] B. Messer, J. H. Song, M. Huang, Y. Wu, F. Kim, P. Yang *Adv. Mater.* **2000**, 12, 1526.

[69] P. Buffat , J. P. Borel *Phys. Rev. B*. **1976**, 13, 2287.

[70] Y. Wu , P. Yang *Adv. Mater.* **2001**, 13, 520.

[71] Y. Y. Wu , P. Yang *Appl. Phys. Lett.* **2000**, 77, 43.

[72] T. H. X. Lu, K. P. Johnston, B. A. Korgel *Nano Lett.* **2003**, 3, 93.

[73] J. F. Wang, M. S. Gudiksen, X. F. Duan, Y. Cui, C. M. Lieber *Science*. **2001**, 293, 1455.

[74] H. W. Kroto, J. R. Heath, S. C. OBrien, R. F Curl, R. E. Smalley *Nature*. **1985**, 318, 162.

[75] S. Iijima *Nature*. **1991**, 354, 56.

[76] H. Marsh, Introduction to Carbon Science, Butterworths, London, **1989**.

[77] M. S. Dresselhaus, G. Dresselhaus , P. Eklund, Science of Fullerenes and Carbon Nanotubes, Academic, San Diego, **1996**.

[78] M. Meyyappan, Carbon Nanotubes: Science and Applications, CRC Press, Boca Raton, City, **2005**.

[79] P. J. F. Harris in Carbon Nanotubes and Related Structures—New Materials for the Twenty-First Century, Cambridge, **2001**.

[80] T. W. Ebbesen, P. M. Ajayan *Nature*. **1992**, 358, 220.

[81] T.W. Ebbesen, H. Hiura, J. Fujita, Y. Ochiai, S. Matsui , K. Tanigaki *Chem. Phys. Lett.* . **1993**, 209, 83.

[82] S. Seraphin, D. Zhou, J. Jiao, J.C. Withers , R. Loufty *Carbon*. **1993**, 31, 685.

[83] S. Iijima, T. Ichihashi *Nature*. **1993**, 363, 603.

[84] D. S. Bethune, C.H. Kiang, M. S. de Vries, G. Gorman, R. Savoy, J. Vazquez, R. Beyers *Nature*. **1993**, 363, 605.

[85] Y. Satio, M. Okuda, N. Fujimoto, T. Yoshikawa, M. Tomita , T. Hayashi *Jpn. J. Appl. Phys.* **1994**, 33, L526.

[86] D. Zhou, S. Seraphin , S. Wang *Appl. Phys. Lett.* **1994**, 65, 1593.

[87] S. Subramoney, R. S. Ruoff, D. C. Lorents , R. Malhotra *Nature*. **1993**, 366, 637.

[88] S. Seraphin , D. Zhou *Appl. Phys. Lett.* **1994**, 64, 2087.

[89] Y. Saito, M. Okuda , T. Koyama *Surf. Rev. Lett.* **1996**, 3, 63.

[90] Y.S. Park, K.S. Kim, H. J. Jeong, W.S. Kim, J.M. Moon, K.H. An, D.J. Bae, Y.S. Lee, G. S. Park, Y.H. Lee *Synt. Metals* **2002**, 126, 245.

[91] T. Guo, P. Nikolaev, A.G. Rinzler, D. Tomanek, D.T. Colbert , R.E. Smalley *J. Phys. Chem.* **1995**, 99, 10694.

[92] T. Guo, e. al. *Chem. Phys. Lett.* . **1995**, 243, 49.

[93] A. Thess, R. Lee, P. Nikolaev, H. J. Dai, P. Petit, J. Robert, C. H. Xu, Y.H. Lee, S.G. Kim, A.G. Rinzler, D.T. Colbert, G.E. Scuseria, D. Tomanek, J.E. Fischer, R.E. Smalley *Science*. **1996**, 273, 483.

[94] C. Journet, W.K. Maser, P. Bernier, A. Loiseau, M. L. de la Chapelle, S. Lefrant, P. Deniard, R. Lee , J.E. Fischer *Nature*. **1997**, 388, 756.

[95] G.S. Duesberg, J. Muster, H.J. Byrne, S. Roth, M. Burghard *Appl. Phys. A*. **1999**, 69, 269.

[96] A.G. Rinzler, J. Liu, H. Dai, P. Nikolaev, C.B. Huffman, F.J. Rodriguez-Macias, P.J. Boul, A.H. Lu, D.Heymann, D.T. Colbert, R.S. Lee, J.E. Fischer, A.M. Rao, P.C. Eklund, R.E. Smalley *Appl. Phys. A*. **1998**, 67, 29.

[97] A. Fonseca, K. Hernadi, J.B. Nagy, D. Bernaerts, A.A. Lucas *J. Mol. Catal. A*. **1996**, 107, 159.

[98] A. Fonseca, K. Hernadi, P. Piedigrosso, J.F. Colomer, K. Mukhopadhyay, R. Doome, S. Lazarescu, L.P. Biro, Ph. Lambin, P.A. Thiry, D. Bernaerts, J.B. Nagy *Appl. Phys. A*. **1998**, 67, 11.

[99] I. Williems, Z. Konya, J.F. Colomer, G. Van Tendeloo, N. Nagaraju, A. Fonseca, J.B. Nagy *Chem. Phys. Lett.* **2000**, 317, 71.

[100] C. N. R. Rao, A. Govindaraj in Nanotubes and Nanowires, The RSC Nanoscience & Nanotechnology series, Royal Society of Chemistry, **2005**.

[101] T. W. Ebbesen, J. Tabuchi , K. Tanigaki *Chem. Phys. Lett.* **1992**, 191, 336.

[102] Y. Saito, T. Yoshikawa, M. Inagaki, M. Tomita , T. Hayashi *Chem. Phys. Lett.* **1994**, 204, 277.

[103] D. H. Robertson, D. W. Brenner , C. T. White *J. Phys. Chem.* **1992**, 96, 6133.

[104] S. Amelinckx, X. B. Zhang, D. Bernaerts., X. F. Zhang, V. Ivanov , J. B. Negy *Science*. **1994**, 265, 635.

[105] A. Maiti, C. T. Brabec, J. Bernholc *Phys. Rev. B.* **1997**, 55, R6097.

[106] A. Moisala, A. G Nasibulin, E.I. Kaeuppinen *J. Phys.: Condens. Matter.* **2003**, 15, S3011.

[107] K.Tohji, T. Goto, H. Takahashi, Y. Shinoda, N. Shimizu, B. Jeyadevan, I. Matsuoka, Y. Saito, A. Kasuya, T. Ohsuna, K. Hiraga, Y. Nishina *Nature*. **1996**, 383, 679.

[108] K. Tohji, T. Goto, H. Takahashi, Y. Shinoda, N. Shimizu, B. Jeyadevan, I. Matsuoka, Y. Saito, A. Kasuya, S. Ito, Y. Nishina *J. Phys. Chem.* **1997**, B101, 1974.

[109] Y. Miyamoto, A. Rubio, M. L. Cohen , S. G. Louie *Phys. Rev. B.* **1994**, 50, 4976.

[110] B. C. Satishkumar, A. Govindaraj, K. R. Harikumar, J. P. Zhang, A. K. Cheetham, C. N. R. Rao *Chem. Phys. Lett.* **1999**, 300, 473.

[111] O. Stephan, P. M. Ajayan, C. Colliex, Ph. Redlich, J. M. Lambert, P. Bernier , P. Lefin *Science*. **1994**, 266, 1683.

[112] Y. Zhang, H. Gu, K. Suenaga, S. Iijima *Chem. Phys. Lett.* **1997**, 279, 264.

[113] M. Terrones, A. M. Benito, C. Mantega-Diego, W. K. Hsu, O. I. Osman, J. P. Hare, D. G. Reid, H. Terrones, A. K. Cheetham, K. Prassides, H. W. Kroto , D. R. M. Walton *Chem. Phys. Lett.* **1996**, 257, 576.

[114] R. Sen, B. C. Satishkumar, A. Govindaraj, K. R. Harikumar, G. Raina, J. P. Zhang, A. K. Cheetham , C. N. R. Rao *Chem. Phys. Lett.* **1998**, 287, 671.

[115] M. Nath, B. C. Satishkumar, A. Govindaraj, C. P. Vinod , C. N. R. Rao *Chem. Phys. Lett.* **2000**, 322, 333.

[116] S. L. Sung, S. H. Tsai, C. H. Tseng, F. K. Chiang, X. W. Liu , H. C. Shih *Appl. Phys. Lett.* **1999**, 74, 197.

[117] K. Suenaga, M. Yusadaka, C. Colliex, S. Iijima *Chem. Phys. Lett.* **2000**, 316, 365.

[118] R. Sheshadri, A. Govindaraj, H. N. Aiyer, R. Sen, G. N. Subbanna, A. R. Raju, C. N. R. Rao *Current Science*. **1994**, 66, 839.

[119] J. M. Holden, P. Zhou, X-X Bi, P.C. Eklund, S. Bandow, R. A. Jishi, L. Venkataraman, M. S. Dresselhaus, G. Dresselhaus *Chem. Phys. Lett.* **1994**, 220, 186.

[120] R. Graupner *J. Raman Spectrosc.* **2007**, 38, 673.

[121] M. S. Dresselhaus, G. Dresselhaus, A. Jorio, A. G. S. Filho, R. Saito *Carbon* **2002**, 40, 2043.

[122] R. T. K. Baker, P. S. Harris in *Chemistry and Physics of Carbon, Vol. 14* (Ed. P. A. T. P. L. Walker, Marcel Dekker), New York, **1978**.

[123] H. Dai, A. Z. Rinzler, P. Nikolaev, e. al. *Chem. Phys. Lett.* **1996**, 260, 471.

[124] A. Oberlin, M. Endo, T. Koyama *J. Cryst. Growth.* **1976**, 32, 335.

[125] M. Endo, H. W. Kroto *J. Phys. Chem.* **1992**, 96, 6941.

[126] S. Iijima, P. M. Ajayan, T. Ichihashi *Phys. Rev. Lett.* **1992**, 69, 3100.

[127] W. A. d. Heer *MRS Bulletin*. **2004**, 354, 281.

[128] J. Robertson *Materials Today*. **2004**, 46.

[129] N. d. Jonge, J. -M. Bonard *Phil. Trans. R. Soc. Lond. A*. **2004**, 362, 2239.

[130] W. I. Milne, K.B.K. Teo, G.A.J. Amaratunga, P. Legagneux, L. Gangloff, J.-P. Schnell, V. Semet, V. T. Binh, O. Groening *J. Mater. Chem.* **2004**, 14, 933.

[131] W. A. de Heer, A. Chatelain , D. Ugarte *Science*. **1995**, 270, 1179.

[132] A. G. Rinzler, J. H. Hafner, P. Nikolaev, L. Lou, S. G. Kim, D. Tomanek, P. Nordlander, D. T. Colbert , R. E. Smalley *Science*. **1995**, 269, 1550.

[133] N. S. Lee, D. S. Chung, I. T. Han, J. H. Kang, Y. S. Choi, H. Y. Kim, S. H. Park, Y. W. Jin, W. K. Yi, M. J. Yun, J. E. Jung, C. J. Lee, Y. J. H, S. H. Jo, C. G. Lee , J. M. Kim *Diamond Relat. Mater.* **2001**, 10, 265.

[134] Y. Saito , S. Uemura *Carbon*. **2000**, 38, 169.

[135] R. Rosen, W. W. Simendinger, C. Debbault, H. Shimoda, L. Fleming, B. Stoner , O. Zhou *Appl. Phys. Lett.* **2000**, 76, 1668.

[136] H. Sugie, M. Tanemura, V. Filip, K. Iwata, K. Takahashi, F. Okuyama *Appl. Phys. Lett.* . **2001**, 78, 2578.

[137] K. H. An, W. S. Kim, Y. S. Park, J.-M. Moon, D. J. Bae, S. C. Lim, Y. S. Lee, Y. H. Lee *Adv. Funct. Mater.* **2001**, 11, 387.

[138] C. Niu, E. K. Sickel, R. Hoch, D. Moy, H. Tennent *Appl. Phys. Lett.* **1997**, 70, 1480.

[139] C. Niu, J. Kupperschmidt, R. Hock in Proceedings of the 39th Power Sources Conference (Maple Hill, NJ) **2000**, pp.314–317.

[140] R. H. Baughman, C. Cui, A. A. Zakidov, Z. Iqbal, J. N. Berisci, G. M. Spinks, G. G. Wallace, A. Mazzoldi, D. De Rossi, A. G. Rinzler, O. Jaschinski, S. Roth , M. Kertesz *Science*. **1999**, 284, 1340.

[141] C. L. Cheung, J.H. Hafner, T.W. Odom, K. Kim, C.M. Lieber *Appl. Phys. Lett.* **2000**, 76, 3136.

[142] J. Kong, N. Franklin, C. Zhou, M. Chapline, S. Peng, K. Cho, H. Dai *Science*. **2000**, 287, 622.

[143] S. S. Wong, E. Joselevich, A. T. Wolley, C. L. Cheung, C. M. Liebe, . *Nature*. **1998**, 394, 52.

[144] P. G. Collins *Science*. **2000**, 287, 1801.

[145] M. Eswaramoorthy, R. Sen , C. N. R. Rao *Chem. Phys. Lett.* **1999**, 304, 207.

[146] M. I. Katsnelson *Mater. Today*. **2007**, 10, 20.

[147] C. N. R. Rao, Kanishka Biswas, K. S. Subrahmanyam, A. Govindaraj *J. Mater. Chem.* **2009**, 19, 2457

[148] C. Oshima, A. Nagashima *J. Phys.: Condens. Matter.* **1997**, 9, 1.

[149] R. E.Peierls *Helv. Phys. Acta*. **1934**, 7, 81.

[150] L. D. Landau *Phys. Z. Sowjet Union*. **1937**, 11, 26.

[151] L. D. Landau, E. M. Lifshitz, Statistical Physics, Part I,, Pergamon, Oxford, UK, **1980**.

[152] N. D. Mermin *Phys. Rev. B*. **1968**, 176, 250.

[153] K. S. Novoselov, D. Jiang, F. Schedin, T. J. Booth, V. V. Khotkevich, S. V. Morozov, A. K. Geim *Proc. Natl. Acad. Sci. USA*. **2005**, 102, 10451.

[154] K. S. Novoselov, A. K. Geim, S. V. Morozov, D. Jiang, Y. Zhang, S. V. Dubonos, I. V.Grigorieva, A. A. Firsov *Science*. **2004**, 306, 666.

[155] G. W. Semenoff *Phys. Rev. Lett.* **1984**, 53, 2449.

[156] F. D. M. Haldane *Phys. Rev. Lett.* **1988**, 61, 2015.

[157] M. I. Katsnelson, K. S. Novoselov , A. K. Geim *Nature Phys.* **2006**, 2, 620.

[158] A. K. Geim, K. S. Novoselov *Nature Mater.* **2007**, 6, 183.

[159] K. S. Novoselov, A. K. Geim, S. V. Morozov, D. Jiang, M. I. Katsnelson, I. V. Grigorieva, S. V. Dubonos, A. A. Firsov *Nature*. **2005**, 438, 197.

[160] K. S. Novoselov, Z. Jiang, Y. Zhang, S. V. Morozov, H. L. Stormer, U. Zeitler, J. C. Maan, G. S. Boebinger, P. K. and, A. K. Geim *Science*. **2007**, 315, 1379.

[161] J. S. Bunch, A. M. V. D. Zande, S. S. Verbridge, I. W. Frank, D. M. Tanenbaum, J. M. Parpia, H. G. Craighead, P. L. McEuen *Science*. **2007**, 315, 490.

[162] F. Schedin, A. K. Geim, S. V. Morozov, E. W. Hill, P. Blake, M. I. Katsnelson, K. S. Novoselov *Nature Mater.* **2007**, 6, 652.

[163] K. S. Novoselov, E. McCann, S. V. Morozov, V. I. Fal'ko, M. I. Katsnelson, U. Zeitler, D. Jiang, F. Schedin, A. K. Geim *Nat. Phys.* **2006**, 2, 177.

[164] B. Partoens , F. M. Peeters *Phys. Rev. B.* **2006**, 74, 075404.

[165] K. S. Novoselov, E. McCann, S. V. Morozov, V. I. Fal'ko, M. I. Katsnelson, U. Zeitler, D. Jiang, F. Schedin, A. K. Geim *Nature Nanotechnol.* **2006**, 2, 177.

[166] E. McCann *Phys. Rev. B.* **2006**, 74, 161403.

[167] E. V. Castro, K. S. Novoselov, S. V. Morozov, N. M. R. Peres, J. M. B. Lopes dos Santos, J. Nilsson, F. Guinea, A. K. Geim, A. H. C. Neto *Phys. Rev. Lett.* **2007**, 99, 216802.

[168] T. A. Land, T. Michely, R. J. Behm, J. C. Hemminger, G. Comsa *Surf. Sci.* . **1992**, 264, 261.

[169] A. J. van Bommel, J. E. Crombeen, A. van Tooren *Surf. Sci.* **1975**, 48, 463.

[170] K. S. Subrahmanyam, S. R. C. Vivekchand, A. Govindaraj, C. N. R. Rao *J. Mater. Chem.* **2008**, 18, 2007.

[171] P. R. Somani, S. P. Somani, M. Umeno *Chem. Phys. Lett.* **2006**, 430, 56.

[172] O. E. Andersson, B. L. V. Prasad, H. Sato, T. Enoki, Y. Hishiyama, Y. Kaburagi, M. Yoshikawa , S. Bandow *Phys. Rev. B.* **1998**, 58, 16387.

[173] H. C. Schniepp, J.-L. Li, M. J. McAllister, H. Sai, M. Herrera-Alonso, D. H. Adamson, R. K. Prud'homme, R. Car, D. A. Saville, I. A. Aksay *J. Phys. Chem. B.* **2006**, 110, 8535.

[174] L. Staudenmaier *Ber. Dtsch. Chem. Ges.* **1898**, 31, 1481.

[175] X. K. Wang, X. W. Lin, M. Mesleh, M. F. Jarrold, V. P. Dravid, J. B. Ketterson, R. P. H. Chang *J. Mater. Res.* **1995**, 10, 1977.

[176] X. K. Wang, X. W. Lin, V. P. Dravid, J. B. Ketterson, R. P. H. Chang *Appl. Phys. Lett.* **1995**, 66, 2430.

[177] A. Malesevic, R.Vitchev, K. Schouteden, A. Volodin, L. Zhang, G. V. Tendeloo, A. Vanhulsel, C. V. Haesendonck *Nanotechnology*. **2008**, 19, 305604.

[178] A. Gupta, G. Chen, P. Joshi, S. Tadigadapa, P. C. Eklund *Nano Lett.* **2006**, 6, 2667.

[179] A. C. Ferrari *Solidstate Commun.* **2007**, 143, 47.

[180] A. C. Ferrari, J. C. Meyer, V. Scardaci, C. Casiraghi, M. Lazzeri, F. Mauri, S. Piscanec, D. Jiang, K. S. Novoselov, S. Roth, A. K. Geim *Phys. Rev. Lett.* **2006**, 97, 187401.

[181] M. A. Pimenta, G. Dresselhaus, M. S. Dresselhaus, L. A. Cancado, A. Jorio , R. Sato *Phys. Chem. Chem. Phys.* **2007**, 9, 1276.

[182] D. Graft, F. Molitor, K. Ensslin, C. Stampfer, A. Jungen, C. Hierold, L. Wirtz *Nano Lett.* **2007**, 7, 238.

[183] I. Calizo, A. A. Balandin, W. Bao, F. Miao, C. N. Lau *Nano Lett.* **2007**, 7, 2645.

[184] K. Sumino, M. Imai *Philos. Mag. A.* **1983**, 47, 753.

[185] K. Sumino, I. Yonenaga, M. Imai, T. Abe *J. Appl. Phys.* . **1983**, 54, 5016.

[186] D. Wei, Y. Liu, Y. Wang, H. Zhang, L. Huang, G. Yu *Nano Lett.* **2009**, 9, 1752.

[187] H. W. X. Li, J.T. Robinson, H. Sanchez, G. Diankov, H. Dai *J. Am. Chem. Soc.* **2009**, 131, 15939.

[188] X. Wang, X. Li, L. Zhang, Y. Yoon, P.K. Weber, H. Wang, J. Guo, H. Dai *Science* **2009**, 324, 768.

[189] A. Das, S. Pisana, B. Chakraborty, S. Piscanec, S. K. Saha, U. V. Waghmare, K. S. Novoselov, H. R. Krishnamurthy, A. K. Geim, A. C. Ferrari, A. K. Sood *Nature Nanotechnol.* **2008**, 3, 210.

[190] B. Das, R. Voggu, C. S. Rout, C. N. R. Rao *Chem. Commun.* **2008**, 5155.

[191] R. Voggu, B. Das, C. S. Rout, C. N. R. Rao *J. Phys.: Condensed Mater.* **2008**, 20, 472204.

Chapter-2

Synthesis, Characterization and Properties of ZnO Nanostructures

Summary*

This chapter of the thesis deals with the synthesis, characterization and application of ZnO nanostructures such as nanoparticles, nanorods and thin films. The chapter is divided into six parts. The first three parts of the chapter deal with the synthesis of nanoparticles, nanorods and thin films of ZnO by simple chemical routes, whereas the fourth part deals with the synthesis of N-doped ZnO nanobullets by the solvothermal method. Field emission and generation of white light from ZnO nanostructures are respectively described in the fifth and sixth parts of the chapter.

Solvothermal reaction of aliphatic alcohols such as methanol, ethanol and *t*-butanol with Zn powder provides a simple method to produce nanoparticle of ZnO. Addition of ethylenediamine to the reaction mixture helps to obtain ZnO nanorods.

*Papers based on these studies have appeared in J. Clust. Sci. (2007), J. Solid State Chem. (2007), Inorg. Chim. Acta (2010), Mater. Res. Bull. (2007), Adv. Func. Mater. (2009) and Nanotechnology (2010).

We have found a new and simple method for preparing ZnO nanorods by the reaction of the zinc powder or zinc foils with water at relatively low temperatures. Addition of ethylenediamine to water favors the formation of the ZnO nanorods. Thus, the reaction time is considerably reduced in the presence of ethylenediamine. Reaction of Al powder or Al foils with water gives rise to $Al(OH)_3$ nanorods. The formation of ZnO and $Al(OH)_3$ nanorods from the metals are both governed by the basic reaction between the metals and water giving hydrogen. The growth of the nanorods could be occurring at the small oxide nuclei that may be present on the metal surfaces.

Liquid-liquid interface has been used to prepare nanostructures of ZnO. The nanostructures of ZnO produced at the interface include both one-dimensional nanorods and two-dimensional thin films, while both the nanorods and films are single-crystalline, a feature that is noteworthy. The ZnO films are extremely thin, obtaining such films by other means is difficult.

Solvothermal synthesis and nitrogen doping of ZnO with unique features are presented. The preparation conditions induce a unilateral growth from base to tip of nanobullet-like structures, despite the absence of any template. The reduction in the bullet diameter takes place in steps, rather than being continuous. Detailed investigations revealed a self-template mechanism to be responsible for their growth. This synthesis procedure was further extended for the purpose of nitrogen doping, this being the first solution-based approach for N-doped ZnO. Investigations of

the cathodoluminescence (CL) properties on individual nanobullets revealed that the N doping might not be uniform within a single structure, but the core is N-rich while the surface is N-poor. It should be noted that such inhomogeneity in properties is not detectable with photoluminescence measurements and must be given due consideration before fabricating single-nanostructure devices. Our investigations showed a remarkable improvement in the field-emission properties of ZnO by reason of N doping.

Photoluminescence emission from ZnO nanoparticles originating from defects gives rise to white light when mixed with few layer graphene. Thus it seems possible that the ZnO nanoparticles + graphene system can be exploited for producing white light emission. The results obtained with boron-doped graphene are noteworthy considering that ZnO is a n-type material whereas boron-doped graphene is of p-type.

2.1 Introduction

Zinc oxide (ZnO) is a II^b–VI compound semiconductor. The lack of a centre of symmetry in wurtzite, combined with large electromechanical coupling results in strong piezoelectric and pyroelectric properties and the consequent use of ZnO in mechanical actuators and piezoelectric sensors. In addition, ZnO is a wide band-gap (3.37 eV) compound semiconductor that is suitable for short wavelength optoelectronic applications. The high exciton binding energy (60 meV) in ZnO crystal can ensure efficient excitonic emission at room temperature and room temperature ultraviolet (UV) luminescence. ZnO crystallizes preferentially in the hexagonal wurtzite-type structure. It occurs in nature with the mineral name zincite. The mineral usually contains a certain amount of manganese and other elements and is of yellow to red colour. Due to its large band gap, pure ZnO is colourless and clear [1-3]. The possibility of growing epitaxial layers, quantum wells, nanorods and related objects or quantum dots gave the hope to obtain:

(a) A material for blue/UV optoelectronics, including light-emitting or even laser diodes in addition to (or instead of) the GaN-based structures

(b) A radiation hard material for electronic devices in a corresponding environment

(c) A material for electronic circuits, which is transparent in the visible region

(d) A transparent highly conducting oxide (TCO) when doped with Al, Ga, In or similar elements as a cheaper alternative to indium tin oxide (ITO).

Structure of ZnO

Zinc oxide crystallises in the hexagonal wurtzite-type structure shown in Fig. 2.1. It has a polar hexagonal axis, the c axis, chosen to be parallel to z. The point group is in the various notations 6 mm or C_{6v}, the space group $P6_3mc$ or C_{6v}^4. One zinc ion is surrounded tetrahedrally by four oxygen ions and vice versa. The primitive unit cell contains two formula units of ZnO. The ratio c/a of the elementary translation vectors, with values around 1.60, deviates slightly from the ideal value c/a= 1.633. In contrast to other II^b–VI semiconductors, which exist both in the cubic zinc blende and the hexagonal wurtzite- type structures (like ZnS, which gave the name to both structures), ZnO crystallises with great preference in the wurtzite-type structure. The cubic zinc blende-type structure can, to some extent, be stabilized by epitaxial growth of ZnO on suitable cubic substrates, while the rock salt structure is stable only under pressure [3]. The tetrahedrally coordinated diamond, zinc blende, and wurtzite-type crystal structures are characteristic for covalent chemical bonding with sp^3 hybridisation. While the Group IV element semiconductors like diamond, silicon and germanium have completely covalent bonding, one has an increasing admixture of ionic binding when going from the Group IV over the III–V and II^b–VII to the I^b–VII semiconductors, ending with completely ionic binding for the II^a–VI and I^a–

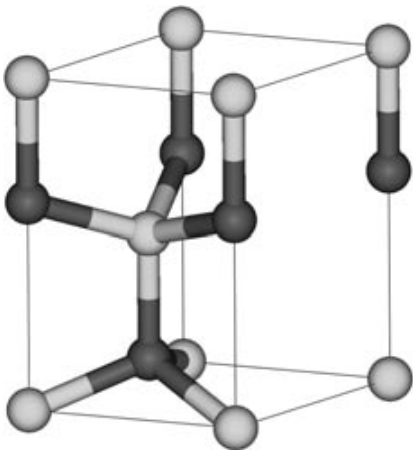

Fig. 2.1 Unit cell of the crystal structure of ZnO. The light grey pheres corresponds to oxygen, the dark ones to zinc.

VII insulators like MgO or NaCl, which frequently crystallise in the rock salt structure[3].

ZnO already has a substantial ionic bonding component, which shows ZnO in the “centre of solid state physics”. Because of this fraction of ionic binding, the bottom of the conduction band, or the lowest unoccupied orbital (LUMO), is formed essentially from the 4s levels of Zn^{2+} and the top of the valence band, or highest occupied molecular orbital (HOMO), from the 2p levels of O^{2-}. The band gap between the conduction and valence bands is about 3.437 eV at low temperatures [3].

2.2 Scope of the present investigations

2.2.1 Solution synthesis of ZnO nanoparticles and nanorods

Nanostructured ZnO materials have received broad attention due to their distinguished performance in electronics, optics and photonics. From the 1960’s, synthesis of ZnO thin films has been an active field because of their applications as sensors, transducers and catalysts. In the last few decades, study of zero dimensional (0D) and one dimensional (1D) materials has become a leading edge in nanoscience and nanotechnology. With reduction in size, novel electrical, mechanical, chemical and optical properties are introduced, which are largely believed to be the result of surface and quantum confinement effects. Nanowire-like structures are the ideal system for studying the transport process in one-dimensionally (1D) confined objects, which are of benefit not only for understanding the

fundamental phenomena in low dimensional systems, but also for developing new generation nanodevices with high performance [1, 2].

Nanoparticles of ZnO have been prepared by both physical methods and soft chemical methods [4-9]. In example, ZnO nanoparticles have been prepared by the solvothermal route in the presence of various capping agents, using Zn^{2+}-cupferron complex as the precursor [5]. Precipitation of Zn^{2+} by OH^- ions in alcoholic solutions gives nanoparticles of ZnO [6], while precipitation through acid-catalyzed esterification of zinc acetate dihydrate with 1-pentanol at 130 °C also yields ZnO nanoparticles [7]. Decomposition of Zn(II)acetylacetonate in acetonitrile under solvothermal conditions at 100 °C gives ZnO nanoparticles [8]. Organic-capped ZnO nanocrystals have been prepared by injecting Zn/O precursors into trioctylphosphineoxide (TOPO) [9]. ZnO nanostructures are obtained by solvent evaporation from a reaction mixture containing an organozinc compound in tetrahydrofuran, the shape depending on the solvent, ligand and concentration [10]. Sol-gel process has also been employed by several workers to prepare ZnO nanoparticles [11-13]. This method involves the hydrolysis of zinc salts with strong bases in an alcoholic medium and the polycondensation of the metastable hydroxide into ZnO crystals.

A great deal of work has been carried out on 1-D ZnO nanostructures (nanorods and nanowires) due to their tunable electronic and optoelectronic properties [2, 14-18]. Some of the methods developed to produce ZnO nanorod arrays are chemical vapor deposition [19, 20], physical vapor deposition [21-23], metal-organic vapor phase epitaxy [24], and use of

anodic aluminum oxide templates [25, 26]. Haidong et al. [27] developed a low-temperature chemical-liquid-deposition method to grow oriented ZnO nanorods by continuously supplying Zn ions from Zn foil to the ZnO-thin film coated substrate in aqueous formaldehyde solution. Reaction of a Zn^{2+} precursor with an organic base in alcohol/water solution gives 1-D nanostructures of ZnO [28]. Reaction of zinc acetate with NaOH in the presence of polyvinylpyrrolidone (PVP) at 80 °C in ethanol, under solvothermal conditions, gives ZnO nanorods [29]. Hydrothermal reactions have been used for the preparation of the ZnO nanorods as well. Thus, heating zinc nitrate hexahydrate and NaOH in a mixture of ethylenediamine and water at 180 °C for 20 h gives rise to thin (~50nm dia) ZnO nanorods [30]. In the presence of ethylenediamine, reaction of a Zn metal foil in water at 150-230 °C yields arrays of ZnO nanorods [31].

Generally, most of the above methods require relatively high temperatures or involve the use of expensive chemicals or apparatus. It is therefore of value to find simple methods to produce ZnO nanostructures employing inexpensive chemicals. A detailed study of the interaction of alcohols with Zn metal has shown that the C-O bond of the alcohol is readily cleaved on Zn metal surfaces giving hydrocarbons and the oxidic species on the metal surface [32, 33]. We therefore sought to examine the simple reaction of alcohols with Zn metal to find out whether we can obtain ZnO nanostructures by this means. Interestingly, we have found that ZnO nanoparticles are readily produced by the reaction of aliphatic alcohols at 330 °C in the absence of any surfactant. Addition of ethylenediamine to the alcohols gives rise to ZnO nanorods.

2.2.2 ZnO nanorods from the reaction of Zn metal with liquid water

While investigating the cleavage of the C–O bond of the aliphatic alcohols on zinc metal surfaces, which giving rise to ZnO nanoparticles, it occurred to us that the reaction of Zn metal with liquid water may also produce ZnO nanostuctures, since the reaction would be associated with the evolution of hydrogen [34, 35]. We have, therefore, investigated the reaction of Zn metal powder and Zn foils with water at room temperature as well as with water maintained at a temperature in the 25–75 ºC range. The present study differs from literature reports in that we have examined the interaction of zinc metal with liquid water at or close to room temperature without any additives. The literature methods generally use amines and other additives or zinc compounds and employ higher temperatures. Encouraged by the results obtained by the reaction Zn metal with water, we have also examined the reaction of aluminum metal with water. The present study provides a very simple method of generating nanorods of ZnO and $Al(OH)_3$ by the reaction of liquid water with the metals. To our knowledge, $Al(OH)_3$ nanorods have been not reported in the literature.

2.2.3 ZnO nanostructures generated at the liquid-liquid interface

It has been shown recently that the liquid-liquid (organic-aqueous) interface can be exploited to generate nanocrystalline films of a variety of inorganic materials such as metals, metal alloys and metal chalcogenides [36-39]. Nanocrystalline films synthesized at the interface are 40 to 80 nm thick and generally consist of small nanocrystalline particles. In some

instances, the films are single-crystalline, as exemplified by CuS [37]. Nonlinear viscoelastic properties, interfacial rheology of such ultrathin nanocrystalline films generated by this method have been studied [40, 41]. The liquid-liquid interface method involves taking an organo-metallic compound in the organic phase and the relevant reactant in the aqueous phase. The reaction occurs at the interface giving rise to ultrathin films or different nanostructures depending on the concentration of the reactants. Adding a small concentration of surfactant to the organic or aqueous phase affects the morphology of the nanostructures formed at the interface [42]. We considered it important to investigate ZnO nanostructures formed at the liquid-liquid interface, in view of their potential applications in optical, electronic and optoelectronic devices [1, 43-45]. The high electron mobility and visible transparency of ZnO thin films helps to use in thin film transistors, UV detectors, UV and blue light emitting diodes (LEDs) and laser diodes [46]. Several methods have been employed to synthesize the ZnO nanostructures which have been discussed in section 2.2.1. ZnO nanofilms can be prepared by standard methods employed for thin films such as chemical vapour deposition, pulsed laser deposition and electrodeposition [47-49]. None of these methods produces thin single-crystalline films. We felt that the liquid-liquid interface may provide nanofilms as well as other nanostructures of ZnO with novel morphologies and properties. Here we present the synthesis and properties of ultrathin films and other nanostructures of ZnO generated at the liquid-liquid interface. Interestingly both the films and nanorods are formed to be single-crystalline.

2.2.4 Pure and nitrogen-doped ZnO nanobullets by the solvothermal method

ZnO has a strong potential for various short-wavelength optoelectronic device applications. In order to attain the potential offered by ZnO, both high-quality *n*- and *p*-type ZnO are indispensable. ZnO with a wurtzite structure is naturally an *n*-type semiconductor because of a deviation from stoichiometry due to the presence of intrinsic defects such as oxygen vacancies (V_o) and zinc interstitials (Zn_i). *n*-type doping of ZnO is relatively easy compared to *p*-type doping. Group-III elements Al, Ga, and In as substitutional elements for Zn and group-VII elements Cl and I as substitutional elements for O can be used as *n*-type dopants [50].

It is very difficult to obtain *p*-type doping in wide-band-gap semiconductors. The difficulties can arise from a variety of causes. Dopants may be compensated by low-energy native defects, such as Zn_i or V_o, [51] or background impurities (H). Low solubility of the dopant in the host material is also another possibility [52]. Deep impurity level can also be a source of doping problem, causing significant resistance to the formation of shallow acceptor level. Known acceptors in ZnO include group-I elements such as Li [53-55], Na and K copper [56], silver [57], Zn vacancies, and group-V elements such as N, P and As. However, many of these form deep acceptors and do not contribute significantly to *p*-type conduction. It has been believed that the most promising dopants for *p*-type ZnO are the group-V elements, although theory suggests some difficulty in achieving shallow acceptor level [58]. A number of theoretical studies have addressed the

fundamental microscopic aspects of doping in wide band-gap semiconductors. The majority of these studies have dealt with the manner in which dopant solubility [52, 59] or native defects [60, 61] such as vacancies, interstitials, and antisites interfere with doping.

*I*n ZnO, *p*-type doping may be possible by substituting either group-I elements (Li, Na, and K) for Zn sites or group-V elements (N, P, and As) for O sites. It was shown that group-I elements could be better *p*-type dopants than group-V elements in terms of shallowness of acceptor levels [58]**.** However, group-I elements tend to occupy the interstitial sites, in part mitigated by their small atomic radii, rather than substitutional sites, and therefore, act mainly as donors instead [62]. Moreover, significantly larger bond length for Na and K than ideal Zn–O bond length (1.93 Å) induces lattice strain, increasingly forming native defects such as vacancies which compensate the dopants. These are among the many causes leading to difficulties in attaining *p*-type doping in ZnO. A similar behavior is observed for group-V elements except for N. Both P and As also have significantly larger bond lengths and, therefore, are more likely to form antisites to avoid the lattice strain. The antisites, A_{Zn}, are donor like and provide yet another unwelcome possible mechanism for compensating acceptors. It then appears that perhaps the best candidate for *p*-type doping in ZnO is N because among the group-V impurities, N has the smallest ionization energy, it does not form the N_{Zn} antisite, and the *AX* center of N is only metastable [58].

In the literature, thin films of N-doped ZnO have been prepared by metal organic chemical vapor deposition (MOCVD) [63] or by the arc method [64]. In the MOCVD method, N-doped ZnO films were grown on a sapphire

substrate in a horizontal MOCVD reactor by using dimethyl zinc, *t*-butanol and diallylamine as zinc, oxygen and nitrogen sources, respectively, with hydrogen as a carrier gas at a temperature between 420 and 480 °C. N-doped ZnO thin films have also been deposited on silicon or quartz substrates by the filtered cathodic vacuum arc method from a zinc target in an oxygen/nitrogen atmosphere at 350 °C at 10^{-4} Torr pressure. N-doped ZnO nanorods have been prepared recently by combining a wet-chemical process with post treatment by NH_3 plasma [65]. In this method, p-type Si (100) substrates are initially sputter-coated with a ZnO film and the film was placed in a glass bottle filled with 0.01 M aqueous solution of zinc(II)nitrate hexahydrate and hexamethylenetetramine (mole ratio, 1:1) at 75 °C for 10 h. The ZnO nanorods which formed perpendicular to the substrate were exposed to NH_3 plasma for different times to obtain N-doped ZnO nanorods. N-doped ZnO nanorods have also been prepared by the dc thermal plasma technique, wherein the Zn powder is fed into plasma flame generated by nitrogen and argon with air as the carrier gas [66].

We have found that nitrogen-doped ZnO nanorods can be conveniently prepared by the solvothermal reaction by adding liquid ammonia to a reaction mixture of zinc acetate with ethanol in the presence of ethylenediamine at 250 °C.

2.2.5 Cathodoluminescence (CL) and field emission (FE) properties of pure and N-doped ZnO nanobullets

Cathodoluminescence is the emission of light as a result of electron bombardment. As compared to other techniques, such as

photoluminescence spectroscopy, CL has the advantage of much higher spatial resolution, up to few nanometers [67]. Moreover, by using electron beams with different energies, it is possible to probe the optical behavior of a material at different depths from the surface. Field emission is the extraction of electrons from a negatively biased material by applying a strong electric field [68, 69]. FE, also called cold emission, is a more effective process over the normally employed thermionic emission because of its higher energy efficiency. This is even more important for nanostructures because of their faster device turn-on time, compactness, and sustainability.

In this chapter the details of CL and FE properties of N doping of the unique ZnO nanobullets synthesized through a solvothermal technique have been presented. N doping causes a significant 0.024 eV redshift of the CL emission peak. Moreover, the larger red-shifts in the CL spectra taken at higher accelerating voltages imply greater dopant concentrations at the cores of the nanostructures than on their surfaces. FE measurements show an order of magnitude increase in the emission currents due to N doping. Thus, the results presented here are not only intriguing for fundamental studies but also show interesting application prospects.

2.2.6 Photoluminescence and white-light emission from ZnO-graphene mixtures

Emerging electronic and optoelectronic systems require the development of new devices with multifunctionality [70, 71]. An important emerging technology is that of solid-state lighting technology which offers the potential to save energy and protect the environment by producing light

more efficiently. Cerium-doped yttrium aluminum garnet (YAG:Ce) is generally used in white light-emitting diodes [72], as a coating on a high-brightness blue InGaN diode, converting part of the blue light into yellow, which then appears as white light. Because of the broad spectrum of YAG:Ce emission and the two-color nature of such an LED, however, the color-rendering index is not high. For this reason, technologies that avoid phosphors deserve attentions. Use of quantum well structures (e.g., InGaN\GaN QW structures) and core-shell structures (e.g., CdSe\ZnS) [73] are two alternative approaches. Absorption efficiency, emission efficiency, materials toxicity, cost effectiveness and simplicity of design are some of the major concerns related to the materials selection and the device structure. Defects in ZnO give rise to characteristic bands in the photoluminescence spectrum causing a peak in the green-yellow region. It should be possible to generate white light by using blue emitting materials in combination with ZnO. There has been some effort in this direction, but many of reported studies are far from completion [74, 75]. Some of the concerns in this context are the range of wavelength, flatness of the PL spectra and external quantum yield and there is a need for new materials to be tested in admixture with ZnO nanoparticles for possible white-light emission. Graphenes and GaN nanoparticles emit in blue region and are therefore, expected to yield white light with the green-yellow emission of zinc oxide.

We have examined the photoluminescence (PL) of ZnO nanoparticles in admixture with graphene. For this purpose, we have used graphene prepared by arc-discharge of graphite in hydrogen (HG). In addition to pure

HG, we have examined the effects of addition of boron- and nitrogen-doped HG on the PL of ZnO nanoparticles.

2.3 Experimental and related aspects

(a) Synthesis of ZnO nanoparticles

In a typical synthetic procedure for the nanoparticles, 10 mg of Zn metal powder (Ranbaxy; ~ 10 μm dia) was added to 10 ml of anhydrous alcohol (methanol, ethanol or *t*-butanol). The reaction mixture was sonicated for 10 minutes, transferred into a stainless steel autoclave (Swagelok) of 20 mL capacity and sealed under inert conditions inside a glove box. The reaction mixture was heated slowly (1 °C /min) to the 330 °C and maintained at this temperature for 18 hours. The resulting suspension was centrifuged to retrieve the product, washed with ethanol for three times and dried.

(b) Synthesis of ZnO nanorods

ZnO nanorods could be prepared by the addition of 1 ml ethylenediamine to a mixture of 10 mg of Zn metal powder and 10 ml of the anhydrous alcohol (ethanol or *t*-butanol) and heating the mixture in a Swagelok autoclave (1 °C/min) to 330 °C. The reaction mixture was maintained at that temperature for 18 hours.

(c) Synthesis of ZnO nanorods by Reaction of the Zn Metals with Liquid Water

In a typical synthesis of the ZnO nanorods from Zn metal powder (Ranbaxy, ≥10 μm diameter), 10 mg of Zn the powder was taken in a vial containing 10 ml of double distilled water (pH 6.5). The reaction mixture was kept at a desired temperature. At 25 °C (room temperature), the reaction mixture was kept for 72 h. Reaction of zinc foils with double distilled water carried out by immersion the foil in 10 ml of water and maintained the temperature at desired value at 25 °C for 72 h. At 50 and 75 °C, the reaction mixture was kept for 24 h. The $Zn+H_2O$ reaction was also carried out at 25 °C by adding ethylenediamine (1 ml) to 10 ml of water.

(d) Synthesis of $Al(OH)_3$ nanorods by Reaction of the Al Metals with Liquid Water

In a typical synthesis, 10 mg of Al metal powder (Ranbaxy, ≥10 μm diameter), was taken in a vial containing 10 ml of double distilled water (pH 6.5). The reaction mixture was kept at a desired temperature at 25 °C (room temperature), the reaction mixture was kept for 120 h. Reaction of Al foils with double distilled water carried out by immersion of the foil in 10 ml of water and maintained the temperature at desired value at 25 °C for 120 h. At 50 and 75 °C, the reaction mixture was kept for 24 h.

(e) Synthesis of ZnO nanorods at the liquid-liquid interface

The procedure to prepare ZnO nanorods at the liquid-liquid interface involved taking the zinc(II) cupferron $[Zn(Cup)_2]$ as the zinc source in the

toluene phase, and NaOH as the reactant in the water phase. $Zn(cup)_2$ was prepared by the reaction of cupferron with zinc acetate in water at 0 ^oC, then filtered and dried in a vacuum tube. $Zn(cup)_2$ along with appropriate amount of an organic amine in toluene was added to the NaOH aqueous phase with suitable pH. The reactions at the interface were all carried out at 30 ^oC. To examine the effect of OH^- concentration relative to Zn^{2+} concentration, we kept the trioctylamine concentration constant at 4.58 mM and varied the concentration ratio between Zn^{2+} and OH^-. In a typical experiment, we have taken 25 mL of 0.04 M NaOH solution in three separate 100 mL beakers. To these, we added 2, 10 and 20 mg of $Zn(cup)_2$ in 25 mL of toluene containing 4.58 mM trioctylamine, so that the actual concentrations of $Zn(Cup)_2$ were 0.24, 1.18, 2.36 mM respectively. The interface attains a white colour after a few hours indicating the formation of ZnO nanostructures. The thickness of the layer at the interface increases with time. After 10 hours, the organic phase was removed and the film containing ZnO nanostructures carefully lifted on to a silicon substrate for characterization. In order to study the effect of chain length of the amine on the nanorods, we kept the $Zn(Cup)_2$ concentration in the organic phase at 0.24mM, and 0.04 M NaOH in the aqueous phase constant. Different amines were added to the organic phase to attain an actual concentration of 2.29 mM. The amines used were n-butylamine, n-octylamine, n-dodecyl amine and n-hexadecyl amine. We also studied the effect of amine concentration on nanorods formation. For this purpose, we took 2.36 mM $Zn(Cup)_2$ in the organic phase and 0.04 M NaOH in the aqueous phase in

three separate beakers. The concentration of the trioctylamine in the organic phase was varied as 2.29, 4.58 and 18.32 mM.

(f) Synthesis of ZnO thin films at the liquid-liquid interface

For preparing thin films of ZnO, we took 25 mL of 0.04 M of NaOH in a 100 mL beaker, to which 25 mL of 0.12 mM $Zn(Cup)_2$ in toluene was added slowly at 30 ^oC. The interface attains a white colour after a few hours, and a distinct film is formed after 10 h.

(g) Synthesis of undoped and nitrogen-doped ZnO nanobullets

ZnO nanobullets, with a flat base and a sharp tip, were prepared by using a solvothermal method. In a typical synthesis, 50mg of zinc acetate, 9mL of ethylenediamine, and 6 mL of absolute alcohol were placed in a teflon-lined autoclave and stirred for 10 min. The autoclave was then sealed and placed in a hot air oven, which was preheated to 250 ^oC. The synthesis was carried out at this temperature for 20 h before naturally cooling down to room temperature. The white precipitates thus obtained were harvested by centrifugation and washed thoroughly with pure ethanol and air-dried at 40 ^oC.

N-doped ZnO nanorods were prepared by the addition of 1mL of liquid ammonia to the above mixture (50mg of zinc acetate, 9mL of ethylenediamine, and 6 mL of absolute alcohol) and then carrying out the reaction at 250 ^oC for 20 h.

Techniques used for characterization

X-ray diffraction (XRD): X-ray diffraction (XRD) patterns of the samples were recorded in the θ-2θ Bragg-Bretano geometry with a Siemens D5005 diffractometer using Cu Kα (λ=0.151418 nm) radiation.

Scanning electron microscope (SEM): Scanning electron microscope images of the samples were recorded using a LEICA S440i scanning electron microscope.

Field emission scanning electron microscope (FESEM): FESEM images were recorded with a FEI NOVA NANOSEM 600.

UV-Vis absorption and Photoluminescence: UV-Vis absorption measurements were carried out at room temperature with a Perkin-Elmer model Lambda 900 UV/Vis/NIR spectrometer.

Photoluminescence (PL) measurements were carried out at room temperature with a Perkin-Elmer model LS50B luminescence spectrometer. The excitation wavelengths used depends on the samples studied.

Raman spectroscopy: Raman spectra were recorded with LabRAM HR high resolution Raman spectrometer (Horiba Jobin Yvon) using He-Ne Laser (λ=630 nm).

Transmission electron microscopy (TEM): Transmission electron microscope (TEM) images were obtained with a JEOL JEM 3010, operating with an accelerating voltage of 300 kV. The samples were prepared by

dispersing the product in CCl_4. A drop of the suspension was then put on a holey carbon coated Cu grid and allowed to evaporate slowly. Some of the samples were analyzed with TEM (JEM-3000F) microscope.

Cathodoluminescence measurements: CL spectra were collected with a highresolution CL system at different accelerating voltages and at a constant beam current of 1000 pA at room temperature, by using ultra-high-vacuum SEM and a Gemini electron gun (Omicron, Germany) equipped with a CL system. The vacuum of the specimen chamber was maintained at 10^{-11} mbar (1 mbar=100 Pa).

Field emission measurements: FE measurements were conducted in a vacuum chamber at a pressure of 3.0 x 10^{-6} Pa at room temperature. A rod-like aluminum probe with a 1 mm^2 cross-section area was used as an anode, and a silicon substrate coated with a film of ZnO nanobullets served as the cathode. A dc voltage sweeping from 100 to 900 V was applied to a sample in steps of 5 V. The spacing between the anode and the cathode was set at 100, 150, and 200 mm.

2.4 Results and discussion

2.4.1 Solution synthesis of ZnO nanoparticles and nanorods

In Figures 2.2 (a) and (b), we show the low and high magnification FESEM images of the ZnO nanoparticles obtained by the reaction of Zn metal powder with methanol under solvothermal conditions at 330 °C. The nanoparticles are not entirely spherical in shape and have diameters varying between 50 and 300 nm, with an average diameter of 150 nm as can be seen from the inset of Fig. 2.2 (a). In Figures 2.3 (a) and (b), we show the low and high magnification FESEM images of the ZnO nanoparticles prepared solvothermally at 330 °C by reaction with ethanol. The images reveal short rod-like ZnO nanoparticles with an average diameter of 17 nm and average length of 35 nm (see inset of Fig. 2.3 (b)). Thus, the average particle size of the ZnO nanoparticles obtained from the reaction with ethanol is smaller than that obtained with methanol. In Fig. 2.4 (a), we show a TEM image of the ZnO nanoparticles prepared by using ethanol. The diameter of the ZnO nanoparticles ranges from 10-40 nm, with an average value of 17 nm as seen from the inset in Fig. 2.4 (a). The selected area electron diffraction pattern shown as an inset in Fig. 2.4 (a) confirms the crystalline nature of the ZnO nanoparticles.

In Figures 2.5 (a) and (b), we show the high and low magnification FESEM images of the ZnO nanoparticles obtained by the reaction of Zn powder with *t*-butanol at 330 °C. The nanoparticles are nearly spherical in shape with variable size in the 20-180 nm range. The average diameter of

the particles is 50 nm. In some regions we notice that big nanoparticles (average diameter ~ 650 nm) are surrounded by smaller nanoparticles (average diameter ~ 50 nm) as shown in Fig. 2.5 (b). In Fig. 2.4 (b), we show

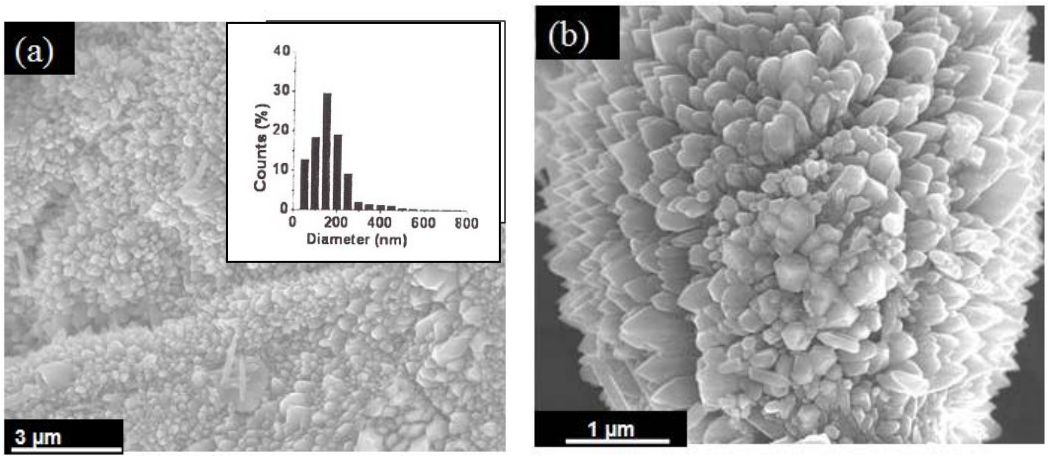

Fig. 2.2 Low (a) and high (b) magnification FESEM images of ZnO nanoparticles prepared at 330 °C by reaction with methanol. Inset in (a) shows the particle size distribution, histogram.

a TEM image of the ZnO nanoparticles obtained with *t*-butanol.

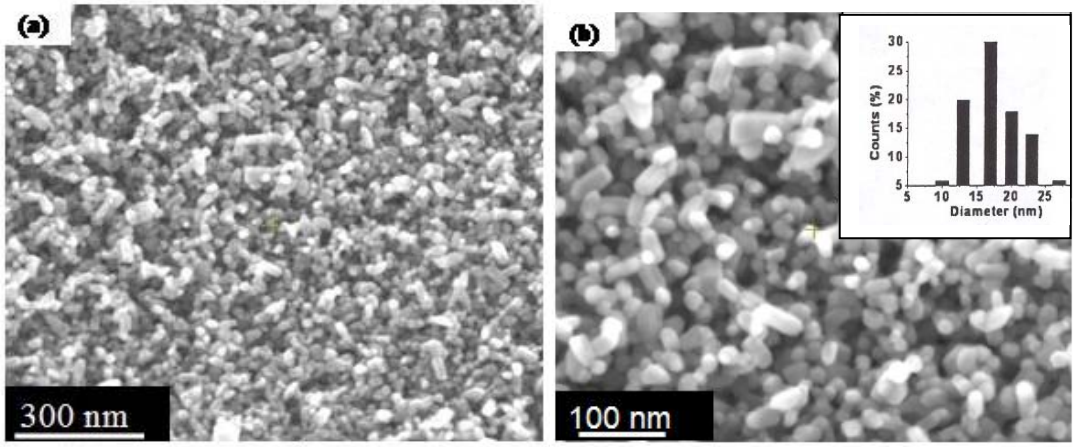

Fig. 2.3 Low (a) and high (b) magnification FESEM images of ZnO nanoparticles prepared at 330 °C by reaction with ethanol. Inset in (b) shows the particle size histogram.

The diameter of the ZnO nanoparticles ranges from 40 to 100 nm. The selected area electron diffraction pattern shown in the inset of Fig. 2.4 (b) confirms the crystalline nature of the ZnO nanoparticles. We have also

observed the presence of short nanorods (average diameter ~ 125 nm with the length varying form 400 nm to 700 nm) occasionally in the TEM images.

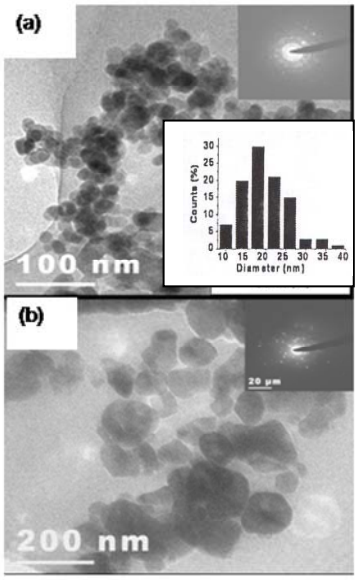

Fig. 2.4 TEM images of ZnO nanoparticles prepared at 330 °C by reaction with (a) ethanol and (b) t-butanol. Insets at the top right hand sides of (a) and (b) show the ED patterns. Inset in the bottom right hand side in (a) shows the particle size distribution, histogram.

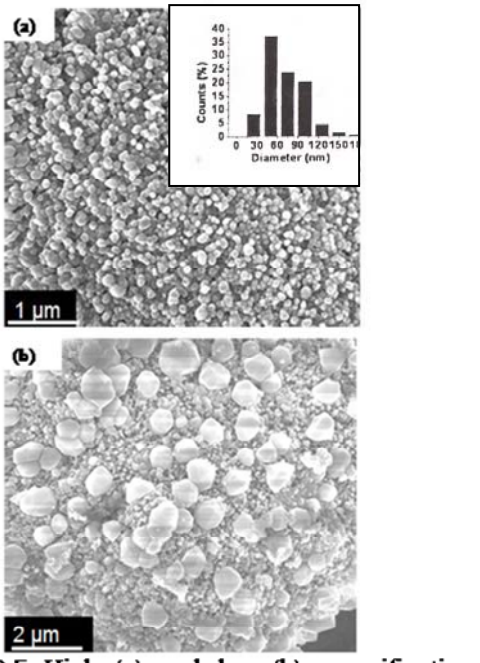

Fig. 2.5 High (a) and low (b) magnification FESEM images of ZnO nanoparticles prepared at 330 °C by reaction with t-butanol. Inset in (a) shows the particle size distribution, histogram.

Addition of 1 ml of ethylenediamine to the reaction mixture of zinc metal powder and alcohol gives ZnO nanorods. In Figures 2.6 (a) and (b), we show the FESEM images of the ZnO nanorods obtained by the addition of ethylenediamine to ethanol and *t*-butanol respectively. The nanorods obtained with ethanol have an average diameter of 250 nm and lengths up to several micrometers. We also observe the occurrence of smaller ZnO nanorods with an average diameter of 9 nm and average length of 150 nm (see inset of Fig. 2.6 (a)). The nanorods obtained with *t*-butanol have diameters ranging from 25 to 120 nm with lengths going up to 1-2 µm. The effect of addition of ethylenediamine to the alcohols suggests the shape-directing effect of the amine in agreements with the literature [30, 31].

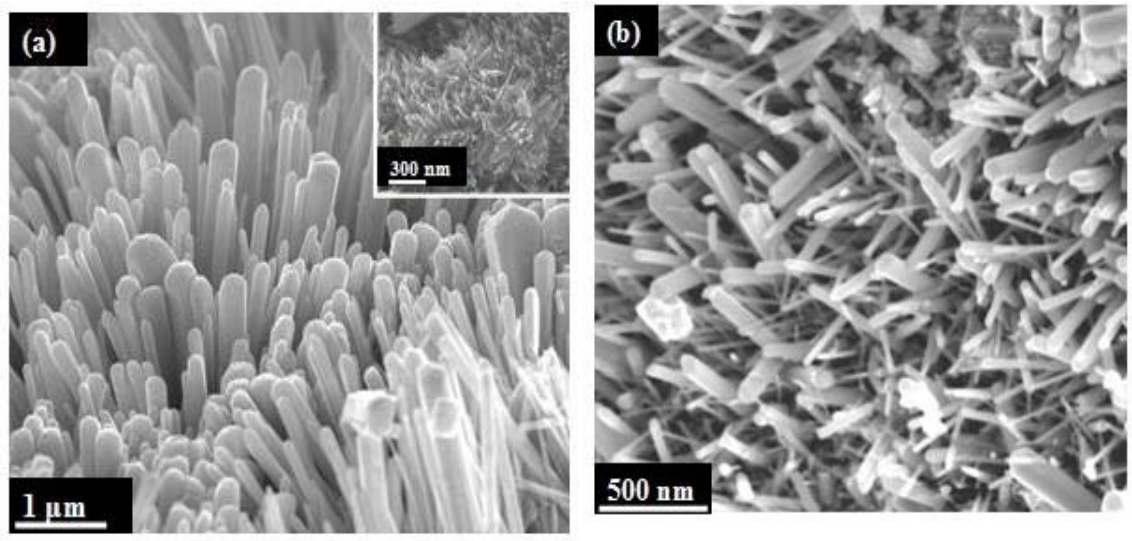

Fig. 2.6 FESEM images of ZnO nanorods prepared at 330 °C by the addition of 1 ml of ethylenediamine to the reaction mixture containing (a) ethanol and (b) *t*-butanol.

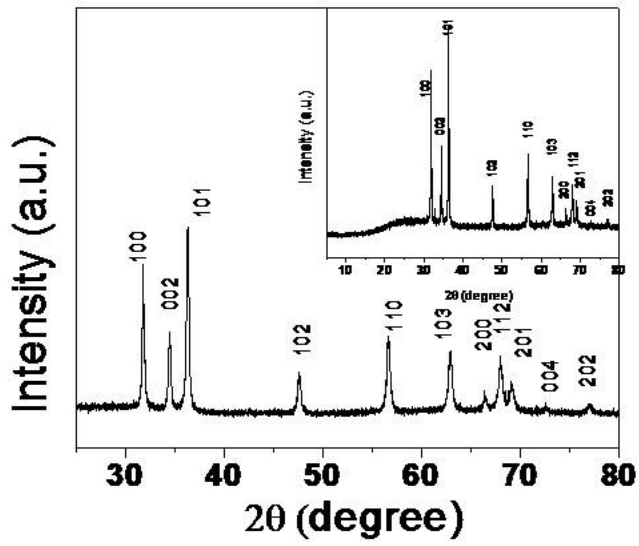

Fig. 2.7 XRD pattern of ZnO nanorods prepared at 330 °C by the addition of 1 ml of ethylenediamine to the reaction mixture containing ethanol. Inset shows the XRD pattern of ZnO nanoparticles prepared at 330 °C by reaction of **ethanol with Zn metal**

The XRD patterns of the ZnO nanoparticles and nanorods (Fig. 2.7) could be indexed to the hexagonal wurtzite structure (space group: $P6_3mc$; a = 0.3249 structure (space group: $P6_3mc$; a = 0.3249 nm, c =0.5206 nm, JCPDS card no. 36-1451). The UV absorption spectrum of the ZnO nanoparticles gives a band around 375 nm as shown in Fig. 2.8 (a). The spectrum shows well-defined exciton absorption peaks characteristic of ZnO, with a significant blue shift compared to bulk ZnO [76]. The room-temperature PL spectrum of the ZnO

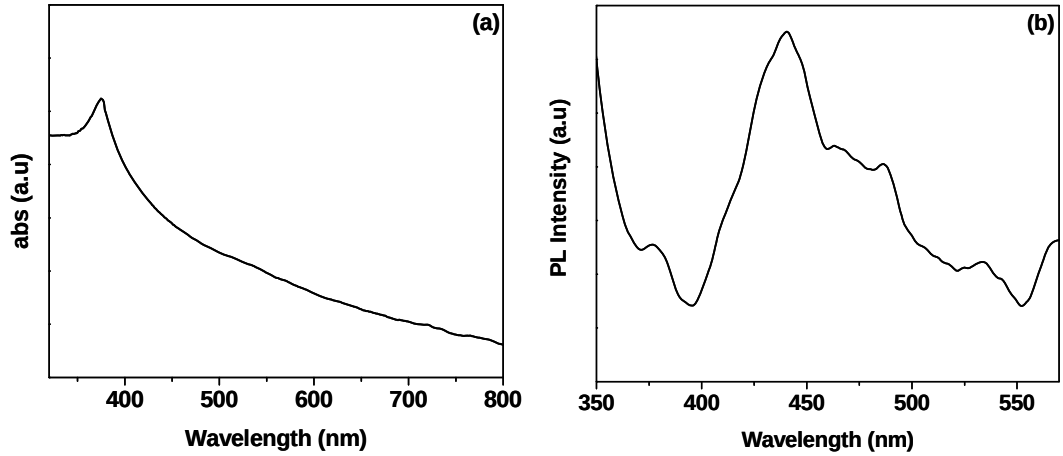

Fig. 2.8. (a) UV-Vis spectrum of ZnO nanoparticles. (b) Photoluminescence spectrum of ZnO nanoparticles.

nanoparticles (Fig. 2.8 (b)) shows a UV emission at 380 nm and broad bands centered at 424 nm, 445 nm, 485 nm and 528nm. The UV emission corresponds to exciton recombination related near-band edge emission [77] and the deep-level visible emission from the localized levels in the band gap [31]. The visible emission is considered to originate from the electron transition from a singly ionized oxygen vacancy to the photoexcited hole [78].

The following scheme describes the sequence of events in the reaction of alcohols (ROH, R=CH_3, C_2H_5 and *t*-C_4H_9) with zinc.

Here (s), (a) and (g) represents solid, adsorbed species and gas respectively. O(a) is adsorbed on Zn later forming ZnO.

$$Zn(s) + ROH \longrightarrow Zn + ROH(a)$$

$$ROH(a) \longrightarrow RO(a) + H(a)$$

$$2RO(a) \longrightarrow 2O(a) + R_2(g)$$

$$O(a) + 2e^- \longrightarrow O^{2-}(s)$$

2.4.2 ZnO nanorods from the reaction of Zn metal with liquid water

In Figures 2.9-2.11, we show FESEM images of ZnO nanorods obtained by the reaction of Zn metal powder with water at different temperatures. Of these, Figure 2.9 (a), (b) show FESEM images of the nanorods obtained after the reaction at 25 °C for 72 h. The nanorods have diameters varying between 40 and 150 nm, with an average diameter of around 75 nm, and an average length of 300 nm (see inset in Fig. 2.9 (a)). FESEM images of the ZnO nanorods obtained after reaction at 50 °C for 24 h are shown in Fig. 2.10. These nanorods have diameters in the range 20–100 nm, with an average diameter of 50 nm and the length ranging from 1 to 3 μm (see inset in Fig. 2.10 (a)). TEM image of a ZnO nanorod prepared at 50 °C is shown in Inset Fig. 2.10. The nanorods prepared at 75 °C have diameters in the 20–140 nm range, with an average diameter of 40 nm and the length in the 1–3 μm range (Fig. 2.11). Inset in Fig. 2.11 (a) shows the particle size distribution, histogram. The XRD patterns of the ZnO nanorods (Fig. 2.12) obtained from the different preparations could be indexed on the hexagonal wurtzite structure (space group: $P6_3mc$; a = 0.3249 nm, c = 0.5206 nm, JCPDS card no. 36-1451). Our studies of the reaction of Zn powder with liquid water in the 25–75 °C range indicate that the average diameter of the ZnO nanorods decreases with the increase in temperature, accompanied by an increase in the aspect ratio.

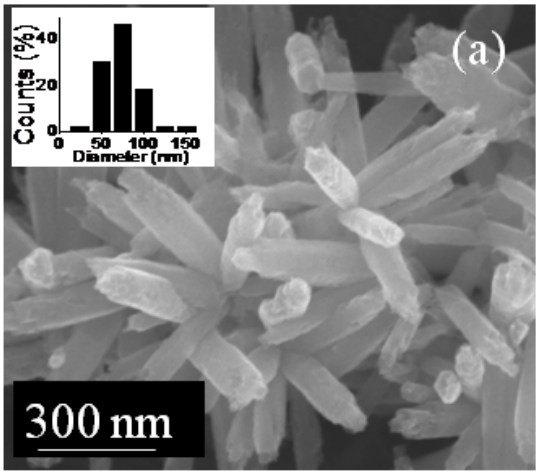

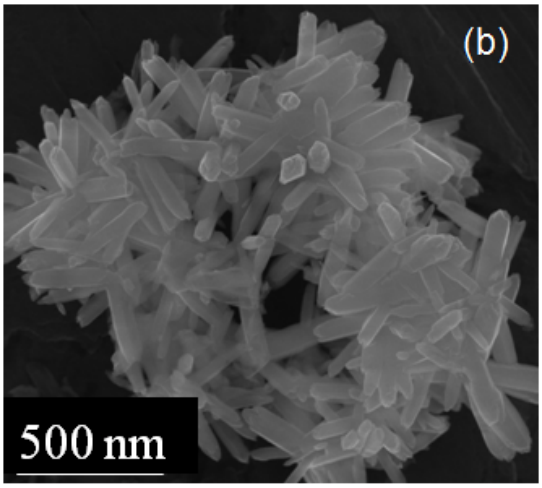

Fig. 2.9 High (a) and low (b) magnification FESEM images of ZnO nanorods prepared at 25 °C by the reaction of Zn metal with water. Inset in (a) shows a diameter distribution, histogram.

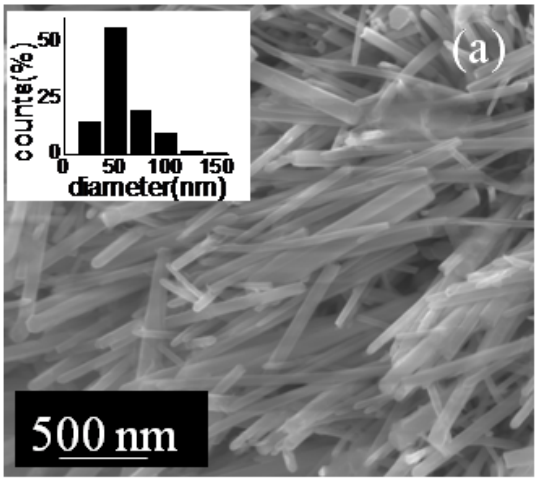

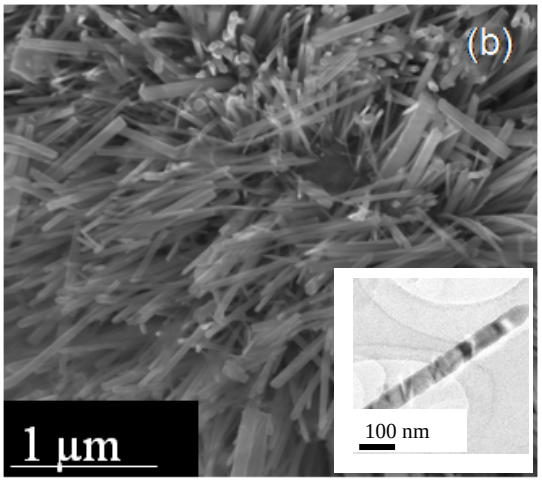

Fig. 2.10 High (a) and low (b) magnification FESEM images of ZnO nanorods prepared at 50 °C by the reaction of Zn metal with water. Inset in (a) shows a diameter distribution, histogram. Inset in (b) whows the TEM image of a ZnO nanorod

We have examined the effect of addition of ethylenediamine on the formation of ZnO nanorods by the reaction of water with Zn metal powder. By adding 1 ml of ethylenediamine to 10 ml of water, we found that the reaction occurs faster. Thus, at 25 °C, ZnO nanorods were produced (Fig. 2.13) just after 36 h. The diameter of the nanorods was, however, a little larger. In Fig. 2.14 (a) and (b), we show the FESEM image of a Zn foil. In Fig. 2.14 (c) and (d), we show a FESEM image of ZnO nanorods obtained by the

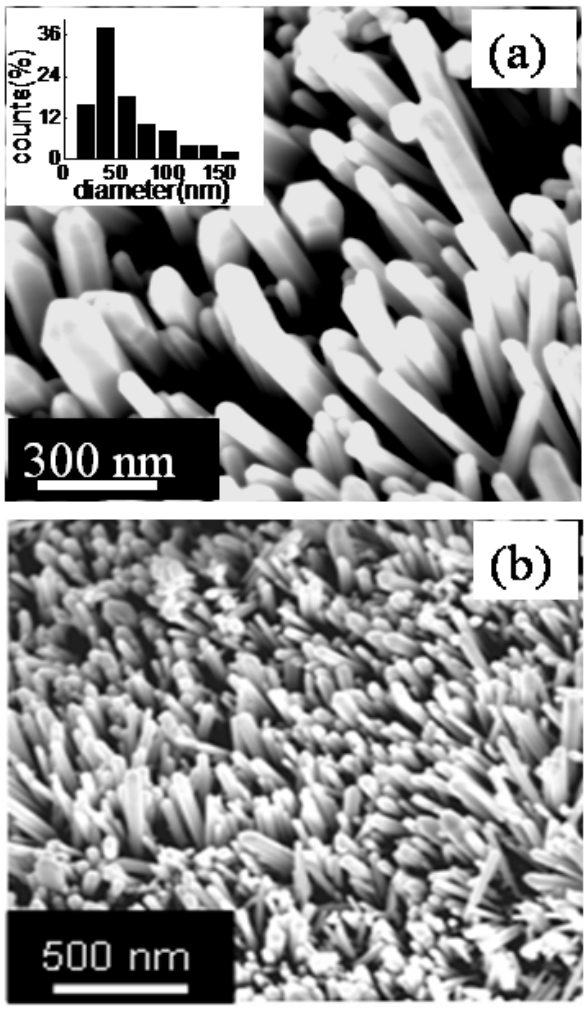

Fig. 2.11 High (a) and low (b) magnification FESEM images of ZnO nanorods prepared at 75 °C by reaction of Zn metal with water. Inset in (a) shows the diameter distribution, histogram.

reaction of the Zn foil with water at 50 °C. The diameter of the nanorods varies between 80 and 400 nm, with an average value of 150 nm. The average length of the nanorods is 1 μm. The XRD pattern of these nanorods was also characteristic of the wurtzite structure.

The UV-Vis absorption spectrum of the ZnO nanorods gives the characteristic band round 365 nm (see Fig. 2.15 (a)) [76]. The room- temperature PL spectra of the ZnO nanorods (Fig. 2.15 (b)) show a UV emission band at 380 nm due to the radiative recombination between the electrons in the conduction band and the holes in the valence band [31, 79], and broad bands in the 420–530 nm range. The visible emission originates from the localized levels in the band gap [31]. The UV emission band is present prominently in the sample prepared at 75 °C, but is weak in the one prepared at 25 °C. The intensity of the UV emission band increases with the temperature of preparation of the nanorods, where as the intensity of the bands in the visible region decreases (Fig. 2.15 (b)). This variation correlates

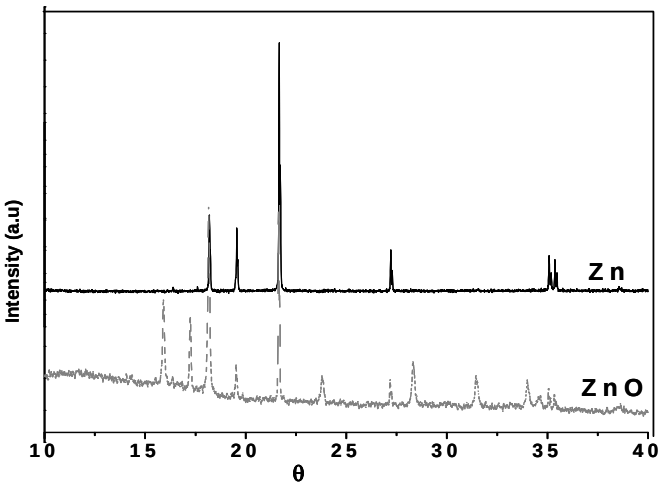

Fig. 2.12 XRD patterns of ZnO nanorods along with the starting metal sample

well with that of the 580 cm^{-1} Raman band (Fig. 2.16) which arises from intrinsic lattice defects [80]. The intensity of the 580 cm^{-1} Raman band decreases with the increasing temperature of the reaction. The Raman bands at 433 and 378 cm^{-1} are attributed to E_2 mode and A_1 (TO) modes, respectively (*80, 82*). The band at 331 cm^{-1} could arise from a multiphonon process [81].

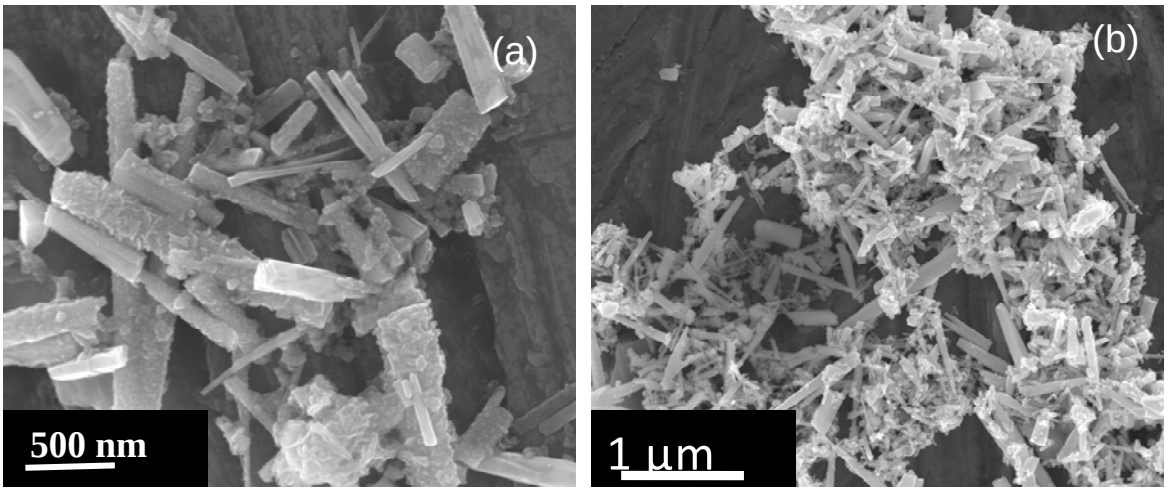

Fig. 2.13 High (a) and low (b) magnification FESEM images of ZnO nanorods prepared at 25 °C by the reaction of Zn metal with water by adding 1 ml ethylenediamine

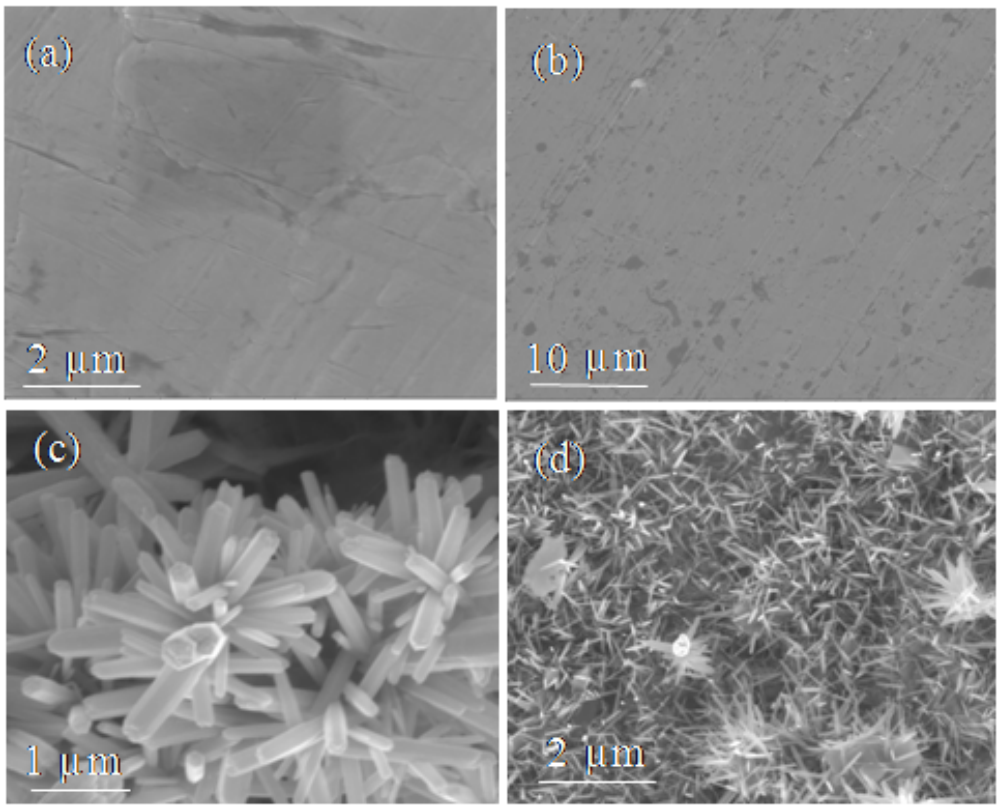

Fig. 2.14 FESEM images of Zn foil (a and b) and of ZnO nanorods (c and d) obtained at 50 °C by the reaction of water with the Zn foil.

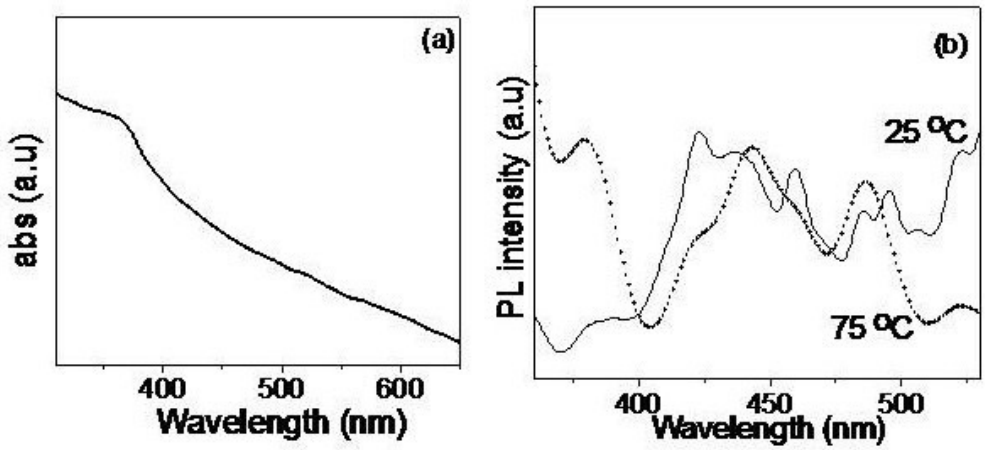

Fig. 2.15 (a) UV-Vis spectrum of ZnO nanorods (b) PL spectra of ZnO nanorods obtained at 25 °C and 75 °C

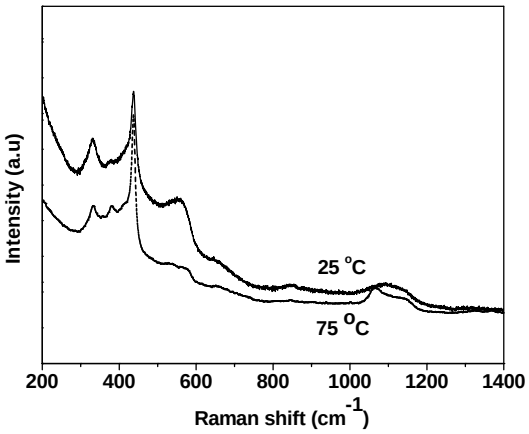

Fig. 2.16 Raman spectra of ZnO nanorods obtained at 25 °C and 75 °C

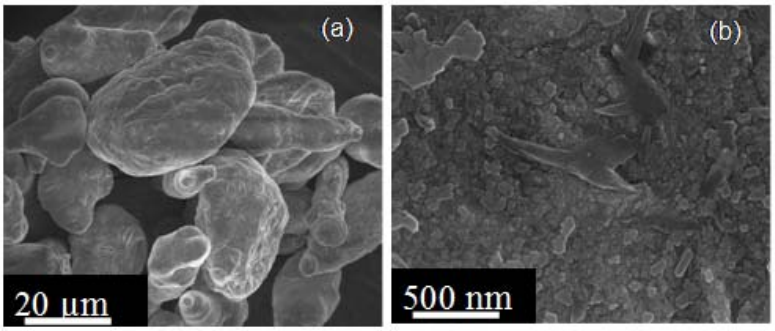

Fig. 2.17 Low (a) and high (b) magnification FESEM images of Zn metal powder

The mechanism of the formation of ZnO nanorods can be described as follows. Zinc metal on reaction with water slowly gives out hydrogen. The oxygen liberated reacts with Zn metal to give the oxide as given by the following reaction:

$$Zn(s) + H_2O(l) \longrightarrow ZnO(s) + H_2(g)$$

Here (s), (l) and (g) represent solid, liquid and gas, respectively. It may be noted that the evolution of hydrogen accompanying the reaction of Zn metal with water has been documented in the literature [34, 35]. In the reaction of zinc metal with water, it is reported that ZnO is formed first and $Zn(OH)_2$ at a later stage [82, 83]. The growth of ZnO nanorods probably occurs by making use of the oxide nuclei (Fig. 2.17) that may be present on the metal surface.

$Al(OH)_3$ nanorods

We have carried out the reaction of Al metal powder with water. Fig. 2.18 (a) shows a FESEM image of the Al metal surface. Fig. 2.18 (b) shows a FESEM image of the nanorods obtained by the reaction of Al powder with water at 75 °C. The nanorods are uniform in diameter varying between 7 and 14 nm, with an average diameter of 10 nm and an average length of 300 nm. Fig. 2.18 (c) shows a TEM image of $Al(OH)_3$ nanorods obtained at 50 °C and d shows a TEM image of the $Al(OH)_3$ nanorods obtained at 75 °C. The diameters of the nanorods are in the 8–14 nm range with an average length of 250 nm. The XRD patterns of the nanorods (Fig. 2.19) were characteristic of the bayerite phase of $Al(OH)_3$ (a = 0.501 nm, c = 0.469 nm, JCPDS data, card no. 12-0457).

The formation of $Al(OH)_3$ nanorods by the reaction of Al metal with water can be explained as follows. Al metal also gives hydrogen on reaction with water [34, 35]:

$$2Al(s) + 3H_2O(l) \longrightarrow Al(OH)_3(s) + 3/2H_2(g)$$

Unlike the reaction of Zn metal with water, the reaction of Al metal with water gives rise to the hydroxide instead of the oxide. Formation of $Al(OH)_3$ by reaction of Al metal with water has been reported in the literature [84, 85]. The formation of $Al(OH)_3$ is also promoted by the presence of Al_2O_3 [86].

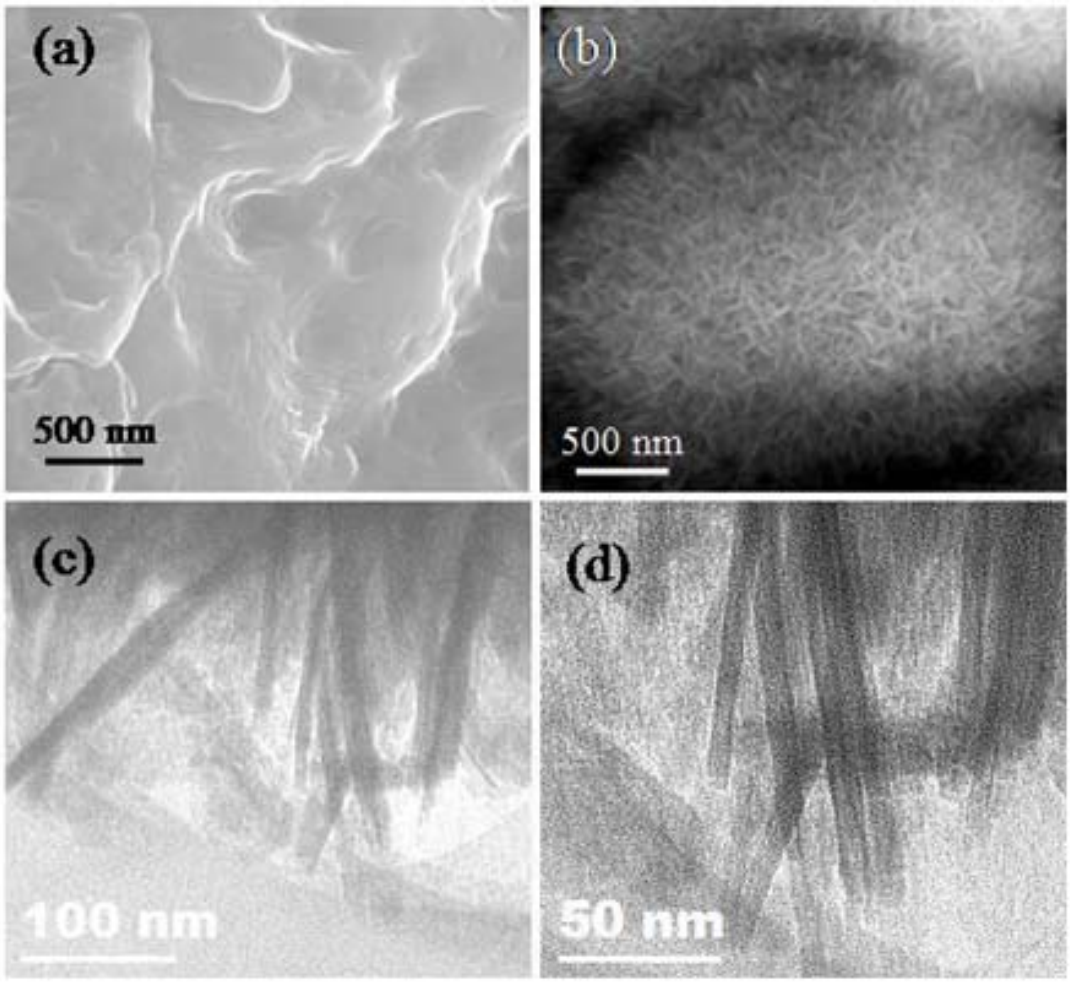

Fig. 2.18 (a) and (b) FESEM images of the Al metal surface and $Al(OH)_3$ nanorods obtained by the reaction of Al metal powder with water at 75 °C respectively. c and d are TEM images of the $Al(OH)_3$ nanorods obtained at 50 °C and 75 °C respectively.

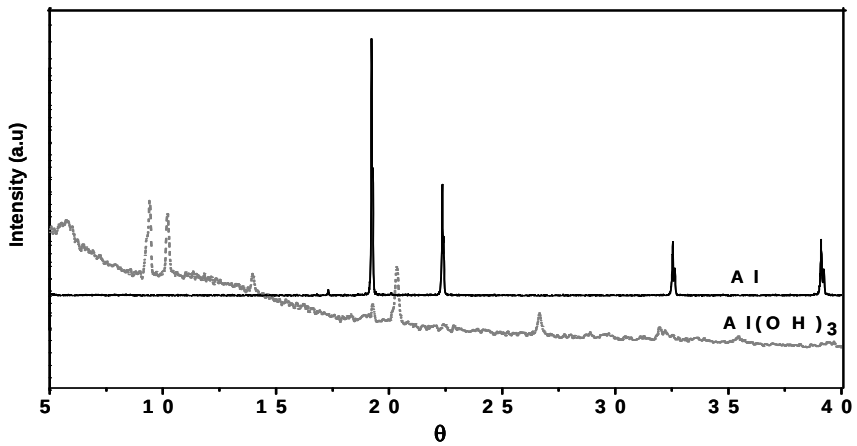

Fig. 2.19 XRD patterns of $Al(OH)_3$ nanorods along with the starting metal

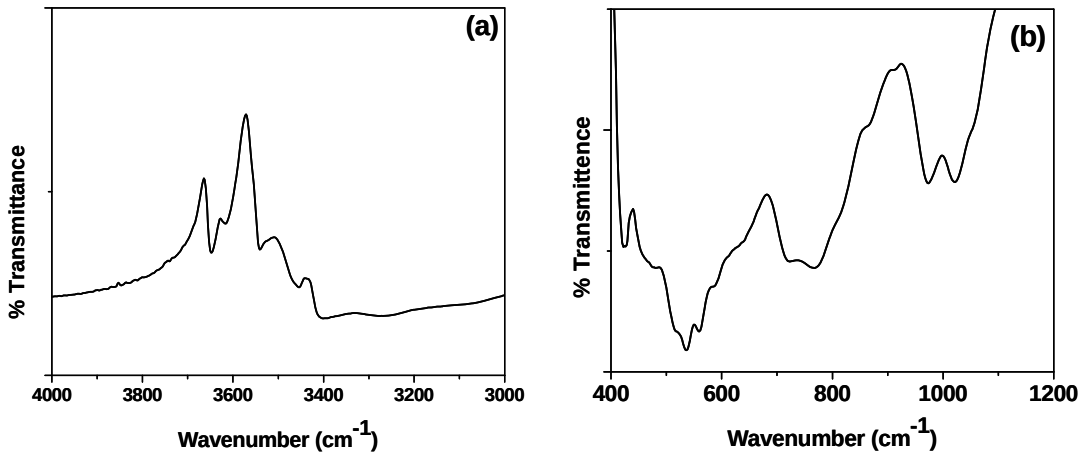

Fig. 2.20 Near-IR (a) and mid-IR (b) spectra of $Al(OH)_3$

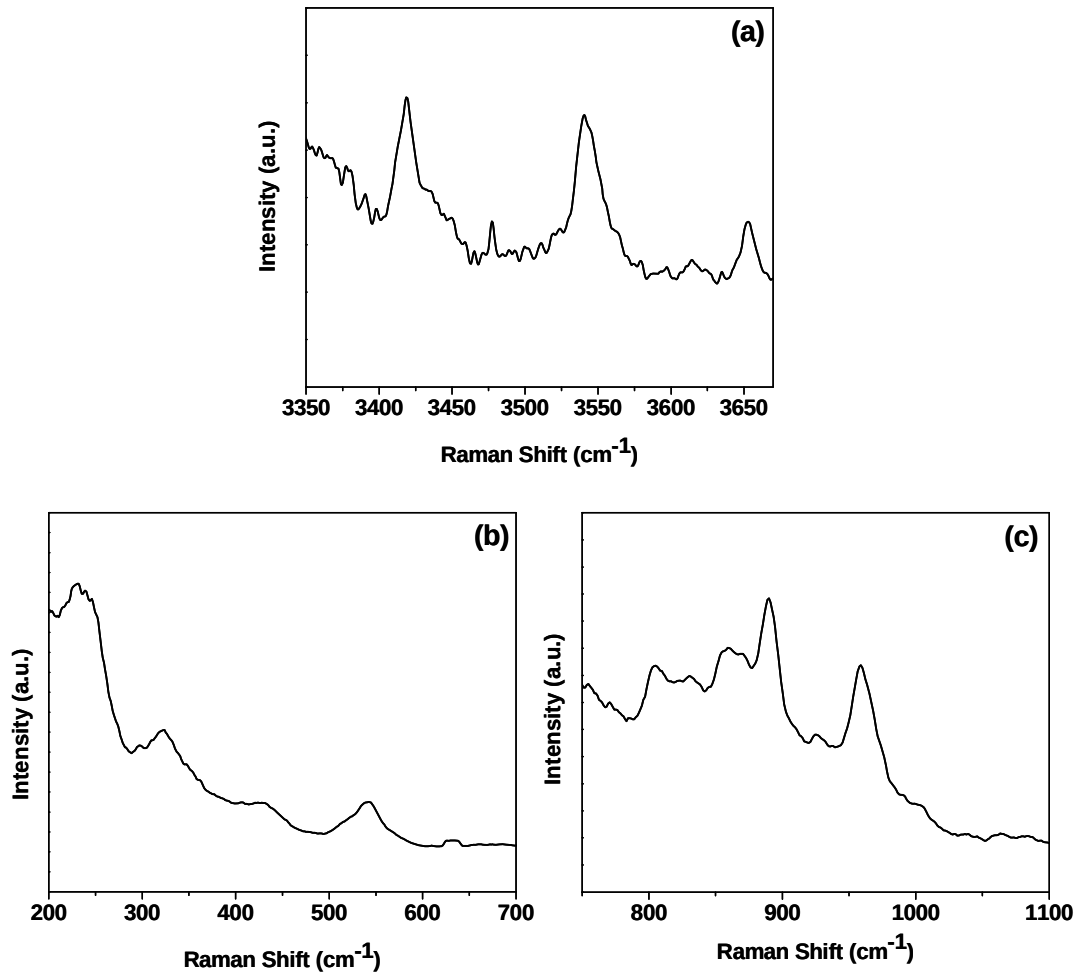

Fig. 2.21 Raman spectra of high-wavenumber region (a) and low-wavenumber region (b and c) of $Al(OH)_3$

We have confirmed the formation of $Al(OH)_3$ by IR spectroscopy (see Fig. 2.20) as well as Raman spectroscopy (see Fig. 2.21). In the fundamental hydroxyl stretching region, we are observed peaks in IR spectra (Fig. 2.20 (a)) at 3648, 3618, 3540, 3453 and 3402 cm^{-1}. Bayerite mid-IR spectra (Fig. 2.20 (b)) show high intense bands at 1020 cm^{-1} (hydroxyl deformation), 976, 768 cm^{-1} (hydroxyl translation), and 535 and medium intense bands at 717, 586, 560, 475 and 424 cm^{-1}. Gibbsite and bayerite (polytypes of aluminum trihydroxides) have the same structural sheet-like unit, which consists of a layer of aluminium ions sandwiched between two layers of hexagonally packed hydroxyl ions, in the plane defined by the *a* and *b* axes. The oxygens of one layer lie directly above the oxygens at the top of the layer below. The sheet-like units are stacked along the *c* axis [87-89]. The difference in structure between gibbsite and bayerite is that one can be generated from the other by a rotation about the *c* axis of one of the sheet-like units by 60° [89]. The Raman bands (see Fig. 2.21) agree with those reported in the literature [90, 91]. Raman spectrum of the bayerite nanorods shows three major bands at 3653, 3541 and 3418 cm^{-1} and three shoulder bands at about 3624, 3450 and 3439 cm^{-1} (Fig. 2.21 (a)) are similar with those found by Raoul Island in New Zealand [91]. Bayerite consists of the same hexagonally packed hydroxyl group as does gibbsite. The crystal structure of both minerals is monoclinic, *P*21/*n*. Differences in the Raman spectra in the stretching vibration region reflect the Al-OH distance of 1.74–2.06 Å for bayerite compared with 1.73–2.14 Å for gibbsite, and the OH-OH distance of 2.92–3.24 Å for bayerite compared with 2.75–3.24 Å for gibbsite [90]. The shoulder peaks at 3450 and 3439 cm^{-1} may be attributed to surface

hydroxyl groups in the bayerite structure. The bayerite spectrum in the low-wavenumber region (Fig. 2.21 (b) and (c)) is not as complex as the gibbsite spectrum and these two phases are therefore well distinguished, although bands at 1005, 976, 890, 433 and 322 cm^{-1} may overlap with the gibbsite bands at 1019, 980, 892, 444 and 321 cm^{-1}. However, other bands of bayerite are well resolved and are distinctly different from those of gibbsite. The bands with greatest intensity are at 542 and 296 cm^{-1} [90].

2.4.3 ZnO nanostructures generated at the liquid-liquid interface

We could prepare nanorods as well as nanofilms of ZnO at liquid-liquid interface. We first studied the effects of concentrations of the zinc precursor, $Zn(cup)_2$, NaOH as well as the organic amine on the ZnO nanostructures formed at the liquid–liquid interface. XRD patterns of the ZnO nanostructures (Fig-2.22) obtained at the liquid-liquid interface could

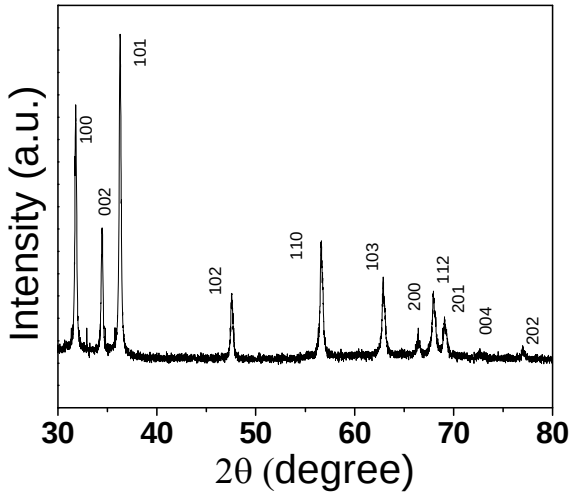

Fig. 2.22 XRD pattern of ZnO nanorods obtained at liquid-liquid interface by using TOA (4.58mM), NaOH (0.04 M) and $Zn(cup)_2$ (0.24 mM)

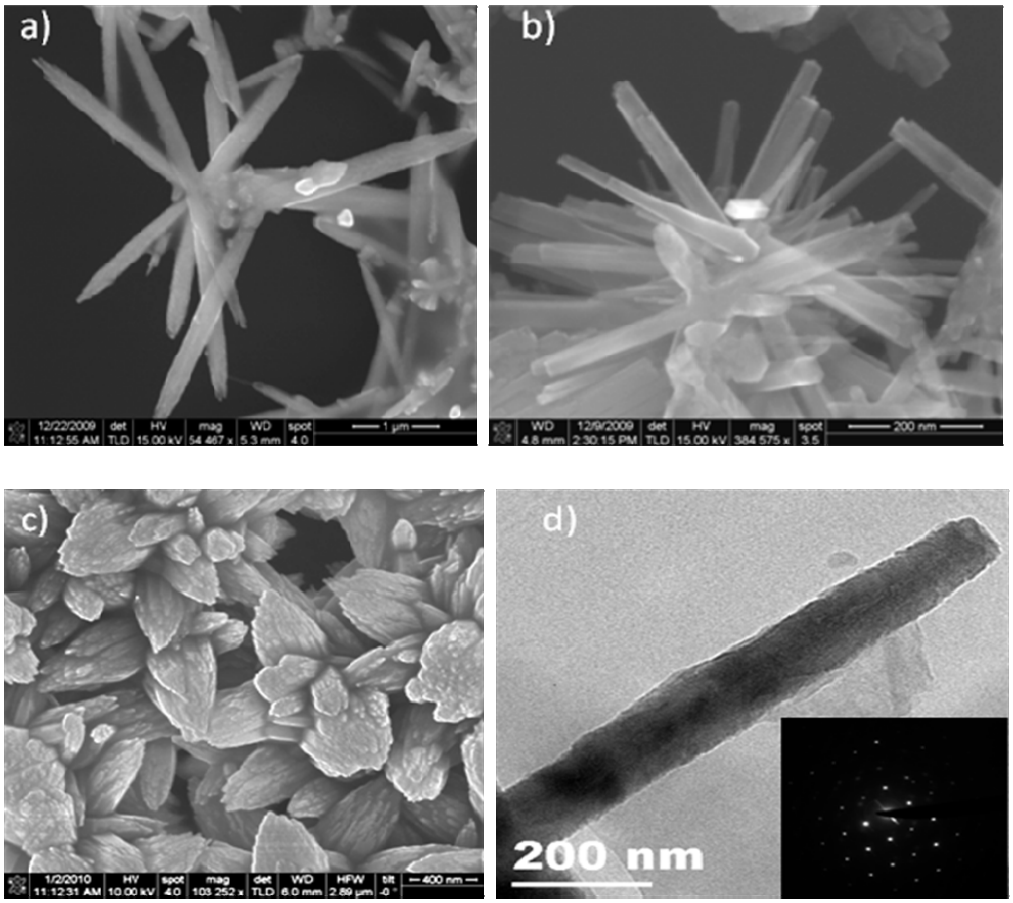

Fig. 2.23 FESEM images of ZnO nanorods, with variation of the concentration of zinc $(cup)_2$: (a) 0.24mM, (b) 1.17mM, and (c) 2.36 mM with a fixed concentration of NaOH (0.04M), trioctyl amine (4.58mM). (d) TEM image of a ZnO nanorod along with the SAED pattern.

all be indexed on the hexagonal wurtzite structure (space group: P63mc; a = 0.3249 nm, c = 0.5206 nm, JCPDS card No. 36-1451). In the presence of an amine such as trioctylamine (TOA), the reaction between the $Zn(cup)_2$ and NaOH primarily yields nanorods. Fig. 2.23 shows FESEM images of the nanorods obtained with varying concentrations of $Zn(cup)_2$, keeping NaOH (0.04 M) and amine (4.58 mM) concentrations constant. When the $Zn(cup)_2$ concentration was 0.24 mM, well-defined nanorods of ZnO were formed at the interface as seen in Fig. 2.23 (a), the average diameter of the nanorods

being around 250 nm with lengths up to 2–3 μm. In Fig. 2.23 (b) and (c), we show FESEM images of ZnO nanorods obtained with the $Zn(cup)_2$ concentrations of 1.17 and 2.36 mM respectively. The corresponding diameters of the nanorods obtained are 30 and 20 nm with lengths of around 300 and 450 nm respectively. At lower concentrations of $Zn(cup)_2$ relative to NaOH, the nanorods are less agglomerated but at the higher concentrations bundles of nanorods with agglomerated structures are obtained. Furthermore, as the relative concentration of $Zn(cup)_2$ is increased, the diameters of the synthesised nanorods decreases. All the nanorods obtained at the liquid–liquid interface, are generally single-crystalline. A typical TEM image of a ZnO nanorod synthesised using 0.24 mM of $Zn(Cup)_2$ is shown in Fig. 2.23 (d). The selected area electron diffraction (SAED) pattern shows the single-crystalline nature of nanorods (see inset of Fig. 2.23 (d)). It is remarkable that the nanorods formed at room-temperature at the liquid–liquid interface are single-crystalline without involvement of vapour or liquid.

The bundle of nanorods prepared using a high concentration of $Zn(cup)_2$ of 2.36 mM, shows an absorption band at 367 nm (Fig. 2.24 (a)) due to the smaller size of nanorods compared to those prepared by using less concentration of $Zn(cup)_2$ of 0.24 mM, which show a band at 370 nm (see inset of Fig. 2.24 (a)). Room-temperature PL spectra of bundles of ZnO nanorod bundles (Fig. 2.24 (b)) shows a weak UV emission band at 382 nm along with emission in the visible region. The UV emission is due to the radiative recombination between the electrons in the conduction band and the holes in the valence band. The bands around 404 and 425 nm are due

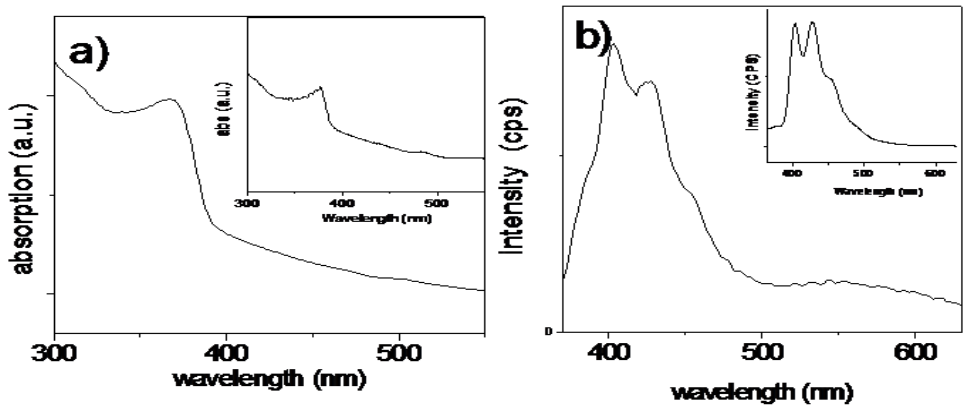

Fig. 2.24 (a) UV-Vis absorption spectrum of ZnO nanorods obtained with 2.36 mM of $Zn(cup)_2$ and 0.04M NaOH and inset shows ZnO nanorods obtained at 0.24 mM of $Zn(cup)_2$. (b) PL spectrum of ZnO nanorods obtained with 2.36 mM of $Zn(cup)_2$ and inset shows ZnO nanorods obtained at 0.24 mM of $Zn(cup)_2$.

to Zn vacancies (V_{Zn}) and Zn interstitials (Zn_i) respectively [92-94]. We also see a feature around 450 nm the origin of which is not clear [78, 94]. The weak band around 550 nm is due to the localised levels in the band gap. The most probable origin for green emission lies in the oxygen vacancies [78]. Nanorods prepared using a lower concentration of $Zn(cup)_2$ (0.24 mM) show little difference in the PL spectrum. They show negligible band edge as well as green emissions, but show a strong emission at 404 and 425 nm in the violet region as seen in the inset of Fig. 2.24 (b). It is to be noted that V_{zn} and Zn_i quench the band edge emission.

The effect of amine chain length on the ZnO nanostructures formed at the liquid–liquid interface was studied by keeping $Zn(cup)_2$ and NaOH concentrations constant at 0.24 mM and 0.04 M respectively and the amine concentration at 4.58 mM. The amines studied were n-butylamine, n-octylamine, n-dodecylamine and n-hexadecylamine. In Fig. 2.25 (a) and (b), we show the FESEM images of nanorods at the interface using butylamine and hexadecylamine respectively. The morphology is not sensitive to the

chain length of the amine. The corresponding PL spectra are shown in Fig. 2.25 (c) and (d) respectively. As the chain length of the amine increases, one notices a decrease in the oxygen defect band intensity (550 nm).

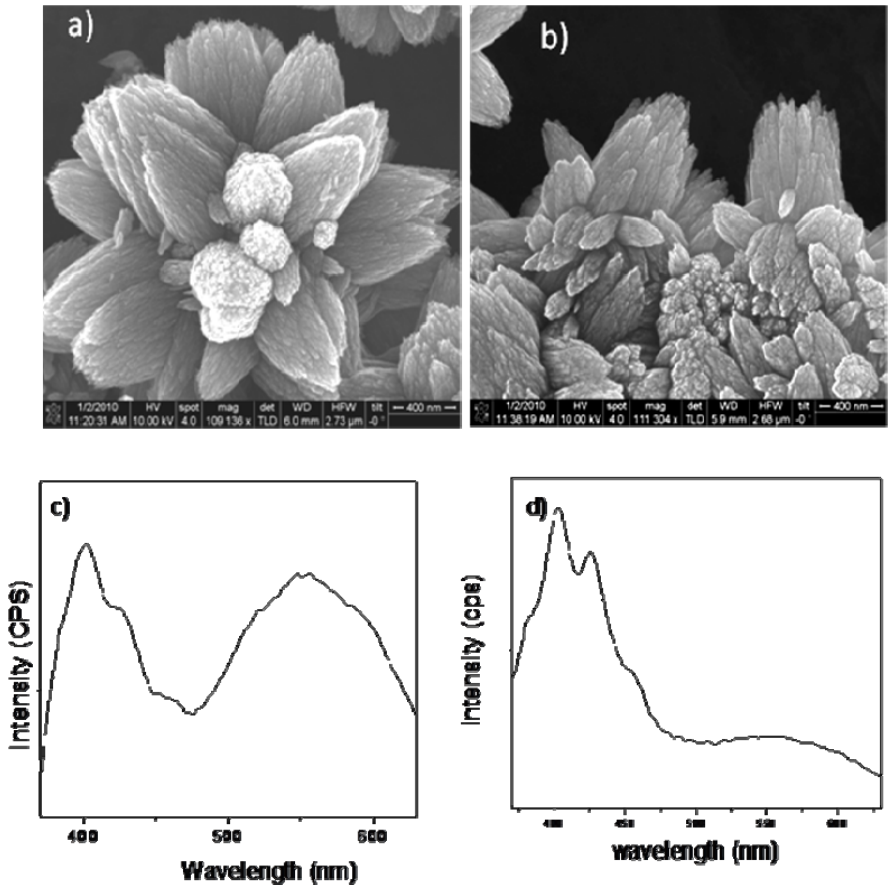

Fig. 2.25 FESEM images of ZnO nanoflowers obtained with 2.36 mM of $Zn(cup)_2$, 0.04 M of NaOH with variation of amine chain length using (a) butylamine and (b) hexadecyl amine, of concentrations 2.29 mM. The corresponding PL spectra of ZnO nanoflowers prepared using (c) butyl amine (d) hexadecyl amine

We have studied the effect of concentration of the amine on the ZnO nanostructures by keeping the concentration of $Zn(cup)_2$ (1.17 mM) and NaOH (0.04 M) constant. In Fig. 2.26 (a)–(c), we have shown FESEM images of the nanorods obtained at the interface using TOA concentrations of 2.29, 4.58 and 18.32 mM respectively. The average diameters of the nanorods

obtained with the amine concentrations are 200, 30 and 20 nm respectively. It is interesting that, as the amine concentration is increased, the aspect ratio of the nanorods increases. PL spectra of these samples were similar (as in Fig. 2.24 (b)). Fig. 2.26 (d) shows a TEM image of the bundles of ZnO nanorods. The nanorods are single-crystalline as confirmed by the SAED pattern shown as an inset in Fig. 2.26 (d).

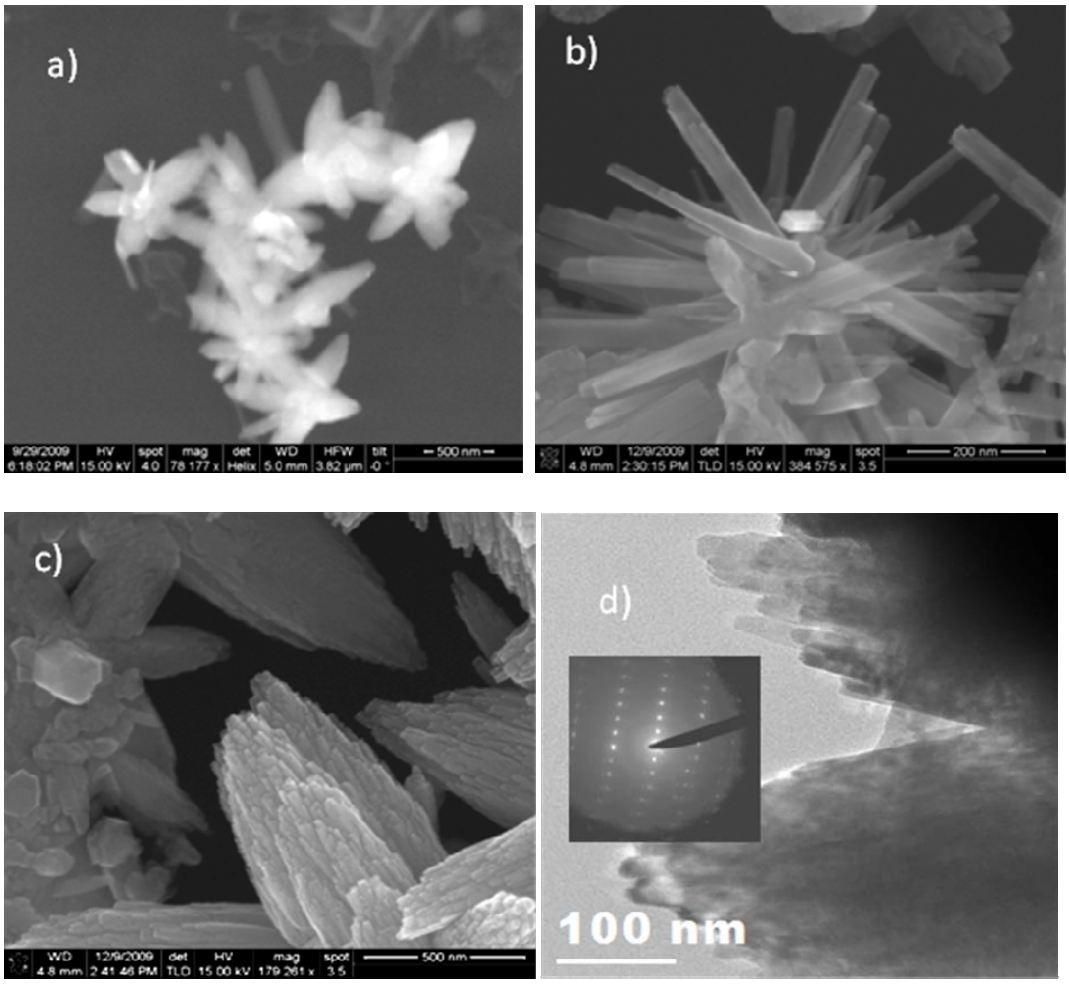

Fig. 2.26 FESEM images of ZnO nanorods obtained with 1.17 mM of $Zn(cup)_2$ 0.04 M of NaOH, with the variation of trioctyl amine concentration (a) 2.29 mM, (b) 4.58 mM, (c) 18.32 mM and (d) TEM image of bundles of ZnO nanorods obtained at trioctyl amine concentration 18.32 mM, along with SAED pattern

In the absence of an amine, we obtain ultrathin films of ZnO at the liquid–liquid interface when the concentration of $Zn(cup)_2$ was sufficiently low. This method enables us to obtain substrate-free films of ZnO. The as-synthesised ZnO films at the interface are readily transferred on to any solid substrate. A TEM image of a film obtained with a $Zn(cup)_2$ concentration 0.12 mM and a NaOH concentration of 0.04 M is shown in Fig. 2.27 (a). The SAED pattern reveals that the films were single-crystalline which is noteworthy. A contact mode AFM image of the ZnO thin film taken on a Si-

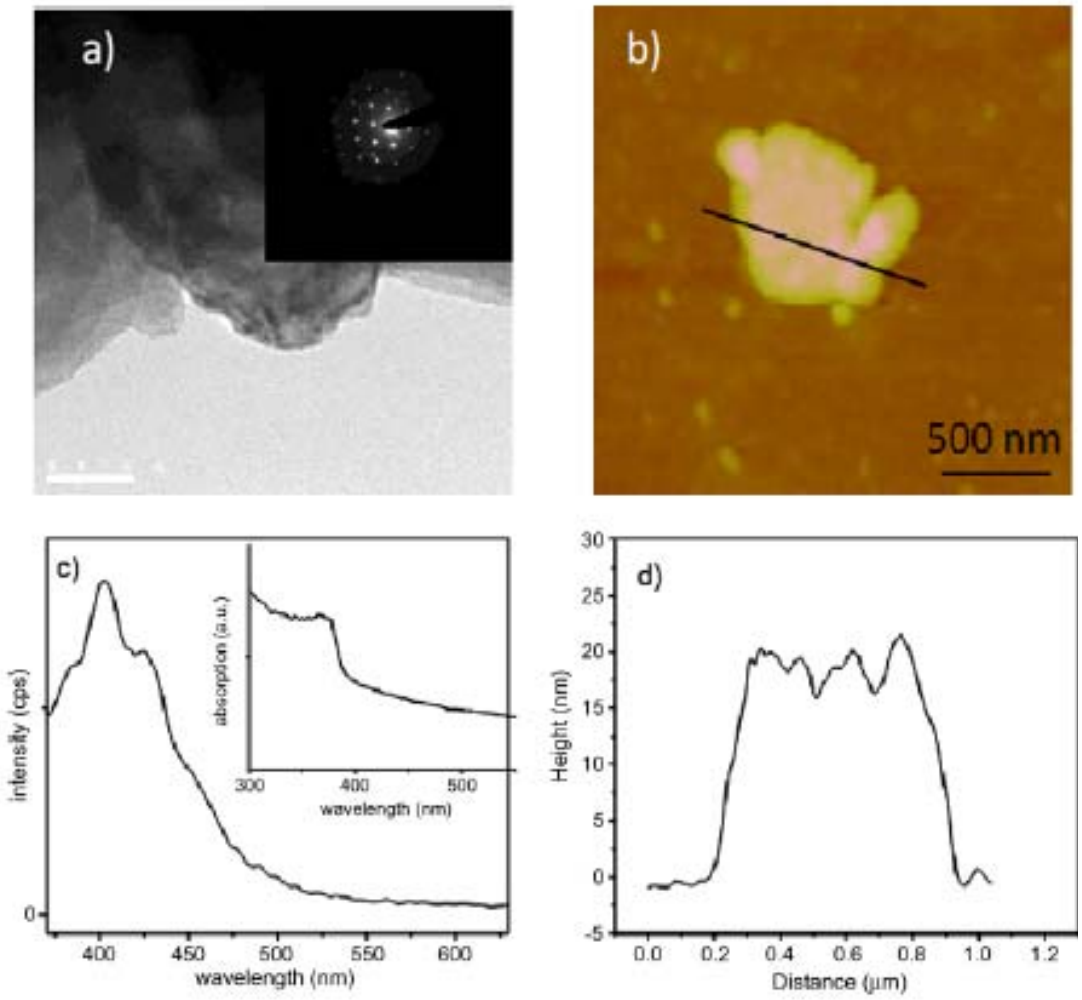

Fig. 2.27 ZnO single-crystalline ultrathin films obtained with 0.12 mM of $Zn(cup)_2$ and 0.04 M NaOH. (a) TEM image along with SAED pattern, (b) contact mode AFM image, (c) PL spectrum with inset UV–Vis absorption spectrum and (d) height profile of thin film obtained by AFM.

substrate is shown in Fig. 2.27 (b). The image reveals a film over an area of nearly 1 μm x 1 μm and its surface topology. The height profile in Fig. 2.27 (d) shows the ZnO film have to have a thickness of 20 nm. This is indeed a unique feature of the film generated at the liquid–liquid interface. The PL spectrum depicted in Fig. 2.27 (c), shows a weak band edge emission at 382 nm and defect bands at 404 and 424 nm along with a weak band at 450 nm. The inset in Fig. 2.27 (c) shows the UV–Vis absorption peak at around 370 nm.

2.4.4 Pure and nitrogen-doped ZnO nanobullets by the solvothermal method

We found that the optimal conditions to obtain the ZnO nanobullets require a large excess of ethanol (Zn : ethanol concentration of ~1:500). Figures 2.28 (a) and (b) show scanning electron microscope (SEM) images of the nanobullets at two different magnifications. These have a unique morphology with two distinct ends, blunt end sharp. Fig. 2.28 (c) is the X-ray diffraction (XRD) pattern of the as-prepared nanobullets. All the peaks in the pattern can be indexed on the wurtzite ZnO phase, with no apparent impurity phases. A careful review of the SEM images suggests the following: i) the bases of the nanobullets are hexagonal, indicating a growth direction along the wurtzite *c* axis, ii) the growth mode leads to tapering with a curved surface, i.e. clearly, from the base to the tip of the nanobullets is not a straight line, but a curved line. Yield of such nanobullets can be varied by controlling the reaction conditions and the remaining of the reaction product consists of nanorods. The diameter of the hexagonal base varies

from 500 nm to a 2-3 μm, the diameter at the tip is merely a few nanometers, while measuring 5-10 μm in length.

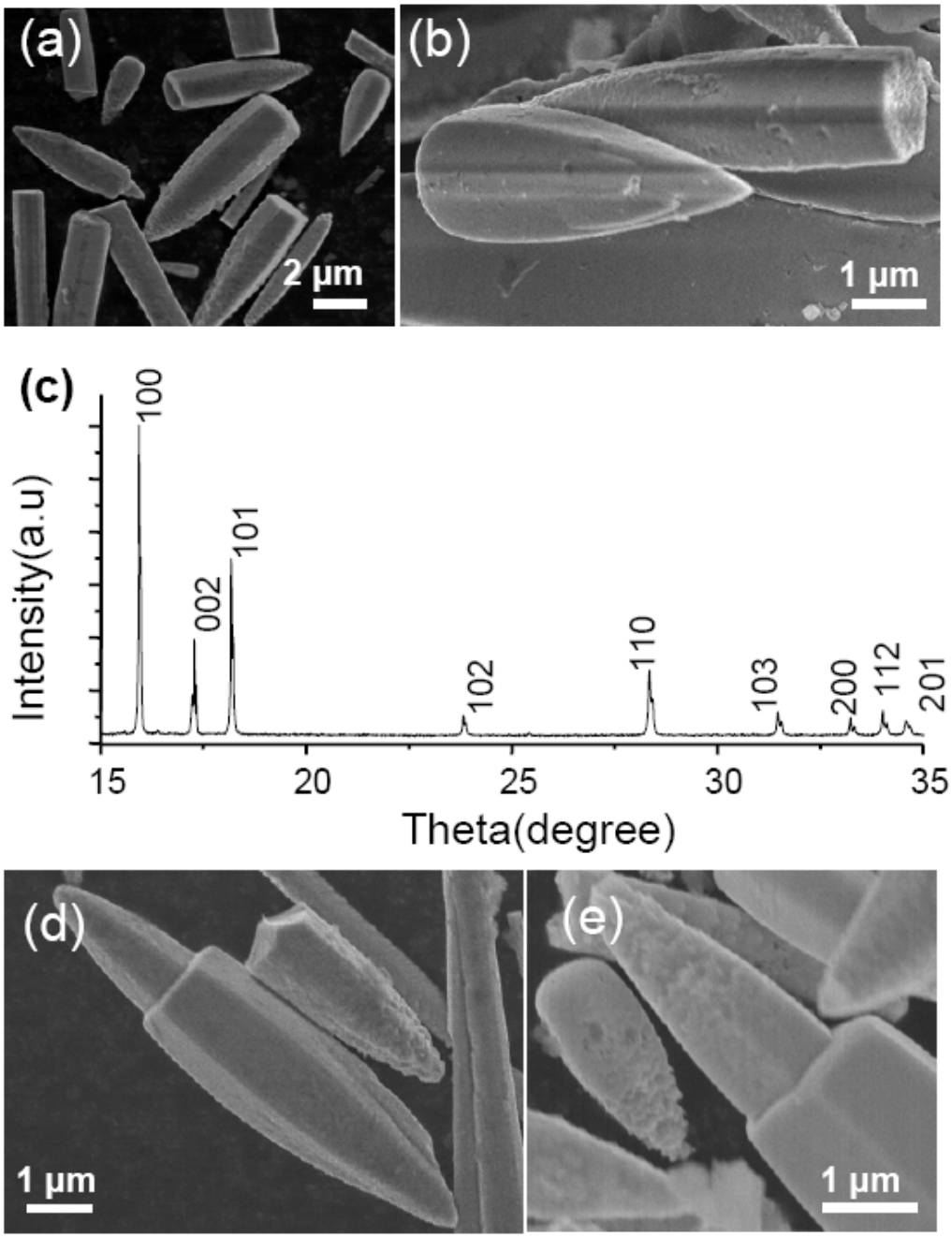

Fig. 2.28: Low magnification SEM image of ZnO nanobullets. (b) A high magnification image of two nanobullets showing the two distinct ends, the sharp tip as well as the hexagonal base. (c) XRD pattern of the as synthesized nanobullets. (d) and (e) shows high magnification SEM images of two unusual nanobullets in which growth was found to take place on both side from the base.

Several other nanostructures are also observed that are closely related to the nanobullet morphology. In Figures 2.28 (d) and (e), we present SEM

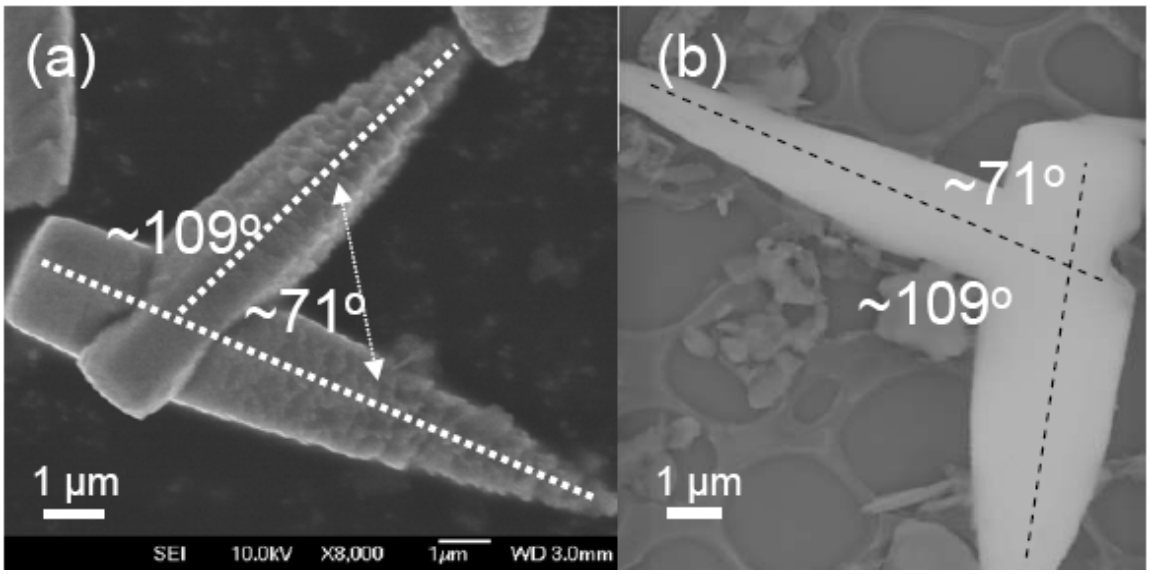

Fig. 2.29: (a) SEM image of conjoined twin ZnO nanobullets. (b) TEM image of another conjoined ZnO crystallite with the inverse orientation of the tips when compared with the one in (a). The angle between the two arms, in both the structures, is close to the tetrahedral angle of ~ 71°.

images showing secondary growth from the base of the nanobullet. Figures 2.29 (a) and (b) show conjoined ZnO twin nanobullets, where they are oriented at an angle of ~71°. This orientation angle is close to that of tetrahedra and suggests that the entire structure is single-crystalline [95]. As will be discussed later, these images give important clues to the growth mechanism of the nanobullets.

Nitrogen doping was successfully carried out as follows. The reaction of zinc nitride with water to form ammonia and zinc oxide is well known [96].

$$Zn_3N_2 + 3H_2O \Leftrightarrow 3ZnO + 2NH_3$$

In the ambient conditions, this is a violent and spontaneous reaction. We explored the feasibility of the reverse reaction, keeping in mind (i) the

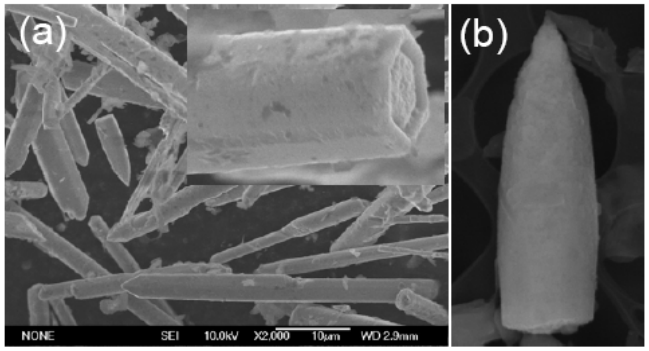

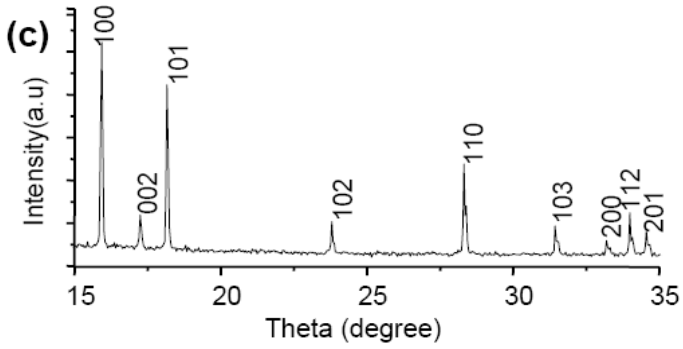

Fig. 2.30: (a) Low magnification SEM image of N-doped ZnO nanobullets. Inset shows the hexagonal base of these nanobullets. (b) High magnification image of a nanobullet. (c) XRD pattern of the as synthesized N-doped ZnO nanobullets.

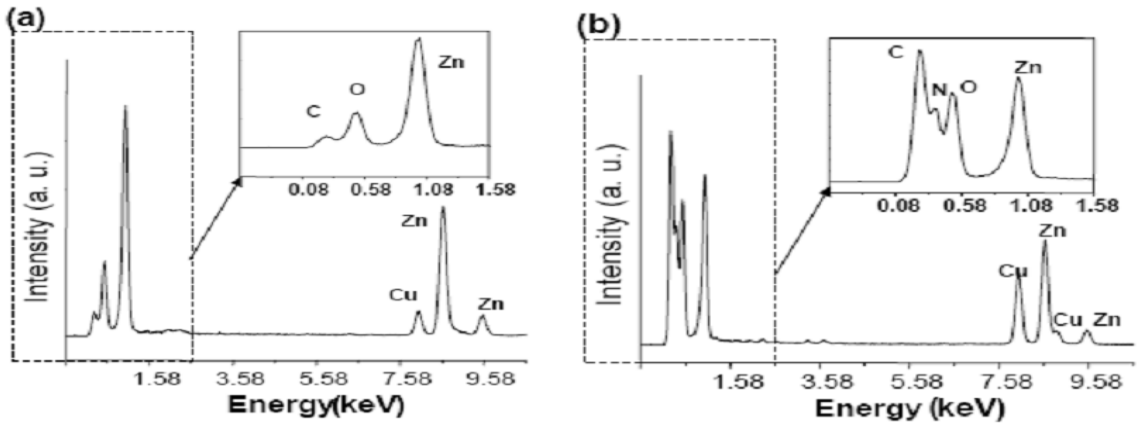

Fig. 2.31: EDS patterns acquired from a (a) pure and (b) N-doped ZnO nanobullet. The region of interest is highlighted with a dotted box and enlarged in the insets. The nitrogen peak in the N-doped sample confirms the successful doping of the nanobullets.

extreme solvothermal conditions [97], (ii) large excess of ZnO and NH_3 and (iii) high reactivity of the nascent ZnO species. Thus, Fig. 2.30 (a) shows a SEM image of the N-doped ZnO nanobullets. The addition of ammonia has affected the morphology of the ZnO nanostructures to some extent. Herein, nanobullets seem to have grown longer, giving a more pencil like appearance

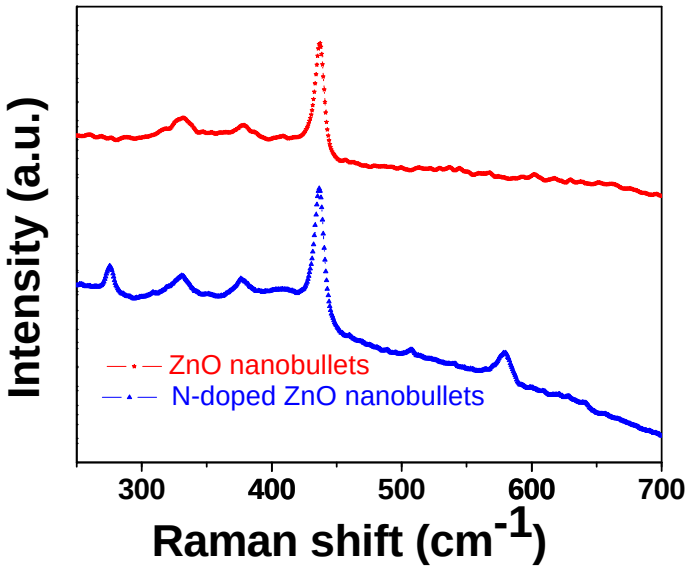

Fig. 2.32: Raman spectra of pure and N-doped ZnO nanobullets.

to the nanostructures. The base of the nanostructures is, like in the previous case, hexagonal (inset in Fig. 2.30 (a)). Fig. 2.30 (b) is the SEM image of a single N-doped ZnO nanobullet. Fig. 3 (c) displays the XRD pattern of the sample confirming the purity and high crystallinity. Fig. 2.31 (a) and (b) further show energy dispersive X-ray spectroscopy (EDS) patterns acquired from single nanobullets. The carbon signal originates from the TEM grid. Even though owing to low molecular weight, a quantative estimation of the N content is non-trivial, a clear N peak can be observed in the doped sample. The intensity of the peaks in various parts of the same structure, investigated with a nano-beam, was comparable. Raman spectroscopy was also employed to further confirm N doping. ZnO nanorods exhibit Raman bands at 332, 378, 437 cm^{-1} (see Fig. 2.32). The bands at 437 and 378 cm^{-1} are attributed to E2 (high) mode and A1 (TO) mode respectively and the band at 332 cm^{-1} could arise from a multiphonon

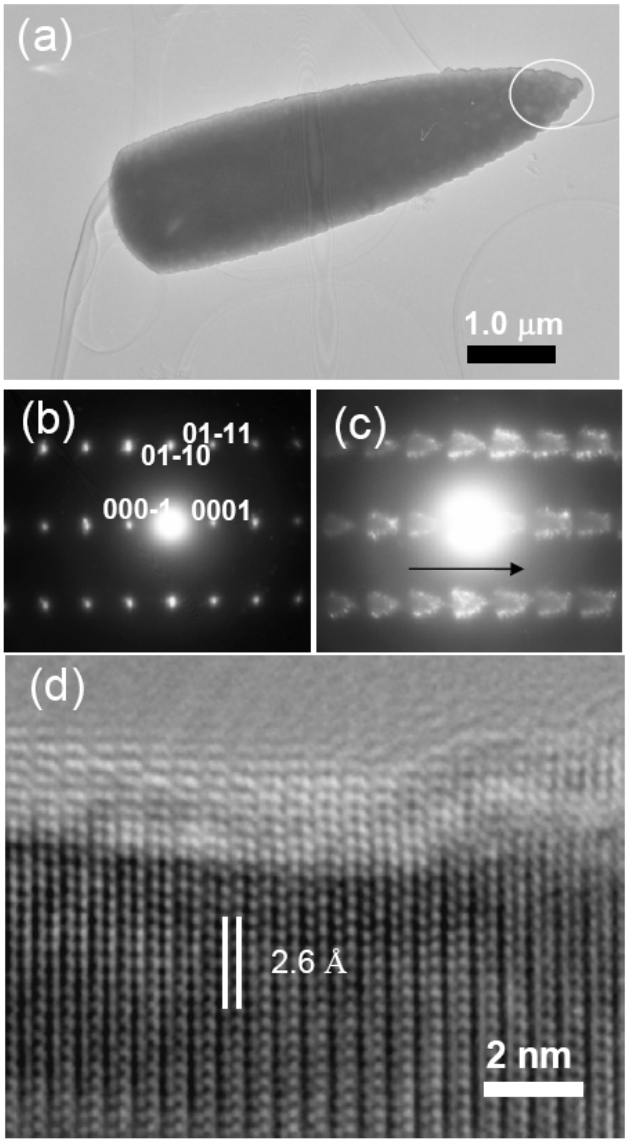

Fig. 2.33: Low magnification TEM image of a pure ZnO nanobullet. (b) A representative SAED pattern along the [2-1-10] zone-axis acquired from the part of the nanobullet marked with a while circle in (a). (c) A defocused SAED pattern acquired at the same region and same orientation as that of (b) confirming that the growth direction is indeed [0001]. (d) An HREM image of the nanobullet.

process. We observe four additional bands at 275, 507, 579 and 642 cm^{-1} in the case of N-doped ZnO (see Fig. 2.32). These modes correspond to the silent modes of wurtzite-ZnO and arise from the breakdown of the translational crystal symmetry induced by defects and impurities.

Fig. 2.33 (a) shows a low magnification TEM image of a pure ZnO nanobullet. Fig. 2.33 (b) is a selected area electron diffraction (SAED) pattern obtained from the tip of the nanostructure. The pattern can be indexed in the (01-10) zone axis of the wurtzite ZnO and confirms the single-crystalline nature. The growth direction can be easily established from the defocused SAED pattern in Fig. 2.33 (c), which is [0001] as expected. Fig. 2.33 (d) shows a high resolution TEM (HREM) image of the nanobullet revealing that the nanobullets are defect

free. The separation between two lattice planes is ~2.6 Å, equivalent to the separation between the (0002) planes. As the tip diameter reduces, the concentration of crystal defects also increases gradually, the tip having a large number of defects and dislocations (see Fig. 2.34). The structure of the N-doped ZnO nanobullets was found identical to that of the pure ones (Fig. 2.35).

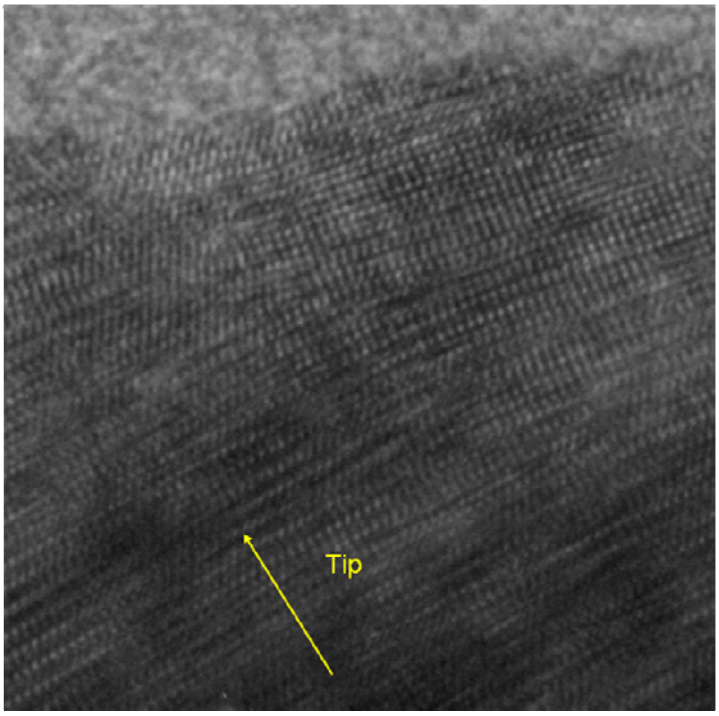

Fig. 2.34: HREM image at the tip of a nanobullet showing large number of defects and dislocations.

Many questions arise for the growth mode of the nanobullets. Do they grow from the center towards both the ends? Or do they grow only in one side, such as from the base to the tip or vice versa? What makes their growth to be asymmetric? Some of the observations from SEM and TEM images may give vital clues to their growth mechanism. These are as follows: i) the secondary growth observed in the Fig. 2.28 (d) and (e) indicate that the

growth takes place from the base towards the tip. An equal growth in both the directions, from the center, would have led to the symmetric faceted or oval shaped crystals [98]. In absence of an apparent template, the growth of nanobullet is indeed unusual. ii) Presence of conjoint twin structures with a tetrahedral angle (and none other), as the ones seen in Figures 2.29 (a) and (b), rules out the possibility of the inner surface of the reaction vessel acting as a template, since presence of two nucleating centers at this angle would be extremely rare.

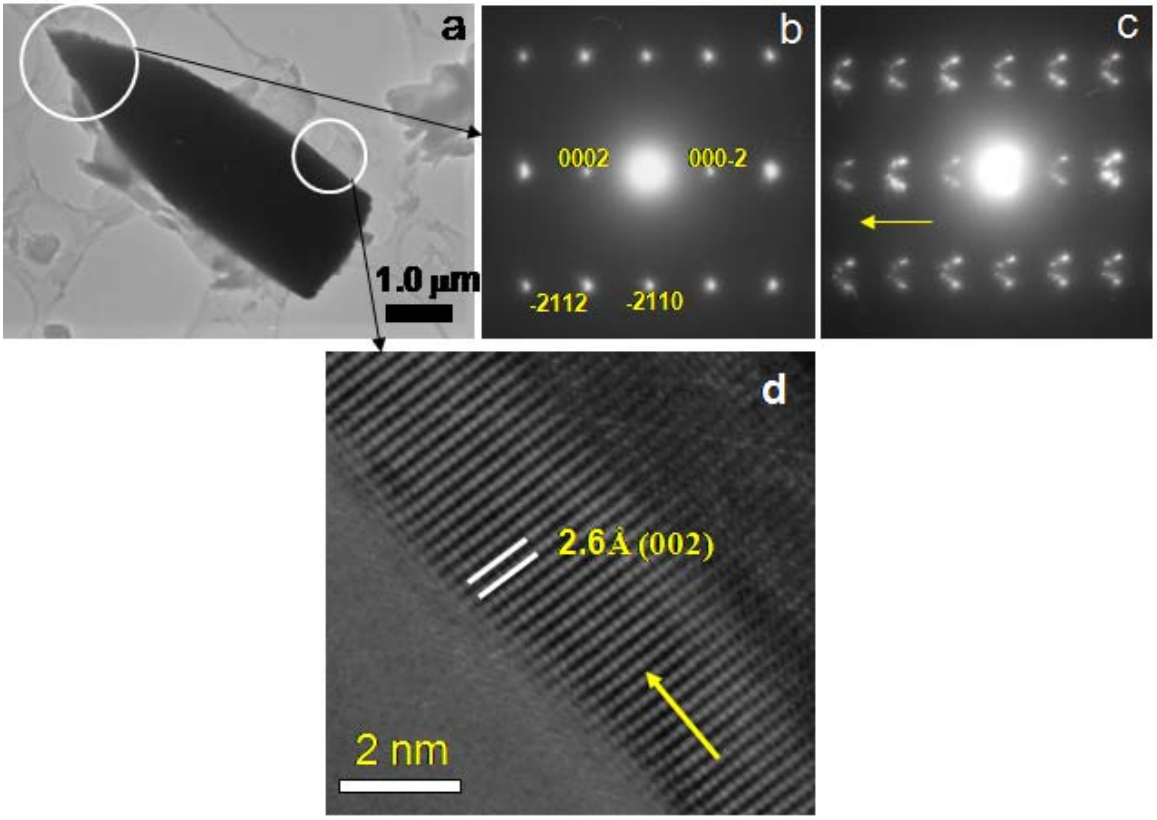

Fig. 2.35: (a) Low magnification TEM image of a N-doped ZnO nanobullet. (b) SAED pattern along the [2-1-10] zone-axis acquired from the part of the nanobullet marked with a while circle in (a). (c) A defocused SAED pattern acquired at the same region and same orientation as that of (b) confirming that the growth direction is indeed [0001]. (d) An HREM image of the nanobullet.

Here, we propose a novel self-template growth mechanism. We found that $Zn(OH)_2$ is generated as a reaction intermediate, by carrying out the solvothermal synthesis for a shorter duration. $Zn(OH)_2$ is a layered material with a sheet like morphology (in Fig. 2.36) [99]. The in-plane symmetry of these sheets is hexagonal, which is identical with the base-plane symmetry of the nanobullets. Hence it would be logical to assume that the $Zn(OH)_2$ acts as transient templates on which the nanobullets grow. Gradually in the course of time, the $Zn(OH)_2$ dissolves away, leaving behind the ZnO nanobullets.

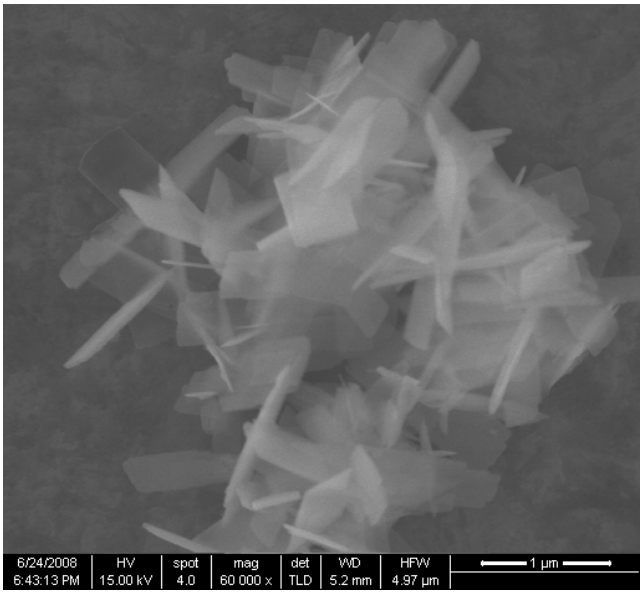

Fig. 2.36: SEM image of $Zn(OH)_2$ sheets obtained after a short duration of the reaction. The same reaction after a prolonged time yields ZnO nanobullets. Thus, it is possible that these sheets act like a self sacrificing template for the nanobullet growth.

The growth mode has another interesting feature i.e. the reduction of the diameter in steps of a few nanometers, but not continuously. As was mentioned earlier, the nanobullets were bound between curved surfaces suggesting a continuous change of the exposed crystal facets. This is unlikely, as each facet cannot be energetically stable. Fig. 2.37 (a) shows a typical TEM image of a nanobullet tip. The steps are not in the same position in all the six facets and the step edges are not atomically abrupt. Figures 2.37 (b) and c show HREM images of such steps

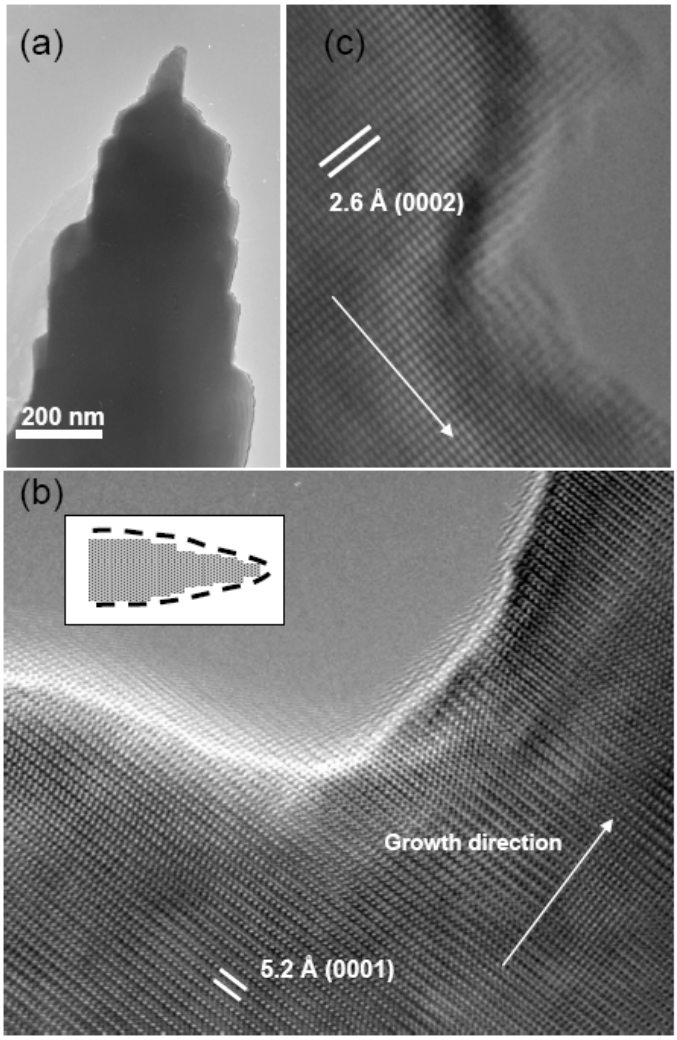

Fig. 2.37: (a) Low magnification TEM image of the tip of a ZnO nanobullet. (b) The corresponding HREM image of the nanobullet. The image confirms single-crystalline nature of the step edges that are responsible for the tapering of the nanostructure tip. Inset is a schematic showing the morphology of a tip while the low magnification images give an apparent impression of a smooth exterior as shown by the broken line. (c) Typical HREM image of a step edge observed in N-doped ZnO nanobullets.

in pure and N-doped ZnO nanobullets respectively. The steps are entirely single-crystalline and defect free in nature. Inset in the figure shows schematic of a nanobullet. This mechanism is unlike the surfactant mediated stepwise growth proposed by Lie and Zeng [100], rather should be

a consequence of ever-reducing reactant-concentrations and its effect on growth kinetics.

Photoluminescence spectra of ZnO and N-doped ZnO nanobullets show similar bands. PL spectrum of ZnO nanobullets is shown in Fig. 2.38. Inset in Fig. 2.38 shows PL spectrum of N-doped ZnO nanobullets. We observe bands centered at 407 nm, 432 nm and 456 nm. Photoluminescence features of N-doped ZnO nanorods are compared here with undoped ZnO nanorods, which are prepared at similar conditions without adding ammonia to the reaction mixture.

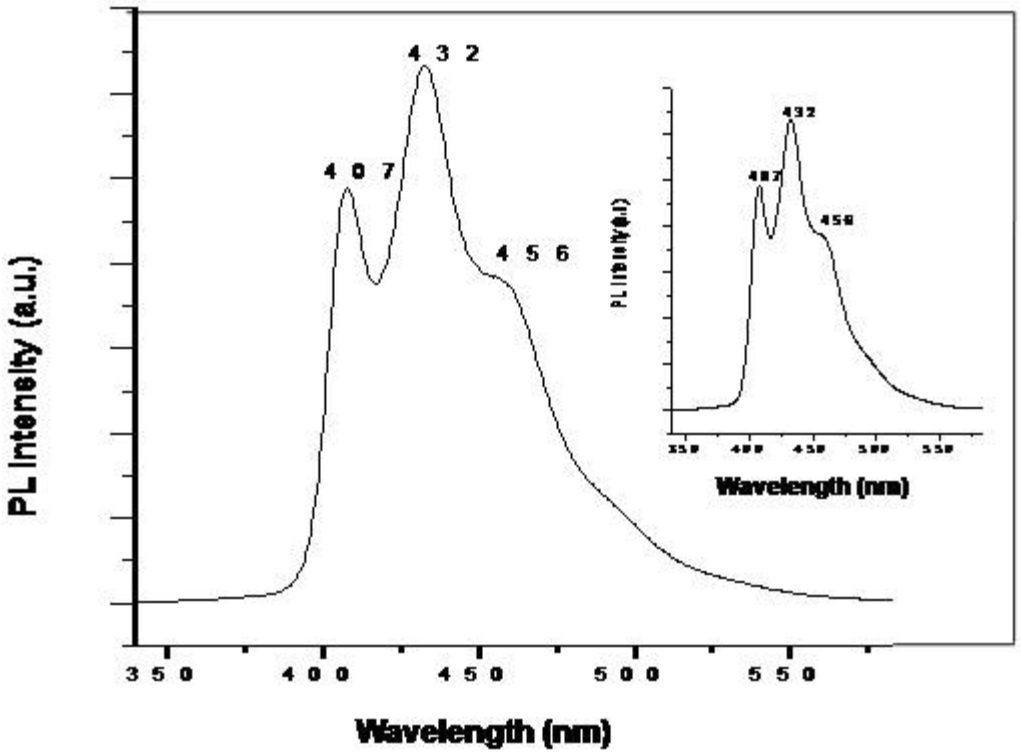

Fig. 2.38 PL spectrum of ZnO nanobullets. Inset shows the PL spectrum of nitrogen-doped ZnO nanobullets.

2.4.5 Cathodoluminescence (CL) and field emission (FE) properties of pure and N-doped ZnO nanobullets

Cathodoluminescence: Cathodoluminescence is one of the most widely used techniques to investigate local optical properties of materials due to its high spatial resolution [67]. In one of the first demonstrations in 1985, Boyes and coworkers showed that the CL spectra acquired from ZnO catalyst not only revealed the band gap luminescence but also could detect the donor level transitions with a resolution of few micrometers [101]. ZnO nanostructures are promising for many potential applications such as UV lasers, sensors and solar cells [45, 102]. Their optical properties can be tuned by doping with donor (n type) and acceptor (p type) impurities. Recently, violet electroluminescence from homo-structural p–i–n junctions is demonstrated at room-temperature, using high quality pure and N-doped ZnO films. However, investigations of optical properties acceptor doped ZnO are limited to epitaxial films [103]. Motivated by their importance, we have explored the optical properties of the pure and N-doped nanobullets by employing high spatial resolution CL spectroscopy. While the pure nanobullets exhibited remarkable uniformity and emission stability, N doping was found to induce a large red-shift (0.024 eV) of the ZnO band-edge emission as compared to samples obtained by any other synthesis technique.

Fig. 2.39 (a) displays a typical CL spectrum acquired from a pure ZnO nanobullet (seen in the SEM image in Fig. 2.39 (b)). The spectrum consists of a narrow and strong UV peak centered on 381 nm (~3.2 eV) and broad,

low intense luminescence in the visible region. Spectra recorded from many other nanobullets showed similar features. It was observed that the UV peak varies from 380 to 385 nm while the visible luminescence was absent in many nanobullets. Fig. 2.39 (c) is the corresponding CL images of the nanobullet showing uniform luminescence that arises entirely from the nanostructure alone.

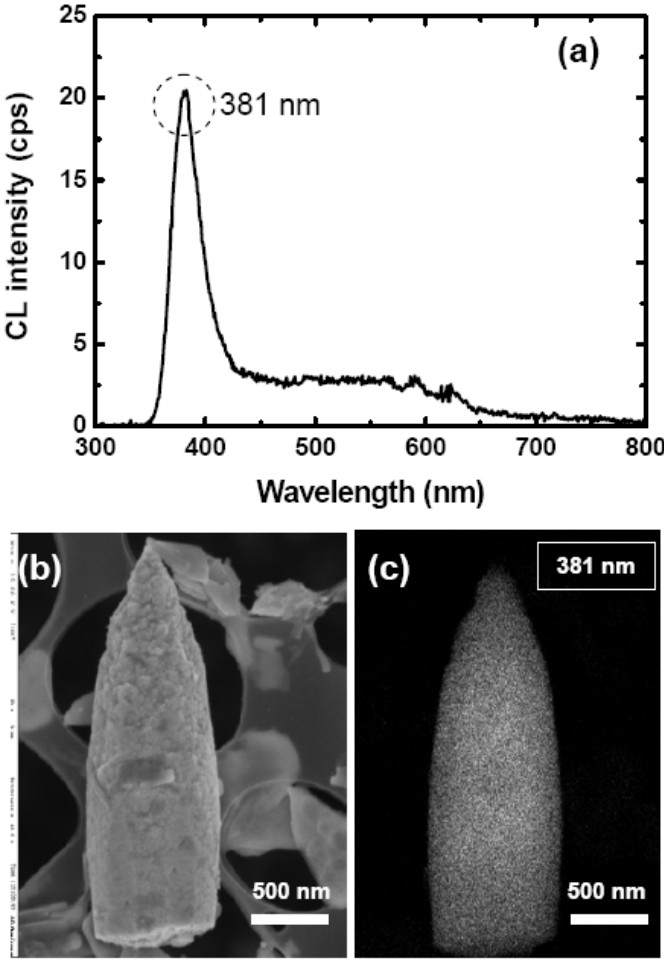

Fig. 2.39: (a) CL spectrum recorded from the ZnO nanobullet seen in the SEM image in (b). (c) Corresponding CL image of the nanobullet.

In order to study spatial variation of optical property, we have recorded CL spectra in various locations within the same nanobullet. Fig. 2.40 (a) shows a CL image of such a ZnO nanobullet. A number of CL spectra, acquired at various locations along the line shown in this image is plotted Fig. 2.40 (b).

The spectra are fairly uniform, while the intensities of the UV peak (385 nm in this case) gradually changes along the nanostructure. This is low near the bullet tip, and increases gradually with size. Investigation of several other structures yielded similar results and thus confirmed uniformity in optical transitions within the nanobullet.

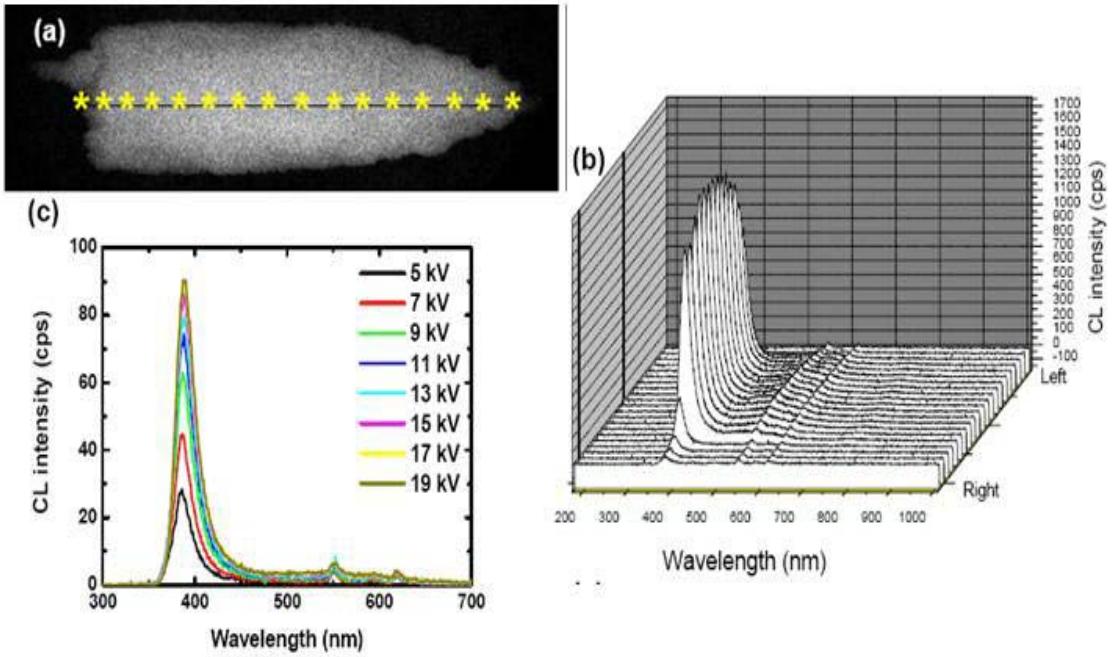

Fig. 2.40: (a) CL image of a pure ZnO nanobullet acquired using a 385 nm emission window. CL spectra were acquired at various locations along the nanobullet as marked in the image and are plotted in (b). (c) CL spectra acquired at various accelerating voltages of the probe electron beam.

CL properties of the ZnO nanostructures have been investigated by several others [104-107]. The UV peak observed in theis study can be ascribed to the near band-edge emission (NBE: 385 nm) and visible one to the deep level emissions (DE: 550 nm). Chang *et al.* found that stoichiometry is key to the a strong CL emission near the band-edge (382 nm) while large oxygen vacancy lead to a strong green emission around 550

nm [106, 108]. Schirra *et al.* in a detailed analysis established that the NBE peak constricts of multiple transitions involving donor bound excitation recombination [109]. Another study by Dang and coworkers indicated that large lattice defects at the nanowires bottoms, grown on a substrate, leads to variation in CL transitions [107]. Thus, the UV peak in the present sample is the NBE peak while the visible emission may be caused by oxygen vacancies.

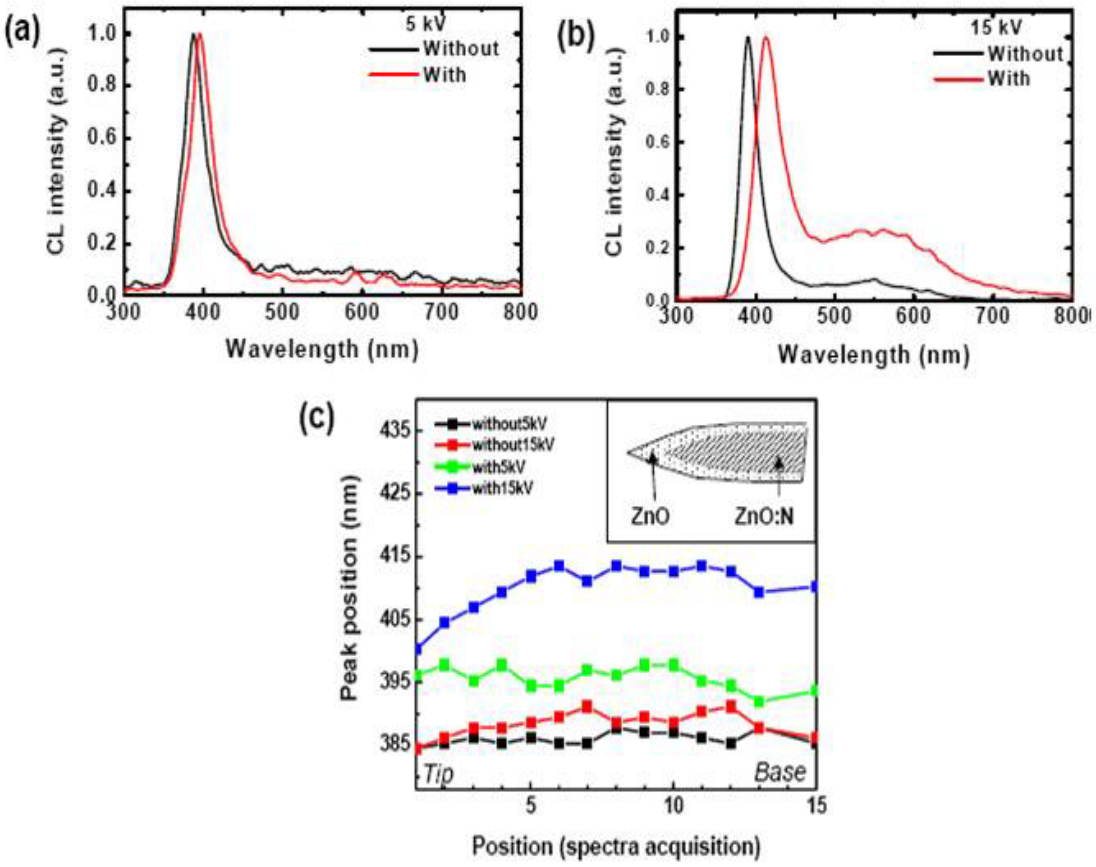

Fig. 2.41: Typical CL spectra acquired from a pure (black) and an N-doped (red) ZnO nanobullet at (a) 5 kV and (b) 15 kV respectively. (c) Plots showing the variations of the luminescence peak positions within a single nanobullet, observed at two different accelerating voltages.

We further investigated the emission properties at various depths from the surface of the nanobullet. Increasing the probe electron acceleration voltage increases the penetration-depth and the CL generation volume [67]. Fig. 2.40 (c) shows the CL spectra acquired at different voltages. The intensity gradually increases as the applied voltages changes from 5 to 19 kV. On the other hand, the peak position has a marginal red shift from 385 nm to 389 nm, showing that the optical transitions near the surface and the core of the structure are nearly identical.

Investigation of the CL properties of the N-doped ZnO sample shows interesting features. The CL spectra for the pure and the doped samples are nearly identical at 5 kV, as observed in Fig. 2.41 (a). However at 15 kV, there is a red-shift of the NBE peak position of the N-doped sample by ~ 30 nm (0.024 eV, Fig. 2.41 (b)). In addition, the relative intensity of the DE peak increases. The optical properties of N-doped ZnO thin-films have been explored earlier [110-112]. For example, controlled increase of N concentrations in ZnO films was shown to induce gradual and systematic red-shift of the NBE emission band [111]. XPS investigations on N-doped ZnO revealed multiple occupancy for the dopant atom [113] that might lead to multiple and complex optical transitions in the present nanobullets. To the best of our knowledge however, the present results reveals the largest shift of the ZnO NBE by N doping reported till date.

Fig. 2.41 (c) surmises the differences in optical properties within a pure and an N-doped ZnO nanobullet. CL spectra were acquired from fifteen equally spaced spots (beginning from the tip) along each nanobullet. Before acquiring the spectra, the nanobullets were exposed to the electron beam for

a long time for stabilization [105]. The 5 kV electrons were used to probe near the surface while the 15 kV electrons can penetrate deep inside. In Fig. 2.41 (c), we show the plot of the NBE peak positions observed along the nanobullets. Clearly, the variations of the NBE peaks within a pure nanobullet is minimal (standard deviations<2). Similar uniformity with a slight red-shift is also observed near the surface (at 5 kV) for the N-doped sample. On the other hand, probing using 15 kV electron beam, we found larger shifts and variations (standard deviations>3.9) in the NBE peak positions. This indicates N concentration at the exterior of the ZnO nanobullets is less and uniform, while their core is N rich (schematic in the inset of Fig. 2.41 (c)). It might be that the limited supply of ammonia effects the nitrogen incorporation and maximum doping takes place at the early stage of their growth, or the electron beam induces desorption of the nitrogen near the surface.

Variations of the CL peak positions observed here are indeed limited by the resolution of the detector. A number of luminescence mechanisms may exist at different locations within a single structure resulting from the varied local electronic structure. Such considerations would be of importance in order to fabricate a single nanostructure based electronic device.

Field emission properties: Emission of electrons from nanostructure, when subjected to an electric field is of great commercial interest in displays and other electronic devices. Emission properties of the nanostructures are normally improved by tailoring the geometry (such as

aspect ratio) and spatial distribution (such as alignment and density) of nanomaterials [68]. Besides, it is also possible to improve the emission of electrons by tailoring the work function, ϕ, of the materials [114]. Doping creates additional energy levels within the band-gap of a semiconductor and thus reduces the effective ϕ. ZnO nanostructures are usually doped with trivalent metal atoms such as Ga and Al in order to improve their FE characteristics [115]. Encouraged by these studies, we have investigated, for the first time, the effect of anion doping on the FE characteristics of ZnO nanostructures. Our investigations establish that N doping in ZnO can improve FE current up to an order of magnitude higher.

Fig. 2.42 (a) shows typical FE currents obtained from the pure ZnO nanobullets acquired with increasing applied electric field at three different anode-sample distances of 100, 150 and 200 μm. Emission current gradually increases with reducing the cathode-anode distance. The highest current density of 0.35 $mAcm^{-2}$ was obtained at a cathode anode distance of 100 μm and at an applied macroscopic field of 800 V, while the same was found to be 0.12 $mAcm^{-2}$ and 0.08 $mAcm^{-2}$ at 150 μm and 200 μm respectively. A turn on field is defined as the field applied to generate a macroscopic emission current density of 10 μAcm^{-2}. The corresponding turn on fields, for the sample, were recorded to be 541, 638 and 671 V respectively. Inset in Fig. 2.42 (a) displays a plot of the same at different distances which shows a linear increase. Fig. 2.42 (b) shows the plots of FE current obtained for the N-doped ZnO sample at various sample anode distances. Current densities up to 1.51, 0.78 and 0.39 $mAcm^{-2}$ were

acquired from a distance of 100, 150 and 200 μm respectively. Inset in the figure shows the corresponding turn-on voltages of 520, 549 and 581 V observed at these distances.

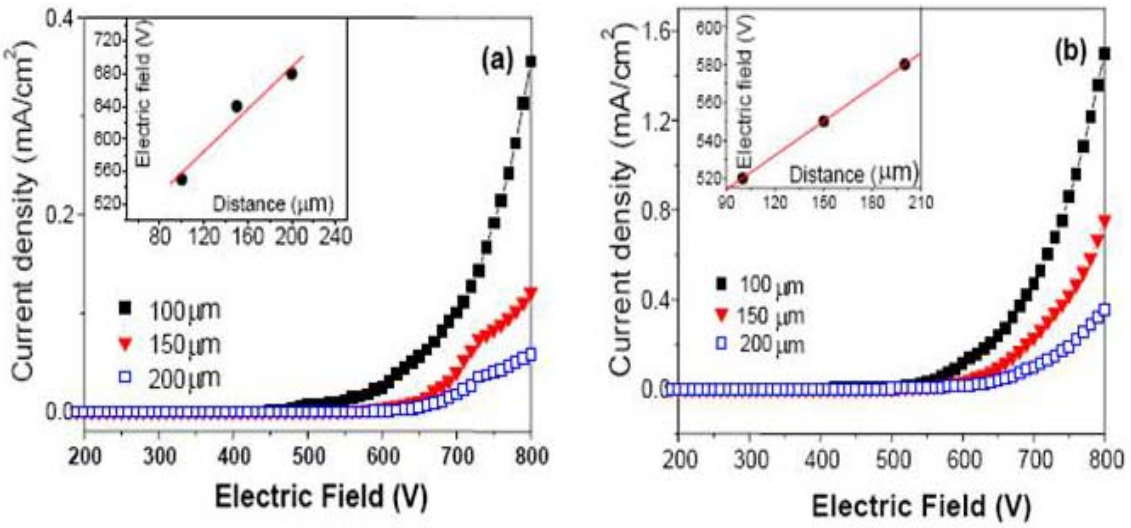

Fig. 2.42: Plots showing field-emission currents acquired with increasing applied voltages at different anode sample distances. (a) Pure ZnO nanobullets and (b) N-doped ZnO nanobullets. Insets show the variation of turn on fields at the measured anode-sample distances.

Besides carbon nanotubes, ZnO constitutes the second most widely studied class of field emitting nanostructures because of its stability in oxidizing atmospheres [116]. It is already proven that the FE efficiency not only depends upon the intrinsic properties of the nanostructure, but also on other factors, such as the substrate, effect of coating and surface treatment [117]. Table 1 compares the FE characteristics of different nanostructures obtained by low as well as high temperature synthetic technique. Among these reports, the millimeter long ZnO nanobelts reported by Ren and coworkers are perhaps the most promising where a turn-on field of ~1.3 V/μm and a very high β of 1.4×10^4 were estimated [118]. Cationic doping

Solution Synthesis		
Types of ZnO nanostructures	Turn on field (V/μm)	β
nanorods	2.85	1680
nanowires	9.5	1334
nanotubes	7 at 0.1 μA/cm^2	910
Others(needles)	4.2	2350
High temperature Synthesis		
nanorods	5.1	1069
nanowires	6 at 0.1 μA/cm^2	847
nanobelts	1.3	1.4×10^4
Others (micro towers)	1.8	3150
This work		
Pure nanobullet	3.4	1.3×10^3
N doped nanobullet	2.9	1.8×10^3

Table 1: Field-emission characteristics of ZnO nanostructures with different morphologies obtained by solution as well as high temperature methods. Herein we define the turn-on field as the field producing emission current density of 10 μA/cm^2. If other values are used, it is separately mentioned.

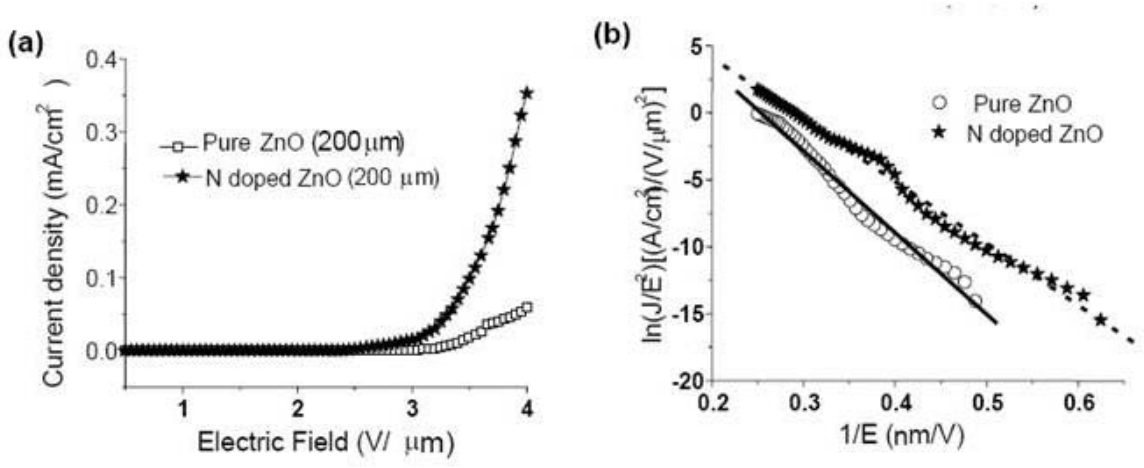

Fig. 2.43: Comparison of Field-emission properties of pure and N-doped ZnO nanobullets. (a) *J* - *E* plots, (b) the corresponding Fowler-Nordheim ln (*J*/*E*2) - (1/*E*) plots.

has already been shown to improve FE properties of ZnO nanowires [114, 115], while the effect of anion doping has not been investigated so far.

Herein, for the purpose of comparison, we show the J-E plots of the pure and N-doped nanobullets in Fig. 2.43 (a). The plot clearly reveals an increase of the FE current by an order of magnitude in the case of the N-doped nanobullets, when measured at a distance of 100 μm. Nitrogen was proposed and later confirmed by theoretical studies to be superior acceptor dopent for ZnO as it enhances p type conductivity.[35] Hence the improved FE characteristic of the doped nanobullets due to enhanced intrinsic conductivity is understandable.

The Fowler-Nordheim (FN) formalism is used in order to quantitatively describe the FE process for solids which takes into account the electrons arriving at the surface from the bulk and the tunneling probability thereafter [68]. Thus the current density produced by a given electric field is described by the following FN equations:

$$J = (A\beta^2E^2/\phi) \exp(-B\phi^{3/2}/\beta E), \quad (1)$$

$$I = S \times J, \; E = V/d, \quad (2)$$

$$\text{or } \ln(J/E^2) = \ln(A\beta^2/\phi) - B\phi^{3/2}/\beta E \quad (3)$$

where A and B are constants, ($A = 1.54\times10^{-6}$ A eV V^{-2}, $B = 6.83\times10^{3}$ $eV^{-3/2}V$ mm^{-1}), S is the emitting area, V is the applied potential, I is the emission current, β is the field-enhancement factor and d is the distance between a sample and the anode [118]. ϕ is the work function of the emitting materials and 5.3 eV for ZnO. β can be calculated from the slope of FN plot (equation 3). From the slopes of $\ln(J/E^2) - (1/E)$ plots in Fig. 2.43 (b), the field-

enhancement factors β for the pure and the doped samples were calculated to be 1.3×10^3 and 1.8×10^3 respectively. We recently showed that increasing aspect ratio, alignment of nanostructures as well as creating hierarchical nanostructures can cause large enhancement of emission efficiency of the nanostructures [68, 119]. The increase in β, herein on the other hand, is achieved by band-gap engineering of the emitting material. Thus, the N-doped sample is comparable to the best ZnO field-emitters and provides a suitable alternative.

2.4.6 Photoluminescence and white-light emission from ZnO-graphene mixtures

ZnO nanoparticles used for the present experiments were spherical in shape and had an average diameter of 4.5 nm as confirmed by TEM. XRD patterns of the ZnO nanoparticles could be indexed on the hexagonal wurtzite structure (space group: $P6_3mc$; a=0.3249 nm, c=0.5206 nm, JCPDS card no. 36-1451). The crystallite sizes of the nanoparticles calculated from the X-ray line widths are consistent with TEM results. The ZnO nanoparticles show an absorption band at 360 nm, which is blue-shifted relative to that of bulk ZnO due to quantum confinement [120].

In Fig. 2.44, we show typical PL spectra of ZnO nanoparticles in admixture with different weight percentages of RGO dispersed in DMF. ZnO

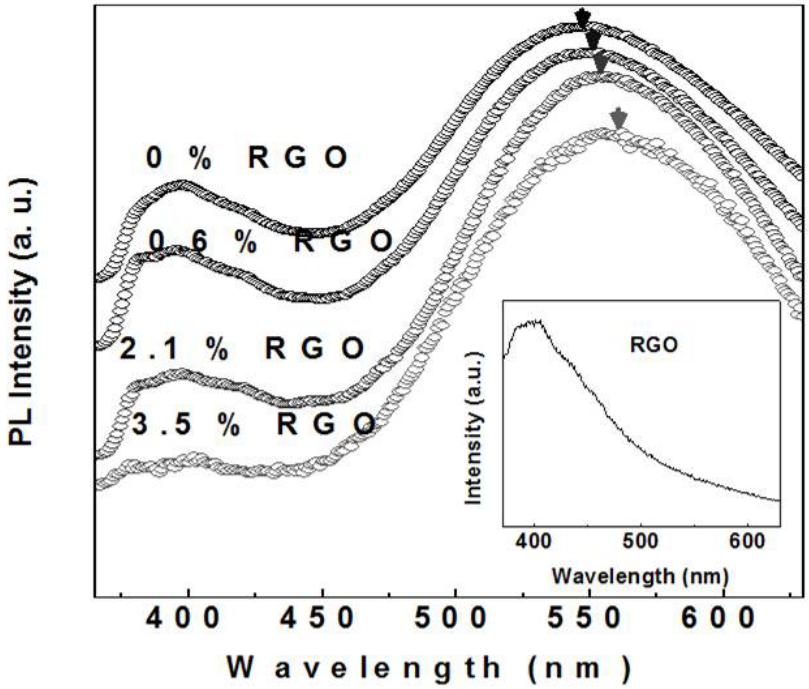

Fig. 2.44 PL spectra of ZnO nanoparticles admixed with different weight percentages of single layer reduced graphene oxide (RGO). Inset shows the PL spectrum of RGO.

nanoparticles give a band at 380 nm and a broad band at 450-650 nm region [121]. The UV emission band at 380 nm (band-edge luminescence) is due to the radiative recombination between the electrons in the conduction band and the holes in the valence band [122]. The broad band in the visible region around 530 nm originates from localized levels in the band gap, the most probable origin for the green emission being the oxygen vacancies [78]. RGO in DMF shows a band at 400 nm region (see inset of Fig. 2.44). As the weight percentage of RGO increases (with a fixed amount of ZnO), the 450 nm region in the PL spectrum becomes broader and the relative intensity of the visible emission increases relative to the 380 nm band. This observation shows that the RGO-ZnO composite in DMF is not suitable for generating white light.

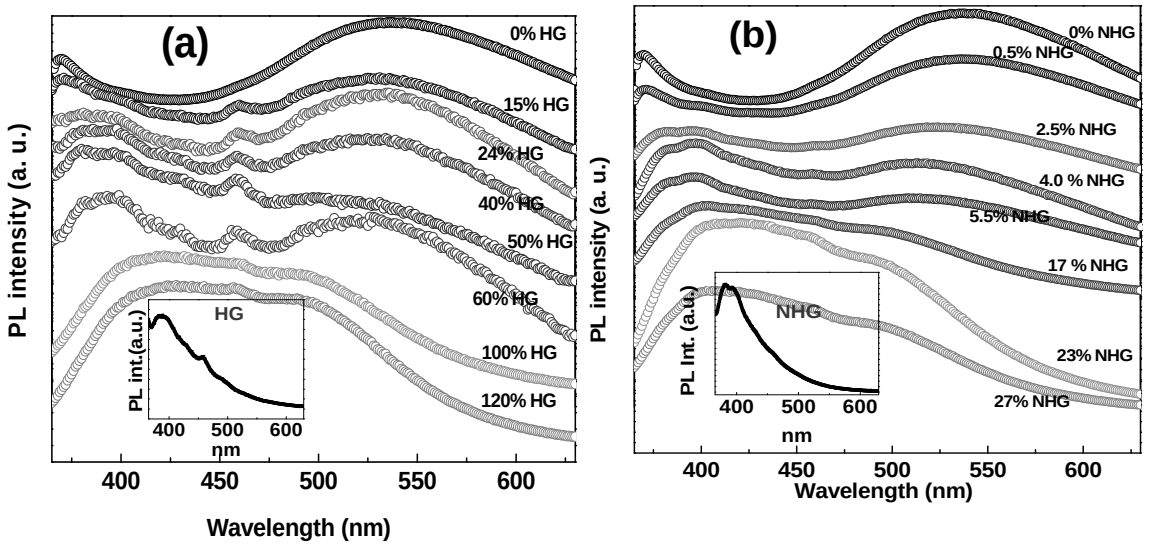

Fig. 2.45 PL spectra of ZnO nanoparticles admixed with different weight percentages of (a) HG and (b) nitrogen-doped graphene (NHG). Insets in Figs. 2(a) and (b) show the PL spectra of HG and NHG respectively.

In Fig. 2.45 (a), we show the PL spectra of ZnO nanoparticles in admixture with HG suspended in ethanol. HG gives a band at 400 nm in the PL spectrum (see inset of Fig. 2.45 (a)). As the weight percentage of HG is increased, the PL spectrum gets broader covering the entire visible spectral region when it reaches 60 weight percentage. Thus, ZnO-HG appears to be a good candidate to produce white light. The chromaticity diagram in Fig. 2.46 (a) shows that a fairly high percentage of HG is required to obtain greenish white light. We have examined the emission properties of nitrogen-doped (NHG) as well as boron-doped (BHG) graphene samples in mixture with ZnO nanoparticles. We show the PL spectrum of NHG in ethanol in the inset of Fig. 2.45 (b) exhibiting a band around 400 nm. As the weight percentage of NHG is increased, the PL spectrum becomes broader and covers the entire visible spectral region when it reaches 17 wt % as shown in Fig. 2.45 (b). The chromaticity diagram in Fig. 2.46 (a) reveals emission of bluish white light. BHG gives a broad band (380-470 nm) in the PL spectrum as can be

seen in the inset of Fig 2.47 (a). In Fig. 2.47 (a), we show the PL spectra of ZnO-BHG mixtures in ethanol with different wt % of BHG. It can be seen from the spectra that even at the 13 wt % of BHG, the PL spectrum covers the entire visible region. The chromaticity diagram in Fig. 2.46 (a) shows greenish white light emitted by the ZnO-BHG mixture.

We have examined the PL spectra of mixture of BHG and ZnO in DMF and obtained remarkable results. We obtain white light with 7 wt % of BHG dispersed with ZnO nanoparticles in DMF. PL spectra of ZnO nanoparticles in DMF are shown in Fig. 2.47 (b) as a function of wt % of BHG. The inset of Fig. 2.47 (b) shows the PL spectrum of BHG in DMF which demonstrates that the band is much broader in DMF. The chromaticity diagram in Fig. 2.45 (b) shows that greenish white light is emitted by a mixture of ZnO with 7.5 wt % of BHG. It is to be noted that different liquids interact differently with graphene and the ZnO nanoparticles, the polarity of the medium itself being an important factor; which will give the observed differences in PL spectra for the composition. A solid mixture of ZnO nanoparticles with BHG did not exhibit the features in the PL spectrum as in Fig 2.47 (b). Instead, the relative intensity of the defect band decreased with increasing BHG content. Graphene oxide is known to exhibit luminescence. After reduction, there is a blue-shift in emission [123]. Blue emission from graphene samples is attributed to the presence of oxygenated (quinoid) species [124]. The blue light from graphene admixed with the yellow-green light emission from ZnO is responsible for the white light emission in our experiments.

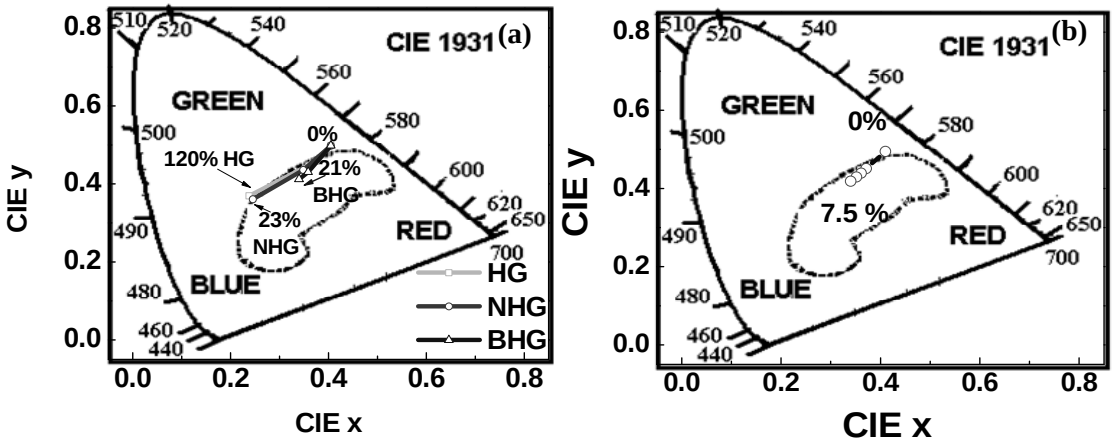

Fig. 2.46 CIE 1931 colour diagram for the admixture of ZnO with different graphene samples: (a) HG, NHG and BHG in ethanol medium (b) BHG in DMF medium. The area bounded by broken lines corresponds to white light.

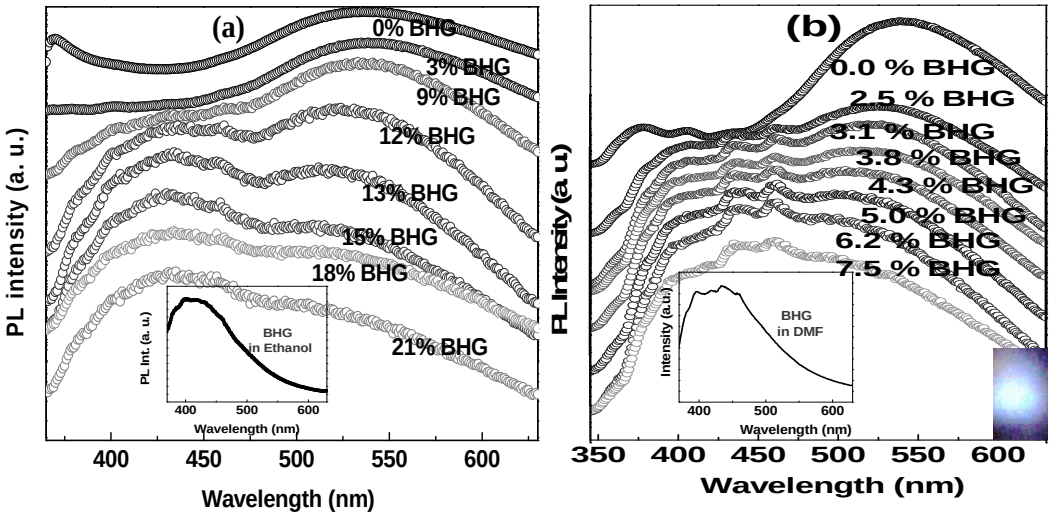

Fig. 2.47 PL spectra of ZnO nanoparticles admixed with different weight percentages of BHG in (a) ethanol and (b) DMF. Insets in Figs. 4(a) and (b) show the PL spectra of BHG in ethanol and DMF respectively. Photograph of white light is also shown as an inset in Fig.-4(b).

Quantum yield calculations of ZnO nanoparticle based white light sources reveal that ZnO nanoparticle admixed with HG in ethanol medium has the least quantum yield value of 1.7 %. However, ZnO nanoparticles admixed with N- and B-doped HG in ethanol medium show quantum yields

of 4 and 5.2 % respectively. B-doped HG in DMF shows a quantum yield of 6%

2.5 Conclusions

Nanoparticles, nanorods as well as thin films of ZnO have been synthesized by a variety of methods. Solvothermal reaction of aliphatic alcohols such as methanol, ethanol and *t*-butanol with zinc powder provides a simple procedure to produce nanoparticles of ZnO. This is in accordance with the finding that the C-O bond of alcohols is readily cleaved by Zn metal. Addition of ethylenediamine to the reaction mixture helps to obtain ZnO nanorods. A new and simple method for preparing ZnO nanorods has been found by the reaction of the zinc powder or zinc foils with water at relatively low temperatures. Addition of ethylenediamine to water favors the formation of the ZnO nanorods. Thus, the reaction time is considerably reduced in the presence of ethylenediamine. Reaction of Al powder or Al foils with water gives rise to $Al(OH)_3$ nanorods. The formation of ZnO and $Al(OH)_3$ nanorods from the metals are both governed by the basic reaction between the metals and water giving hydrogen. Nanorods as well as thin films of ZnO have been produced at the organic-aqueous interface, while both the nanorods and films are single-crystalline, a feature that is noteworthy. The ZnO films are extremely thin, obtaining such films by other means is difficult.

Solvothermal synthesis of ZnO nanostructures with unique features and N-doping in the nanostructures has been accomplished. The preparation conditions induce a unilateral growth of the nanobullets from its base to the

tip, despite absence of any template. The reduction in the bullet diameter takes place in steps, rather than being continuous. Detailed investigations revealed a self-template mechanism for their growth. This synthesis procedure was further extended for the purpose of nitrogen doping, this being the first solution-based approach for N-doped ZnO.

Investigations of the cathodoluminescence of nanobullets have revealed that N doping might not be uniform within a single structure, but the core is N rich while the surface is N poor. It should be noted that such inhomogeneity in properties is not detectable with photoluminescence measurements and must be given due consideration before fabricating single nanostructure devices. Our investigations have also shown large improvement in the field emission properties of ZnO by N doping.

It is significant that the emission from ZnO nanoparticles originating from defects gives rise to white light when mixed with few layer graphene. Thus it seems possible that ZnO nanoparticles + graphene system can be exploited for producing white light emission.

References

[1] Z. L. Wang *Mater. Today* **2004**, 7, 26.

[2] C. N. R. Rao, A. Govindaraj *"Nanotubes and Nanowires"*, *The RSC Nanoscience & Nanotechnology series*, (Eds. H. Kroto, P. O'Brien, H. Craighead) Royal Society of Chemistry (London) **2005**.

[3] C. Klingshirn *Chem. Phys. Chem.* **2007**, 8, 782.

[4] H. Usui, Y. Shimizu, T. Sasaki, N. Koshizaki *j. Phys. chem. B*. **2005**, 109, 120.

[5] M. Ghosh, R. Seshadri, C. N. R. Rao *J. Nanosci. Nanotechnol.* **2004**, 4, 136.

[6] U. Koch, A. Fojtik, H. Weller, A. Henglein *Chem. Phys. Lett.* **1985**, 122, 507.

[7] M. M. Demir, R. Muñoz-Espí, I. Lieberwirth, G. Wegner *J. Mater. Chem.* **2006**, 16, 2940.

[8] J. Buha, I. Djerdj, M. Niederberger *Crystal Growth & Design*. **2007**, 7, 113.

[9] M. Shim, P. Guyot-Sionnest *J. Am. Chem. Soc.* **2001**, 123, 11651.

[10] M. Monge, M. L. Kahn, A. Maisonnat, B. Chaudret *Angew.Chem. Int. Ed.* . **2003**, 42, 5321.

[11] L. Spanhel, M. A. Anderson *J. Am. Chem. Soc.* **1991**, 113, 2826.

[12] M. S. Tokumoto, S. H. Pulcinelli, C. V. Santilli, V. Briois *J. Phys. Chem. B*. **2003**, 107, 568.

[13] B. J. Joo, S. G. Kwon, J. H. Yu, T. Hyeon *Adv. Mater.* **2005**, 17, 1873.

[14] Z. R. Qiu, K. S. Wong, M. M. Wu, W. J. Lin, H. F. Xu *Appl. Phys.Lett.* . **2004**, 84, 2739.

[15] B. P. Zhang, N. T. Binh, Y. Segawa, Y. Kashiwaba, K. Haga *Appl. Phys. Lett.* . **2004**, 84, 586.

[16] S. F. Yu, C. Yuen, S. P. Lau, W. I. Park, G. C. Yi *Appl. Phys. Lett.* **2004**, 84, 3241.

[17] Q. X. Zhao, M. Willander, R. E. Morjan, Q. H. Hu, E. E. B. Campbell *Appl. Phys. Lett.* . **2003**, 83, 165.

[18] C. J. Lee, T. J. Lee, S. C. Lyu, Y. Zhang, H. Ruh, H. J. Lee *Appl. Phys. Lett.* . **2002,**, 81, 3648.

[19] J. J. Wu, S. C. Liu *Adv. Mater.* **2002**, 14, 215.

[20] X. Liu, X. H. Wu, H. Cao, R. P. H. Chang *J. Appl. Phys.* **2004**, 95, 3141.

[21] Y. Zhang, H. B. Jia, R. M. Wang, C. P. Chen, X. H. Luo, D. P. Yu, C. J. Lee *Appl. Phys. Lett.* **2003**, 83, 4631.

[22] Y. C. Kong, D. P. Yu, B. Zhang, W. Fang, S. Q. Feng *Appl. Phys. Lett.* **2001**, 78, 407.

[23] S. C. Lyu, Y. Zhang, C. J. Lee, H. Ruh, H. J. Lee *Chem. Mater.* . **2003**, 15, 3294.

[24] W. I. Park, D. H. Kim, S. W. Jung, G. C. Yi *Appl. Phys. Lett.* . **2002**, 80 4232.

[25] Y. Li, G. W. Meng, L. D. Zhang, F. Phillipp *Appl. Phys. Lett.* . **2000**, 76, 2011.

[26] C. Liu, J. A. Zapien, Y. Yao, X. Meng, C. S. Lee, S. Fan, Y. Lifshitz, S. T. Lee *Adv. Mater.* . **2003**, 15, 838.

[27] H. Yu, Z. Zhang, M. Han, X. Hao, F. Zhu *J. Am. Chem. Soc.* . **2005**, 127, 2378.

[28] B. Cheng, W. S. Shi, J. M. Russell-Tanner, L. Zhang, E. T. Samulski *Inorg. Chem.* . **2006**, 45, 1208.

[29] C. Wang , E. Shen, E. Wang, L. Gao, Z. Kang, C. Tian, Y. Lan, C. Zhang *Mater. Lett.* . **2005**, 59, 2867.

[30] B. Liu, H . C. Zeng *J. Am. Chem. Soc.* **2003**, 125, 4430.

[31] A. Dev, S. Kar, S. Chakrabarti, S. Chaudhuri *Nanotechnology* **2006**, 17, 1533.

[32] K. R. Harikumar, C. P. Vinod, G. U. Kulkarni, C. N. R. Rao *J. Phys. Chem. B.* **1999**, 103, 2445.

[33] K. R. Harikumar, C. N. R. Rao *Chem. Commun.* **1999**, 341.

[34] L. Liepina, A. Tetere, *Doklady Akademii Nauk SSSR* **1953**, 90, 413.

[35] A. Zuttel *Naturwissenschaften* **2004**, 91, 157.

[36] C.N.R. Rao, G.U. Kulkarni, P. Thomas, V.V. Agrawal, P. Saravannan *J. Phys. chem. B.* **2003**, 107, 7391.

[37] U.K. Gautam, M. Ghosh, C.N.R. Rao *Langmuir.* **2004**, 20, 10775.

[38] C.N.R. Rao, G.U. Kulkarni, V.V. Agrawal, U.K. Gautham, M. Ghosh, U. Tumkurkar *J. Colloid Interface Sci.* **2005**, 289, 305.

[39] C.N.R. Rao, K.P. Kalyanikutty *Acc. Chem. Res.* . **2008**, 41, 489.

[40] R. Krishnaswamy, S. Majumdar, R. Ganapathy, V.V. Agrawal, A.K. Sood, C. N. R. Rao *Langmuir.* **2007**, 23, 3084.

[41] R. Krishnaswamy, K.P. Kalyanikutty, K. Biswas, A.K. Sood, C. N. R. Rao *Langmuir.* **2009**, 25, 10954.

[42] V.V. Agrawal, G.U. Kulkarni, C. N. R. Rao *J. Colloid Interface Sci.* **2008**, 318, 501.

[43] R.F. Service *Science*. **1997**, 276, 895.

[44] S.C. Minne, S.R. Manalis, C.F. Quate *Appl. Phys. Lett.* **1995**, 67, 3918.

[45] M.H. Huang, S. Mao, H. Feick, H. Yan, Y. Wu, H. Kind, E. Weber, R. Russo, P. Yang *Science*. **2001**, 292, 1897.

[46] D.M. Bagnall, Y.F. Chen, Z. Zhu, T. Yao, M.Y. Shen, T. Goto *Appl. Phys. Lett.* **1998**, 73, 1038.

[47] J. Hu, R.G. Gordan *J. Appl. Phys.* **1992**, 71, 880.

[48] S.V. Prasad, S.D. Walck, J.S. Zabinski, *Thin Solid Films*. **2000**, 360, 107.

[49] T. Yoshida, H. Minoura *Adv. Mater.* . **2000**, 12, 1219.

[50] H. Kato, M. Sano, K. Miyamoto, T. Yao, *J. Cryst. Growth* **2002**, 538, 237.

[51] W. Walukiewicz *Phys. Rev. B*. **1994**, 50, 5221.

[52] C. G. Van de Walle, D. B. Laks, G. F. Neumark, S. T. Pantelides *Phys. Rev. B*. **1993**, 47, 9425.

[53] F. Schirmer, D. Zwingel *Solid State Commun.* . **1970**, 8, 1559.

[54] F. Schirmer *J. Phys. Chem. Solids*. **1968**, 29, 1407.

[55] A. Valentini, F. Quaranta, M. Rossi, G. Battaglin *J. Vac. Sci. Technol. A*. **1991**, 9, 286.

[56] Y. Kanai *Jpn. J. Appl. Phys., Part 1*. **1991**, 30, 703.

[57] Y. Kanai *Jpn. J. Appl. Phys., Part 1* **1991**, 30, 2021.

[58] C. H. Park, S. B. Zhang, S.-H. Wei *Phys. Rev. B*. **2002**, 66, 073202.

[59] D. C. Reynolds, D. C. Look, B. Jogai, T. C. Collins *Appl. Phys. Lett.* **2001**, 79, 3794.

[60] D. B. Laks, C. G. Van de Walle, G. F. Neumark, S. T. Pantelides *Phys. Rev. Lett.* . **1991**, 66, 648.

[61] A. Garcia, J. E. Northrup *Phys. Rev. Lett.* **1995**, 4, 1131.

[62] D. C. Look, R. L. Jones, J. R. Sizelove, N. Y. Garces, N. C. Giles, L. E. Halliburton *Phys. Status Solidi A.* **2004**, 195, 171.

[63] N. H. Nickel, F. Friedrich, J. F. Rommeluère, P. Galtier, *Appl. Phys. Lett.* **2005**, 87, 211905-211901.

[64] Y. G. Wang, S. P. Lau, X. H. Zhang, H. W. Lee, H. H. Hng, B. K. Tay *J. Crystal Growth* **2003**, 252, 265.

[65] C. C. Lin, H. P. Chen, S. Y. Chen, *Chem. Phys. Lett.* **2005**, 404, 30.

[66] C. Liao, H. F. Lin, S. W. Hung, C. T. Hu, *J. Vac. Sci. Technol. B.* **2006**, 24, 1322.

[67] B. G. Yacobi, D. B. Holt, Cathodoluminescence Microscopy of Inorganic Solids, Plenum Press, New York, **1990**.

[68] X. Fang, Y. Bando, U. K. Gautam, C. Ye, D. Golberg *J. Mater. Chem.* **2008**, 18, 509.

[69] L. Li, X. S. Fang, H. G. Chew, F. Zheng, T. H. Liew, X. J. Xu, Y. X. Zhang, S. S. Pan, G. H. Li, L. D. Zhang *Adv. Funct. Mater.* **2008**, 18, 1080.

[70] N. Stutzmann, R. H. Friend, H. Sirringhaus *Science*. **2003**, 299, 1881.

[71] G. Thomas *Nature*. **1997**, 389, 907.

[72] D. S. P. Nakamura S, Speck J S, Schmidt M C, K C Kim, R M Farrell, Feezell D F,, S. M. Cohen D A, Sato H, Asamizu H, Tyagi A, Zhong H,

Masui H, Fellows N N, Iza M,, F. K. Hashimoto T in Current status of GaN-based nonpolar/semipolar/polar blue and white LEDs, Conference poster, White LEDs-07, **2007**.

[73] S. Nizamoglu, T. Ozel, E. Sari, H. V. Demir *Nanotechnology*. **2007**, 18, 065709.

[74] P. Thiyagarajan, M. Kottaisamy, N. Rama, M. R. Rao *Scripta Materialia*. **2008**, 59, 722.

[75] M. Willander, O. Nur, N. Bano, K. Sultana *New Jour. Phys.* **2009**, 11, 125020.

[76] N. S. Pesika, K. J. Stebe, a. P. C. Searson, *J. Phys. Chem. B*. **2003**, 107, 10412.

[77] X.Q. Meng, D.Z. Shen, J.Y. Zhang, D.X. Zhao, Y.M. Lu, L. Dong, Z.Z. Zhang, Y. C. Liu, a. X. W. Fan, *Solid State Commun.* . **2005**, 135, 179.

[78] K. Vanheusden, W. L. Warren, C. H. Seager, D. R. Tallant, J. A. Voigt, a. B. E. Gnade *J. Appl. Phys.* . **1996**, 79, 7983.

[79] J. Liang, J. Liu, Q. Xie, S. Bai, W. Yu, and Y. Qian *J. Phys. Chem.* **2005**, 109, 9463.

[80] C. Bundesmann, N. Ashkenov, M. Schubert, D. Spemann, T. Butz, E. M. Kaidashev, M. Lorenz, a. M. Grundmann *Appl. Phys. Lett.* . **2003**, 83, 1974.

[81] T. C. Damen, S. P. S. Porto, a. B. Tell *Phys. Rev. B*. **1966**, 142, 570.

[82] M. Kitano, T. Okabe, a. M. Shiojiri *J. Cryst. Growth*. **1995**, 152, 73.

[83] M. Kitano, a. M. Shiojiri *J. Electrochem. Soc.* . **1997**, 144, 809.

[84] A. R. Studart, M. D. M. Innocentini, I. R. Oliveira, and V. C. Pandolfelli *J. European Ceramic Soc.* . **2005**, 25, 3135.

[85] A. Y. Godymchuk, V. V. An, and A. P. Il'in *Fizika i Khimiya Obrabotki Materialov* **2005**, 5, 69.

[86] E. S. Martin, M. L. Weaver, J. E. Marhanka, A. Pearson, and M. Madono US Patent 87-137159 19871223, 199, **1993**.

[87] J. T. K. R. L. Frost, S. C. Russell, Szetu, *J. Appl. Spectrosc.* **1999**, 53, 423.

[88] P. H. Hsu, T. F. Bates *Mineral. Mag.* . **1964**, 33, 749.

[89] J. L. Bersillow, D. W. Brown, F. Fiessinger, J. D. Hem *J. Res. US Geol Surv.* **1978**, 6, 325.

[90] R. L. Frost, H. D. Ruan, and J. T. Kloprogge *J. Raman Spectroscopy* **2001**, 32, 745.

[91] K. A. Rodgers, M. R. Gregory, R. P. Cooney, C. Miner. **1989**, 24, 531.

[92] A.B. Djurisic, Y.H. Leung, K.H. Tam, Y.F. Hsu, L. Ding, W.K. Ge, Y.C. Zhong, K.S. Wong, W.K. Chan, H.L. Tam, K.W. Cheah, W.M. Kwok, D.L. Phillips *Nanotechnology* **2007**, 18, 095702.

[93] X. Zhou, S. Gu, Z. Wu, S. Zhu, J. Ye, S. Liu, R. Zhang, Y. Shi, Y. Zheng *Appl. Surf. Sci.* **2006**, 253 2226.

[94] H. Zeng, W. Cai, J. Hu, G. Duan, P. Liu, Y. Li *Appl. Phys. Lett.* **2006**, 88, 171910.

[95] M. C. Newton, P. A. Warburton *Mater. Today*. **2007**, 10, 50.

[96] H. E. Roscoe, H. Enfield, C. Schorlemmer, , A Treatise on Chemistry, , Macmillan, London **1907**.

[97] M. Rajamathi, R. Seshadri *Solid State Mater. Sci.* **2002**, 6, 337.

[98] Z. Guo, F. Du, G. Li, Z. Cui *Crystal Growth Design*. **2008**, 8, 2674.

[99] C. H. Liang, Y. Shimizu, M. Masuda, T. Sasaki, N. Koshizaki *Chem. Mater.* **2004**, 16, 963.

[100] B. Liu, H. C. Zeng *Langmuir*. **2004**, 20, 4196.

[101] E. D. Boyes, P. L. Gai, C. Warwick *Nature*. **1985**, 313, 666.

[102] M. Law, L. E. Greene, J. C. Johnson, R. Saykally, P. D. Yang *Nat. Mater.* **2005**, 4, 455.

[103] A. Tsukazaki, A. Ohtomo, T. Onuma, M. Ohtani, T. Makino, M. Sumiya, K. Ohtani, S. F. Chichibu, S. Fuke, Y. Segawa, H. Ohno, H. Koinuma, M. Kawasaki *Nat. Mater.* **2005**, 4, 42.

[104] N. Pan, X. Wang, M. Li, F. Li, J. G. Hou *J. Phys. Chem. C*. **2007**, 111, 1265.

[105] X. L. Y. B. Dierre, N. Ohashi, T. Sekiguchi *J. Appl. Phys*. **2008**, 103, 083551.

[106] Y. C. Chang, L. J. Chen *J. Phys. Chem. C*. **2007**, 111, 1268.

[107] B. Piechal, J. Yoo, A. Elshaer, A. C. Mofor, G.-C. Yi, A. Bakin, A. Waag, F. Donatini, L. S. Dang *Phys. Status Solidi B*. **2007**, 244, 1458.

[108] N. E. Hsu, W. K. Hung, Y. F. Chena *J. Appl. Phys*. . **2004**, 96, 4671.

[109] M. Schirra, A. Reiser, G. M. Prinz, A. Ladenburger, K. Thonke, R. Sauer *J.Appl.Phys*. **2007**, 101, 11509.

[110] Y. Nakano, T. Morikawa, T. Ohwaki, Y. Taga *Appl. Phys. Lett.* **2006**, 88, 172103.

[111] A. Nakagawa, F. Masuoka, S. Chiba, H. Endo, K. Megro, Y. Kashiwaba, T. Ojima, K. Aota, I. Niikura, Y. Kashiwaba *Appl. Surf. Sci.* **2007**, 254, 164.

[112] X. Wang, Y. M. Lu, D. Z. Shen, Z. Z. Zhang, B. H. Li, B. Yao, J. Y. Zhang, D. X. Zhao, X. W. Fan *J. Luminescence* **2007**, 122–123, 165.

[113] C. L. Perkins, S.-H. Lee, X. Li, S. E. Asher, T. J. Coutts *J. Appl. Phys.* **2005**, 97, 034 907.

[114] H. Pan, Y. Zhu, H. Sun, Y. Feng, C.-H. Sow, J. Lin *Nanotechnology*. **2006**, 17, 5096.

[115] Y. Huang, Y. Zhang, Y. Gu, X. Bai, J. Qi, Q. Liao, J. Liu *J. Phys. Chem. C*. **2007**, 111, 9039.

[116] W.-K. Hong, J. I. Sohn, D.-K. Hwang, S.-S. Kwon, G. Jo, S. Song, S.-M. Kim, H.-J. Ko, S.-J. Park, M. E. Welland, T. Lee *Nano Lett.* . **2008**, 8, 950.

[117] D. Banerjee, S. H. Jo, Z. F. Ren *Adv. Mater.* . **2004**, 16, 2028.

[118] W. Z. Wang, B. Q. Zeng, J. Yang, B. Poudel, J. Y. Huang, M. J. Naughton, Z. F. Ren *Adv. Mater.* **2006**, 18, 3275.

[119] U. K. Gautam, X. Fang, Y. Bando, J. Zhan, D. Golberg *ACS Nano*. **2008**, 2, 1015.

[120] Y. D. Jin, J. P. Yang, P.L. Heremans, M. V. Auweraer, E. Rousseau, H. J. Geise, G. Borghs *Chem. Phys. Lett.* **2000**, 320, 387.

[121] C. Pacholski, A. Kornowski, H. Weller *Angew. Chem. Int. Ed. Engl.* . **2002**, 41, 1188.

[122] J. Liang, Q. Liu, S. Xie, W. Bai, Y. Q. Yu *J. Phys. Chem. B* **2005** 109, 9463.

[123] T. V. Cuong, V. H. Pham, Q. T. Tran, S. H. Hahn, J. S. Chung, E. W. Shin, E. J. Kim *Materials Letters*. **2010**, 64 399.

[124] T. Gokus, R. R. Nair, A. Bonetti, M. B. hmler, A. Lombardo, K. S. Novoselov, A. K. Geim, A. C. Ferrari, A. Hartschuh *ACS Nano*. **2009**, 3, 3963.

Chapter-3

Surface Ferromagnetism Universally Exhibited by Nanostructures of ZnO and Other Oxides

Summary*

Occurrence of ferromagnetism in nanoparticles of otherwise non-magnetic oxides seems to be well established. It is, however, necessary to understand the origin of ferromagnetism in these materials. In this chapter, we present a combined study of magnetic and photoluminescence (PL) properties of nanoparticles of ZnO, ZrO_2 and MgO annealed at different temperatures, and therefore are of different sizes. We find that magnetization and intensity of the band due to defects vary parallely in all these materials. Adsorption of ethanol decreases the magnetization and defect PL band intensity of ZnO nanoparticles while UV irradiation has the opposite effect. We have also examined the effect of morphology of ZnO.

---

*Paper based on these studies has appeared in ChemPhysChem (2010).

3.1 Introduction

Over the past few years, several workers have reported room-temperature ferromagnetism in films as well as polycrystalline samples of metal oxides such as ZnO doped with Mn^{2+} and Co^{2+} and other transition metal ions [1-5]. This finding was considered to have direct bearing on the use of such materials in spintronics [6]. Many of the recent studies have, however, shown that Mn^{2+} and Co^{2+} doped ZnO and such materials are not ferromagnetic [7-11]. Furthermore, room-temperature ferromagnetism has been found to be a universal characteristic of nanoparticles of inorganic material which are otherwise nonmagnetic [12, 13]. Thus, ferromagnetism of transition metal ion doped oxides reported in the literature could arise from the nanoparticulate nature of the oxide host. Ferromagnetism reported in thin films of certain non-magnetic oxides such as HfO_2 [14] can also be understood in terms of the properties of nanoparticles [15, 16]. The origin of magnetism of inorganic nanoparticles itself has been explained on the basis of defects present on the surfaces of oxides [17]. It, therefore, seems necessary to understand the relation between the defects and magnetism in the oxide nanoparticles.

3.2 Scope of the present investigations

We have carried out a systematic investigation of the magnetic properties of a few metal oxide nanoparticles along with their optical properties. For this purpose, we have made use of the photoluminescence spectra of metal oxides which show defect-related bands, and have investigated the changes

in the photoluminescence bands accompanying the changes in the magnetic properties as the particle size or temperature of annealing is varied. The nanoparticles examined by us are those of ZnO, ZrO_2 and MgO. We have paid specific attention to not only the effect of particle size, but also to the effects of particle morphology, UV irradiation and adsorption of molecules.

3.3 Experimental and related aspects

(a) Synthesis of ZnO nanoparticles

ZnO nanoparticles with an average size of 4-5 nm were prepared by a procedure described in the literature [18]. The method involves hydrolysis of zinc acetate in methanol using KOH. In a typical synthesis, zinc acetate (0.01 mol) was dissolved in methanol (125 ml) under vigorous stirring at about 60 ^oC. Subsequently, a solution of KOH (0.03 mol, 65 ml) in methanol was added drop wise at 60 ^oC. The reaction mixture was stirred for 6 h at 60 ^oC. The white precipitate thus obtained was harvested by centrifugation and washed thoroughly with HPLC grade ethanol and air-dried at 40 ^oC. The as-prepared ZnO nanoparticles so obtained were annealed in 500 sccm oxygen flow at different temperatures ranging in the 150 ^oC – 1200 ^oC range for 10 hours to get particles with different sizes. The one annealed at 1200 ^oC result in bulk zinc oxide. The as-prepared ZnO nanoparticles were annealed at 150 ^oC for 5, 10 and 20 h in oxygen atmosphere to see the variation of properties with time. The effects of adsorption of ethanol and UV irradiation were studied on a suitably dried sample of ZnO nanoparticles.

(b) Synthesis of ZnO nanobullets

ZnO nanobullets were prepared by using a solvothermal method. In a typical synthesis, 50 mg of zinc acetate, 9 mL of ethylenediamine, and 6mL of absolute alcohol were placed in a teflon-lined autoclave and stirred for 10 min. The autoclave was sealed and placed in a hot air oven, which was preheated to 250 ^{o}C. The synthesis was carried out at this temperature for 5 hours before cooling down to room-temperature. The white precipitate was harvested by centrifugation and washed thoroughly with HPLC grade ethanol and air-dried at 40 ^{o}C.

(c) Synthesis of ZnO nanoflowers and thin films at liquid-liquid interface

Single crystalline thin films and nanoflowers of ZnO were synthesized by the reaction of zinc cupferronate (Zn $(cup)_2$) with NaOH at the aqueous-organic interface. For preparing a single crystalline film of ZnO, 0.16 g of NaOH is dissolved in 25 mL of water (0.04 M) in a 100 mL beaker, and 1mg of Zn $(cup)_2$ is dissolved in 25 mL of toluene. The toluene solution is slowly added to the aqueous NaOH solution in a 100 mL beaker at 30 ^{o}C. The interface attains white color after few hours, and a distinct film is formed after 10 h. This experiment had repeated several times to get a sufficient amount of ZnO thin film. Nanoflowers of ZnO at the liquid-liquid interface were obtained by adding 50 μL of trioctylamine to the organic phase along with 20 mg of Zn $(cup)_2$ and keeping NaOH concentration in aqueous phase at 0.04M.

(d) Synthesis of MgO nanoparticles

MgO nanoparticles were synthesized using high purity (99.99%) magnesium acetate tetrahydrate $(CH_3COO)_2Mg{\cdot}4H_2O$, polyvinyl pyrrolidone (PVP) and ethylene glycol (EG, 99.5%) [19]. 0.05 mol of magnesium acetate tetrahydrate and 0.3 mmol of PVP as capping agent were dissolved in EG in a round bottom flask. The solution was refluxed at 200 ^oC with constant stirring for 2 h to get a white flocculate. The reaction mixture was allowed to cool down to room-temperature and the flocculate collected by centrifuging the reaction mixture followed by washing with distilled water and then ethanol, to remove the remaining PVP and EG. Final drying of the flocculate was done at 80 ^oC in an oven to get magnesium oxide precursor. This precursor was calcined at 400, 600 and 700 ^oC for 2 h in an oxygen atmosphere to form magnesium oxide nanoparticles of different sizes. Bulk magnesium oxide was prepared by pelletizing the precursor followed by sintering at 1400 ^oC in oxygen.

(e) Synthesis of ZrO_2 nanoparticles

ZrO_2 nanocrystals were prepared by the following procedure [20]. The procedure involves the hydrolysis of $ZrOCl_2$ under microwave irradiation in NaOH aqueous solutions. In a typical synthesis, an aqueous solution containing 0.10 mol L^{-1} $ZrOCl_2$ and 5 mol L^{-1} NaOH was exposed to microwave radiation at a power of 650 W. Microwave irradiation was operated in 30 second cycles (on for 10 s, off for 20 s) for 6 min, and the solutions were then allowed to cool to room temperature. The resulting precipitate was collected, washed with distilled water and HPLC alcohol, and

dried in air for 2 h. The as-prepared ZrO_2 nanoparticles were annealed at 400, 600, 1200 ^oC in oxygen atmosphere for 10 hours to look in to the variation of properties with annealing temperature.

Techniques used for characterization

X-ray diffraction (XRD): X-ray diffraction (XRD) patterns of the samples were recorded in the θ-2θ Bragg-Bretano geometry with a Siemens D5005 diffractometer using Cu Kα (λ=0.151418 nm) radiation.

Field emission scanning electron microscopy (FESEM): FESEM images were recorded with a FEI NOVA NANOSEM 600.

UV-Vis absorption and Photoluminescence: UV-Vis absorption measurements were carried out with a Perkin-Elmer model Lambda 900 UV/Vis/NIR spectrometer. Photoluminescence (PL) measurements were carried out at room temperature with a Perkin-Elmer model LS50B luminescence spectrometer.

Transmission electron microscopy (TEM): TEM images were obtained with a JEOL JEM 3010, operating with an accelerating voltage of 300 kV.

Atomic force microscope (AFM): AFM measurements performed using the NanoMan.

Vibrating sample magnetometer (VSM): Magnetic measurements were performed with a vibrating sample magnetometer using a Physical Properties Measurement System (PPMS, Quantum Design, USA).

3.4 Results and discussion

3.4.1 ZnO

A typical TEM image of the as-prepared ZnO nanoparticles with an average diameter 4.5 nm is shown in Fig. 3.1. The XRD patterns of the ZnO nanoparticles (Fig. 3.2) could be indexed on the wurtzite structure. As the ZnO nanoparticles are annealed at temperatures 150, 200, 400 and 600 ^{o}C, the average particle size increases. The particle sizes increases to 11, 17 and 28 nm when the annealing temperatures were 150, 200 and 400 ^{o}C as shown in Fig. 3.3. The average particle sizes were also estimated from the XRD data (Fig. 3.2) using the widths of the (101) reflection of ZnO. The crystallite sizes of the nanoparticles calculated from the X-ray line widths also shows an increase with the annealing temperature as expected. In Fig. 3.4, we show the variation of the size of the ZnO nanoparticles with the annealing temperature as obtained from XRD and TEM measurements. The strain in the small particle size was calculated from the formula, $(\beta.\cos\theta) / \lambda = 1/\varepsilon + (\tau.\sin\theta) / \lambda$, where β is the measured FWHM (full-width at half maximum), θ the Bragg angle, λ the X-ray diffraction wavelength (λ = 1.54056 Å), ε the effective particle size and τ the effective strain. The effective strain calculated for the ZnO particles annealed at 150, 200, 400, 600 ^{o}C are respectively 0.016, 0.013, 0.01and 0.01. The strain decreases with increase in particle size or annealing temperature.

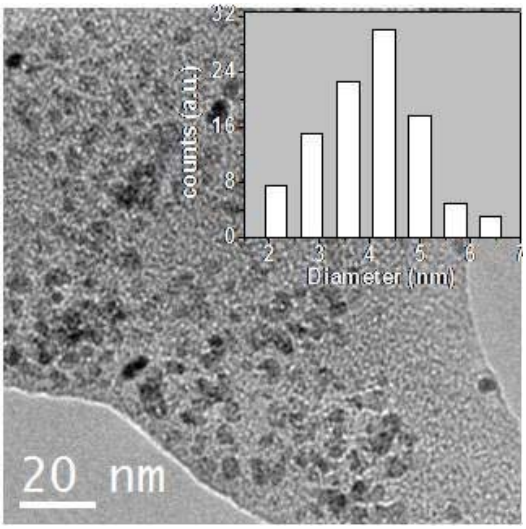

Fig. 3.1 TEM image of as as-prepared ZnO nanoparticles. Inset shows particle size distribution, histogram.

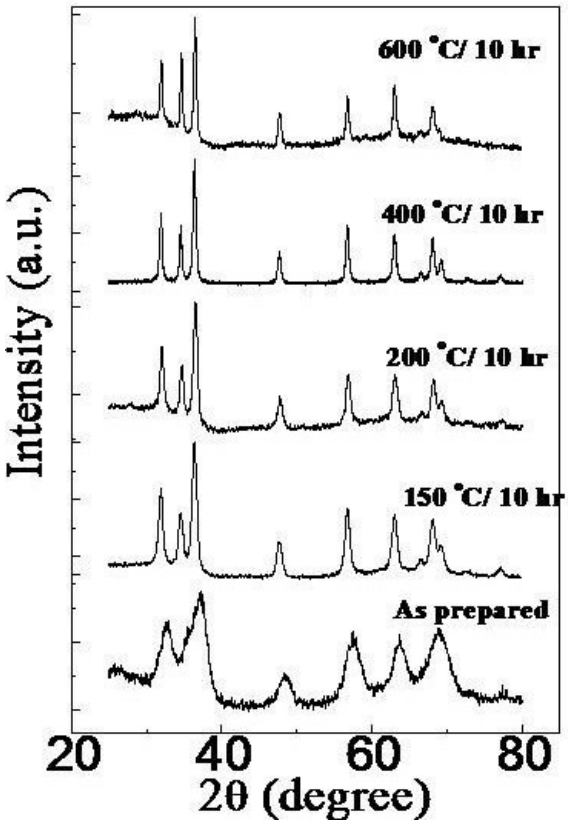

Fig. 3.2 XRD patterns of ZnO nanoparticles annealed at different temperatures

The as-prepared ZnO nanoparticles (4.5 nm, dia) show an absorption band at 360 nm, which gets blue-shifted relative to bulk ZnO, due to quantum confinement (Fig. 3.5) [21]. As the annealing temperature is increased, the absorption band shifts to longer wavelengths due to the increase in the particle size.

Fig. 3.6 (a) shows the room-temperature magnetization M(H) data of the ZnO nanoparticles annealed at different temperatures for 10 h. We clearly see that the saturation magnetization, M_s decreases with increase in

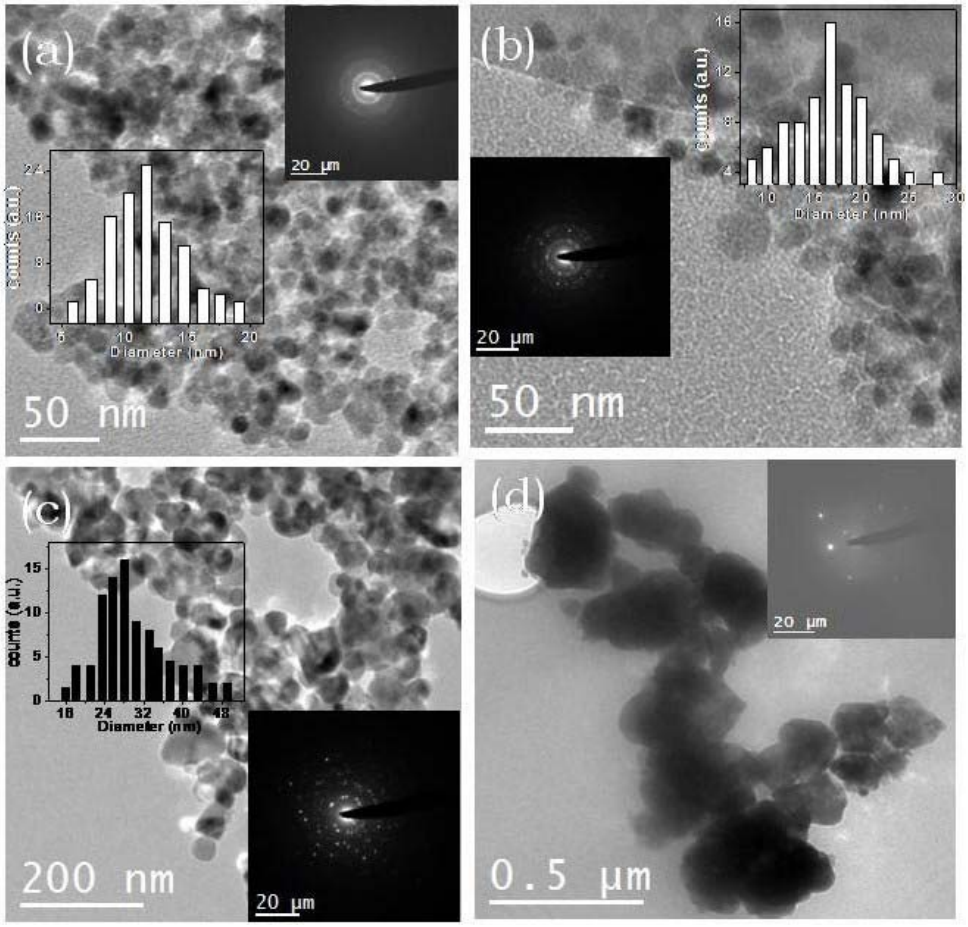

Fig. 3.3 TEM images along with particle size distributions and electron diffraction patterns of ZnO nanoparticles annealed at 150 °C (a), 200 °C (b), 400 °C (c) and 600 °C (d).

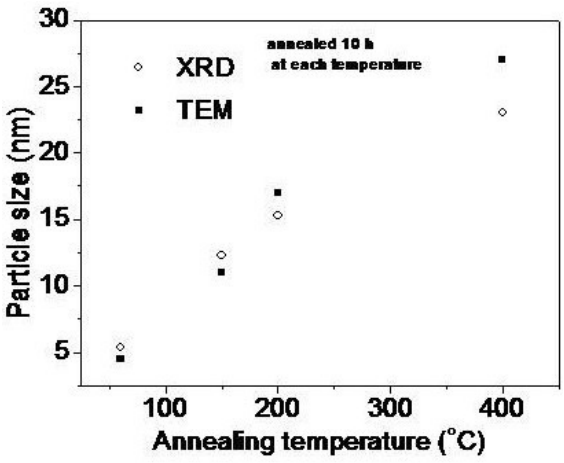

Fig. 3.4 Variation of the size of ZnO nanoparticles with the annealing temperature, obtained from XRD and TEM.

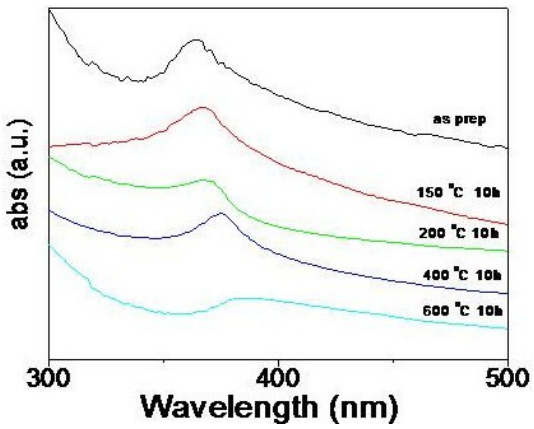

Fig. 3.5 Uv-Vis spectra of ZnO nanoparticles annealed at different temperatures.

annealing temperature. The sample heated at 1200 ^{o}C shows diamagnetic behavior just like bulk ZnO. In Fig. 3.6 (b), we show the room-temperature photoluminescence (PL) spectra of ZnO nanoparticles annealed at different temperatures. The spectra show two important features, one in the UV region and a broad band in the visible region. The UV emission band at 380 nm (band-edge luminescence) is due to the radiative recombination between the electrons in the conduction band and the holes in the valence band [22]. The broad band in the visible region around 530 nm originates from localized levels in the band gap. The most probable origin for the green emission lies in the oxygen vacancies [23]. Annealing the ZnO nanoparticles in oxygen at higher temperatures, causes a dramatic increase in the band-edge luminescence relative to the intensity of the green emission. The increase in particle size with increasing temperature is accompanied by a decrease in the effective surface area of the nanoparticles and hence a decrease in the number of surface oxygen vacancies. The band-edge emission becomes broader on annealing probably due to additional emission bands in the violet region.

In Fig. 3.7 we show a plot of the saturation magnetization in different ZnO samples against the relative PL intensity of the defect emission at 530 nm with respect to band edge emission at 380 nm. This plot indicates how a decrease in the defect band intensity accompanies a decrease in the saturation magnetization, thereby providing evidence for the defect origin of the magnetism of the nanoparticles. On annealing the as-prepared ZnO nanoparticles in oxygen at 150 ^{o}C for 5, 10 and 20 h gives particle sizes of 8, 10.5 and 13.5 nm respectively from XRD and 7.8, 12 and 14.5 nm from

TEM images. The XRD patterns and TEM images of ZnO nanoparticles annealed at 150 ^{o}C in oxygen atmosphere are shown in Figures 3.8 and 3.9 respectively. The value of saturation magnetization is found to decrease with increase in particle size, along with a decrease in the defect band intensity in the PL spectra (see Fig. 3.10). Magnetization values of ZnO nanoparticles in this work are comparable to the values of 6% Co- as well as 6% Mn-doped ZnO nanoparticles reported in the literature [7].

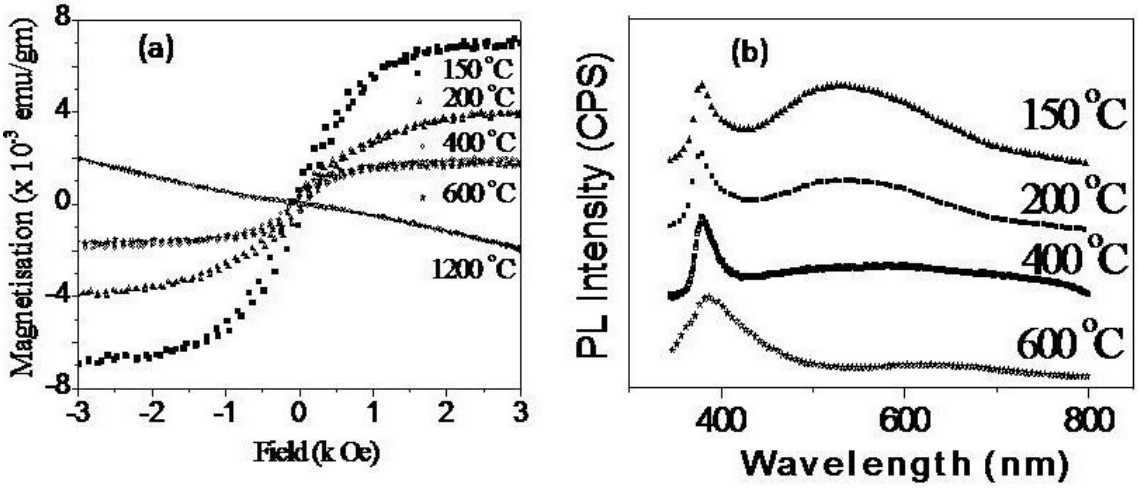

Fig. 3.6. (a) Room-temperature magnetization curves of ZnO nanoparticles at different annealing temperatures. (b) Room-temperature photoluminescence spectra of ZnO nanoparticles at different annealing temperatures.

We have examined the effect of adsorption of ethyl alcohol on the ~7 nm ZnO nanoparticles on the magnetization and PL spectra. We show the magnetization behavior and PL spectra of ZnO nanoparticles before and after adsorption of alcohol in Fig. 3.11. Magnetization of the nanoparticles decreases after treatment with alcohol. At the same time, the defect band in the PL spectrum nearly disappears. This observation suggests that adsorption of alcohol passivates the defects on the surface of ZnO nanoparticles. The magnetic properties and PL spectrum revert back dramatically after drying the sample in vacuum.

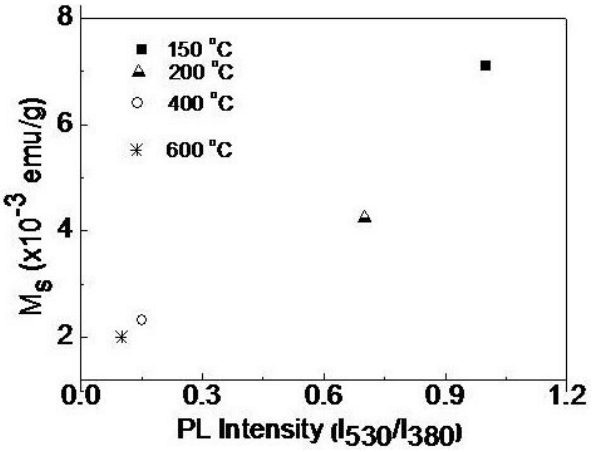

Fig. 3.7. Relation between saturation magnetization Ms(H) and the relative intensity of band-edge-to-defect emission in ZnO nanoparticles as a function of the annealing temperature.

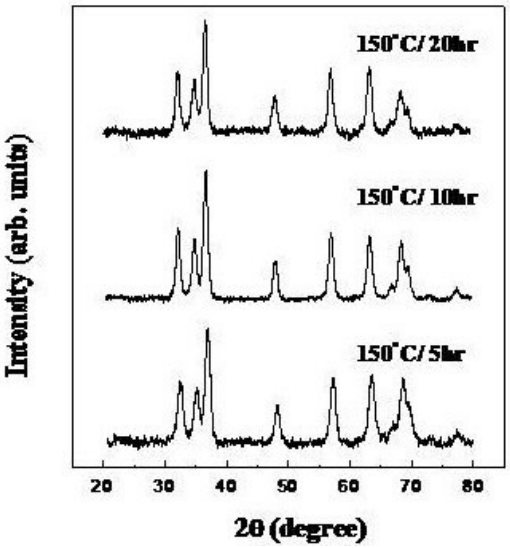

Fig. 3.8. XRD patterns of ZnO nanoparticles annealed at 150 oC for different durations

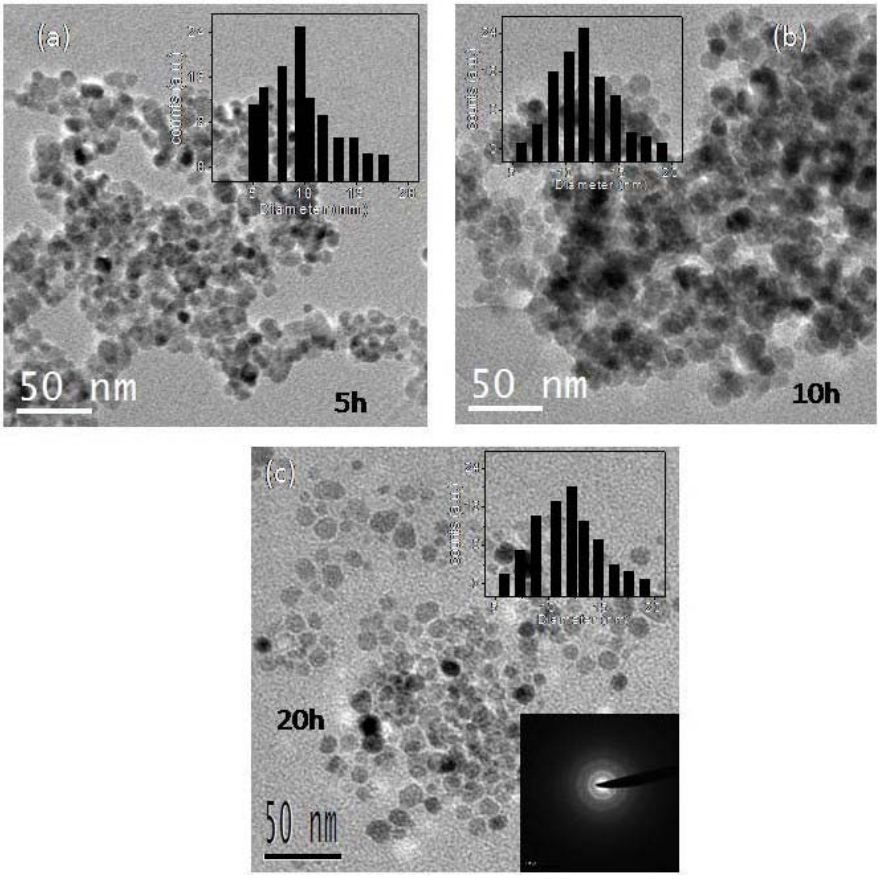

Fig. 3.9. TEM images along with particle size distributions of ZnO nanoparticles annealed at 150 °C for different durations (a) 5h, (b) 10h and (c) 20h.

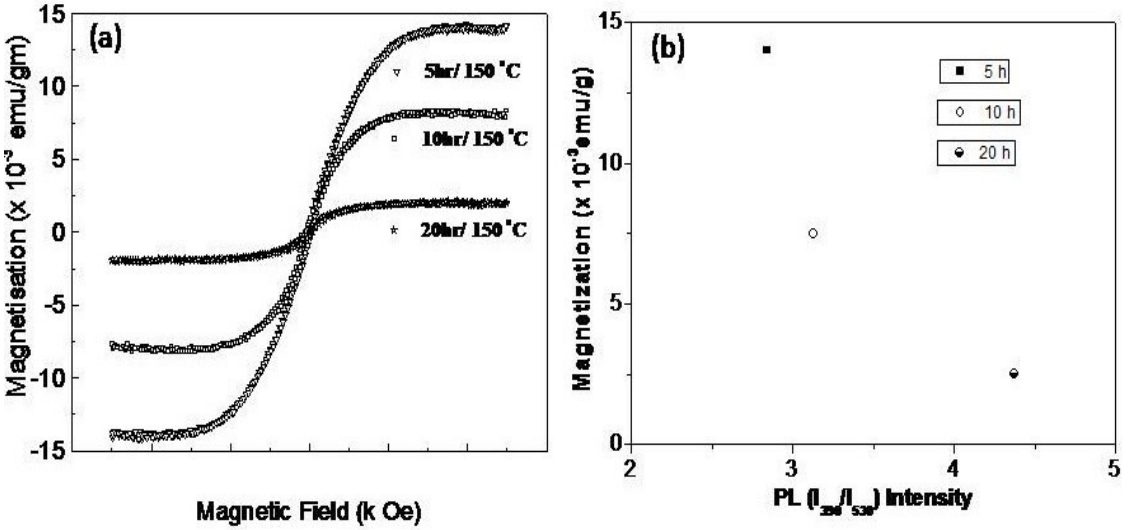

Fig. 3.10. (a) Room-temperature magnetization curves of ZnO nanoparticles at different annealing times at 150 °C. (b) Relation between saturation magnetization Ms(H) and the relative intensity of band-edge-to-defect emission in ZnO nanoparticles as a function of the annealing time at 150 °C.

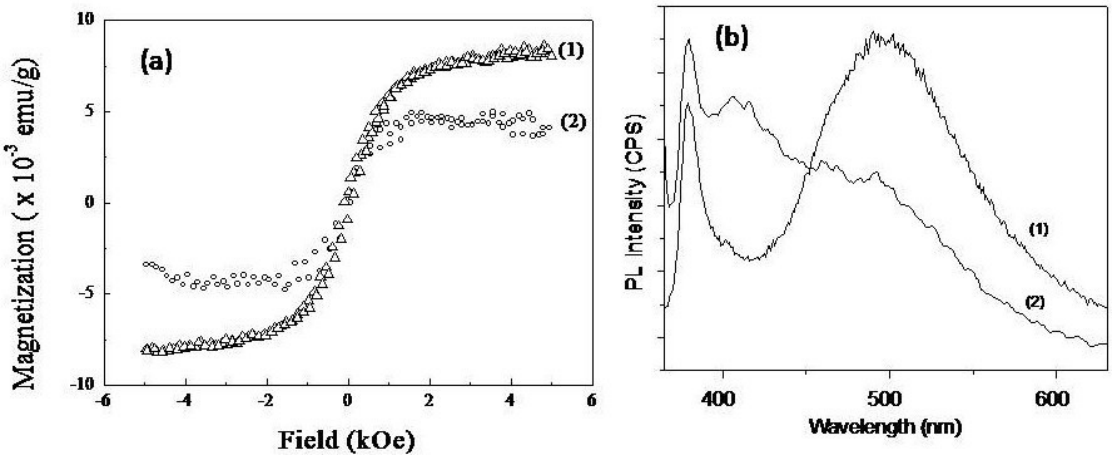

Fig. 3.11. (a) Room-temperature magnetization curves of ZnO nanoparticles: 1) as-synthesised and 2) after treatment with ethanol. (b) Corresponding PL spectra of (1) and (2).

We observe an increase in saturation magnetization of ZnO nanoparticles upon irradiation with UV light (wavelength in the range 250-365 nm) as shown in Fig. 3.12 (a). What is noteworthy is that the increase in magnetization is accompanied by an increase in the intensity of the defect band in the visible region of the PL spectrum as shown in Fig. 3.12 (b). To

the best of our knowledge, this is the first report on UV light-induced increase in magnetization of nanoparticles. It is possible that the increase in M_s value could be due to the increase in defect density by UV irradiation.

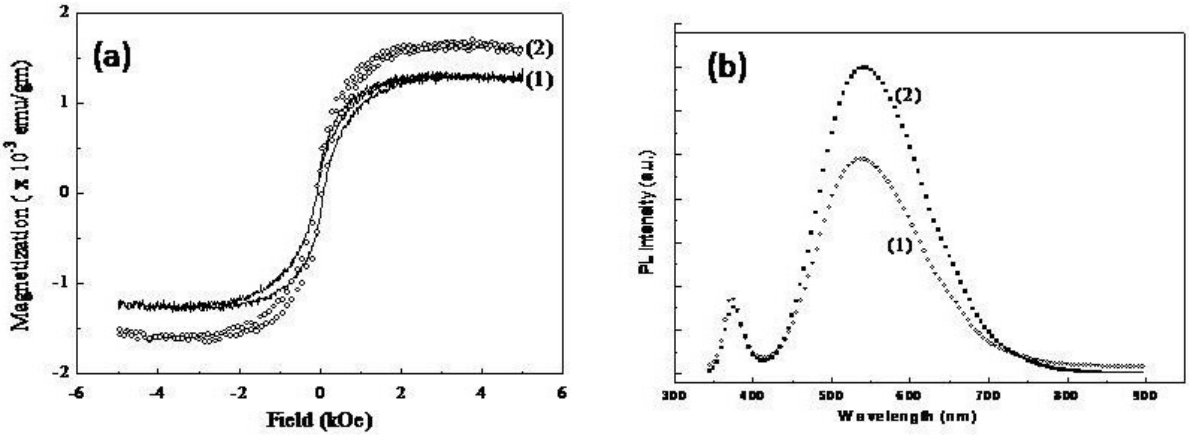

Fig. 3.12. (a) Room-temperature magnetization curves of ZnO nanoparticles (d~5 nm): 1) as-synthesised and 2) after irradiation with UV light. (b) Corresponding PL spectra of (1) and (2).

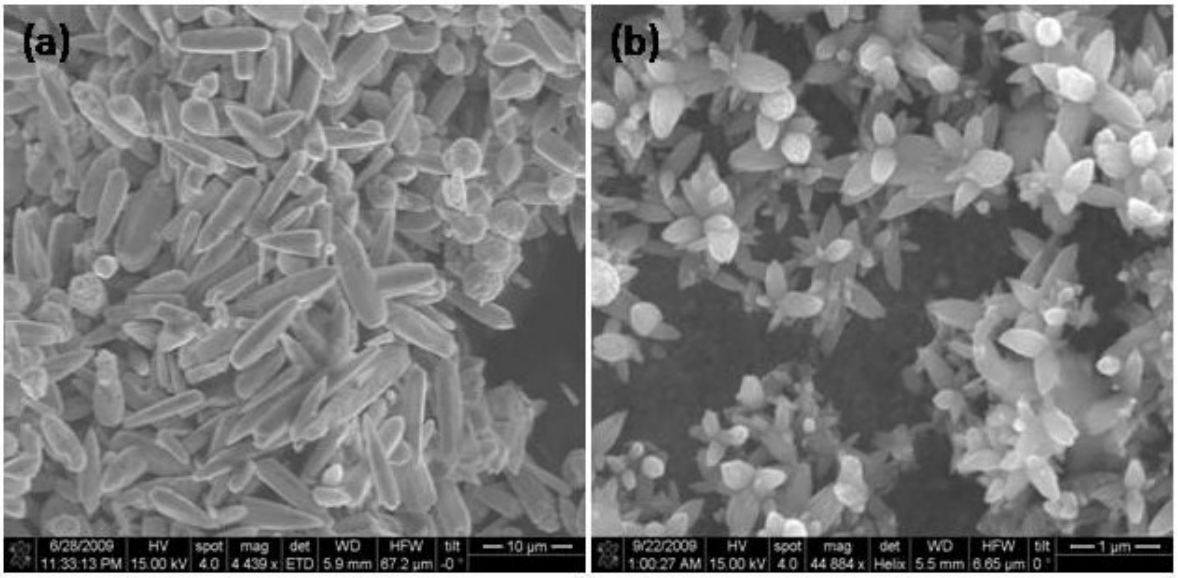

Fig. 3.13. FESEM image of (a) ZnO nanobullets and (b) ZnO nanoflowers.

In order to understand the effect of morphology of the ZnO nanostructures on the magnetic as well as photoluminescence properties, we have examined ZnO nanobullets. A FESEM image of ZnO nanobullets is

shown in Fig. 3.13 (a). The nanobullets have a flat circular base and a sharp tip (diameter ~ 80 nm) at the end. Fig. 3.14 (a) shows hysteresis curve of the ZnO nanobulets with the saturation magnetization $M_s(H)$ = 6.3 x 10^{-3} emu/g. The corresponding PL spectrum, shown in Fig. 3.14 (b), exhibits bands around 404 and 425 nm corresponding to Zn vacancies (V_{Zn}) and Zn interstitials (Zn_i) respectively [24-26], with another band at 455 nm whose origin is not yet clear [27, 28]. The spectrum shows negligible band edge emission at 390 nm as well as green emission at 530 nm. This may be due to the quenching of photo-excited electrons by Zn_i and V_{Zn} before radiative combination. Cation defect-induced magnetism in ZnO has been reported in literature [29, 30]. In our synthetic procedure, we did not use any base, the role of which in the reaction is to make the reaction kinetics slow giving a product in its thermodynamically most stable orientation ((001) orientation in the case of ZnO) avoiding structural defects. The reaction employed occurs fast creating violet or blue emitting defects responsible for the observed magnetism.

We have also studied magnetism in one-dimensional nanoflowers (Fig. 3.13 (b)) and 2-dimensional thin films (Fig.2.27 in chapter-2) of ZnO prepared at the liquid-liquid interface. The inset in Fig. 3.14 (a) show the M(H) plot of the ZnO nanoflowers. The nanoflowers show high saturation magnetization (0.11 emu/g), around two orders higher than that of ZnO nanoparticles prepared by the sol-gel method. The PL spectrum (see inset in fig. 3.14 (b)) exhibits bands similar to those of ZnO nanoparticles. The observation of high saturation magnetization is interesting and is worthy of further study. We have also recorded the magnetic properties and PL

spectrum of ZnO thinfilms (Figures 3.15 (a) and (b)) with a thickness around 50±20 nm, prepared at the liquid-liquid interface. The thin films exhibits high saturation magnetization similar to the nanoflowers. The PL spectrum shows a band at 404 nm and weak feature at 425 nm.

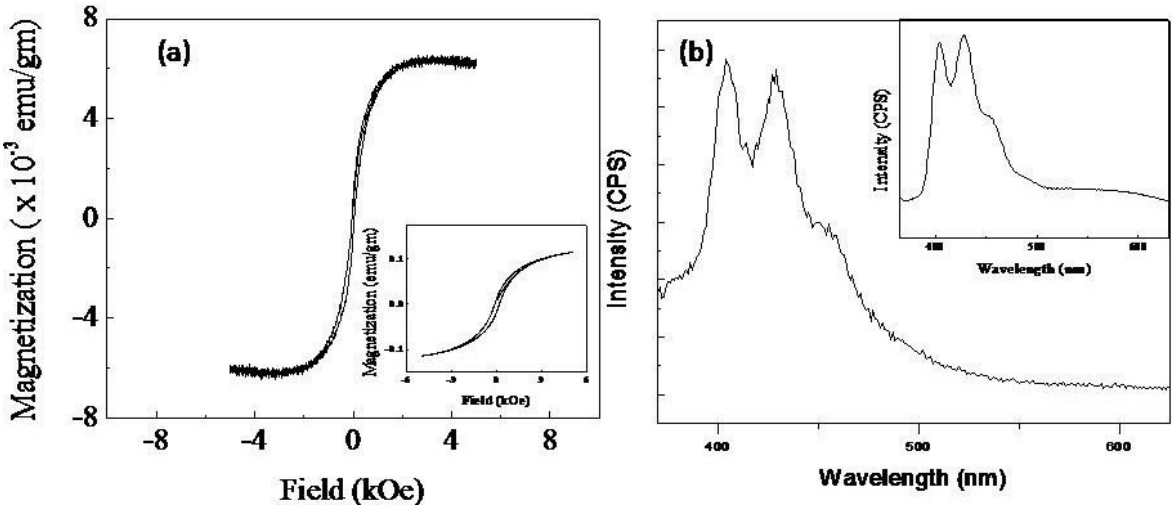

Fig. 3.14. (a) Room-temperature magnetization curve and (b) PL spectrum of ZnO nanobullets. Inset in (a): room-temperature magnetization curve of ZnO nanoflowers synthesized at the liquid–liquid interface, with the corresponding PL spectrum in the inset of (b).

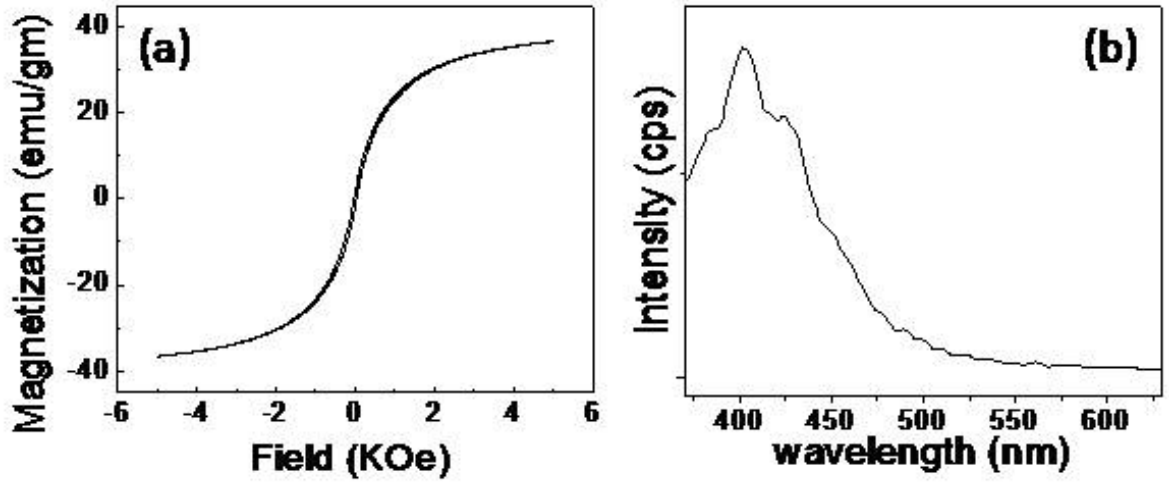

Fig. 3.15. (a) Room-temperature magnetization curve and (b) PL spectrum of ZnO thin films.

3.4.2 MgO

We have carried out studies of the room-temperature ferromagnetism and photoluminescence spectra of nanoparticles of MgO. Figures 3.16 (a) and (b) show the room-temperature magnetization data and photoluminescence spectra of MgO nanoparticles heated at 400, 600, 700 and 1400 ^{o}C for 10 h. The MgO nanoparticles synthesized at 400, 600 and 700 ^{o}C have particle sizes of around 22, 28 and 35 nm respectively. XRD patterns confirm the cubic structure of MgO, the particle sizes of the samples synthesized at 400, 600 and 700 ^{o}C being 17, 21 and 25 nm respectively. It is evident from Fig. 3.16 (a) that the saturation magnetization decreases with increase in annealing temperature and becomes diamagnetic when annealed at 1400 ^{o}C. The saturation magnetization values for MgO nanoparticles annealed at 400, 600 and 700 ^{o}C are respectively 8.3 x 10^{-3}, 2.4 x 10^{-3} and 1.07 x 10^{-3} emu/g. MgO nanoparticles are known to show a broad photoluminescence (PL) band in the violet-blue region due to low coordinated surface ions or defects [31-33]. We observe a broad band centered around 390 nm whose intensity decreases with increase in particle size Fig. 3.16 (b). It should be noted that bulk MgO shows a weak luminescence spectrum consistent with the relatively low concentration of defects. These results on MgO nanoparticles also confirm that ferromagnetism of oxide nanoparticles decreases with increasing particle size.

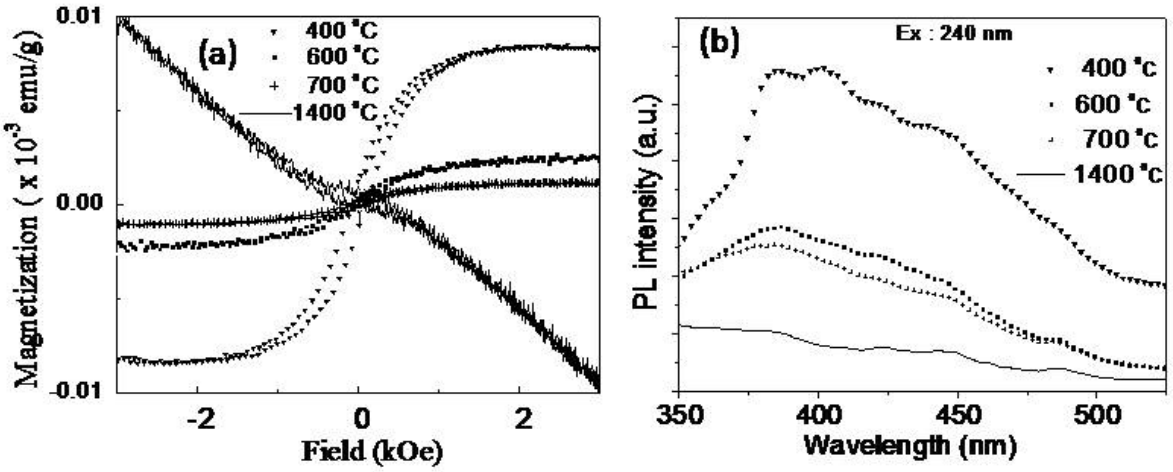

Fig. 3.16. (a) Room-temperature magnetization curves of MgO nanoparticles prepared at different temperatures and (b) corresponding room-temperature photoluminescence spectra.

3.4.3 ZrO_2

We have carried out studies of the room-temperature ferromagnetism and photoluminescence spectra of nanoparticles of ZrO_2. From the TEM images, the average diameter of the ZrO_2 nanoparticles annealed at 400 and 600 ^oC are respectively 5.5 and 8 nm. XRD patterns confirm the tetragonal phase of ZrO_2 nanoparticles with average sizes of 5 and 7.5 nm for the particles annealed at 400 and 600 ^oC respectively. Fig. 3.17 (a) shows a decrease in the room-temperature saturation magnetization of ZrO_2 nanoparticles with increase in particle size or annealing temperature. The saturation magnetization values for ZrO_2 nanoparticles annealed at 400 and 600 ^oC are 3.97 x 10^{-3} emu/g and 1.93 x 10^{-3} emu/g respectively. ZrO_2 particles sintered at 1200 ^oC shows a diamagnetic behavior. The PL spectra of the ZrO_2 nanoparticles show a decrease in the intensity of defect band in the 370-460 nm region [34] with increasing particle size as shown in Fig.

3.17 (b). These results on ZrO_2 nanoparticles further confirm that ferromagnetism of oxide nanoparticles decreases with increasing particle size accompanied by a decrease in the defect PL band intensity.

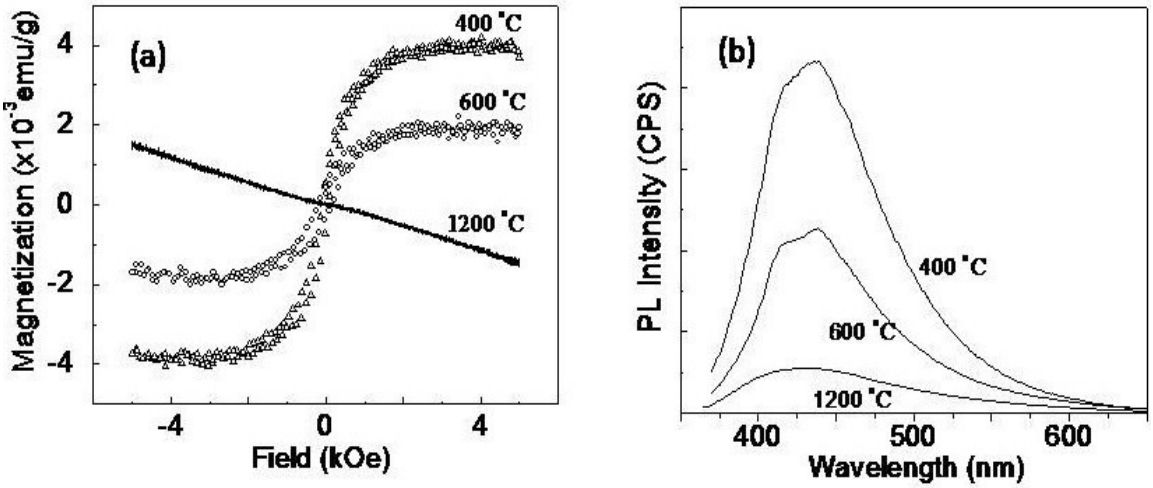

Fig. 3.17. (a) Room-temperature magnetization curves of ZrO2 nanoparticles heated at different temperatures and (b) corresponding room-temperature photoluminescence spectra.

3.5 Conclusions

The present study clearly establishes the occurrence of defect-induced room-temperature ferromagnetism in metal oxide nanoparticles. While the nature of defects can be oxygen or cation vacancies, depending on the sample, it is noteworthy that, the intensities of defect-related bands in the PL spectra decrease as the magnetization of the nanoparticles decreases. There is some dependence of particle morphology on the magnetism. Thus, ZnO thin films and nanoflowers show higher magnetization compared to nanoparticles. We observed, adsorption of ethanol decreases the magnetization and defect PL band intensity of ZnO nanoparticles while UV irradiation has the opposite effect.

References

[1] K. Ueda, H. Tabata, T. Kawai *Appl. Phys. Lett.* **2001,** 79, 988.

[2] A. Tiwari, M. Snure, D. Kumar, J. T. Abiade *Appl. Phys. Lett.* **2008**, 92, 062509.

[3] P. Sharma, A. Gupta, K. V. Rao, F. J. Owens, R. Sharma, R. Ahuja, J. M. O. Guillen, B. Johansson, G. A. Gehring *Nat. Mater.* **2003**, 2, 673.

[4] T. Dietl, H. Ohno, F. J. Matsukura, J. Cibert, D. Ferrand *Science* **2000**, 287, 1019.

[5] C. J. Cong, L. Liao, J. C. Li, L. X. Fan, K. L. Zhang *Nanotechnology*. **2005**, 16, 981.

[6] S. A. Wolf, D. D. Awschalom, R. A. Buhrman, J. M. Daughton, S. von Molnar, M. L. Roukes, A. Y. Chtchelkanova, D. M. Treger *Science*. **2001**, 294, 1488.

[7] C. N. R. Rao, F. L. Deepak *J. Mater. Chem.* **2005**, 15, 573.

[8] R. Seshadri *Curr. Opin. Solid State Mater. Sci.* **2005**, 9, 1.

[9] J. Blasco, F. Bartolome, L. M. Garcia, J. Garcia *J. Mater. Chem.* **2006**, 16, 2282.

[10] S. Yin, M. X. Xu, L. Yang, J. F. Liu, H. Rosner, H. Hahn, H. Gleiter, D. Schild, S. Doyle, T. Liu, T. D. Hu, E. Takayama-Muromachi, J. Z. Jiang, *Phys. Rev. B.* **2006**, 73, 224408.

[11] Z. Zhang, Q. Chen, H. D. Lee, Y. Y. Xue, Y. Y. Sun, H. Chen, F. Chen, W. K. Chu *J. Appl. Phys.* **2006**, 100, 043909.

[12] A. Sundaresan, R. Bhargavi, N. Rangarajan, U. Siddesh, C. N. R. Rao *Phys. Rev. B.* **2006**, 74, 161306.

[13] A. Sundaresan, C. N. R. Rao *Nano today* **2009**, 4, 96.

[14] M. Venkatesan, C. B. Fitzgerald, J. M. D. Coey *Nature*. **2004**, 430, 630.

[15] J. M. D. Coey, S. A. Chambers *MRS Bull.* . **2008**, 33, 1053.

[16] A. Sundaresan, C. N. R. Rao *Solid State Commun.* . **2009**, 149, 1197.

[17] A. M. Stoneham, Oxford University Press, , Oxford, **2001**.

[18] C. Pacholski, A. Kornowski, H. Weller *Angew. Chem. Int. Ed.* . **2002**, 41, 1188.

[19] A. Subramania, G. Vijaya Kumar, A. R. S. Priya, T. Vasudevan *Nanotechnology*. **2007**, 18, 225601.

[20] J. Liang, Z. Deng, X. Jiang, F. Li, Y. Li *Inorg. Chem.* **2002**, 41, 3602.

[21] S. Venkataprasad Bhat, S. R. C. Vivekchand, A. Govindaraj, C. N. R. Rao *Solid State Commun.* **2009**, 149, 510.

[22] J. Liang, J. Liu, Q. Xie, S. Bai, W. Yu, Y. Qian *J. Phys. Chem. B*. **2005**, 109, 9463.

[23] K. Vanheusden, W. L. Warren, C. H. Sesger, D. R. Tallant, J. A. Voigt, B. E. Gnage *J. Appl. Phys.* . **1996**, 79, 7983.

[24] A. B. Djurisic, Y. H. Leung, K. H. Tam, Y. F. Hsu, L. Ding, W. K. Ge, Y. C. Zhong, K. S. Wong, W. K. Chan, H. L. Tam, K. W. Cheah, W. M. Kwok, D. L. Phillips *Nanotechnology*. **2007**, 18, 095 702.

[25] X. Zhou, S. Gu, Z. Wu, S. Zhu, J. Ye, S. Liu, R. Zhang, Y. Shi, Y. Zheng *Appl. Surf. Sci.* . **2006**, 253, 2226.

[26] H. Zeng, W. Cai, J. Hu, G. Duan, P. Liu, Y. Li *Appl. Phys. Lett.* **2006**, 88, 171910.

[27] J. J. Wu, S. C. Liu *Adv. Mater.* **2002**, 14, 215.

[28] J. Wang, L. Gao *J. Mater. Chem.* **2003**, 13, 2551.

[29] Q. Wang, Q. Sun, G. Chen, Y. Kawazoe, P. Jena *Phys. Rev. B.* **2008**, 77, 205411.

[30] A. M. Stoneham, A. P. Pathak, R. H. Bartram *J. Phys. C* **1976**, 9, 73.

[31] S. Stankic, M. Muller, O. Diwald, M. Sterrer, E. Knozinger, J. Bernardi *Angew. Chem. Int. Ed.* **2005**, 44, 4917.

[32] S. G. Maclean, W. W. Duley *J. Phys. Chem. Solids* **1984**, 45, 227.

[33] C. Chizallet, G. Costentin, H. L. Pernot, J. M. Krafft, M. Che, F. Delbecq, a. P. Sautet *J. Phys. Chem. C.* **2008**, 112, 16629.

[34] H. Q. Cao, X. Q. Qiu, B. Luo, Y. Liang, Y. H. Zhang, R. Q. Tan, M. J. Zhao, Q. M. Zhu *Adv. Funct. Mater.* **2004**, 14, 243.

Chapter-4

Boron- and Nitrogen-doped Double-walled Carbon Nanotubes

Summary*

This chapter of the thesis deals with the synthesis and spectroscopic characterization of boron- and nitrogen-doped and undoped double-walled carbon nanotubes (DWNTs) and also deals with the functionalization of DWNTs.

Double-walled carbon nanotubes doped with boron and nitrogen have been prepared by the decomposition of a CH_4+Ar mixture along with diborane and pyridine (or NH_3) respectively, over a $Mo_{0.1}Fe_{0.9}Mg_{13}O$ catalyst, prepared by the combustion route. The doped DWNTs have been characterized by transmission electron microscopy (TEM), X-ray photoelectron spectroscopy, electron energy loss spectroscopy, and Raman spectroscopy. The dopant concentration is around 1 atom % for both boron and nitrogen. The radial breathing modes in the Raman spectra have been

*Papers based on these studies have appeared in ACS Nano (2007) and J. Chem. Sci. (2008).

employed along with TEM to obtain the inner and outer diameters of the DWNTs. The diameter ranges for the undoped, B-doped, N-doped (pyridine) and N-doped (NH_3) DWNTs are 0.73–2.20, 0.74–2.36, 0.74–2.30 and 0.73–2.32 nm, respectively, the boron-doped DWNTs giving rise to a high proportion of the large diameter DWNTs. Besides affecting the G-band in the Raman spectra, B- and N-doping affect the proportion of semiconducting nanotubes.

DWNTs have been functionalized by both covalent and non-covalent means. Covalent functionalization has been carried out by attaching an aliphatic amide functional group to DWNTs which enable its solubilisation in non-polar solvents. Solubilization in non-polar solvents has also been accomplished by non-covalent functionalization by using 1-pyrenebutanoicacid succinimidyl ester (PYBS). Non-covalent functionalization of DWNTs has been carried out by using polyethylene glycol (PEG) and polyoxyethylene(40)nonylphenyl ether (IGPAL), both of which enable solubilization in aqueous media. These functionalized DWNTs have been characterized by transmission electron microscopy, IR and Raman spectroscopy.

4.1 Introduction

Double-walled carbon nanotubes (DWNTs), first observed in 1996, constitute a unique family of carbon nanotubes (CNTs) [1, 2]. DWNTs occupy a position between the single-walled carbon nanotubes (SWNTs) and the multiwalled carbon nanotubes (MWNTs), as they consist of two concentric cylinders of rolled graphene. DWNTs possess useful electrical and mechanical properties with potential applications. Thus, DWNTs and SWNTs have similar threshold voltages in field electron emission, but the DWNTs exhibit longer lifetimes [3]. Unlike SWNTs, which get modified structurally and electronically upon functionalization, chemical functionalization of DWNTs surfaces would lead to novel carbon nanotube materials where the inner tubes are intact. The stability of DWNTs is controlled by the spacing of the inner and outer layers but not by the chirality of the tubes [4]; therefore, one obtains a mixture of DWNTs with varying diameters and chirality indices of the inner and outer tubes. DWNTs have been prepared by several techniques, such as arc discharge [5] and chemical vapor deposition (CVD) using a mixture of ferrocene with a hydrocarbon or alcohol (typical hydrocarbons are methane, n-hexane, and benzene) [6-10]. DWNTs have also been prepared by a sulfur-assisted CVD method using methane as the carbon source [11, 12].

Applications of CNTs based on their electrical properties strongly depend on the diameter and helicity as well as parity [2, 13]. Doping of CNTs by boron and nitrogen renders them p-type and n-type, respectively. MWNTs and SWNTs doped with nitrogen [14-17] and boron [18, 19] have been

reported. Boron-doped carbon nanotubes appear to exhibit enhanced electron field emission due to the presence of the boron atom at the nanotube edges [20, 21]. N-doped CNTs show n-type behavior regardless of tube chirality [22].

4.2 Scope of the present investigations

4.2.1 B- and N-doped double-walled carbon nanotubes

We were interested in the synthesis and characterization of boron- and nitrogen-doped DWNTs in the view of their potential applications. We have focused on the low doping regime (~1 atom %), where the fundamental band structure is expected to be unchanged relative to the all-carbon model. To our knowledge, except for a report on the preparation of nitrogen-doped DWNTs by using a mixture of methane, ammonia, and argon over an iron-molybdenum catalyst [23], there has been no detailed study of these materials. We have prepared nitrogen-doped DWNTs by the thermal decomposition of a CH_4 + NH_3 + Ar mixture as well as a CH_4 + pyridine + Ar mixture over a $Mo_{0.1}Fe_{0.9}Mg_{13}O$ catalyst, prepared by a new procedure. It may be noted that pyridine has been found to be a good nitrogen source to prepare N-doped MWNTs [16]. We have prepared boron-doped DWNTs by the thermal decomposition of a CH_4 + B_2H_6 + Ar mixture over the $Mo_{0.1}Fe_{0.9}Mg_{13}O$ catalyst at 950 °C. The various DWNTs have been characterized with respect to composition and structure. In particular, the effect of B- and N-doping on the dimensions of the nanotubes has been examined by Raman spectroscopy.

4.2.2 Functionalization of double-walled carbon nanotubes

Functionalization and solubilization are important aspects of the chemistry of carbon nanotubes (CNTs), these chemical manipulations being essential for many of the applications of CNTs [2, 24-27]. Multi-walled carbon nanotubes (MWNTs) and single-walled carbon nanotubes (SWNTs) have been functionalized by both covalent and noncovalent means [2, 28-38]. The covalent functionalization method typically involves acid treatment of the CNTs followed by reaction with thionyl chloride followed by reaction with a long chain amine. Such amidation gives rise to SWNTs soluble in non-polar solvents [2, 24-26, 30, 32]. Other methods such as fluorination have also been used for the functionalization of SWNTs [2, 39]. Covalent functionalization, however, has the limitation that it drastically affects the electronic structure of the SWNTs and hence affects their properties. Non-covalent functionalization of CNTs has been carried out by employing surfactants, aromatics and other reagents [34, 35, 40].

We have been interested in the functionalization and solubilization of double-walled carbon nanotubes (DWNTs) by both covalent and non-covalent means, especially because functionalization of DWNTs should affect only the outer nanotube surface, leaving the inner tube intact. This feature is attractive with inherent technological applications. We have therefore carried the functionalization of DWNTs by both covalent and non-covalent means. Thus we have carried out covalent functionalization employing the amidation reaction, giving rise to DWNTs soluble in non-polar solvents. π-π intractions through bezinoid groups and interacion with polymers give high degree of solubility for carbon nanotubes even at low level of

functionalization. Thus, we have carried out functionalization of DWNTs non-covalently by using the long chain polymers such as polyethylene glycol (PEG) and polyoxyehylene(40)nonylphenyl ether (IGPAL) and π-π interactions with 1-pyrenebutanoicacid succinimidyl ester (PYBS). Functionalization of DWNTs with PYBS enables solubilization in non-polar solvents whereas functionalization with IGPAL and PEG results in solubilization in water.

4.3 Experimental and related aspects

(a) Preparation of catalyst ($Mo_{0.1}Fe_{0.9}Mg_{13}O$)

The oxide precursors required to prepare the catalyst for the synthesis of DWNTs were prepared by the combustion route [41, 42]. The required amount of $(NH_4)_6Mo_7O_{24}\cdot 4H_2O$ was added to an aqueous solution containing ferric nitrate ($Fe(NO_3)_3\cdot 9H_2O$) and magnesium nitrate ($Mg(NO_3)_2\cdot 6H_2O$) in a Pyrex dish, keeping the molar ratio of Mo:Fe:MgO at 0.1:0.9:13. To this mixture was added an appropriate amount of urea (three times the stoichiometric ratio), which acts as the fuel in the combustion process. The mixture was dissolved by using a minimum amount of distilled water and kept in an oven at 70 °C for 12 h. The Pyrex dish containing the solution was placed in a furnace preheated at 550 °C. The thick orange-red solution immediately started boiling and underwent dehydration. The resulting thick paste frothed and blazed with a white flame, with the production of a light material which then swelled to the capacity of the Pyrex dish. The total combustion process was over in 10 min. The combustion product was baked

at 550 °C for 3 h and ground to a fine powder. Preparation of the catalyst by conventional methods, such as wet impregnation or co-precipitation, yields inhomogeneous catalyst particles, whereas the combustion route employed here gives homogeneous catalyst particles.

(b) Synthesis of double-walled carbon nanotubes

Synthesis of DWNTs was carried out in a quartz tube reactor. For each synthesis, 200 mg of the supported Fe-Mo catalyst (Fe-Mo/MgO) was placed in a quartz boat by spreading it uniformly. The quartz boat was inserted into the center of the quartz tube (25 mm dia. and 1 m long) mounted inside an electrical tube furnace. Subsequently, the furnace was heated to 950 °C in an argon atmosphere at a heating rate of 3 °C/min. A mixture of methane and Ar gas was introduced into the reactor. The flow rates of methane and Ar were maintained at 50 and 150 sccm (standard cubic centimeters per minute), respectively. After 20 min, the reactor was cooled to room temperature in an Ar atmosphere. The resulting black dense mat contained a homogeneous dispersion of carbon nanotubes around the oxide grains. This crude material was carefully collected from the boat and subjected to purification.

(c) Synthesis of nitrogen-doped double-walled carbon nanotubes

For obtaining nitrogen-doped DWNTs, the procedure was similar to that used for undoped DWNTs, expect that ammonia or pyridine vapor was taken in mixture with CH_4. For doping nitrogen by using ammonia, the

supported Fe-Mo catalyst (200 mg) was placed in a quartz boat at the center of the quartz reactor tube. The quartz tube was heated to 950 °C in an Ar atmosphere. Subsequently, CH_4 (50 sccm), NH_3 (5 sccm), and Ar (150 sccm) were mixed and introduced at the inlet of the reactor tube. After 20 min, the reactor was cooled to room temperature in an Ar atmosphere. For N-doping using pyridine, the supported Fe-Mo catalyst (200 mg) was placed in a quartz boat at the center of the quartz reactor tube. The quartz tube was heated to 950 °C in an Ar atmosphere. Subsequently, 40 sccm of CH_4 was passed through a bubbler containing pyridine, which carries the pyridine vapor to the furnace. These vapors were mixed with 150 sccm of Ar and passed over the MgO-supported catalyst, maintained at 950 °C for 20 min.

(d) Synthesis of boron-doped double-walled carbon nanotubes

For the synthesis of boron-doped DWNTs, diborane (B_2H_6) was used as the boron source, the rest of the procedure being similar to that for undoped DWNTs. B_2H_6 vapor was generated by the addition of BF_3-diethyl etherate to sodium borohydride in tetraglyme [18]. 50 sccm of CH_4 was mixed and passed along with B_2H_6 vapors. These vapors were further mixed with 150 sccm of Ar and passed over the MgO-supported catalyst powder, maintained at 950 °C for 20 min.

(e) Purification of undoped as well as doped double-walled carbon nanotubes

In order to dissolve the metal nanoparticles in the DWNTs, the as-prepared nanotubes were treated with concentrated HCl at 60 °C for 24 h.

The product was washed with distilled water, dried, dispersed in ethanol under sonication, and filtered using Millipore (0.2 μm) filter paper. The filtered product was dried in an oven at 100 °C for 2 h and heated to 850 °C in a furnace at a rate of 3 °C per minute in flowing hydrogen at 100 sccm and held at that temperature for 6 h to remove the amorphous carbon present on the nanotube walls [43]. The resulting sample was again stirred in concentrated HCl at 60 °C for 3 h and heated in a furnace at 850 °C for 6 h in flowing hydrogen (100 sccm). The same procedure was employed to purify doped DWNTs, except that dilute HCl was used instead of concentrated HCl.

(f) Covalent and non-covalent functionalization of DWNTs

To solubilize DWNTs in non-polar solvents, the following procedure was employed. In the first step, acid treated DWNTs were prepared by the following procedure. Concentrated nitric acid (1 ml) and water (15 ml) were added to DWNTs (10 mg) in a teflon lined autoclave and subsequently heated in a microwave oven for 10 minutes under hydrothermal conditions. Further, the Teflon autoclave containing sample was heated at 100 °C for 12 hours. The product was washed with distilled water and centrifuged repeatedly to remove traces of acid. Thus yielded DWNTs were functionalized with –OH and –COOH groups. The acid treated DWNTs were refluxed with excess $SOCl_2$ for 12 hours and the unreacted $SOCl_2$ was removed under vacuum at room temperature. This product was treated with dodecylamine (5 ml) in an autoclave under solvothermal conditions at 100 °C. We adopted another procedure to solubilize DWNTs in non-polar solvents. The reaction

procedure is as follows. Excess amount of PYBS (5 mg) was added to 1 mg of DWNTs in a test tube, which was heated at 150 ^{o}C for 10 min. The resulting mixture was dispersible in dimethylformamide by ultra sonication for 30 minutes. The resulting suspension is stable for several hours.

In order to solubilize DWNTs in water, we functionalized DWNTs with polyethylene glycol (PEG) and polyoxyehylene(40)nonylphenyl ether (IGPAL). PEG-functionalized DWNTs was prepared by reacting acid treated DWNTs with excess of PEG (6 ml) and concentrated HCl (2 ml) under solvothermal conditions at 100 °C for 12 hours. IGPAL-functionalized DWNTs were prepared as follows. Excess amount of IGPAL (10 mg) was added to 2 mg of DWNTs in a test tube, which is heated at 100 ^{o}C for 10 min. Distilled water was added to the resulting mixture and sonicated for 30 minutes. The resulting suspension is stable for more than 7 days.

Techniques used for characterization

Field emission scanning electron microscope (FESEM): FESEM images were recorded with a FEI NOVA NANOSEM 600.

UV-Vis absorption and Photoluminescence: UV-Vis absorption measurements were carried out at room temperature with a Perkin-Elmer model Lambda 900 UV/Vis/NIR spectrometer.

Raman spectroscopy: Raman spectra were recorded with LabRAM HR high resolution Raman spectrometer (Horiba Jobin Yvon) using He-Ne Laser (λ=630 nm).

IR spectroscopy: IR spectra were recorded on KBr pellet with Bruker IFS-66V.

Transmission electron microscopy (TEM): Transmission electron microscope (TEM) images were obtained with a JEOL JEM 3010, operating with an accelerating voltage of 300 kV. The samples were prepared by dispersing the product in CCl_4. A drop of the suspension was then put on a holey carbon coated Cu grid and allowed to evaporate slowly.

Electron energy loss spectroscopy (EELS): EELS were recorded with a transmission electron microscope (FEI, TECNAI F30) equipped with an energy filter for EELS operating at 300 kV.

Thermogravimetric analysis (TGA): Thermogravimetric analysis was carried out using a Mettler Toledo TGA 850 instrument.

X-ray photoelectron spectroscopy (XPS): X-ray photoelectron spectroscopy was recorded using a VG scientific ESCA Laboratory V spectrometer.

4.4 Results and Discussion

4.4.1 B- and N-doped double-walled carbon nanotubes

While the decomposition of the CH_4 + Ar over the $Mo_{0.1}Fe_{0.9}Mg_{13}O$ catalyst at 950 °C yielded undoped DWNTs, decomposition of the CH_4 + NH_3 + Ar and CH_4 + pyridine + Ar mixtures gave nitrogen-doped DWNTs. Decomposition of the CH_4 + B_2H_6 + Ar mixture over the catalyst at 950 °C yielded boron-doped DWNTs. The B- and N-doped DWNTs could not be produced at temperatures lower than 950 °C. The combustion method employed for the preparation of the catalyst seems to help in producing DWNTs exclusively with only a very small or negligible proportion of SWNTs.

We have used both transmission electron microscopy (TEM) and Raman spectroscopy to characterize the different DWNTs samples. TEM allows direct imaging of the DWNTs and gives indications for the presence of other species along with the DWNTs. In the TEM images, we seldom encountered SWNTs or MWNTs. Besides providing information on the nature and dimensions of DWNTs, Raman spectroscopy helps to characterize the purity and quality of the DWNTs. Electron energy loss spectroscopy (EELS), carried out in a high-resolution electron microscope, and X-ray photoelectron spectroscopy have been employed to determine the elemental composition of the DWNTs.

Undoped DWNTs obtained by us generally had outer tube diameters of 2.2-2.8 nm and inner tube diameters of 1.4-2.1 nm, as shown by the high-resolution TEM (HREM) images in Fig. 4.1. In Figures 4.2 and 4.3, we

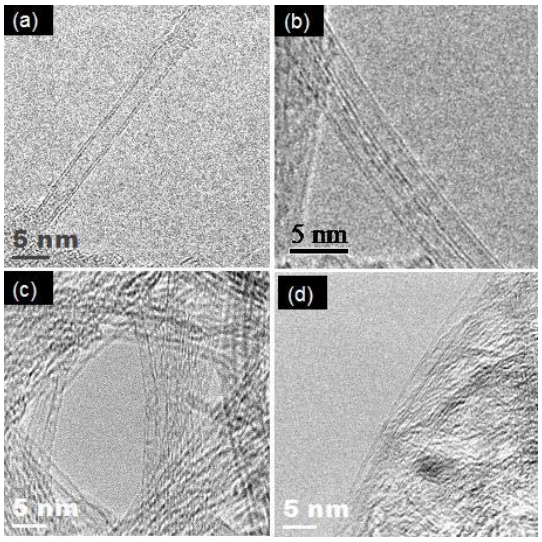

Fig 4.1. HREM images of undoped DWNTs

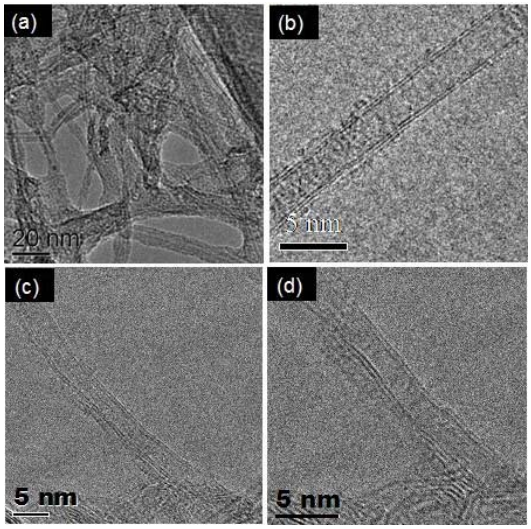

Fig 4.2. TEM (a) and HREM (b-d) images of N-doped DWNTs using ammonia as the nitrogen source.

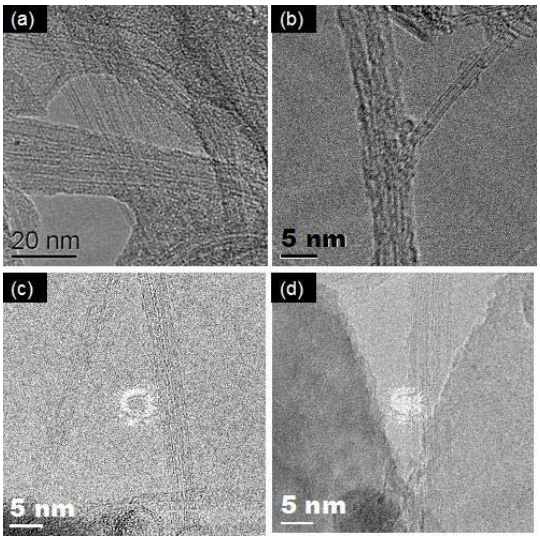

Fig 4.3. TEM (a) and HREM (b-d) images of N-doped DWNTs using pyridine as the nitrogen source

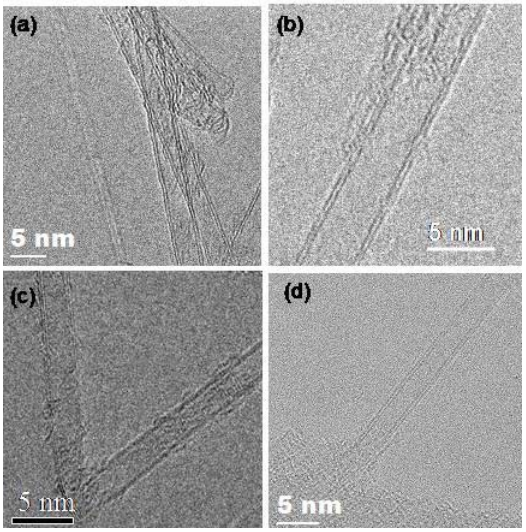

Fig 4.4. HREM images of B-doped DWNTs.

show typical HREM images of purified nitrogen-doped DWNTs synthesized by using NH_3 and pyridine as the nitrogen source, respectively. In Fig. 4.4, we show HREM images of the boron-doped DWNTs. The HREM images indicate that the purified samples of the DWNTs have well-resolved walls and that most of the amorphous carbon was eliminated from the surface during the purification process. HREM images reveal that the outer tube

diameters of the N-doped DWNTs prepared by using NH_3 as the nitrogen source are in the 1.7–3.2 nm range and the inner tube diameters are in the 1–2.4 nm range. The interlayer spacing is around 0.38 nm. In the case of N-doped DWNTs prepared by using pyridine as the nitrogen source, the outer tube diameters are generally in the 1.6–2.6 nm range, while the inner tube diameters are in the 0.9–1.8 nm range. The interlayer spacing ranges from 0.34 to 0.41 nm. From the HREM studies, we surmise that the diameters of the N-doped DWNTs obtained by using pyridine are smaller than those obtained with NH_3. Thus, the diameters of the N-doped DWNTs appear to depend on the nitrogen source and the reaction conditions employed.

HREM images of the boron-doped DWNTs show that they possess larger diameters than the undoped DWNTs as well as the N-doped DWNTs (Fig. 4.4). The outer tube diameters of the B-doped DWNTs range from 2.5 to 4.7 nm, and the inner tube diameters are in the 1.8 –3.9 nm range. The interlayer spacing ranges from 0.35 to 0.41 nm. Fig. 4.4 (b) shows the HREM image of a large diameter B-doped DWNT with an outer diameter of 4.7 nm and an inner diameter of 3.9 nm.

It has been reported in the literature that boron and nitrogen are incorporated to SWNTs to a smaller extent than in MWNTs [14-19]. We have estimated the compositions of the B- and N-doped DWNTs prepared by us by employing X-ray photoelectron spectroscopy. A core-level X-ray photoelectron spectrum of the N-doped DWNTs obtained by using NH_3 as the N-source is shown in Fig. 4.5 (a). The C 1s signal is at 284.3 eV, while the N 1s signal is centered at 399.6 eV, indicating of nitrogen substitution in the graphene sheet. It is possible that there is a small amount of amorphous

carbon, as suggested by the asymmetry of the C 1s signal, although most of it gets removed on treatment with hydrogen (see Experimental Section). The asymmetric shape of the N 1s peak indicates the existence of at least two components and could be deconvoluted into two peaks at 398 and 401.3 eV. The 398 eV feature is characteristic of pyridinic nitrogen (sp^2 hybridization), while the peak centered at 401.3 eV is due to nitrogen present in graphene sheets [15]. The areas of the two bands bear a ratio of 1:1. On the basis of the total N 1s and C 1s intensities, the nitrogen-to-carbon ratio in the nanotubes samples was calculated by taking the photoionization cross sections of the 1s levels into account. The average composition was thus found to correspond to 1.3 atom % nitrogen. This value is lower than that reported in the literature for DWNTs (~2.9 atom%) [13] and MWNTs (3–10 atom %) [16]. The N 1s spectrum of N-doped DWNTs obtained by using pyridine as the nitrogen source shows mainly the band at 398 eV, the intensity of the 401.3 eV band being very small. Thus, there is an intrinsic difference in the nature of N-substitution between the N-doped DWNTs prepared by using NH_3 and pyridine.

Fig. 4.5 (b) shows the core-level spectra of the B-doped DWNTs. The B 1s feature is at 191.4 eV, and the C 1s signal is at 284.3 eV. The shift of the B 1s signal toward higher binding energy compared to that of pure boron (188 eV) indicates that boron is in the sp^2 carbon network. The slight asymmetry of the B 1s signal would, however, suggest the presence of another possible mode of substitution. The boron content works out to be 1 atom %. Around 3 atom % B-doped MWNTs have been reported [18]. EELS measurements in a high resolution electron microscope confirmed the

presence of nitrogen as well as boron in the respective doped DWNTs. The %B and %N were found to be small (~1 atom %), consistent with the XPS data.

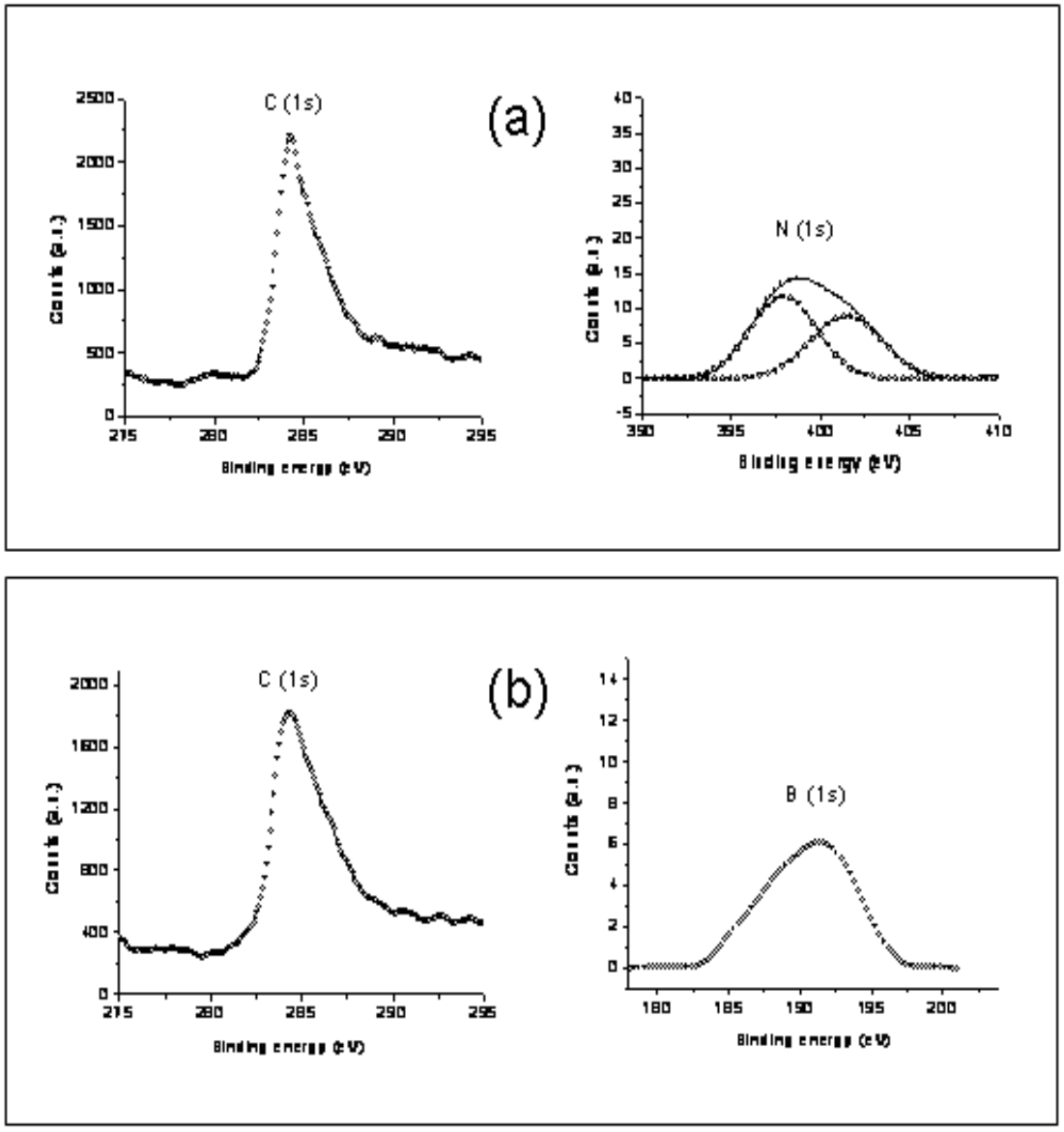

Fig. 4.5. (a) C 1s and N 1s XPS signals of N-doped DWNT prepared using ammonia. (b) C 1s and B 1s signals of B-doped DWNTs.

The resonance Raman spectrum of DWNTs shows three main features: the G band, the D band, and bands due to the radial breathing modes (RBMs). The tangential stretch G-band modes are in the 1550–1600

cm^{-1} range. The disorder-induced D-band is observed between 1200 and 1450 cm^{-1}. The D-band is activated in the second-order scattering process by the presence of in-plane substitutional heteroatoms, vacancies, grain boundaries, or other defects and by finite size effects, all of which lower the crystalline symmetry of the quasi infinite lattice [44]. RBM frequencies provide information about the nanotube diameter in the case of SWNTs and DWNTs. We have recorded the Raman spectra of the undoped as well as the B- and N-doped DWNTs by using 632.8 nm excitation using a He-Ne laser. The spectra were collected in a backscattering geometry at room temperature. Fig. 4.6 (a) shows the G-bands of the pure as well as doped DWNTs. The G-band of the N-doped DWNTs (Py) appears at a lower frequency (1574 cm^{-1}) compared to that of undoped DWNTs (1575 cm^{-1}), whereas the G-band of the B-doped DWNTs appears at a higher frequency (1579 cm^{-1}). The G-band of the N-doped DWNTs (NH_3) also appears at a lower frequency (1571 cm^{-1}). Thus, the shifts of the G-band are opposite for n- and p-doping of the DWNTs. Such shifts of the G-band have been reported for B- and N-doped SWNTs by Yang *et al.* [45] and McGuire *et al.* [19]. The small-intensity shoulder around 1540 cm^{-1} seen in the spectra of undoped DWNTs shows a decrease in intensity in the N-doped DWNTs and is negligible in the case of B-doped DWNTs. This band is related to the metallic nature of the nanotubes [46] and its near absence in B- and N-doped DWNTs suggests a greater prevalence of semiconducting nanotubes. Fig. 4.6 (b) shows that the intensity of the D-band is high in the case of the B-doped DWNTs and low in the case of the N-doped DWNTs. The $I(D)/I(G)$

ratios are 0.04, 0.06, and 0.16 for undoped, N-doped (py), and B-doped DWNTs respectively.

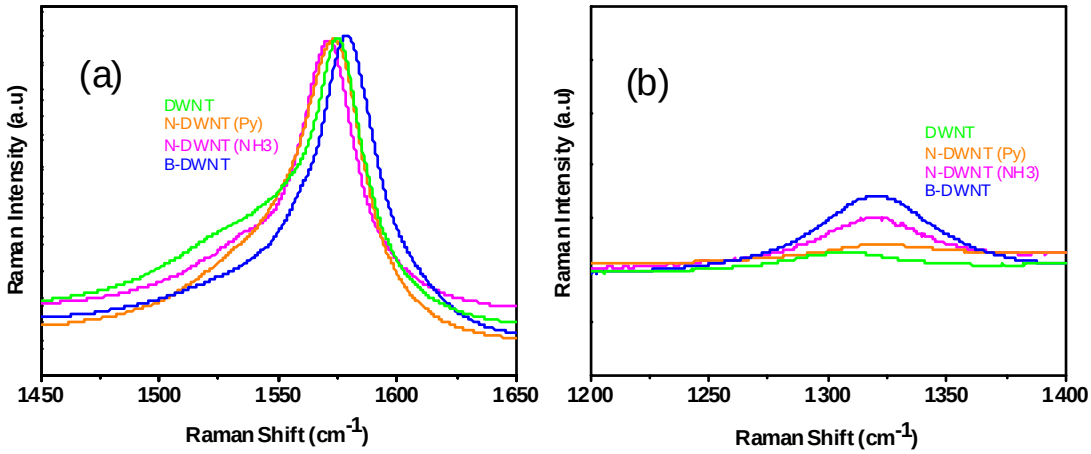

Fig. 4.6 The G-bands (a) and D-bands (b) in the Raman spectra of undoped and doped DWNTs

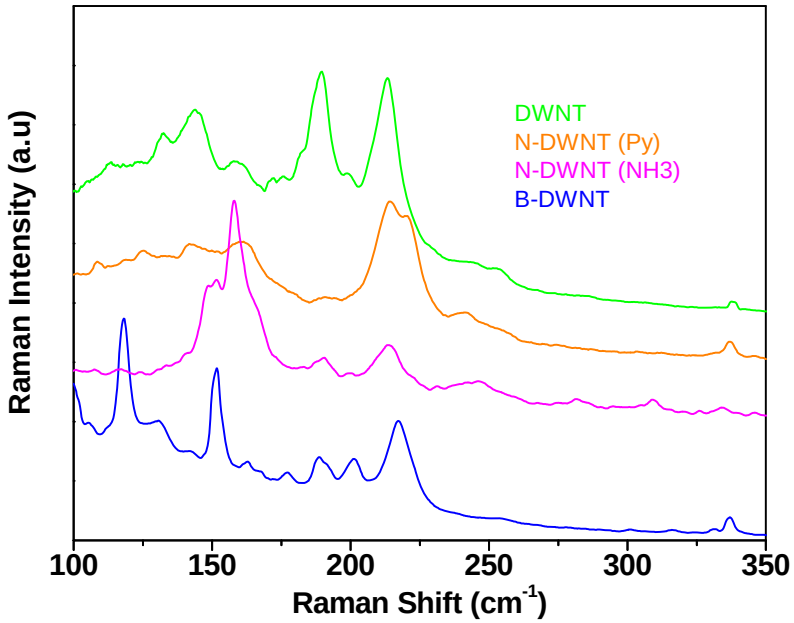

Fig. 4.7 RBM bands of undoped and doped DWNTs

We observe several RBM bands in the DWNTs (Fig. 4.7), resulting from various sizes of the nanotubes, just as in earlier reports [47]. By using the

relation $\omega=248/d$, where ω is the RBM frequency in cm^{-1} and d is the nanotube diameter in nm, we have obtained the diameters of the DWNTs [47]. The RBM frequencies and the corresponding diameters are tabulated in Table 1 for undoped as well as B- and N-doped DWNTs, along with (n,m) indices for the intense features. From the table, we see that the diameter distribution of the nanotubes is markedly affected by B- and N-doping. The undoped DWNTs show the highest intensity RBM bands centered at 213 and 189 cm^{-1}, corresponding to diameters of 1.16 and 1.31 nm, respectively. The slightly lower intensity or medium-intensity RBM bands are at 158, 143, and 132 cm^{-1}, corresponding respectively to diameters of 1.57, 1.73, and 1.88 nm. The N-doped DWNTs (Py) show the highest intensity RBM bands centered at 220 and 214 cm^{-1}, corresponding to diameters of 1.13 and 1.16 nm, respectively. The slightly lower intensity bands centered at 160 and 142 cm^{-1} correspond to 1.55 and 1.75 nm diameters, respectively. The diameters of the N-doped DWNTs (Py) are somewhat smaller compared to those of the undoped DWNTs. This is, however, not the case with N-doped DWNTs prepared using NH_3 as the nitrogen source. The DWNTs (NH_3) show the highest intensity RBM band at 158 cm^{-1}, corresponding to a diameter of 1.57 nm. The slightly lower intensity bands centered at 213, 152, and 147 cm^{-1} correspond to diameters of 1.16, 1.63, and 1.69 nm, respectively. Since the nature of N-substitution as well as the nature of the defects is different in the N-doped DWNTs prepared by using NH_3 and pyridine.

Table-1
RBM frequencies of undoped and N- and B-doped doped DWNTs

DWNTs [a]	N-DWNTs (Py) [b]	N-DWNTs (NH_3) [c]	B-DWNTs [d]
RBM, cm^{-1} (dia, nm)	RBM, cm^{-1} (dia, nm)	RBM, cm^{-1} (dia, nm)	RBM, cm^{-1} (dia, nm)
338(0.73)	337(0.74)	334(0.73)	336(0.74)
252(0.98)	241(1.03)	308(0.81)	*217(1.14)
*213(1.16)	*220(1.13)	281(0.88)	**201(1.23)
199(1.25)	*214(1.16)	247(1.0)	**189(1.31)
*189(1.31)	191(1.30)	**213(1.16)	177(1.40)
175(1.42)	**160(1.55)	199(1.25)	163(1.52)
171(1.45)	**142(1.75)	191(1.30)	*151(1.64)
**158(1.57)	134 (1.85)	*158(1.57)	**130(1.91)
**143(1.73)	125(1.98)	**152(1.63)	*118(2.10)
**132(1.88)	118(2.10)	**147(1.69)	105(2.36)
113(2.20)	108(2.30)	134 (1.85)	
		107(2.32)	

* highest intensity ** medium intensity

The possible (n, m) values for the intense bands are as follows

(a) 213 [(7, 10)], 189 [(3, 15); (6, 13)], 158 [(14, 9); (19, 2)], 143 [(17 ,8)], 132 [(18, 9); (21, 5)]

(b) 220 [(4, 12)], 214 [(7, 10)], 160 [(18, 3); (6, 16)], 142 [(20, 4); (7, 18)].

(c) 213 [(7, 10)], 158 [(7, 10)], 152 [(13, 11); (12, 12)], 147 [(21, 1); (6, 18)].

(d) 217 [(1, 14)], 201 [(3, 14); (7, 11)], 189 [(3, 15)], 151 [(18, 5); (15, 9)], 130 [(16, 12)], 118 [(5, 24); (15, 16)].

The B-doped DWNTs exhibit a high proportion of large-diameter DWNTs compared to the undoped or N-doped DWNTs. The most intense RBM bands of the B-doped DWNTs are at 217, 151, and 118 cm^{-1}, corresponding to diameters of 1.14, 1.64, and 2.1 nm, respectively. The slightly lower intensity bands centered at 201, 189, and 130 cm^{-1}

correspond to diameters of 1.23, 1.31, and 1.91 nm, respectively. Due to a cutoff filter, the peaks below 100 cm^{-1} were not detected.

The diameters of the various DWNTs calculated from the RBM modes are comparable with those obtained from the TEM images, but the larger diameter nanotubes seen in the TEM images are not registered in the Raman spectra since the RBM modes below 100 cm^{-1} could not be recorded by us. We can identify DWNT pairs by taking the difference between the inner and outer diameters to be around 0.7 nm. The frequencies (cm^{-1}) of such pairs of the RBM bands in the case of undoped DWNTs are (252,143), (213,132), and (189,113). The metallic (m) and semiconducting (s) natures of these pairs are respectively (s,m), (m,m) or (m,s), and (m,s) or (s,s). In the N-doped DWNTs (py), the pairs are (241,142), (214,125), (220,134), and (160,108), and they are (s,s), (m,s), (s,s), and (m,m) or (m,s), respectively.

For N-doped DWNTs (NH_3), the pairs are (281,158), (247,147), (213,134), and (152,107), and these pairs are respectively (s,s), (s,s) or (s,m), (m,s), and (m,m) or (m,s) or (s,m) or (s,s). In the B-doped DWNTs, the pairs are (217,130), (177,118), (189,118), and (151,105), and these pairs are (s,s), (m,s) or (s,s), (m,s), and (m,m) or (m,s) or (s,m) or (s,s), respectively. Taking the semiconducting and metallic nature of all the RBM bands, the ratio of semiconductor to metallic nanotubes in the case of undoped DWNTs works out to be 2:1, while it is 2:1, 2.2:1, and 2:1, respectively, in the case of N-doped DWNTs (py), N-doped DWNTs (NH_3), and B-doped DWNTs. Thus, the RBM modes predict a greater proportion of semiconducting nanotubes in the doped DWNTs as well.

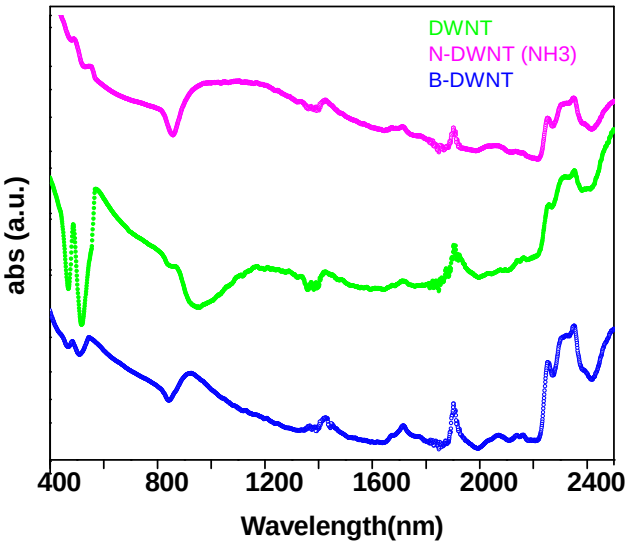

Fig. 4.8 Electronic absorption spectra of undoped and doped DWNTs

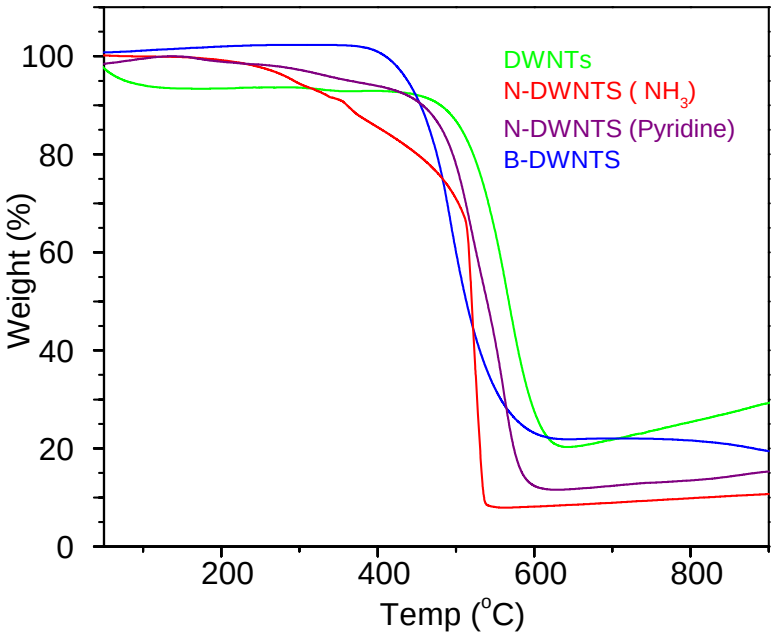

Fig. 4.9 TGA curves of undoped and doped DWNTs

The electronic absorption spectra of undoped as well as doped DWNTs (Fig. 4.8) show bands in the 900–1200 nm region due to overlapping $E_{22}{}^{s}$ (s = semiconductor) features of the outer tubes and $E_{11}{}^{s}$ of inner tubes [48]. The absorption bands in the 1600–2400 nm regions are due to $E_{11}{}^{s}$ of the outer tubes. The absorption bands due to $E_{11}{}^{m}$ (m = metal) of the outer tubes are found in the 400–600 nm region. The metallic feature seems to be prominent in the undoped DWNTs. Accordingly, the 1540 cm^{-1} G^{+}-band in the Raman spectrum is less prominent in the doped nanotubes.

The smaller diameter carbon nanotubes are known to be less stable than their larger diameter counterparts and tend to oxidize at lower temperatures. Amorphous carbon and carbon nanotubes with defects undergo combustion at lower temperatures. In Fig. 4.9, we show the thermogravimetric analysis (TGA) curves of undoped as well as B- and N-doped DWNTs. The decomposition temperatures of all these doped DWNTs are comparable to but slightly lower that the decomposition temperature of pure DWNTs. Derivative TGA curves also shows the same trend. The slight increase in mass at high temperature may be due to the small metallic impurity.

4.4.2 Functionalization of double-walled carbon nanotubes

Covalent functionalization of DWNTs was carried out by the amidation reaction employing the standard procedure [2, 30, 32]. In Fig. 4.10 (a), we show the infrared spectra of DWNTs at various stages of the functionalization process. After acid treatment, DWNTs show a carbonyl

stretching band at 1720 cm^{-1} due to the presence of carboxyl groups. On functionalization with dodecylamine, the -C=O stretching band red shifts due to amide formation, in addition giving rise to -C-H and -N-H stretching bands around 2800 and 3400 cm^{-1} respectively and the CH_2 bending bond appear around 1420 cm^{-1}. Raman spectroscopy is highly useful to characterize DWNTs [44]. Fig. 4.10 (b) shows the Raman spectra of DWNTs in the radial breathing modes (RBM) region at various stages of the functionalization process. Pure DWNTs show the RBM bands, in the 170-350 cm^{-1} region due to the inner wall tube breathing modes and bands below 170 cm^{-1} due to the outer tubes. The RBM bands of the inner tubes are affected only slightly on acid treatment and after amidation. The RBM bands of the outer tubes are, however, suppressed significantly after amidation as can been seen from Fig. 4.10 (b). Thus, the inner wall RBM bands of pure DWNTs are at 189 and 213 cm^{-1}, which are shifted to 185 and 210 cm^{-1} respectively with acid treatment, and to 186 and 210 cm^{-1} respectively after amidation. There is a shift in the G band in Raman spectrum from 1575 cm^{-1} (pure DWNTs) to 1584 cm^{-1} after amidation. The D band shifts from 1310 to 1323 cm^{-1} after amidation with a slight increasing in intensity.

The amide functionalized DWNTs are dispersible in various organic solvents. In Fig. 4.11 (a), we show photographs of the dispersions of amide-functionalized DWNTs in dichloromethane and tetrahydrofuran. In Fig 4.12 (b), we show a TEM image of DWNTs after covalent functionalization. The images are not as sharp after functionalization as in the case of pristine nanotubes (Fig. 4.12 (a)), and the bundles seem to be intact. However, the

images also revealed that the nanotube structure in not disturbed by functionalization.

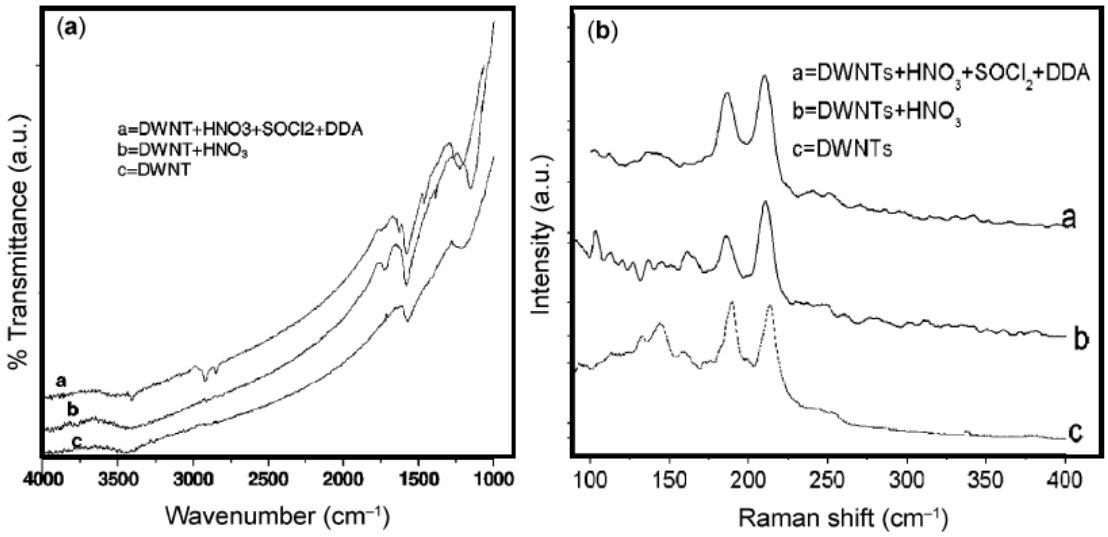

Fig. 4.10 (a) Infrared spectra of DWNTs at various stages of covalent functionalization process through amidation. (b) Raman spectra showing the RBM bands of DWNTs at various stages of functionalization.

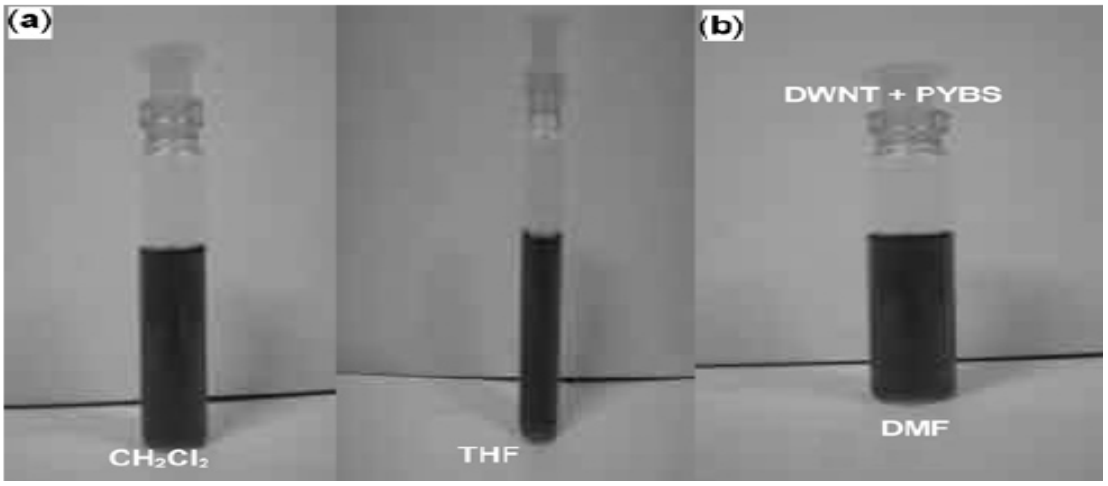

Fig. 4.11 Photographs of vials containing the dispersions of DWNTs in various solvents: (a) amide-functionalized DWNTs, (b) PYBS functionalized DWNTs.

Non-covalent functionalization of DWNTs was carried out by various ways. First, we used 1-pyrenebutanoicacid succinimidylester (PYBS) to functionalize DWNTs. This reagent has been used to functionalize SWNTs

[27]. We observe a shift of the G band in the Raman spectrum from 1575 cm^{-1} (pure DWNT) to 1588 cm^{-1} after treatment with PYBS. The D band shifts from 1310 to 1322 cm^{-1} after treatment with PYBS accompanied by an increase in intensity. PYBS-functionalized DWNTs are readily dispersible in dimethylformamide as shown in Fig. 4.11 (b). That the nanotubes features are retained after functionalization is revealed by the TEM images in Fig. 4.12 (c). We notice debundling of the DWNTs after non-covalent functionalization with PYBS.

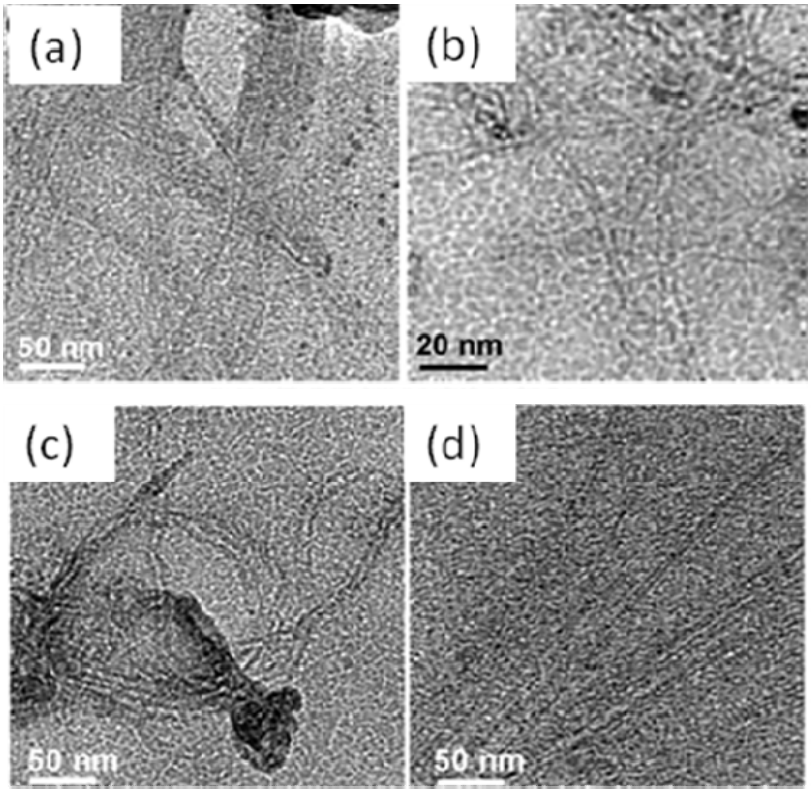

Fig. 4.12 TEM images of DWNTs (a) after covalent functionalization through amidation and (b, c and d) after non-covalent functionalization with PYBS, PEG and IGPAL respectively.

DWNTs could be non-covalently functionalized by using polyethyleneglycol (PEG) as well. Fig. 4.13 (a) shows the Raman spectrum of DWNTs at various stages of the functionalization process. The inner wall

RBM bands at 189 and 213 cm^{-1} of pure DWNTs are shifted to 186 and 211 cm^{-1} after treatment with PEG. The G band of pure DWNTs at 1575 cm^{-1} is shifted to 1581 cm^{-1} after treatment with PEG, while the D band shifts from 1310 to 1322 cm^{-1} accompanied by an increase in intensity. Thus, the RBM bands of inner tubes shift slightly on acid treatment and on further treatment with PEG. The intensities of the RBM bands of the outer tubes, however, get suppressed significantly on functionalization with PEG (Fig. 4.13 (a)). PEG-functionalized DWNTs are dispersible in water as shown in Fig. 4.14 (a). The TEM image of the DWNTs after non-covalent functionalization by PEG is shown in Fig. 4.12 (d). The image shows debundling of the nanotubes.

We have also used polyoxyehylene(40)nonylphenyl ether (IGPAL) to non-covalently functionalize DWNTs. Fig. 4.13 (b) shows the RBM bands of DWNTs before and after functionalization with IGPAL. The RBM bands of the inner walls shift from 189 and 213 cm^{-1} to 185 and 208 cm^{-1} respectively with small changes in intensity after functionalization. The RBM band intensities of the outer walls get suppressed on functionalization. However, when compared to covalent functionalization, the outer wall RBM intensities are not as much affected. Decreasing intensity of the bands below 170 cm^{-1} in functionalzed DWNTs, on the other hand, that external nanotubes were functionalized since a modification of their walls changes their electronic structure and therefore the resonance condition which determines the RBM intensities. There is no shift of the G band where as the D band shifts from 1310 to 1318 cm^{-1} with a slight increase in intensity after functionalization. IGPAL-functionalized DWNTs are dispersible in water are shown in Fig. 4.14

(b). In Fig. 4.12 (e), we show the TEM images of DWNTs after functionalization with IGPAL. The dispersions were found to be stable even after keeping it for 7 days. From the TEM images, we notice significant debundling of the DWNTs after functionalization with IGPAL.

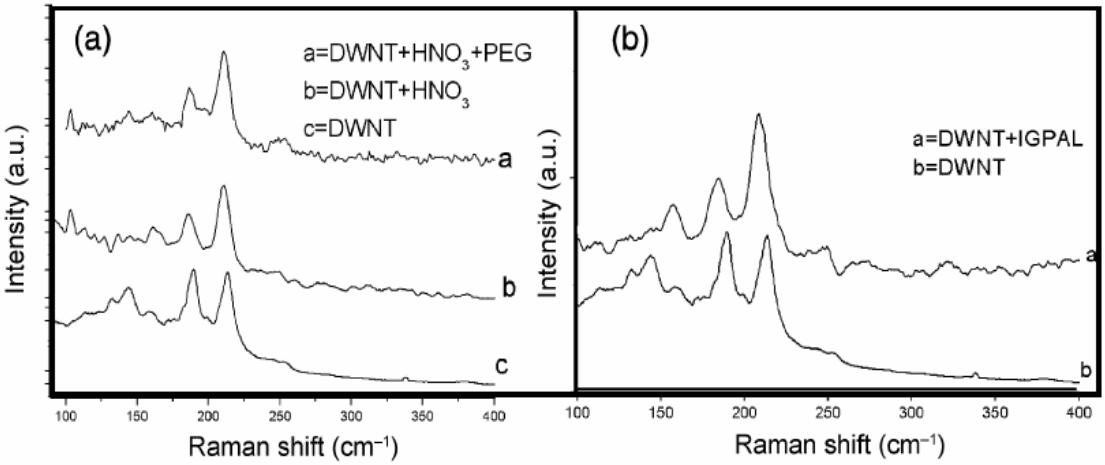

Fig. 4.13 Raman spectra showing the RBM bands of pure and functionalized DWNTs at various stages: (a) with PEG and (b) with IGPAL.

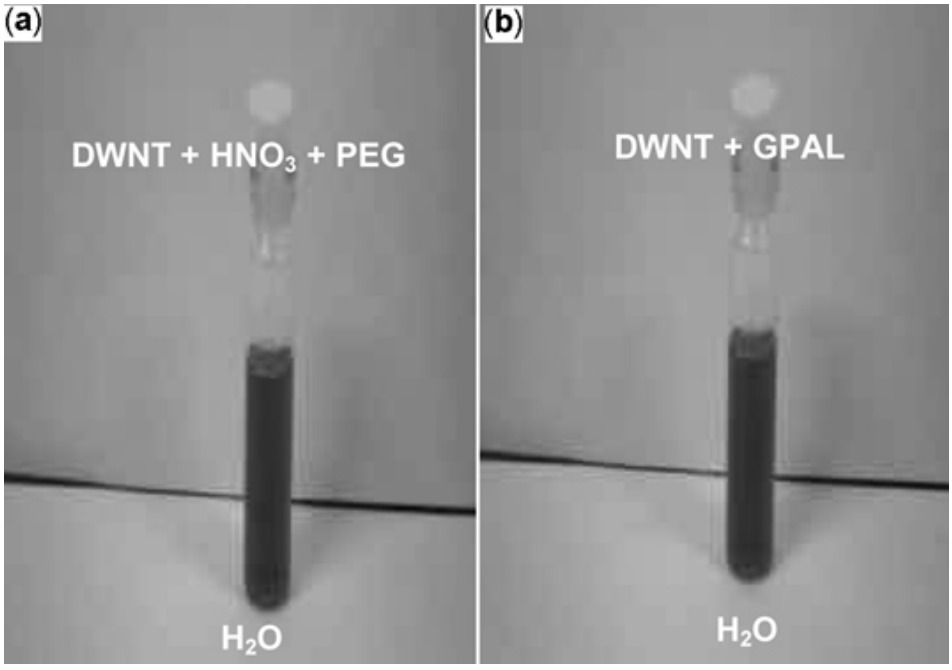

Fig. 4.14 Photographs of vials containing the dispersions of functionalized DWNTs: (a) with PEG in water, (b) with IGPAL in water.

4.5 Conclusions

In conclusion, the $Mo_{0.1}Fe_{0.9}Mg_{13}O$ catalyst prepared by the combustion route preferentially yields DWNTs, the proportion of SWNTs being very small or negligible. The use of this catalyst has enabled the synthesis of 1 atom % B- and N-doped DWNTs. The diameters of the nanotubes obtained from the Raman RBM modes and transmission electron microscopy are comparable. The N-doped nanotubes show the G-band in the Raman spectrum at a lower frequency than the undoped ones, while the B-doped nanotubes show an increase in the frequency. The proportion of the metallic nanotubes appears to decrease on B- or N-doping, but the average diameter is substantially larger in the B-doped DWNTs.

It has been possible to carry out covalent as well as non-covalent functionalization of DWNTs to enable solubilization in various solvents. Covalent functionalization affects only the outer nanotube walls of DWNTs, leaving the inner tube intact as revealed by Raman pectroscopy. Solubilization of DWNTs in non-polar solvents has been achieved through covalent as well as non-covalent functionalization. Non-covalent functionalization of DWNTs with surfactants helps to debundle the nanotubes. The nanotube structure is retained in the dispersions of DWNTs in both non-polar and aqueous media as revealed by Raman spectroscopy and transmission electron microscopy.

References

[1] H . Dai, A. Rinzler, P. Nikolaev, A. Thess, D. Colbert, R. Smalley *Chem. Phys. Lett.* **1996**, 260, 471.

[2] C. N. R. Rao, A. Govindaraj in Nanotubes and Nanowires, The RSC Nanoscience & Nanotechnology series, RSC Publishing: Cambridge, UK, **2005**.

[3] H. Kurachi, S. Uemura, J. Yotani, T. Nagasako, H. Yamada, T. Ezaki, T. Maesoba, R. Loutfy, A. Moravsky, T. Nakazawa, Y. Saito in, Proceedings of the 21st International Display Research Conference in conjunction with the 8th International Display Workshops, **2001**; pp 1237_1240.

[4] R. Saito, R. Matsuo, T. Kimura, G. Dresselhaus, M. S. Dresselhaus *Chem. Phys. Lett.* **2001**, 348, 187.

[5] T. Sugai, H. Yoshida, T. Shimada, T. Okazaki, H. Shinohara *Nano Lett.* . **2003**, 3, 769.

[6] Y. D. Lee, H. J. Lee, J. H. Han, J. E. Yoo, Yun-Hi Lee, J. K. Kim, S. Nahm, B.-K. Ju *J. Phys. Chem. B* **2006**, 110, 5310.

[7] B. C. Liu, S. C. Lyu, T. J. Lee, S. K. Choi, S. J. Eum, C. W. Yang, C. Y. Park, C. J. Lee *Chem. Phys. Lett.* **2003**, 373, 475.

[8] S. C. Lyu, T. J. Lee, C. W. Yang, C. J. Lee *Chem. Comm.* **2003**, 1404.

[9] S. C. Lyu, B. C. Liu, S. H. Lee, C. Y. Park, H. K. Kang, C-W Yang, C. J. Lee *J. Phys. Chem.B.* **2004**, 108, 2192.

[10] S. C. Lyu, B. C. Liu, C. J. Lee, H. K. Kang, C.-W. Yang, C. Y. Park *Chem. Mater.* . **2003**, 15, 3951.

[11] J. Wei, L. Ci, B. Jiang, Y. Li, X. Zhang, H. Zhu, C. Xua, D. Wua *J. Mater. Chem.* **2003**, 13, 1340.

[12] W. Ren, H.-M. Cheng *J. Phys. Chem. B*. **2005**, 109, 7169.

[13] A. Hassanien, M. Tokumoto, Y. Kumazawa, H. Kataura, Y. Maniwa, S. Suzuki, Y. Achida *Appl. Phys. Lett.* . **1998**, 73, 3839.

[14] R. Sen, B. C. Satishkumar, A. Govindaraj, K. R. Harikumar, M. K. Renganathan, C. N. R. Rao *J. Mater. Chem.* **1997**, 7, 2335.

[15] R. Sen, B. C. Satishkumar, A. Govindaraj, K. R. Harikumar, G. Raina, J. -P. Zhang, A. K. Cheetham, C. N. R. Rao *Chem. Phys. Lett.* **1998**, 287.

[16] M. Nath, B. C. Satishkumar, A. Govindaraj, C. P. Vinod, C. N. R. Rao *Chem. Phys. Lett.* **2000**, 322, 333.

[17] F. Villalpando-Paez, A. Zamudio, A.L. Elias, H. Son, E.B. Barros, S.G. Chou, Y.A. Kim, H. Muramatsu, T. Hayashi, J. Kong, H. Terrones, G. Dresselhaus, M. Endo, M. Terrones, M. S. Dresselhaus *Chem. Phys. Lett.* . **2006**, 424, 345.

[18] B. C. Satishkumar, A. Govindaraj, K. R. Harikumar, J. -P Zhang, A. K. Cheetham, C. N. R. Rao *Chem. Phys. Lett.* **1999**, 300, 473.

[19] K. McGuire, N. Gothard, P. L. Gai, M. S. Dresselhaus, G. Sumanasekera, A. M. Rao *Carbon*. **2005**, 43, 219.

[20] J.-C. Charlier, M. Terrones, M. Baxendale, V. Meunier, T. Zacharia, N. L. Rupesinghe, W. K. Hsu, N. Grobert, H. Terrones, G. A. J. Amaratunga *Nano Lett.* **2002**, 2, 1191.

[21] R.B. Sharma, D.J. Late, D.S. Joag, A. Govindaraj, C.N.R. Rao *Chem. Phys. Lett.* . **2006**, 428, 102.

[22] R. Czerw, M. Terrones, J.-C. Charlier, X. Blase, B. Foley, R. Kamalakaran, N. Grobert, H. Terrones, D. Tekleab, P. M. Ajayan, W. Blau, M. Rühle, D. L. Carroll *Nano Lett.* **2001**, 1, 457.

[23] S. Y. Kim, J. Lee, C. W. Na, J. Park, K. Seo, B. Kim *Chem. Phys. Lett.* **2005**, 413, 300.

[24] Dresselhaus M S, D. G, A. P, Carbon Nanotubes: Synthesis, Properties and Applications, Springer, , Berlin, **2001**.

[25] Niyogi S, Hamon M A, Hu H, Zhao B, Bhowinik E, Sen R, Itkis M E, H. M. E *Acc. Chem. Res.* **2002**, 35, 1105.

[26] Feazell R P, Nakayama-Ratchford N, D. H, L. S. J *J. Am. Chem. Soc.* **2007**, 129, 8438.

[27] Chen R J, Zhang Y, Wang D, D. H *J. Am. Chem. Soc.* **2001**, 123, 3838.

[28] Liu J, Rinzler A G, Dai H, Hafner J H, Bradley R K, Boul P J, Lu A, Iverson T, Shelimov K, Huffman C B, R-Macias F, Shon Y-S, Lee T R, C. D. T, S. R. E *Science*. **1998**, 280, 1253.

[29] Boul P J, M. E. T. Liu J, Huffman C B, Ericson L M, Chiang I W, Smith K A, Colbert D T, Hauge R H, M. J. L, S. R. E *Chem. Phys. Lett.* **1999**, 310, 367.

[30] Chen J, Hamon M A, Hu H, Chen Y, Rao A M, Eklund P C, H. R. C *Science* **1998**, 282 95.

[31] Grunian J C, Liu L, K. Y. S *Nano Lett.* **2006**, 6, 911.

[32] Hamon M A, Chen J, Hu H, Chen Y, Itkis M E, Rao A M, Eklund P C, H. R. C *Adv. Mater.* **1999**, 11, 834.

[33] J. C. G. Jeynes, E. Mendoza, D. C. S. Chow, P. C. P. Watts, J. McFadden, S. R. P. Silva *Adv. Mater.* **2006**, 18, 1598.

[34] Nakayama-Ratchford N, Bangsaruntip S, Sun X, Welsher K, D. H *J. Am. Chem.. Soc.* **2007**, 129, 2448.

[35] A. Star, D.W.Steuerman, J. R. Heath, J. F. Stoddart *Angew. Chem. Int. Ed.* **2002**, 41, 2508.

[36] A. K. Bhalchandra, K. P. Vijayamohanan *Applied Surface Science*. **2008**, 254, 4936.

[37] K. Balasubramanian, M. Burghard *J. Mater. Chem.* . **2008**, 18, 3071.

[38] B. A. Kakade, V. K. Pillai *J. Phys. Chem. C*. **2008**, 112, 3183.

[39] V. N. Khabashesku, W. E. Billups, J. L. Margrave *Acc. Chem. Res.* **2002**, 35, 1087.

[40] J. Liu, P. Liang, H.-Y. Zhang, D. Guo *Small* **2006**, 2, 874.

[41] K. C. Patil *Bull. Mater. Sci.* . **1993**, 16, 533.

[42] E. Flahaut, A. Peigney, W. S. Bacsa, R. R. Bacsa, C. Laurent *J. Mater. Chem.* **2004**, 14, 646.

[43] S. R. C. Vivekchand, A. Govindaraj, Md. Motin Seikh, C. N. R. Rao *J. Phys. Chem. B*. **2004**, 108, 6935.

[44] M. S. Dresselhaus, P. C. Eklund *Advances in Physics*. **2000**, 49, 705.

[45] Q. H. Yang, P. X. Hou, M. Unno, S. Yamauchi, R. Saito, T. Kyotani *Nano Lett.* **2005**, 5, 2465.

[46] A. Das, A. K. Sood, A. Govindaraj, A. M. Saitta, M. Lazzeri, F. Mauri, C. N. R. Rao *Phys. Rev. Lett.* . **2007**, 99, 136803.

[47] F. Li, S. G. Chou, W. Ren, J. A. Gardecki, A. K. Swan, M. S. Unlu, B. B. Goldbeg, H-M. Cheng, M. S. Dresselhaus *J. Mater. Res.* . **2003**, 18, 1251.

[48] N. Kishi, S. Kikuchi, P. Ramesh, T. Sugai, Y. Watanabe, H. Shinohara *J. Phys. Chem. B.* **2006**, 110, 24816.

Chapter-5

Boron- and Nitrogen-doped Graphene

Summary*

This chapter deals with the synthesis, characterization, properties and applications of nitrogen- and boron-doped graphene. The chapter is divided into three parts. The first part of the chapter deals with the novel synthesis and characterization of boron- and nitrogen-doped graphene, whereas the second and third parts deal with field emission and sensor properties of doped graphene respectively.

Substitutional doping, universally used in tuning the properties of semiconductors, could be a powerful tool to control the electronic properties of graphene. Here, we present the structure and properties of boron and nitrogen doped graphenes, obtained by more than one method involving arc discharge in appropriate gaseous atmosphere, by using modified graphite electrode or by the transformation of nano-diamond. We demonstrate systematic changes in the carrier-concentration and electronic structure of graphenes with B/N-doping, accompanied by stiffening of the G-band and

*Papers based on these studies have appeared in Adv. Mater. (2009), Appl. Phys. Lett. (2010) and J. Exp. Nanosci. (2009).

intensification of the defect related D-band in the Raman spectra. Both boron and nitrogen doped samples exhibit higher electrical conductivity than the undoped graphene

Field emission studies have been carried out on undoped as well as N- and B-doped graphene samples. These graphene samples exhibit very low turn-on fields. N-doped graphene shows the lowest turn-on field of 0.6 V/μm, corresponding to emission current density of 10μA/cm^2. These characteristics are superior to the other types of nanomaterials reported in the literature. Furthermore, emission currents are stable over the period of more than 3hrs for the graphene samples. The observed emission behavior has been explained on the basis of nanometric features of graphene and resonance tunneling phenomenon.

Sensing characteristics of NO_2 have been investigated with graphene samples doped with boron and nitrogen. Nitrogen-doped graphene (n-type) shows increased sensitivity for NO_2 compared with pure graphene as well as that of boron-doped graphene.

5.1 Introduction

Graphene has emerged to become an exciting material today because of the novel properties associated with its two-dimensional structure [1-3]. The remarkable feature of graphene is that it is a Dirac solid, with the electron energy being linearly dependent on the wave vector near the vertices of the hexagonal Brillouin zone. It exhibits room-temperature fractional quantum Hall effect [4] and ambipolar electric field effect along with ballistic conduction of charge carriers [2]. Substitutional doping in carbon materials brings marked changes in their properties which make them suitable for desired applications as evidenced in the case of carbon nanotubes [chapter 4]. It is appropriate to assume that significant changes would occur in graphene on chemical doping by boron and nitrogen.

5.2 Scope of the present investigations

5.2.1 B- and N-doped graphenes

Doping has been achieved in graphene by different ways. It has been reported recently that a top-gated single layer-graphene transistor is able to reach electron or hole doping levels of upto $5x10^{13}$ cm^{-2}. The doping effects are ideally monitored by Raman spectroscopy [5-11]. Thus, the G band in the Raman spectrum stiffens for both electron and hole doping and the ratio of the intensities of the 2D and G band varies sensitively with doping. Doping graphene through molecular charge-transfer caused by electron-donor and -acceptor molecules also gives rise to significant changes in the

electronic structure of few-layer graphenes, as evidenced by changes in the Raman and photoelectron spectra [6, 7]. Charge-transfer by donor and acceptor molecules softens and stiffens the G band respectively. The difference between electrochemical doping and doping through molecular charge transfer is noteworthy. It is of fundamental interest to investigate how these effects can be compared with the effects of doping graphene by substitution with boron and nitrogen and to understand dopant-induced perturbations on the properties of graphene. Secondly, opening of the band-gap in graphene is essential to facilitate its applications in electronics and graphene bilayers [12] are an attractive option for this. With this motivation, we have prepared, for the first time, B- and N-doped graphene bilayer samples employing different strategies and investigated their structure and properties.

5.2.2 Field emission from graphene and B- and N-doped graphenes

Electron sources are becoming increasingly important for use in both research and technological applications. While conventional thermoelectronic emitters seem to be declining in importance, cold electron emitters using field emission are showing great potential for several applications. Amongst the numerous nanomaterials, electron field emission cathodes based on carbon nanocrystalline materials are being extensively investigated for high current density applications [13-16]. Thus, carbon nanotubes and nanofibres have been frequently used for fabricating field emission cathodes because of their high aspect ratios as well as unique

mechanical and electronic properties. These materials exhibit low turn-on voltages and large emission current densities [17, 18]. Most recently, graphene, the two-dimensional nanocarbon has attracted great attention because of its exceptional properties [19, 20]. In addition to the possible applications in ultra high-speed nanoelectronics [21], graphene promises to be useful in chemical and biosensors [22, 23] appliances. There have been attempts to investigate field emission properties of graphene films recently [24-26]. A spin-coated graphene film is reported to exhibit a threshold field (for a current of 10^{-8} A/cm^2) of 4 V/μm with a field enhancement factor, β, of 1200 [24]. A few-layer graphene film synthesized by chemical vapor deposition exhibits a favorable turn-on field but decays after five cycles, the turn-on field shifting to 3 V/μm and β decreasing to 3000 [25]. Use of electrophoretic deposition appears to lower the turn-on voltage [26]. Besides geometrical factors and spatial distribution, tailoring the work function provides another means to improve the electron field emission. Theoretical studies have shown that substitutional doping can modulate the band structure of graphene [27, 28]. We have carried out a careful investigation of the field emission properties of undoped, as well as boron- and nitrogen-doped graphenes.

5.2.3 Gas sensing properties of doped graphene

Several nanomaterials show good sensor characteristics. Selectivity, however, is a major problem in most cases. One way of achieving selectivity is by synthesizing materials which can interact with adsorbents selectively.

It has been demonstrated theoreticaly [29] and experimentaly [30] that no charge-transfer occurs between CO and pure MWNTs. However, calculations suggest the possibility of using doped MWNTs for sensing purposes [31]. Villalpando-Paez *et al.* [32] designed a NH_3-sensitive device utilizing nitrogen-doped MWNTs. CN_x nanotubes could, therefore, be more efficient in detecting hazardous gaseous species because of the presence of pyridine-type sites on their surface.

Gas sensor characteristics of various nanostructures have been investigated in the past few years [33-35]. Thus, many metal oxide nanostructures show good sensing characteristics for gases, such as NO_2, NH_3, hydrocarbons and ethanol [33-42]. Semiconducting CNTs can be used for detecting a very small concentration of NH_3, NO_2 and other gases [43, 44]. Recent studies on the interaction of graphene with gas molecules have indicated that it can act as a good sensor [45, 46]. Schedin et al. [47] have shown that the increase in the charge carrier concentration induced by gas molecules adsorbed on the surface of graphene can be used to fabricate sensitive gas sensors. On the basis of theoretical investigations on the adsorption of gas molecules on single layer graphene as well as on graphene nanoribbons, it has been predicted that the doping in carbon nanostructures may improve the sensitivity [48, 49]. Ao *et al.* have applied density functional theory to show that aluminium doped graphene can be used as a good detector for carbon monoxide [50]. Functionalized graphite nanostructures are able to sense traces of pollutant gases such as NO_2 [51]. Water vapour sensing characteristics of reduced graphene oxides have been

reported [52]. Reduced graphene oxide is also shown to be a good sensor for toxic vapours [53]. Spin-coated hydrazine-functionalised graphene dispersions are able to detect NO_2, NH_3 and 2,4-dinitrotoluene [54]. We considered it important to examine the gas sensing characteristics of nitrogen- and boron-doped graphene samples (N–HG and B–HG) with NO_2 to study the effect of doping on the gas sensing characteristics.

5.3 Experimental and related aspects

(a) Synthesis of boron-doped graphene

One set of boron-doped graphene samples (BG1) was prepared by carrying out arc discharge of graphite electrodes in the presence of hydrogen, helium and diborane (B_2H_6). B_2H_6 vapor was generated by the addition of BF_3-diethyl etherate to sodium borohydride in tetraglyme. B_2H_6 vapor was carried to the arc chamber by passing hydrogen (200 torr) through B_2H_6 generator and subsequently by passing He (500 torr). The second set of boron-doped samples (BG2) was prepared by carrying out arc discharge using boron-stuffed graphite electrodes (3 at% boron) in the presence of H_2 (200 torr) and He (500 Torr).

(b) Synthesis of nitrogen-doped graphene

One set of nitrogen-doped graphene samples (NG1) was prepared by carrying out arc discharge of graphite electrodes in the presence of H_2, He and pyridine vapor. Pyridine vapor was carried to the arc chamber by passing hydrogen (200 torr) through a pyridine bubbler and subsequently by

passing He (500 torr). The second set of nitrogen-doped samples (NG2) was prepared by carrying out arc discharge of graphite electrodes in the presence of H_2 (200 torr), He (200 torr) and NH_3 (300 torr). Transformation of nanodiamond was carried out in the presence of He and pyridine vapor at 1650 ^oC to obtain N-doped graphene (NG3).

Techniques used for characterization

Field emission scanning electron microscope (FESEM): FESEM images were recorded with a FEI NOVA NANOSEM 600.

Raman spectroscopy: Raman spectra were recorded with LabRAM HR high resolution Raman spectrometer (Horiba Jobin Yvon) using He-Ne Laser (λ=630 nm).

Transmission electron microscopy (TEM): Transmission electron microscope (TEM) images were obtained with a JEOL JEM 3010, operating with an accelerating voltage of 300 kV.

Electron energy loss spectroscopy (EELS): EELS were recorded with a transmission electron microscope (FEI, TECNAI F30) equipped with an energy filter for EELS operating at 300 kV.

Thermogravimetric analysis (TGA): Thermogravimetric analysis was carried out using a Mettler Toledo TGA 850 instrument.

X-ray photoelectron spectroscopy (XPS): X-ray photoelectron spectroscopy was recorded using a VG scientific ESCA Laboratory V spectrometer.

Atomic force microscopy (AFM): AFM measurements were performed using a NanoMan instrument.

Resistivity measurements: DC resistance measurements were carried out by the standard four-probe method using the resistivity option in the Physical Property Measurement System (PPMS), Quantum Design, USA.

Field emission measurements

Electrophoretic deposition was employed for depositing vertically oriented graphene sheets on Si substrate [55]. The graphene samples deposited on Si substrate were loaded independently on a copper stub by using conducting vacuum compatible silver paste in such a manner as to be parallel to the phosphor coated conducting glass anode screen. The distance between the cathode and anode was manipulated by using a linear mechanical drive. After mounting the sample inside the ultra high vacuum chamber, the chamber was baked at 250 ^{o}C for 10 h to achieve a base pressure of 1x10^{-8} mbar. Field emission current density–electric field (J-E) and the emission current–time stability (I-t) characteristics were measured at the same base pressure using a Keithley 6514 picoammeter and a Spellman high voltage DC power supply at room temperature. The inter electrode separation was kept at 1 mm throughout the experiments.

Preparation of sensors

The sensing devices were prepared as follows: 300 nm thick gold film was deposited on a glass substrate by thermal evaporation to make source and drain with a 15 μm separation between the electrodes. Graphene samples were dispersed in methanol using ultrasonication and 5 μL of the dispersion was dropped onto the electrodes by dielectrophoresis.

Gas sensing properties were measured using a home-built computer-controlled characterisation system consisting of a test chamber, sensor holder, a Keithley multimeter-2700, a Keithley electrometer-6517A, mass flow controllers and a data acquisition system. The test gas was mixed with N_2 to achieve the desired concentration and the flow rate was maintained using mass flow controllers. By monitoring the output voltage across the sensor, the resistance of the sensor in dry air or in the test gas can be measured. The resistance of the graphene samples increased in contact with NO_2, while the resistance decreased in contact with water and alcohol vapours. The sensitivity (response magnitude) S was determined as the ratio DR/R_{air}, where DR is the difference of resistance of the graphene sample in the presence of the test gas and in dry air, R_{air} is the resistance of the samples in dry air. The resistance of the sensors prepared by us based on graphene was in the range 0.1–15 kΩ. The response time is defined as the time required for the resistance to reach 90% of the equilibrium value after the test gas is injected and recovery time is taken as the time necessary for the sensor to attain a resistance 10% above the original value in air.

5.4 Results and discussion

5.4.1 B- and N-doped graphene

Doped graphene samples have been characterized in different ways. In Fig. 5.1 (a) and (b) we show the typical core-level X-ray photoelectron spectra (XPS) of BG1 and BG2 along with the elemental mapping from electron energy loss spectroscopy (EELS) carried out on transmission electron microscope (TEM) images. The C 1s signal is at approximately 285 eV, while the B 1s peak is around 189 eV. The position of this feature indicates that boron is bonded to carbon in the sp^2 carbon network [56]. Based on the XPS data, we found that BG1 and BG2 contain 1.2 and 3.1 at.% of boron, respectively. EELS measurements performed on the graphene nanostructures in the electron microscope indicated the content of boron in these samples to be 1.0 and 2.4 at.%, respectively. In Figures 5.2 (a) and (b) we show the typical XPS data for the NG1 and NG2 samples along with the EELS elemental mapping. The asymmetric shape of the N 1s peak indicates the existence of at least two components. On deconvolution, we found peaks at 398.3 and 400 eV, the first one being characteristic of pyridinic nitrogen (sp^2 hybridization) and the second due to nitrogen in the graphene sheets [57]. XPS data along with EELS elemental mapping of NG3 has been shown in Fig. 5.3. XPS data indicated that NG1, NG2, and NG3 contain 0.6, 1, and 1.4 at.% of nitrogen, respectively. EELS results were comparable with that of XPS results.

TEM images clearly show the presence of two to three layers in the BG and NG samples. In Fig. 5.4 a-f, we show the high-resolution electron microscopy (HREM) images of the BG1, BG2, NG1, NG2, NG3 and HG samples, respectively. In Figures 5.5 (a) and (b), we show typical atomic force microscopy (AFM) images of BG1 and NG1. The images correspond to two-layer graphenes. The AFM images generally show the presence of two to three layers in the various BG and NG samples, with the occasional presence of single layers.

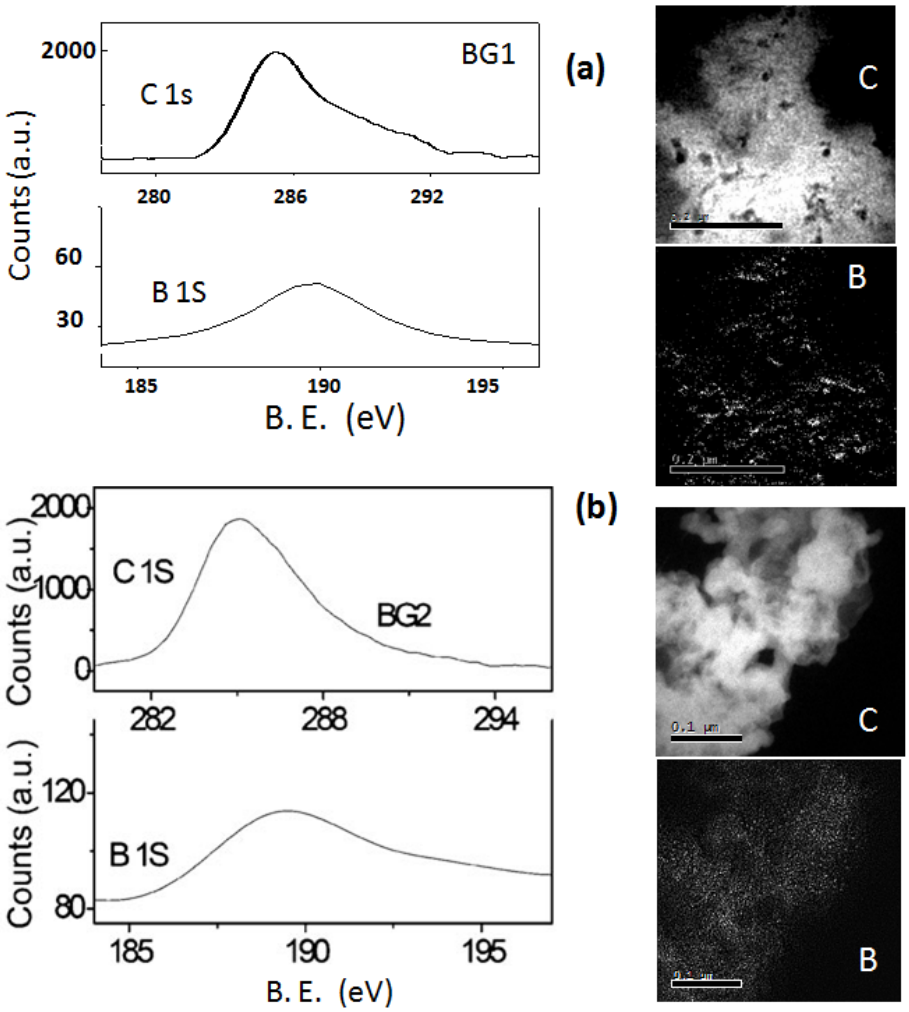

Fig. 5.1 C 1s and B 1s XPS signals along with EELS elemental mapping of C and B of (a) BG1 and (b) BG2

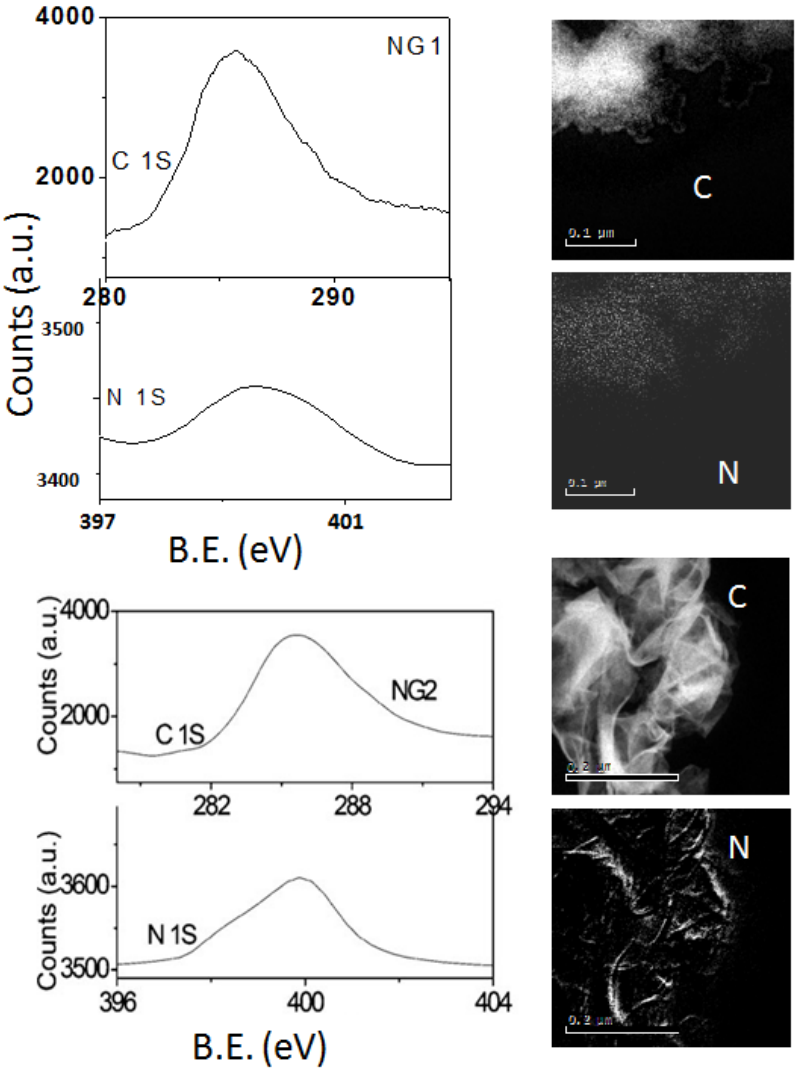

Fig. 5.2 C 1s and N 1s XPS signals along with EELS elemental mapping of C and N of (a) NG1 and (b) NG2

We examined the Raman spectra of all BG and NG samples in comparison with that of HG, i.e., pure graphene, prepared by the H_2-discharge method (Fig. 5.6). The Raman spectra (with 632.8 nm excitation) of these samples show three main features in the 1000–3000 cm^{-1} region, [5, 58] the G-band (~1570 cm^{-1}), the defect-related D-band (~1320 cm^{-1}), and the 2D-band (~2640 cm^{-1}). It is noteworthy that the G-band stiffens both with boron- and nitrogen- doping. This is similar to what happens with

electrochemical doping [5] but differs from what occurs when the doping is done by molecular charge-transfer [6, 7].

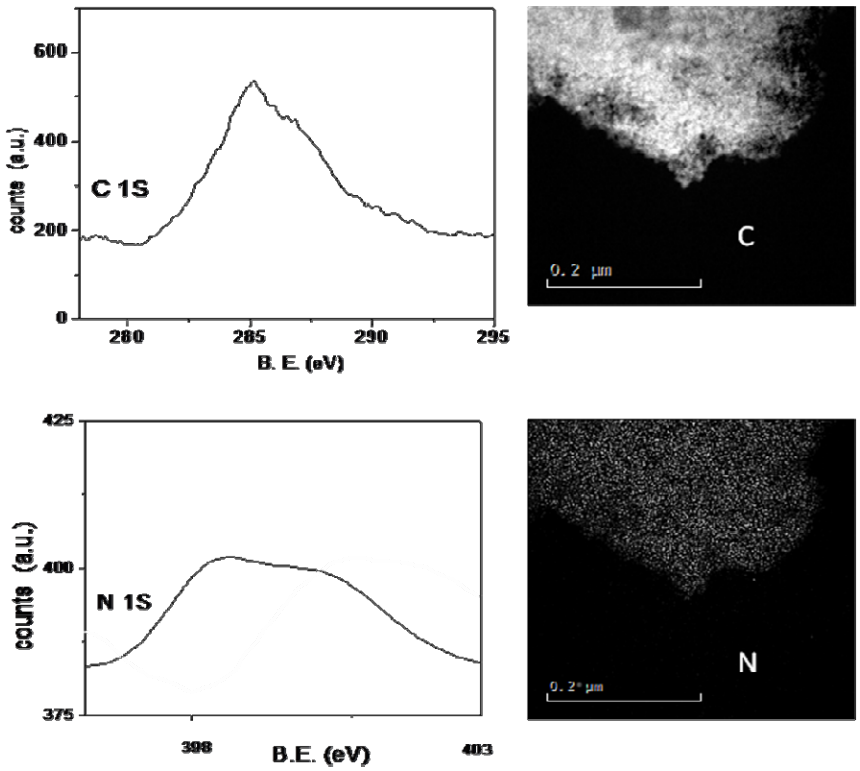

Fig. 5.3 C 1s and N 1s XPS signals along with EELS elemental mapping of C and N of NG3

The blue-shift in the case of BG2, which has a higher B-content, is larger than that of BG1. In the case of NG, the sample with the highest N content, NG3, shows the largest shift. Stiffening of the G-band arises from the nonadiabatic removal of the Kohn anomaly at the G-point, and its broadening is due to the absence of blockage of the decay channels of the phonons into electron–hole pairs [58]. The intensity of the D-band is higher with respect to that of the G-band in all doped samples. On doping, the

relative intensity of the 2D-band generally decreases with respect to that of the G-band.

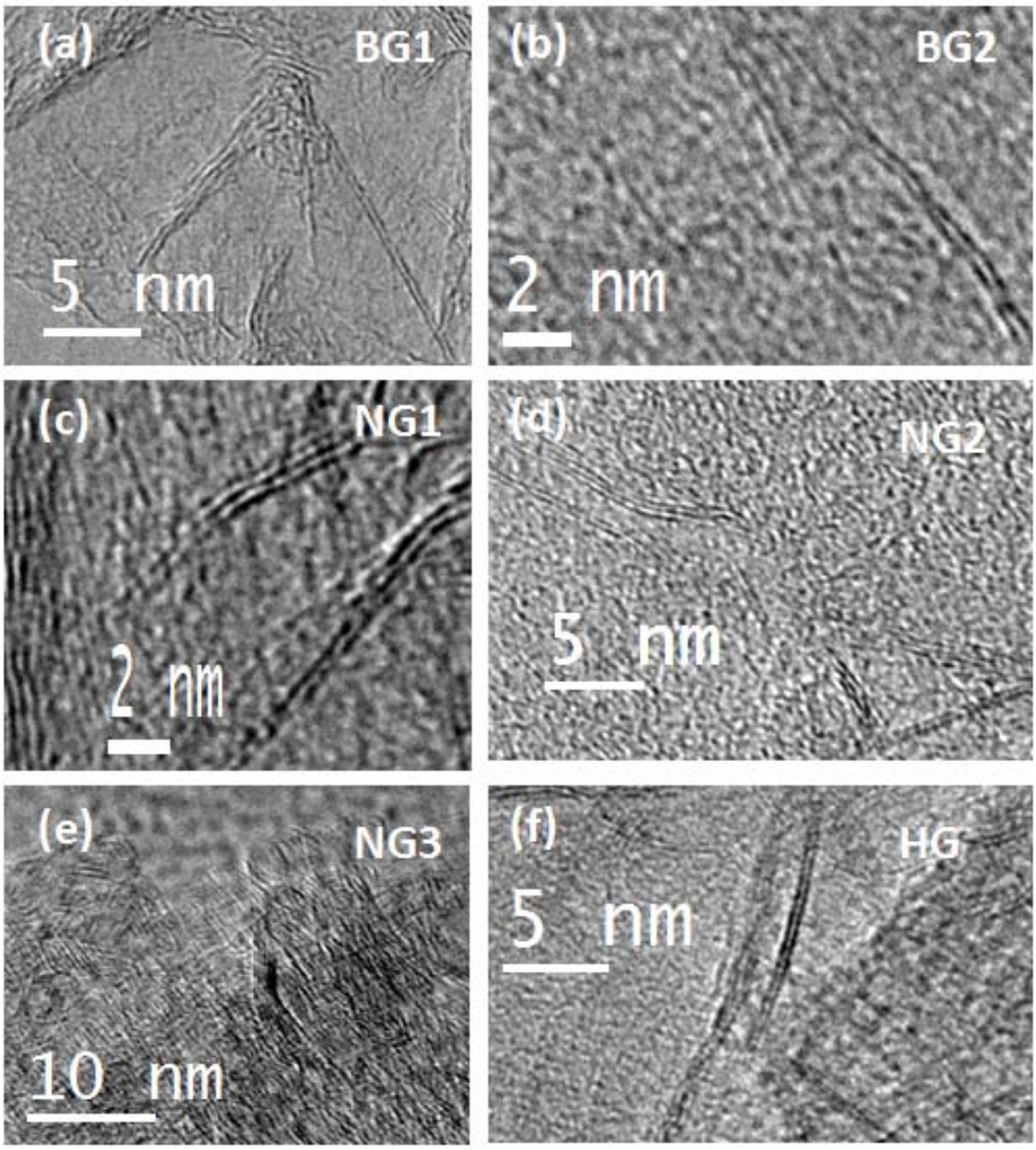

Fig. 5.4 TEM images of doped as well as pure graphene samples (a) BG1 (b) BG2 (c) NG1 (d) NG2 (e) NG3 and (f) HG

It is known that the 2D-band is sensitive to doping [5-7]. The 2D-band can also be deconvoluted to show the presence of more than one layer (2

and/or 3). The changes in the G-band and the other bands in the Raman spectra along with the XPS and EELS results mentioned earlier suggest that the dopant B- and N-atoms occur substitutionally. We calculated the in-plane crystallite sizes (La) of the undoped and doped graphene samples based on Raman data by the formula:[59]

$$L_a(nm) = (2.4 \times 10^{-10})\, \lambda^4\, (I_D/I_G)^{-1} \qquad \text{----------(1)}$$

Here, λ is the wavelength used for Raman measurements while I_D and I_G represent the intensity of the D- and G-bands, respectively. The crystallite sizes of the HG, BG1, BG2, NG1, NG2, and NG3 samples are estimated to be 64, 30, 26, 43, 41, and 19 nm, respectively. The doped graphene samples exhibit smaller crystallite sizes compared to undoped graphene.

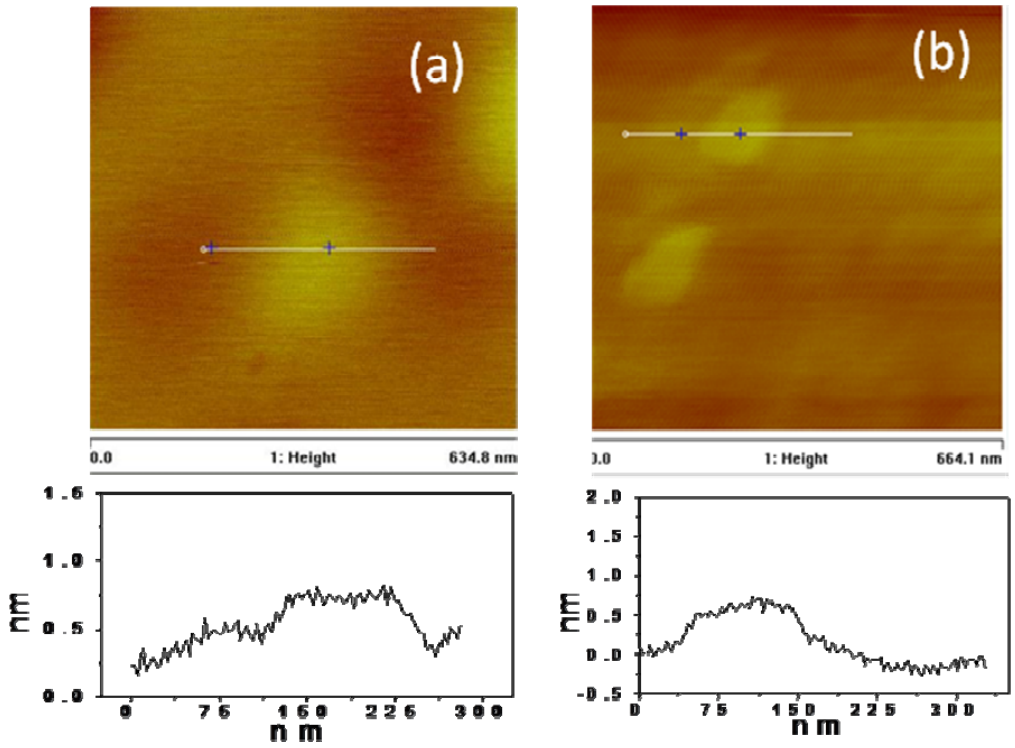

Fig. 5.5 Typical AFM images of flakes of B-and N-substituted graphenes: (a) BG1, (b) NG1

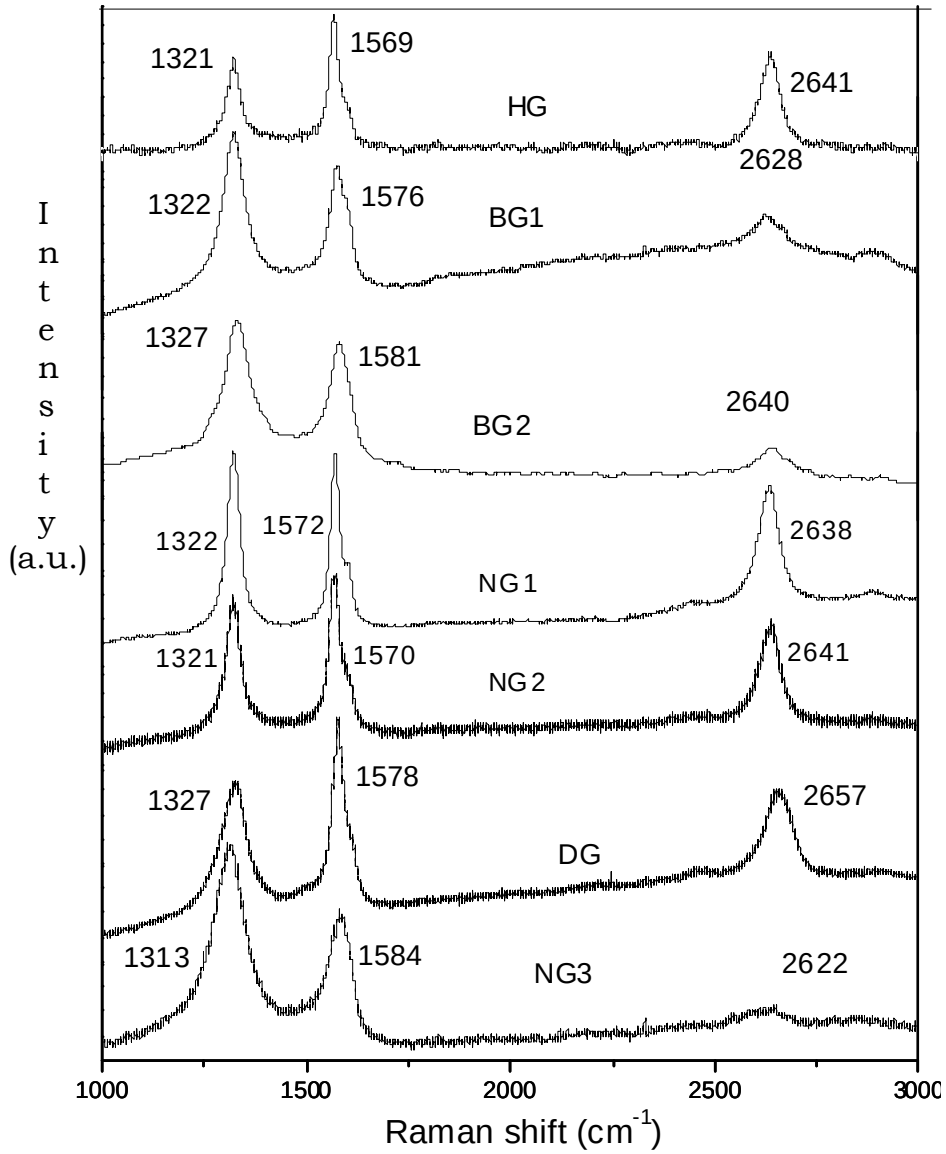

Fig. 5.6 Raman spectra of pure as well as boron and nitrogen doped graphene samples

Electrical conductivity measurements have been measured on doped graphene sampes. In Fig. 5.7, we show electrical conductivity data of BG1, NG1 and HG samples. Boron- and nitrogen-graphene samples exhibit higher electrical conductivity than the undoped graphene. Thermogravimetric analysis indicated that the BG and NG samples undergo

combustion at temperatures only slightly lower than the parent graphene (580 °C).

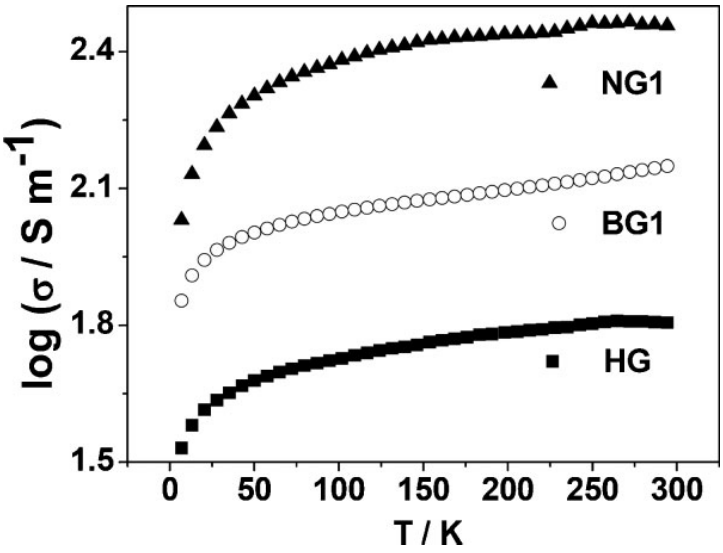

Fig. 5.7 Electrical conducting data of NG1, BG1, and pristine graphene

5.4.2 Field emission properties of B- and N-doped graphenes

We have carried out a careful investigation of the field emission properties of undoped, as well as boron- and nitrogen-doped graphenes. For this purpose, we have used graphene samples of pure, boron-doped graphene (BG1) and nitrogen doped graphene (NG1). Electrophoretic deposition was employed for depositing vertically oriented graphene sheets [55] for the electron field emission measurements. Fig. 5.8 shows field emission scanning electron microscope images of HG, BG, and NG samples obtained after deposition on Si substrate. The films are randomly oriented with high graphene density and uniform morphology. The sharp edges present function as emission sites and enhance the field emission.

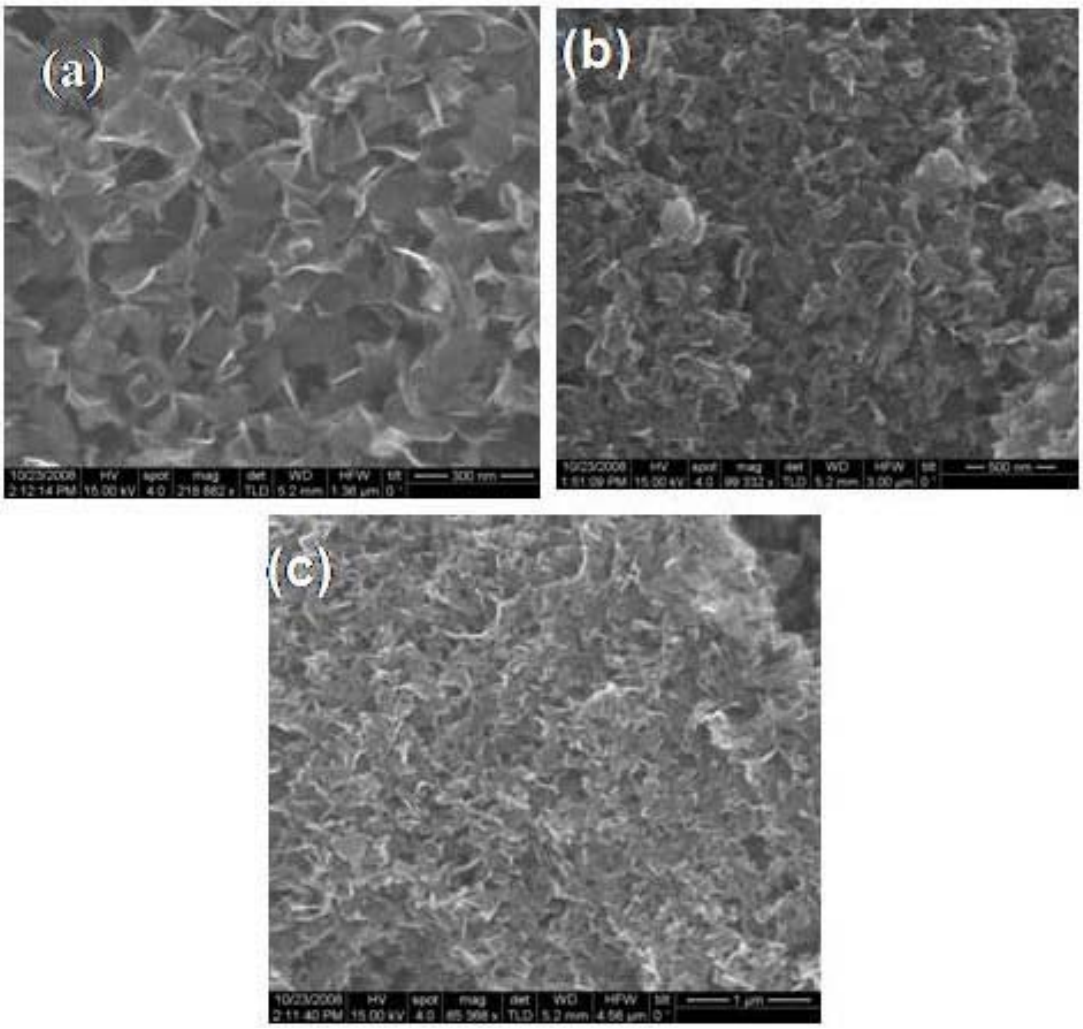

Fig. 5.8 FESEM images of (a) undoped (HG), (b) boron-doped (BG1) and (c) nitrogen-doped (NG1) graphenes obtained after electrophoretic deposition on Si substrate

The graphene samples deposited on Si substrate were loaded independently on a copper stub by using conducting vacuum compatible silver paste in such a manner as to be parallel to the phosphor coated conducting glass anode screen. The distance between the cathode and anode was manipulated by using a linear mechanical drive. After mounting the sample inside the ultrahigh vacuum chamber, the chamber was baked at 250 °C for 10 h to achieve a base pressure of 1×10^{-8} mbar. Field emission

current density–electric field (J-E) and the emission current–time stability (I-t) characteristics were measured at the same base pressure using a Keithley 6514 picoammeter and a Spellman high voltage dc power supply at room temperature. The inter electrode separation was kept at 1 mm throughout the experiments.

Fig. 5.9 (a) shows the variation in J-E characteristics of the HG, BG, and NG samples. The turn-on electric field (defined as the field required to draw the current density of 10 $\mu A/cm^2$) is 0.7, 0.8, and 0.6 V/μm for HG, BG, and NG, respectively. As the applied voltage was increased further, the emission current density of ~ 50 $\mu A/cm^2$ was drawn at an applied field of 0.95, 1.08, and 0.99 V/μm for HG, BG, and NG, respectively. These values are found to be significantly lower than the best values reported for graphene samples [55, 60, 61], subnanometer graphite sheets [62], undoped and doped carbon nanotubes [63-65], and other semiconducting nanomaterials such as CdS aligned nanowires [66], tungsten oxide nanowires [67] and ZnO needles [68]. The smaller turn-on electric field observed by us is thus noteworthy and probably results from the unique characteristics of the graphene prepared by arc discharge in hydrogen.

The Fowler–Nordheim (FN) model of field emission originating from the study of flat metallic surfaces at 0 K is widely used in carbon based electron emitters [69]. We have used Eq. (2) to calculate the field enhancement factor, β.

$$J = A(\beta^2 E^2/\phi)\exp(-B\phi^{1.5}/\beta E) \quad (2)$$

Here, J is the emission current density, A(1.54×10^{-6} A eV/V^2) and B(6.8×10^9 eV$^{-3/2}$ V/m) are constants, Φ is the work function and is assumed to be 5 eV same as that for graphite. The FN theory is valid only for metallic emitters. In the case of semiconducting emitters, effects such as field penetration and band bending will have to be considered but there is no unified equation or theory which accounts for all these parameters for both semiconducting and metallic emitters. Hence, one uses the FN equation for the analysis of field emission data. In the present study, the FN plot is found to be nonlinear and such FN plots have been reported for many semiconducting nanomaterials [70, 71]. The nonlinearity in the FN plot can be resolved into two linear sections with distinct slopes in the high-field and low-field regions [see Fig. 5.9 (b)]. The field enhancement factors (β) are calculated from the slope of the low-field and the high-field regions of the FN plot, using the following equation,

$$\beta = (6.8 \times 10^3 \times \Phi^{3/2}) / \text{slope} \quad (3)$$

are found to be 15740, 11879, 25849 for the low-field region and 24058, 12067, 49690 for the high-field region of HG, BG, NG, respectively. These calculated values of β may be overestimates due to the limitation of the FN equation. The small turn-on field is associated with the edges of vertically oriented graphene sheets. Furthermore, N-doped graphene shows the lowest turn-on field, relative to undoped graphene. One of the reasons probably is the up-shift of the Fermi level of graphene due to N-doping. The turn on

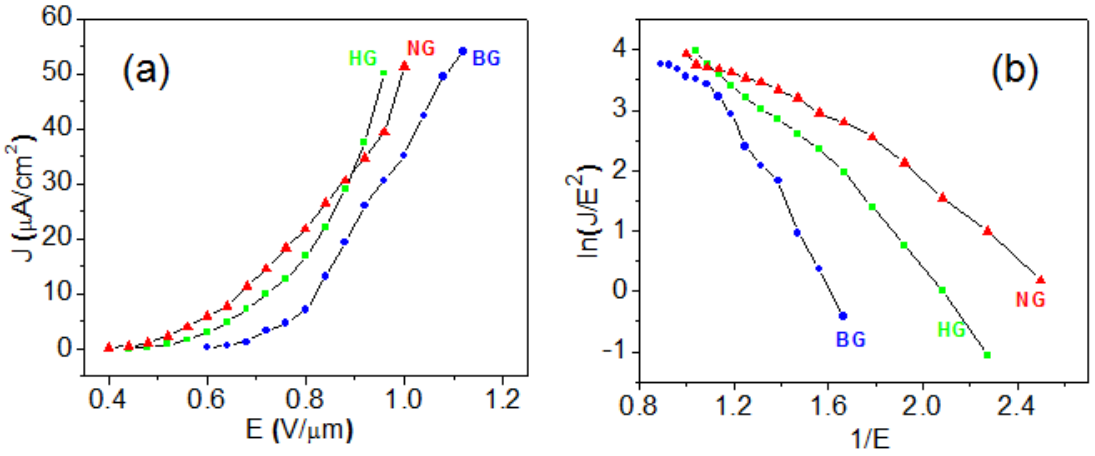

Fig. 5.9 (a) Current density (J) of undoped (HG), boron-doped (BG1) and nitrogen-doped (NG1) graphenes as a function of electric field. (b) F-N plot of HG, BG and NG graphenes.

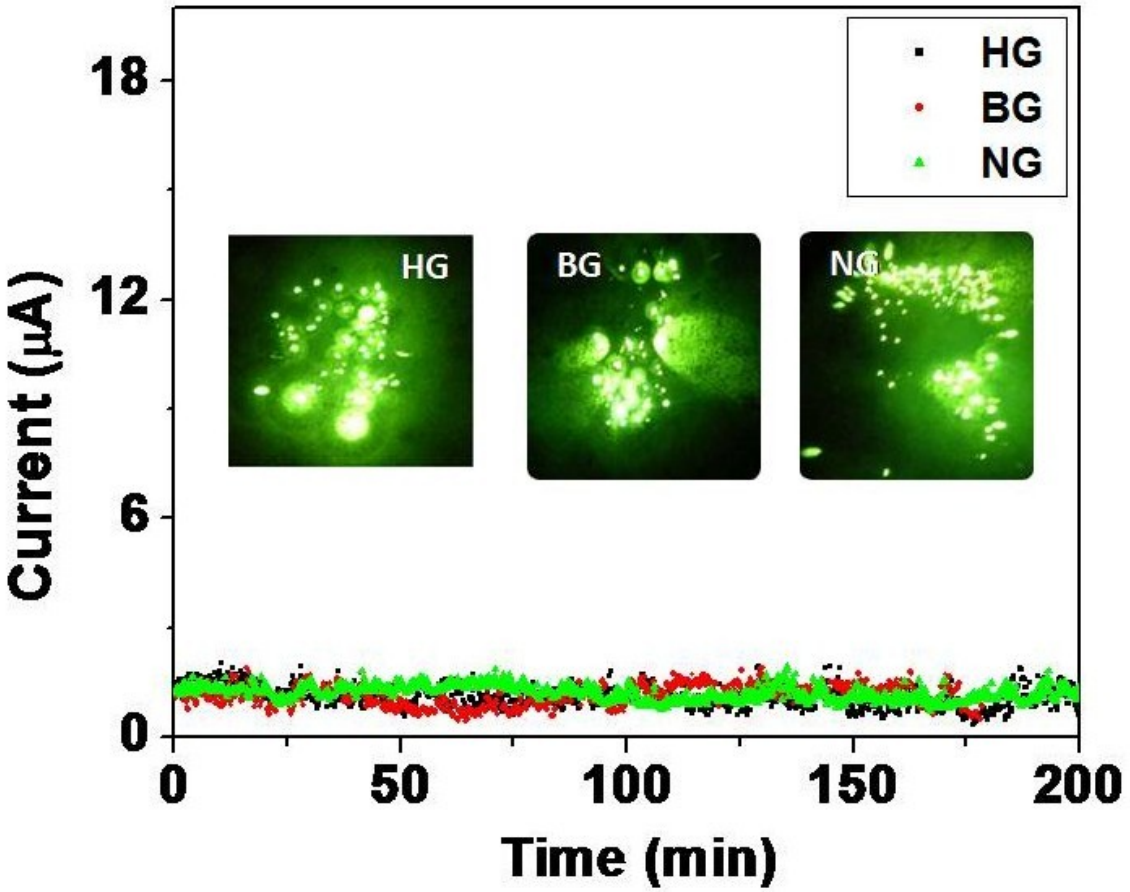

Fig. 5.10 Current stability of undoped (HG), boron-doped (BG) and nitrogen-doped (NG) graphenes (Inset field emission pattern corresponding to HG, BG and NG)

voltage depends upon the local field through β, the charge carrier density, and the type of doping (donor or acceptor). In addition to these parameters, resonance tunneling may also play a role [72]. Our field emission patterns consist of random spots, unlike emission from single graphene sheet [55] suggestive of resonance tunneling. Field emission includes transfer of electrons from the electrode to the field emitting material, and subsequently transit of electrons into the material, finally going to the vacuum. For a given material, the first and the last steps are important factors [25, 61, 73, 74].

Stability of the field emission current is an important requirement for practical applications of cold cathodes. We have measured the stability of HG, BG, and NG at a current value of 1 μA over a duration of more than 3 h by using a controlled data acquisition system, acquiring the emission current data with a sampling time of 10 s. Fig. 5.10 shows the current–time plots measured at a base pressure of 1×10^{-8} mbar. Ignoring short-term fluctuations due to adsorption and desorption of residual gas molecules and diffusion of adsorbed species on the emitter surface, the I-t plots are nearly identical after repetitive measurements with no degradation in the emission current during long term operation (Fig. 5.10). The field emission patterns shown as insets in Fig. 5.10 reveal tiny spots and the number of emission spots does not change during I-t measurements. The postfield-emission surface morphology shows no deterioration of the emitter surface indicating its mechanical robustness against ion bombardment and field-induced stress.

5.4.3 NO_2 sensing properties of doped graphene

We have examined the effect of doping graphene on the NO_2 sensing characteristics. Typical low-magnification FESEM images of dielectrophoretically deposited graphene sample HG between two gold electrodes are shown in Fig. 5.11. We have measured the current–voltage (I–V) characteristics for all the graphene samples at 1000 ppm NO_2. Fig. 5.12 shows the typical Ohmic behaviour of N-doped HG in air and in NO_2. These I–V characteristics demonstrate that the graphene samples can be used for sensing these vapours.

The sensitivity of HG decreases on boron doping and increases significantly on nitrogen doping. Fig. 5.13 shows the sensing characteristics of the pure and doped (NG2 and BG2) samples for different concentrations of NO_2. It appears that n-type graphene is a better sensor for NO_2 as it is an electron withdrawing molecule. The response times with the B- and N-doped HG samples are 15 and 50 min, respectively. In Fig. 5.14, we show the variation of sensitivity for the nitrogen doped graphene sample. We see that the value of the sensitivity increases with NO_2 concentration and is satisfactory beyond 100 ppm. We have carried out sensitivity measurements for NO_2 over repeated cycles and obtained reproducible results. For practical applications, however, it may be necessary to anneal the sensor-device and remove the absorbed NO_2 after each cycle.

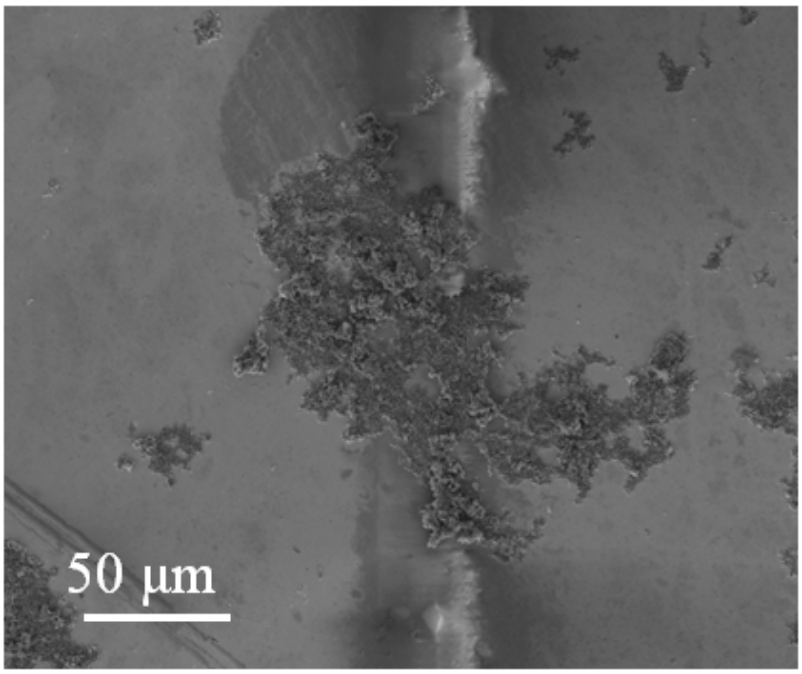

Fig. 5.11 FESEM images of dielectrophoretically deposited HG between two gold electrodes.

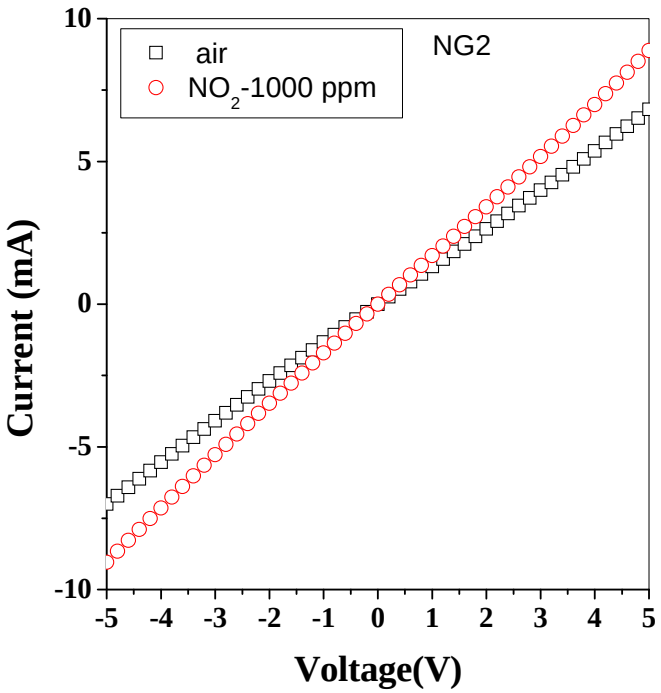

Fig. 5.12 I–V characteristics of (a) N-doped graphene (NG2) at 25 °C in air and in 1000 ppm of NO_2

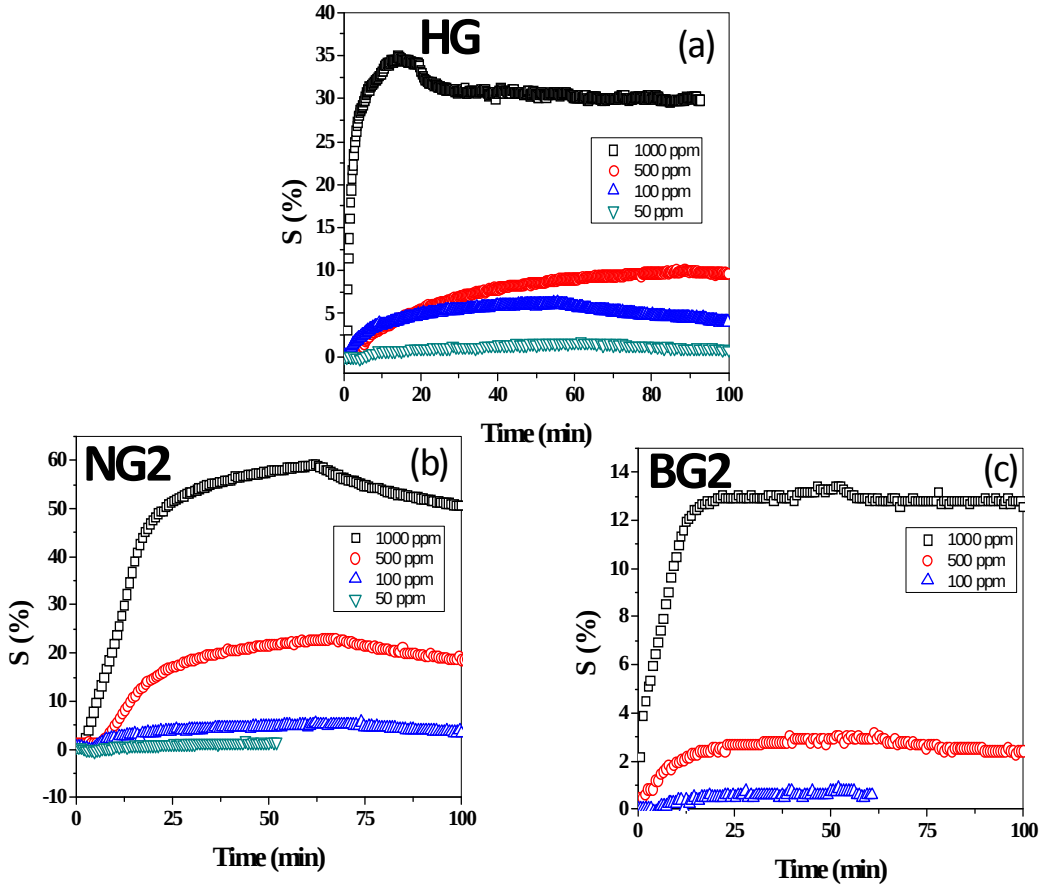

Fig. 5.13 Gas sensing characteristics of (a) HG (b) NG2, and (c) BG2 for 1000, 500, 100 and 50 ppm of NO_2.

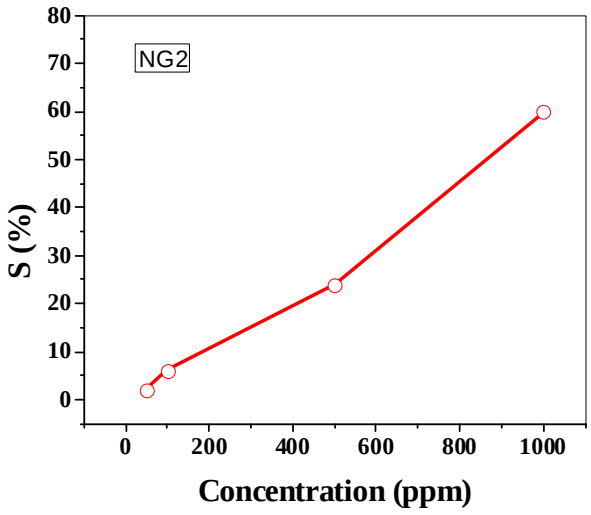

Fig. 5.14 Variation of sensitivity of N-doped HG (NG2) for NO_2 with the concentration of NO_2.

5.5 Conclusions

B- and N-doped graphenes can be synthesized in different ways to exhibit p- and n- type semiconducting electronic properties that can be systematically tuned with the concentration of B and N, and can be characterized with Raman spectroscopy. Interestingly, elemental doping and electrochemical doping produce similar shifts in the Raman G band but molecular charge-transfer gives rise to different effects. Realization of such p- and n-type conducting graphene bilayers should be useful in a variety of devices.

We have employed electrophoresis to fabricate undoped and doped graphene films and studied their field emission properties. These high-density graphene films exhibit better field emission properties than other nanostructures, with a turn-on electric field of ~0.7 V/μm. The excellent field emission properties of graphene appear to arise from the intrinsic properties such as electrical conductivity, morphological features, and resonance tunneling.

N-doped graphene shows enhanced sensitivity for NO_2 compared to pure as well as B-doped graphene since the NO_2 is an electron-withdrawing molecule.

References

[1] A. K. Geim, K. S. Novoselov *Nat. Mater.* **2007**, 6, 183.

[2] K. S. Novoselov, A. K. Geim, S. V. Morozov, D. Jiang, Y. Zhang, S. V. Dubonos, I. V. Grigorieva, A. A. Firsov *Science*. **2004**, 306, 666.

[3] M. I. Katsnelson *Mater. Today*. **2007**, 10, 20.

[4] K. S. Novoselov, Z. Jiang, Y. Zhang, S. V. Morozov, H. L. Stormer, U. Zeitler, J. C. Maan, G. S. Boebinger, P. Kim, A. K. Geim *Science* **2007**, 315, 1379.

[5] A. Das, S. Pisana, B. Chakraborty, S. Piscanec, S. K. Saha, U. V. Waghmare, K. S. Novoselov, H. R. Krishnamurthy, A. K. Geim, A. C. Ferrari, A. K. Sood *Nat. Nanotechnol.* **2008**, 3, 210.

[6] B. Das, R. Voggu, C. S. Rout, C. N. R. Rao *Chem. Commun.* **2008**, 5155.

[7] R. Voggu, B. Das, C. S. Rout, C. N. R. Rao *J. Phys. Condens. Matter*. **2008**, 20, 472204.

[8] W. Chen, S. Chen, D. C. Qi, X. Y. Gao, A. T. S. Wee *J. Am. Chem. Soc.* . **2007**, 129, 10418.

[9] A. C. Ferrari, J. C. Meyer, V. Scardaci, C. Casiraghi, M. Lazzeri, F. Mauri, S. Piscanec, D. Jiang, K. S. Novoselov, S. Roth, A. K. Geim *Phys. Rev. Lett.* **2006**, 97, 187401.

[10] A. C. Ferrari *Solid State Commun.* **2007**, 143, 47.

[11] K. S. Subrahmanyam, S. R. C. Vivekchand, A. Govindaraj, C. N. R. Rao *J. Mater. Chem.* . **2008**, 13, 1517.

[12] T. Ohta, A. Bostwick, T. Seyller, K. Horn, E. Rotenberg *Science*. **2006**, 313, 951.

[13] N. de Jonge, Y. Lamy, K. Schoots, T. Oosterkamp *Nature (London)*. **2002**, 420, 393

[14] R. H. Baughman, A. A. Zakhidov, W. A. Heer *Science*. **2002** 297, 787.

[15] J. Kong, N. R. Franklin, C. W. Zhou, M. G. Chapline, S. Peng, K. J. Cho *Science* **2000**, 287, 622.

[16] P. G. Collins, K. Bradley, M. Ishigami, A. Zett *Science* **2000**, 287, 1801.

[17] W. A. d. Heer, A. Chatelian, D. Ugarte *Science*. **1995**, 270, 1179.

[18] S. I. Cha, K. T. Kim, S. N. Arshad, C. B. Mo, K. H. Lee, S. H. Hong *Adv. Mater.* . **2006**, 18, 553

[19] A. K. Geim *Science*. **2009**, 324, 1530

[20] C. N. R. Rao, A. K. Sood, K. S. Subrahmanyam, A. Govindaraj *Angew. Chem.* . **2009**, 48, 7752

[21] Y. M. Lin, K. A. Jenkins, A. V. Garcia, J. P. Small, P. Avouris *Nano Lett.* . **2009**, 9, 422.

[22] F. Schedin, A. K. Geim, S. V. Morozov, E. W. Hill, P. Blake, M. I. Katsnelson *Nature Mater.* **2007**, 6, 652.

[23] N. M. Mohanty, V. Berry *Nano Lett.* **2008**, 8, 4469.

[24] G. Eda, H. E. Unalan, N. Rupensinghe, G. A. J. Amartunga, M. Chhowalla *Appl. Phys. Lett.* . **2008**, 93, 233502

[25] A. Malesevic, R. Kemps, A. Vanhulsel, M. P. Chowdhary, A. Volodin *J. Appl. Phys.* . **2008**, 104, 084301.

[26] S. M. Jung, J. Hahn, H. Y. Jung, J. S. Suh *Nano Lett.* . **2006**, 6, 1569.

[27] F. Cervantes-Sodi, G. Csanyi, S. Piscanec, A. Ferrari *Phys. Rev. B*. **2008**, 77, 165427

[28] M. Calandra, F. Mauri *Phys. Rev. B* **2007**, 76, 161406.

[29] S. Peng, K. Cho *Nanotechnology*. **2000**, 11, 57.

[30] S. Santucci, S. Picozzi, F.Di. Gregorio, L. Lozzi, C. Cantalini, L. Valentini, J.M. Kenny, B. Delley *J. Chem. Phys.* . **2003**, 119, 10904.

[31] S. Peng, K. Cho *Nano Lett.* . **2003**, 3, 513.

[32] F. Villalpando-Paez, A.H. Romero, E. Munoz-Sandoval, L.M. Martinez, H. Terrones, M. Terrones *Chem. Phys. Lett.* . **2004**, 386, 137.

[33] J. Watson, K. Ihokura (eds), Special issue on gas-sensing materials, MRS Bull. 24 **1999** pp. 14–59.

[34] P. T. Moseley *Meas. Sci. Technol.* **1997**, 8, 223.

[35] S. Capone, A. Forleo, L. Francioso, R. Rella, P. Siciliano, J. Spadavecchia, D.S. Presicce, A. M. Taurino *Adv. Mater.* **2003**, 5, 1335.

[36] C.S. Rout, A. Govindaraj, C.N.R. Rao *J. Mater. Chem.* **2006**, 16, 3936.

[37] C.S. Rout, K. Ganesh, A. Govindaraj, C. N. R. Rao *Appl. Phys. A*. **2006**, 85, 241.

[38] C.S. Rout, M. Hegde, A. Govindaraj, C.N.R. Rao *Nanotechnology*. **2007**, 18, 205504.

[39] D.S. Lee, S.D. Han, J.S. Huh, D. D. Lee *Sens. Actuators B*. **1999**, 60, 57.

[40] J. Wang, M. Tong, X. Wang, Y. Ma, D. Liu, J. Wu, D. Gao, G. Du *Sens. Actuators B* **2002**, 84, 95.

[41] S.H. Wang, T.C. Chou, C.C. Liu *Sens. Actuators B.* **2003**, 94, 343.

[42] D. Zhang, Z. Liu, C. Li, T. Tang, X. Liu, S. Han, B. Lei, C. Zhou *Nano Lett.* **2004**, 4, 1919.

[43] J. Kong, N.R. Franklin, C. Zhou, M.G. Chapline, S. Peng, K. Cho, H. Dai *Science*. **2000**, 287, 622.

[44] E.S. Snow, F.K. Perkins, J.A. Robinson *Chem. Soc. Rev.* . **2006**, 35, 790.

[45] K.S. Novoselov, A.K. Geim, S.V. Morozov, D. Jiang, M.I. Katsnelson, I.V. Grigorieva, S.V. Dubonos, A.A. Firsov *Nature*. **2005**, 438, 197.

[46] C. Berger, Z.M. Song, X.B. Li, X.S. Wu, N. Brown, C. Naud, D. Mayo, T.B. Li, J. Hass, A.N. Marchenkov, E.H. Conrad, P.N. First, W.A. de Heer *Science* **2006**, 312, 1191.

[47] F. Schedin, A.K. Geim, S.V. Morozov, E.W. Hill, P. Blake, M.I. Katsnelson, K.S. Novoselov *Nature Mater.* **2007**, 6, 652.

[48] O. Leenaerts, B. Partoens, F.M. Peeters *Phy. Rev. B.* **2008**, 77, 125416.

[49] B. Huang, Z. Li, Z. Liu, G. Zhou, S. Hao, J. Wu, B.L. Gu, W. Duan *J. Phys. Chem.* . **2008**, 112, 13442.

[50] Z.M. Ao, J. Yang, S. Li, Q. Jiang *Chem. Phys. Lett.* **2008**, 461, 276.

[51] M. Qazi, T. Vogt, G. Koley *Appl. Phys. Lett.* . **2007**, 91, 233101.

[52] I. Jung, D. Dikin, S. Park, W. Cai, S.L. Mielke, R.S. Ruoff *J. Phys. Chem. C* **2008**, 112, 20264.

[53] J.T. Robinson, F.K. Perkins, E.S. Snow, Z. Wei, P. E. Sheehan *Nano Lett.* **2008**, 8, 3137.

[54] J.D. Fowler, M.J. Allen, V.C. Tung, Y. Yang, R.B. Kaner, B.H. Weiller *ACS Nano*. **2009**, 3, 301.

[55] Z. S. Wu, S. Pei, W. Ren, D. Tang, L. Gao, B. Liu, F. Li, C. Liu, H. M. Cheng *Adv. Mater.* . **2009**, 21, 1756

[56] K. Raidongia, D. Jagadeesan, M. Upadhyay-Kahaly, U. V. Waghmare, S. K. Pati, M. Eswaramoorthy, C. N. R. Rao *J. Mater. Chem.* **2008**, 18, 83.

[57] R. Sen, B. C. Satishkumar, A. Govindaraj, K. R. Harikumar, G. Raina, J.-P. Zhang, A. K. Cheetham, C. N. R. Rao *Chem. Phys. Lett.* **1998**, 287, 671.

[58] S. Pisana, M. Lazzeri, C. Casiraghi, K. S. Novoselov, A. K. Geim, A. C. Ferrari, F. Mauri *Nat. Mater.* . **2007**, 6, 198.

[59] L. G. Cancado, K. Takai, T. Enoki, M. Endo, Y. A. Kim, H.Mizusaki, A. Jorio, L. N. Coelho, R. M. Paniago, M. A. Pimenta *Appl. Phys. Lett.* **2006**, 88, 163106.

[60] J. L. Qi, X. Wang, W. T. Zheng, H. W. Tian, C. Q. Hu, Y. S. Peng *J. Phys. D: Appl. Phys.* **2010**, 43, 055302.

[61] M. Qian, T. Feng, H. Ding, L. Lin, H. Li, Y. C. Z. Sun *Nanotechnology*. **2009**, 20, 425702.

[62] J. J. Wang, M. Y. Zhu, R. A. Outlaw, X. Zhao, D. M. Manos, B. C. Holloway, V. P. Mammana *Appl. Phys. Lett.* **2004**, 85, 1265.

[63] J. M. Bonard, J. P. Salvetat, T. Stockli *Appl. Phys. Lett.* **1998,** 73, 918.

[64] J. C. Charlier, M. Terrones, M. Baxendale, V. Meunier, T. Zacharia, N. L. Rupensinghe, W. K. Hsu, N. Grobert, H. Terrones, G. A. J. Amartunga *Nano Lett.* **2002**, 2, 1191.

[65] S. K. Srivastava, V. D. Vankar, D. V. Sridhar, V. Kumar *Thin Solid Films*. **2006**, 515, 1851.

[66] A. Datta, P. G. Chavan, F. J. Sheini, M. A. More, D. S. Joag, A. Patra *Cryst. Growth Des.* **2009**, 9, 4157.

[67] D. J. Late, R. V. Kashid, C. S. Rout, M. A. More, D. S. Joag *Appl. Phys. A: Mater. Sci. Process.* **2010**, 98, 751.

[68] C. J. Park, D. K. Choi, J. Yoo, G. C. Yi, C. J. Lee *Appl. Phys. Lett.* **2007**, 90, 083107.

[69] R. H. Fowler, L. W. Nordheim *Proc. R. Soc. London, Ser. A* **1928**, 119, 173.

[70] N. S. Ramgir, D. J. Late, A. B. Bhise, I. S. Mulla, M. A. More, D. S. Joag, V. K. Pillai *Nanotechnology*. **2006**, 17, 2730

[71] N. S. Ramgir, D. J. Late, A. B. Bhise, M. A. More, I. S. Mulla, D. S. Joag, K. Vijayamohanan *J. Phys. Chem. B*. **206**, 110, 18236.

[72] J. W. Gadzuk *Phys. Rev. B* **1993**, 47, 12832.

[73] T. Connolly, R. C. Smith, Y. Hernandez, Y. G. Ko, J. N. Coleman, J. D. Carey *Small* **2009**, 5, 826.

[74] R. C. Smith, J. D. Carey, R. J. Murphy, W. J. Blau, J. N. Coleman, S. R. P. Silva *Appl. Phys. Lett.* **2005**, 87, 263105.

Chapter-6

Laser-induced Unzipping of Carbon Nanotubes to Yield Graphene Nanoribbons

Summary*

Irradiation of multi-walled carbon nanotubes (MWNTs) by an excimer laser (energy ~ 200-350 mJ) is shown to yield clean graphene nanoribbons (GNRs). We have investigated unzipping of different types of MWNTs which includes MWNTs prepared by CVD method, MWNTs prepared by arc-discharge method as well as MWNTs doped with boron and nitrogen. The GNRs so obtained have been characterized by transmission electron microscopy, atomic force microscopy and Raman spectroscopy.

---

*Paper based on these studies has been submitted for publication (2011).

6.1 Introduction

Graphene nanoribbons (GNRs), which are quasi-1D graphene nanostructures, have attracted widespread interest due to their unique structure, electronic properties, and promising applications in electronic and spintronic devices [1-6]. Narrow GNRs have been used as semiconducting wires in field-effect transistors with high on/off ratios at room temperature [1, 7, 8]. Narrow GNRs show semiconductor properties due to quantum confinement and edge effects with the energy gap depending on the edge type and ribbon width [4]. GNRs are predicted to exhibit several other novel phenomena, such as half-metallic nature, spin-polarized ground state in zig-zag shaped samples and enhanced excitonic effects [4-6]. Theoretical studies suggest that GNRs could possess interesting magnetoelectronic properties with a large magnetoresistance [9-12]. Experimental studies confirm large magnetoresistance in GNRs [13]. To date, several methods have been developed for the synthesis of GNRs, which include lithographical patterning of graphene [3, 14], bottom-up organic synthesis [2], sonochemical cutting of exfoliated expandable graphite [1], chemical vapor deposition [15, 16], oxygen plasma etching of graphene using nanowires as a physical protection mask [17], Li intercalation followed by exfoliation [18] and longitudinal unzipping of multi-walled carbon nanotubes (MWNTs) [19, 20].

6.2 Scope of the present investigations

Among the various methods to prepare GNRs, longitudinal unzipping of MWNTs gives relatively high yields, but GNRs prepared by this method as well as others contain high proportion of oxygen functionalities which alter the properties of graphene nanoribbons. This is because of the use of strong acids and oxidizing agents such as $KMnO_4$ to accomplish unzipping. It is, therefore, desirable to find a simple method which would avoid oxidation and also help to produce large quantities of GNRs. We have explored a single-step method of unzipping MWNTs by employing laser irradiation. This method requires little time and does not use any acid or oxidizing agent thereby yielding clean GNR samples.

6.3 Experimental and related aspects

(a) Synthesis of MWNTs

One set of MWNTs was prepared by generating a electric arc-discharge, between two graphite electrodes in a helium atmosphere [21]. MWNTs were also prepared by chemical vapour deposition (CVD) involving pyrolysis of ferrocene following the literature procedure [22]. A quartz tube (16 mm diameter) carrying a known quantity (600 mg) of ferrocene was placed inside the first furnace of a dual furnace system. The ferrocene was then heated at 400 °C to sublime. Ferrocene vapour was mixed with argon gas (flow rate ~ 600 sccm) at the inlet of the first furnace, The flow rate of argon being controlled by a mass flow controller. This mixture was then carried to the

second furnace, maintained at 1050 °C. Pyrolysis of ferrocene occurs in the second furnace. Fast heating (100 °C min^{-1}) of ferrocene and high flow rate of argon yielded copious quantities of carbon nanotubes deposited on quartz tube walls.

(b) Synthesis of boron- and nitrogen-doped MWNTs

Boron- and nitrogen- doped carbon nanotubes (CNTs) were grown by the pyrolysis of ferrocene (presublimed, ca. 99.99% purity) using the similar experimental set up mentioned above [22, 23]. In a dual furnace system, diborane (B_2H_6) gas was mixed with the ferrocene vapour at the inlet of the first furnace, using argon as the carrier gas (flow rate ~ 600 sccm). The flow rate of argon was controlled by a mass flow controller. This mixture was then carried to the second furnace, maintained at 1050 °C. Pyrolysis of ferrocene with diborane occurs in the second furnace. Fast heating (100 °C min^{-1}) of ferrocene and high flow rate of argon yielded abundant quantities of B-doped carbon nanotubes deposited on quartz tube walls.

For obtaining nitrogen-doped CNTs, ammonia gas (600 sccm) was mixed with ferrocene vapour in the first furnace and the mixture was carried by argon to the second furnace maintained at 1050 °C. All the other parameters were kept same as for B-doped CNTs.

(c) Purification of carbon nanotubes

The as-prepared nanotubes were purified by acid washing followed by hydrogen treatment to remove metal particles and amorphous carbon respectively [24].

(d) Unzipping of carbon nanotubes by laser irradiation

The purified carbon nanotubes were sonicated in N-methyl-2-pyrrolidone to achieve dispersions and were spin-coated onto cleaned quartz substrate. The selection of quartz substrate is to avoid any contamination of nanotubes by the possible laser ablation of the substrate material itself. The films so obtained were air dried. After complete drying, the films were covered by another quartz plate so that the samples do not easily delaminate from the quartz surface when laser irradiation is carried out. An excimer laser (Lambda Physik KrF excimer laser, 248 nm, 30 ns and 100-500 mJ laser beam energy) was employed to irradiate solid samples sandwiched between two quartz plates with the laser beam perpendicular to the quartz surface. The number of laser pulses was kept constant (200 pulses) in all the experiments.

Techniques used for characterization

Field emission scanning electron microscope (FESEM): FESEM images were recorded with a FEI NOVA NANOSEM 600.

Transmission electron microscope (TEM): Transmission electron microscope (TEM) images were obtained with a JEOL JEM 3010, operating with an accelerating voltage of 300 kV.

Atomic force microscope (AFM): Thin films of ZnO formed at the liquid-liquid interface were transformed on to the silicon substrates and AFM measurements performed using the NanoMan.

Raman spectroscopy: Raman spectra were recorded with LabRAM HR high resolution Raman spectrometer (Horiba Jobin Yvon) using He-Ne Laser (λ=630 nm).

6.4 Results and discussion

In order to carry out unzipping of MWNTs, we have employed an excimer laser (100-500 mJ energy). The MWNTs from arc-discharge and CVD had average outside diameters of 22 and 25 nm respectively. We show typical transmission electron microscope (TEM) images of the nanotubes in Fig. 6.1. We have also carried out laser irradiation of N- and B-doped MWNTs with diameters in the 50-70 nm range prepared by CVD. We varied the laser energies in the 100-500 mJ range to examine how it plays a role in opening the nanotubes. We observed little effect of irradiation when the laser energy was less than 150 mJ. Laser energy in excess of 350 mJ destroyed the nanotubes.

In Fig. 6.2 (a) and (b), we show typical TEM images of GNRs obtained when CVD-MWNTs were subjected to 250 and 275 mJ laser irradiation respectively. The width of GNRs is around 60 nm as revealed by the TEM images. Atomic force microscope (AFM) image of the GNRs shown in Fig. 6.3 (a) reveals a width of 75 nm. Arc-MWNTs subjected to 300 and 350 mJ laser

energy also yielded GNRs and corresponding TEM images are shown in Figures 6.2 (c) and (d) respectively. The width of these GNRs obtained from TEM is around 65 nm which is comparable to the width obtained from AFM (70 nm) Fig. 6.3 (b). The insets in Figures 6.2 (a) and (c) show field emission scanning electron microscope (FESEM) images of GNRs. MWNTs prepared by arc method required greater laser energy (350 mJ) compared to those prepared by CVD (250 mJ) to get converted to GNRs. Both CVD and arc MWNTs got fragmented when the laser energy was higher. CVD MWNTs got fragmented when laser energy was higher than 350 mJ (see inset in Fig. 6.2 (b)) and 450 mJ for arc MWNTs (see inset in Fig. 6.2 (d)).

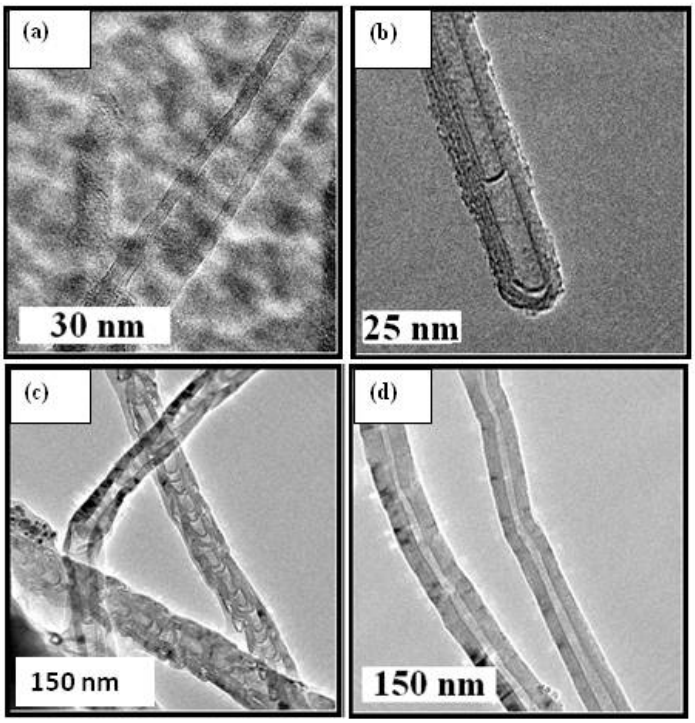

Fig. 6.1 TEM images of MWNTs: (a) CVD-MWNT, (b) arc-MWNT, (c) N-MWNT and (d) B-MWNT.

Raman spectroscopy provides useful information about the quality of nanocarbons. Raman spectra of MWNTs show the characteristic G-band due

to the tangential mode, the defect-induced D-band and the 2D-band [25]. The G-band is highly sensitive to Fermi-level shifts caused by doping or by other means [26-33]. The typical Raman spectra of CVD and arc MWNTs are respectively shown in Figures 6.4 (a) and (b). The G, D and 2D bands of CVD-MWNTs occur at 1572, 1324 and 2650 cm^{-1} respectively where as MWNTs prepared by arc-discharge show these bands at 1581, 1330 and 2654 cm^{-1} respectively. Raman spectra of GNRs are shown in Fig. 6.5. GNRs prepared from both CVD and arc MWNTs exhibit the G band at a lower

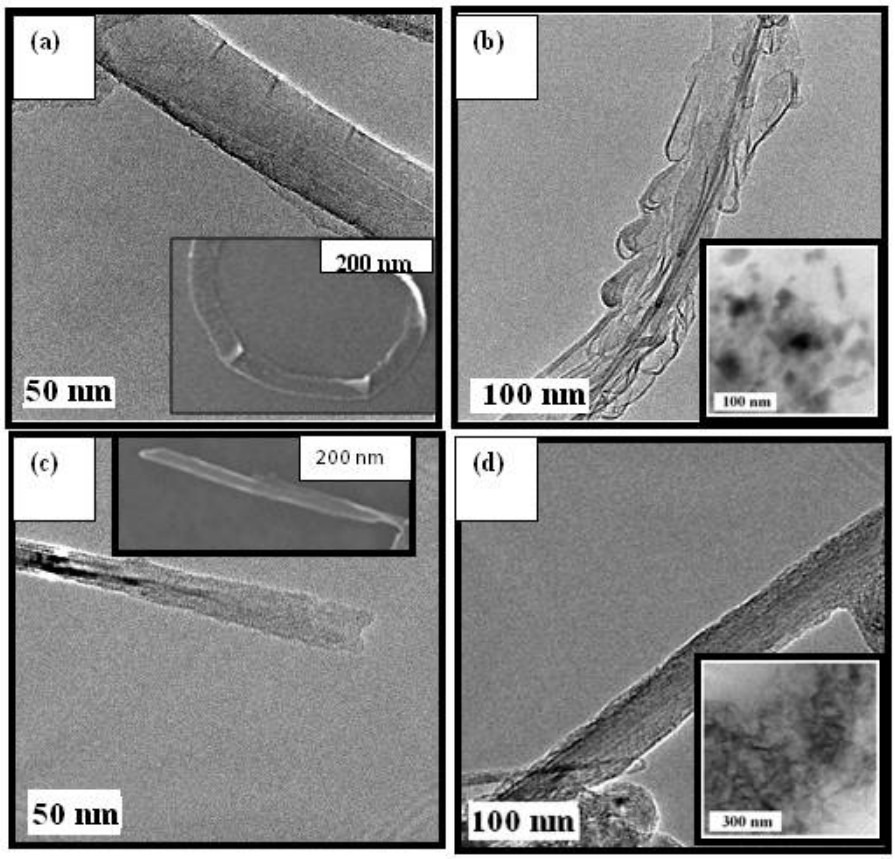

Fig. 6.2 TEM images for GNR obtained by laser irradiation of MWNTs: (a) and (b) CVD MWNT sample irradiated at 250 and 275 mJ respectively. Inset in (a) corresponding FESEM imge where as inset in (b) shows nanosized features CVD MWNT was irradiated at 350 mJ. (c) and (d) arc discharge MWNT sample irradiated at 300 and 350 mJ respectively. Inset in (c) corresponding FESEM imge where as inset in (d) shows nanosized features when arc discharge MWNT was irradiated at 450 mJ.

frequency (1570 cm^{-1}) compared to the MWNTs. The ratio of intensities of the D and G bands (I_D / I_G) increases significantly in GNRs compared to the parent MWNTs, due to the increased number of defects. Thus, I_D/I_G is in the range of 0.2-0.6 in MWNTs and 0.8-1.0 in the GNRs produced by laser irradiation. The I_{2D}/I_G ratio decreases in GNRs relative to that of MWNTs, the value being in the range of 0.3-0.6 in MWNTs and 0.1-0.5 in GNRs. The Raman band positions, widths as well as intensity ratios (I_D/I_G and I_{2D}/I_G) of the GNRs obtained from different MWNTs are given in Table 1.

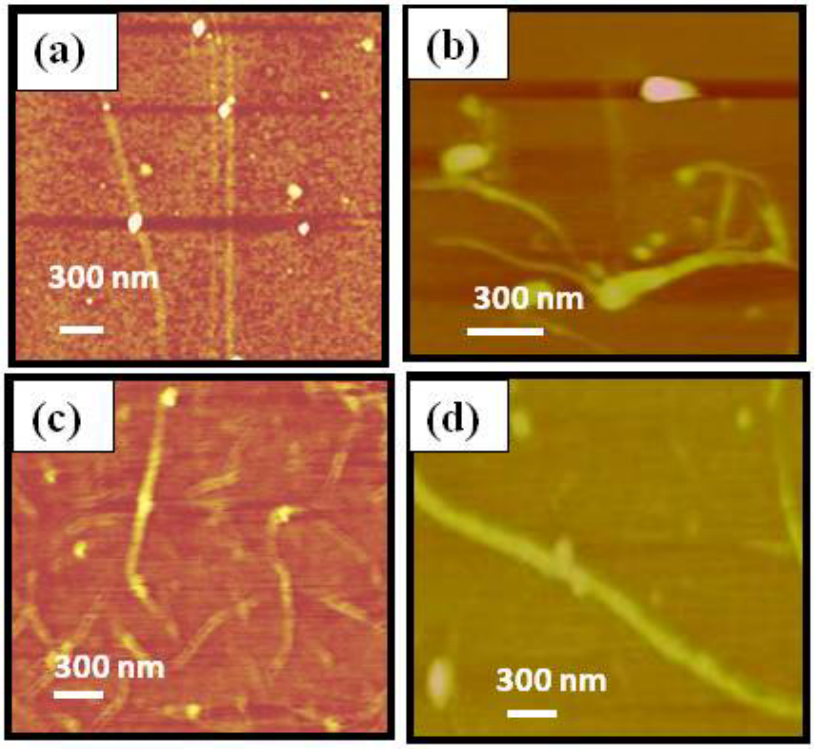

Fig. 6.3 AFM images for GNRs obtained by laser irradiation of (a) CVD-MWNT irradiated at 250 mJ (b) arc discharge-MWNT irradiated at 350 mJ, (c) N-doped CVD- MWNT- irradiated at 250 mJ and (d) B-doped CVD- MWNT irradiated at 250 mJ laser energy.

TEM images of N-MWNTs and B-MWNTs shown in Figures 6.1 (c) and (d) respectively have diameters of 60 and 65 nm respectively. On laser

irradiation (250 mJ), we obtain N- and B-doped GNRs. We note that there is not much significant change in the laser energy required to unzip pure and doped MWNTs. In Figures 6.6 (a) and (b), we show TEM images of N-GNRs and B-GNRs with widths of 150 and 160 nm respectively (Table 1). The widths obtained from AFM images are comparable to those from TEM. Typical AFM images of N-GNRs and B-GNRs are shown in Figures 6.3 (c) and (d) respectively. The insets in Figures 6.6 (a) and (b) show the corresponding FESEM images. The bottom inset in Fig. 6.6 (b) shows a TEM image of B-GNR obtained after irradiation with a laser energy of 200 mJ. This image clearly reveals partial opening of the CNT when less energy is applied.

Table 1 Dimensions and Raman data on GNRs

Method of prep^{n}	MWNTs dia (nm)	GNR-width (nm) TEM (AFM)	D-band (cm^{-1})	G-band (cm^{-1})	2D-band (cm^{-1})	I_D/I_G	I_{2D}/I_G
CVD-MWNTs	25	60 (75)	1328	1570	2643	0.80	0.50
arc-MWNTs	22	65 (70)	1327	1571	2641	1.02	0.13
N-MWNTs	60	150 (140)	1329	1574	2654	0.92	0.56
B-MWNTs	65	160 (165)	1330	1585	2662	1.27	0.69

N-GNRs and B-GNRs show the D-, G- and 2D-bands in the Raman spectra at 1329, 1574, 2654 cm^{-1} and 1330, 1585 and 2662 cm^{-1} respectively (Fig. 6.5). The G-band frequency of doped GNRs is slightly up-

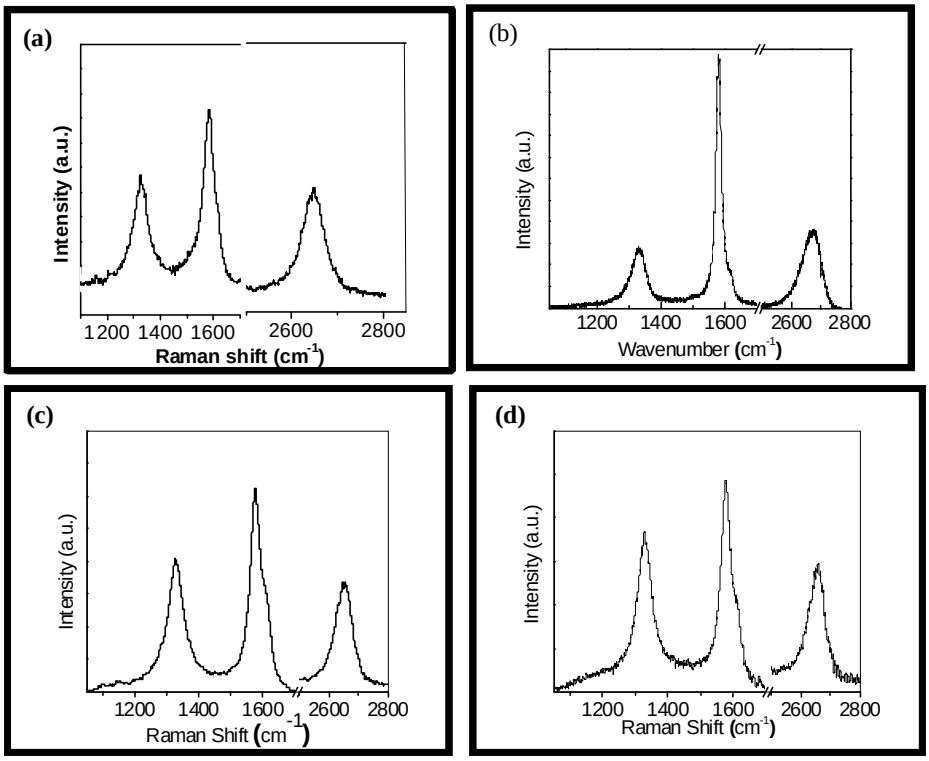

Fig. 6.4 Raman spectra for (a) CVD-MWNT, (b) arc discharge-MWNT, (c) CVD-N-MWNT and (d) CVD-B-MWNT

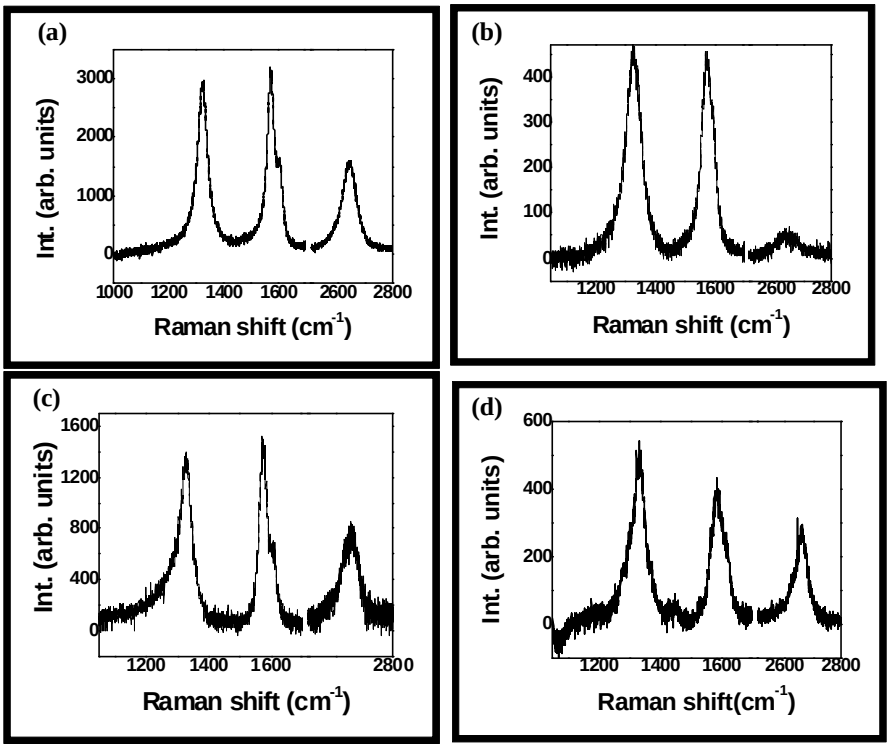

Fig. 6.5 Raman spectra for GNRs obtained by laser irradiation of (a) CVD MWNT sample irradiated at 250 mJ, (b) arc discharge MWNT sample irradiated at 350 mJ (c) N-doped CVD MWNT sample irradiated at 250 mJ and (d) B-doped CVD MWNT sample irradiated at 250 mJ laser energy.

shifted compared to the parent MWNTs. The I_D / I_G ratios in both N- and B-GNRs are higher (0.9-1.3) than in the MWNTs (0.6-0.8). There is a negligible change in the I_{2D}/I_G ratio in the GNRs.

On laser irradiation of MWNTs, defect sites are likely to attain higher temperatures than the non-defect sites, giving rise to a local heating and trigging longitudinal unzipping. Evidence for this suggestion is found from the partially opened MWNTs (see Fig. 6.6 (b)). With little more laser energy, these MWNTs open up completely. Both pure and doped MWNTs got fragmented when the laser energy was higher than 350 mJ for CVD MWNTs and 450 mJ for arc MWNTs. CVD MWNTs required lower energy to unzip, probably because of a higher concentration of defects.

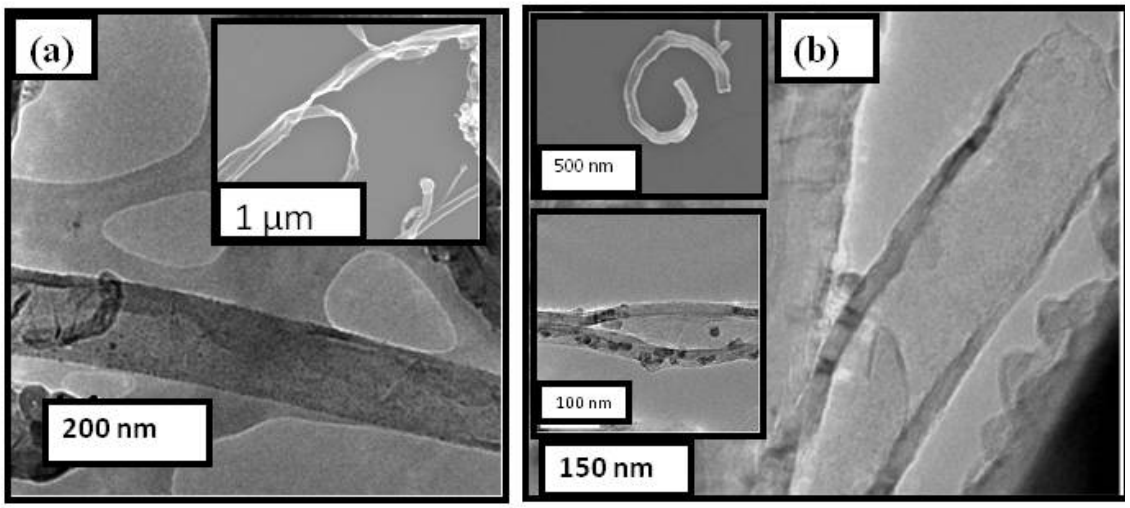

Fig. 6.6 TEM and FESEM images of N- and B-doped GNRs obtained by laser irradiation of doped MWNTs: (a) N-MWNT irradiated at 250 mJ. Inset shows the corresponding FESEM image. (b) B-MWNT sample irradiated at 250 mJ. Top inset shows the corresponding FESEM image. Bottom inset shows a TEM image of partially opened B-MWNT irradiated at 200 mJ.

6.5 Conclusions

The present study shows that the laser irradiation of CNTs provides an easy method of producing GNRs without surface contamination. We could prepare both nitrogen- and boron- doped GNRs. CVD MWNTs required lower energy to unzip compared to arc MWNTs.

References

[1] X. L. Li, X. R. Wang, L. Zhang, S. W. Lee, H. J. Dai *Science*. **2008**, 319, 1229.

[2] X. Yang, X. Dou, A. Rouhanipour, L. Zhi, H. J. Rader, K. Mullen *J. Am. Chem. Soc.* **2008**, 130, 4216.

[3] M. Y. Han, Ouml, B. zyilmaz, Y. Zhang, P. Kim *Phys. Rev. Lett.* **2007**, 98, 206805.

[4] Y.-W. Son, M. L. Cohen, S. G. Louie *Nature*. **2006**, 444, 347.

[5] A. Yamashiro, Y. Shimoi, K. Harigaya, K. Wakabayashi *Phys. Rev. B.* **2003**, 68, 193410.

[6] L. Yang, M. L. Cohen, S. G. Louie *Nano Lett.* **2007**, 7, 3112.

[7] X. Wang, Y. Ouyang, X. Li, H. Wang, J. Guo, H. Dai *Phys. Rev. Lett.* **2008**, 100, 206803.

[8] L. A. Ponomarenko, F. Schedin, M. I. Katsnelson, R. Yang, E. W. Hill, K. S. Novoselov, A. K. Geim *Science*. **2008**, 320, 356.

[9] Y. W. Son, M. L. Cohen, S. G. Louie *Phys. Rev. Lett.* **2006**, 97, 216803.

[10] W. Y. Kim, K. S. Kim *Nature Nanotech.* **2008**, 3, 408.

[11] T. S. Li, Y. C. Huang, S. C. Chang, C. P.Chang, M. F. Lin *Phil. Mag.* . **2009**, 89, 697.

[12] Mu, ntilde, F. oz-Rojas, Fern, aacute, J. ndez-Rossier, J. J. Palacios *Phys. Rev. Lett.* **2009**, 102, 136810.

[13] J. Bai, R. Cheng, F. Xiu, L. Liao, M. Wang, A. Shailos, K. L. Wang, Y. Huang, X. Duan *Nat. Nanotechnol.*, **2010**, 5, 655.

[14] L. Tapaszto, G. Dobrik, P. Lambin, L. P. Biro *Nat. Nanotechnol.* **2008**, 3, 397.

[15] J. Campos-Delgado, J. M. Romo-Herrera, X. Jia, D. A. Cullen, H. Muramatsu, Y. A. Kim, T. Hayashi, Z. Ren, D. J. Smith, Y. Okuno, T. Ohba, H. Kanoh, K. Kaneko, M. Endo, H. Terrones, M. S. Dresselhaus, M. Terrones *Nano Lett.* **2008**, 8, 2773.

[16] D. Wei, Y. Liu, H. Zhang, L. Huang, B. Wu, J. Chen, G. Yu *J. Am. Chem. Soc.* **2009**, 131, 11147.

[17] J. Bai, X. Duan, L. Huang *Nano Lett.* **2009**, 9, 2083.

[18] A. G. Cano-Marquez, F. J. Rodriguez-Macas, J. Campos-Delgado, C. G. Espinosa-Gonzalez, F. Tristan-Lopez, D. Ramirez-Gonzalez, D. A. Cullen, D. J. Smith, M. Terrones, Y. I. Vega-Cantu *Nano Lett.* **2009**, 9, 1527.

[19] L. Jiao, L. Zhang, X. Wang, G. Diankov, H. J. Dai *Nature*. **2009**, 458, 877.

[20] D. V. Kosynkin, A. L. Higginbotham, A. Sinitskii, J. R. Lomeda, A. Dimiev, B. K. Price, J. M. Tour *Nature*. **2009**, 458, 872.

[21] R. Seshadri, A. Govindaraj, H. N. Aiyer, R. Sen, G. N. Subbanna, A. R. Raju, C. N. R. Rao *Curr. Sci.* **1994**, 66, 839.

[22] C.N.R. Rao, R. Sen, B.C. Satishkumar, A. Govindaraj *Chem. Commun.* **1998**, 10, 1525.

[23] R. B. Sharma, D. J. Late, D. S. Joag, A. Govindaraj, C. N. R. Rao *Chem. Phys. Lett.* **2006**, 428, 102.

[24] S. R. C. Vivekchand, A. Govindaraj, M. Motin Seikh, C. N. R. Rao *J. Phys. Chem. B* **2004**, 108, 6935.

[25] M. S. Dresselhaus, P. C. Eklund *Adv. Phys.* **2000**, 49, 705.

[26] L.S. Panchakarla, K.S. Subrahmanyam, S.K. Saha, A. Govindaraj, H.R. Krishnamurthy, U.V. Waghmare, C.N.R. Rao *Adv. Mater.* **2009**, 21, 4726.

[27] L. S. Panchakarla, A. Govindaraj, C. N. R. Rao *ACS Nano*. **2007**, 1, 494.

[28] K. T. Nguyen, A. Gaur, M. Shim *Phys. Rev. Lett.* . **2007**, 98, 145504.

[29] A. Das, A. K. Sood, A. Govindaraj, A. Marco Saitta, M. Lazzeri, F. Mauri, C. N. R. Rao *Phys. Phys. Lett.* **2007**, 99, 136803.

[30] A. Das, S. Pisana, B. Chakraborty, S. Piscanec, S. K. Saha, U. V. Waghmare, K. S. Novoselov, H. R. Krishnamurthy, A. K. Geim, A. C. Ferrari, A. K. Sood *Nat. Nanotechnol.* **2008**, 3, 210.

[31] B. Das, R. Voggu, C. S. Rout, C. N. R. Rao *Chem. Commun.* **2008**, 5155.

[32] R. Voggu, B. Das, C. S. Rout and C N R Rao *Journal of Physics: Condensed Matter*. **2008**, 20, 472204.

[33] Y. C. Lin, C. Y. Lin, P. W. Chiu *Appl. Phys. Lett.* **2010**, 96, 133110.

Chapter-7

Carbon Nanostructures and Graphite-Coated Metal Nanostructures Obtained by the Pyrolysis of Ruthenocene and Ruthenocene-Ferrocene Mixtures

Summary*

Pyrolysis of ruthenocene carried out in an atmosphere of argon or hydrogen is found to give rise to spherical nanoparticles of carbon with diameters in the 10-200 nm range. Pyrolysis of ruthenocene as well as mixtures of ruthenocene and ethylene in hydrogen gives rise to spherical nanoparticles, which contain a high proportion of sp^3 carbon. Under certain conditions, pyrolysis of ruthenocene gives rise to graphite coated ruthenium nanoparticles as well as worm-like carbon structures. Pyrolysis of mixtures of ruthenocene and ferrocene gives rise to nanoparticles or nanorods of FeRu alloys inside carbon nanotubes.

* Paper based on this study has been published in *Bull. Mater. Sci.* (2007)

7.1 Introduction

Pyrolysis of organometallic precursors has been employed to prepare novel carbon structures by several workers [1-5]. Thus, pyrolysis of metallocenes such as ferrocene, cobaltocene and nickelocene in the presence or absence of other hydrocarbons gives carbon nanotubes without any external metal catalyst [6]. Such pyrolysis also gives rise to metal particles such as Co and Fe covered by graphite sheets or carbon coated metal nanoparticles [7]. The nature of the pyrolysis of hydrocarbons such as benzene in an inert atmosphere gives rise to fine uniform size spherical particles of carbon, which are established to be graphite type [8]. Even though several studies have been carried out on the preparation of ruthenium particles decorated on carbon structures [9-11], there has been no systematic study on the pyrolysis of ruthenocene, $Ru(C_5H_5)_2$, to generate carbon-supported metal structures. Like other metallocenes, ruthenocene also sublimes and by using an inert carrier gas one can transport and decompose this ruthenocene vapor at high temperatures.

7.2 Scope of the present investigations

We have carried out the pyrolysis of ruthenocene to study the nature of nanoparticles obtained from the decomposition of ruthenocene. Pyrolysis of ruthenocene with different carbon sources (hydrocarbons), different carrier gases and temperatures have been studied. We have also studied the

incorporation of Ru and Fe inside the carbon nanotubes by pyrolysis of different molar ratios of ruthenocene and ferrocene.

7.3 Experimental and related aspects

The two procedures used for the pyrolysis of ruthenocene are as follows.

(a) Synthesis of carbon spheres

In Procedure 1, typically 100 mg of ruthenocene was taken in a stainless steel autoclave (Swagelok) of 20 ml capacity and then sealed in an argon atmosphere. The autoclave was then placed inside a horizontal tube furnace maintained at 1000 °C for 10 min (in an inert atmosphere) and then cooled to room temperature. After opening the autoclave the black pyrolyzed product was collected and analyzed. This procedure is similar to that reported by Shanmugam and Gedanken [12] for the preparation of carbon nanotubes by the pyrolysis of Ru(III) acetylacetonate.

(b) Synthesis of Ru containing carbon materials

In Procedure 2, Ru containing carbon materials were prepared by the pyrolysis of ruthenocene along with ethylene using a procedure similar to that for the synthesis of carbon nanotubes [6]. A known quantity of ruthenocene was placed in a quartz boat located at one end of a narrow quartz tube (10 mm inner diameter) which in turn was placed in a duel (two-stage) furnace system. The part of the quartz tube containing the ruthenocene was in the first furnace and ruthenocene was sublimed by raising the temperature to 400 °C at a

heating rate of 50 °C/min. Argon (hydrogen in the case of synthesis of elongated particles) was used as a carrier gas for carrying the ruthenocene vapors into the second furnace. The role of ethylene was to provide an additional carbon source. Ethylene was admitted into the reaction tube just before the sublimation of ruthenocene. The flow rates of the gases were controlled using the UNIT mass flow controllers. Pyrolysis takes place inside the second furnace and its temperature was maintained constant for each reaction and was varied from 900 °C to 1300 °C (from one reaction to other). Pyrolysis yielded profuse quantities of carbon deposits at the centre and outlet of the second furnace. The samples were collected from the interior of the quartz reaction tube gives elongated carbon spheres, carbon coated metal particles and worm-shaped carbon structures. Similar experiments were carried out to prepare FeRu metal alloy nanorods inside the carbon nanotubes (CNTs). In this case, we used 1:1, 1:4 and 4:1 (molar ratios) of ruthenocene-ferrocene mixtures for the pyrolysis.

Techniques used for characterization

X-ray diffraction (XRD): X-ray diffraction (XRD) patterns of the samples were recorded in the θ-2θ Bragg-Bretano geometry with a Siemens D5005 diffractometer using Cu Kα (λ=0.151418 nm) radiation.

Scanning electron microscope (SEM): Scanning electron microscope images of the samples were recorded using a LEICA S440i scanning electron microscope.

Field emission scanning electron microscope (FESEM): FESEM images were recorded with a FEI NOVA NANOSEM 600.

Raman spectroscopy: Raman spectra were recorded with LabRAM HR high resolution Raman spectrometer (Horiba Jobin Yvon) using He-Ne Laser (λ=630 nm).

Transmission electron microscopy (TEM): Transmission electron microscope (TEM) images were obtained with a JEOL JEM 3010, operating with an accelerating voltage of 300 kV and JEOL JEM 3010 and FEI Tecnai S30 operating at 300 kV. The samples were prepared by dispersing the product in CCl_4. A drop of the suspension was then put on a holey carbon coated Cu grid and allowed to evaporate slowly.

Vibrating sample magnetometer (VSM): Magnetic measurements were carried out for different samples by using the vibrating sample magnetometer (VSM) in PPMS (Physical Property Measurement System).

7.4 Results and Discussion

SEM images of the carbon spheres obtained by the pyrolysis of ruthenocene in an Ar atmosphere at 1000 °C, using procedure 1, are shown in figure 7.1a and b. These unconnected spheres are graphitic, with having diameters ranging from 500 nm to 1 μm. Carbon spheres of uniform size were also obtained by the pyrolysis of ruthenocene in the presence or absence of hydrocarbons using procedure 2. Figure 7.2a shows a SEM image of uniform-sized carbon spheres of ~ 300 nm diameter obtained in the presence of 200 sccm (sccm=standard cubic centimeter per minute) of argon carrier gas at 1300 °C.

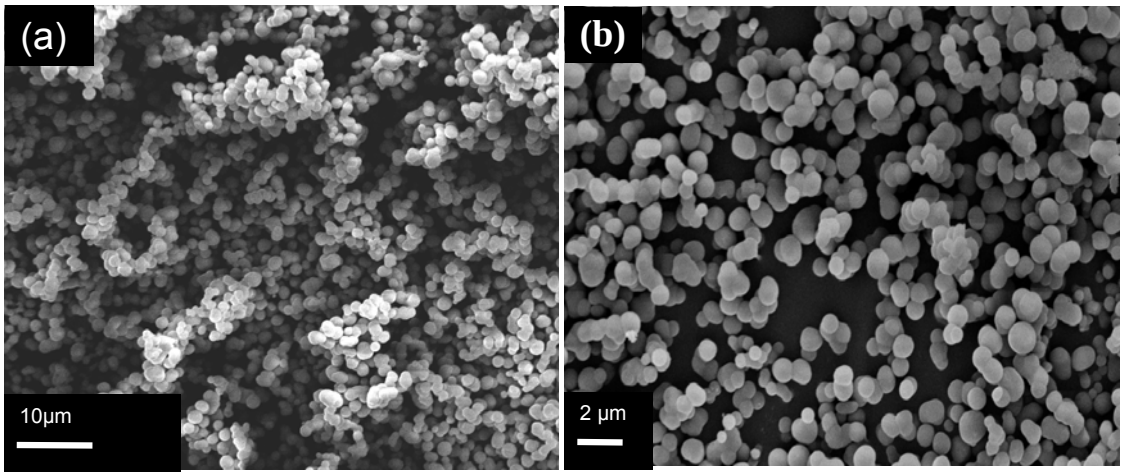

Fig. 7.1. low (a) and high (b) magnification SEM images of ruthenium supported carbon spheres prepared by pyrolysis of ruthenocene at 1000 °C in argon atmosphere using Procedure 1

Reactions carried out using procedure 2 at different temperatures in the 1000°C - 1300°C range, under similar conditions yielded similar carbon spheres of uniform size. However, pyrolysis of the ruthenocene-ethylene mixture at 1350 °C (with hydrogen and ethylene flow rates of 150 and 50 sccm

respectively) gives connected carbon spheres of around 70 nm diameter, as shown in the FESEM image of figure 7.2b. Interestingly, these carbon spheres are different from the spheres obtained in the absence of the hydrocarbon

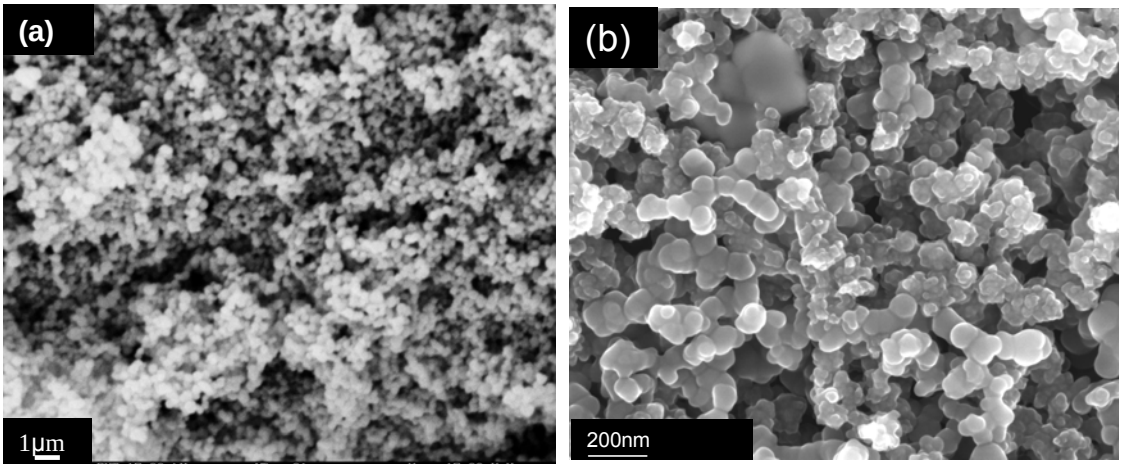

Fig. 7.2. (a) SEM images of ruthenium supported carbon spheres prepared by pyrolysis of ruthenocene at 1300 °C in the presence of argon 200 sccm by using Procedure 2, (b) FESEM images of rutheniumsupported carbon spheres prepared by pyrolysis of ruthenocene at 1350 °C in the presence of hydrogen and ethylene flow rates 150 and 50 sccm respectively, by using Procedure 2.

(shown in Fig. 7.1 and Fig. 7.2a). The Raman spectrum of these carbon spheres is shown in figure 7.3a. We observe intense bands at 1340 and 1593 cm^{-1}, the former being due to sp^3 carbon as in diamond and the latter due to graphitic (sp^2) carbon. The relative intensities of these two bands indicate the dominance of sp^3 carbon over sp^2 carbon and the material looks almost pure glassy carbon or diamond-like carbon. Pyrolysis of ruthenocene with a mixture of argon and ethylene with flow rates of 150 and 50 sccm respectively at 1100 °C gives carbon spheres with diameters in the 500-800 nm range, as shown in figure 7.4a. The Raman spectrum of these spheres is shown in figure 7.3b which shows bands at 1330 and 1593 cm^{-1} of similar intensities, indicating the

presence of equal amount of sp^2 and sp^3 carbon. In figure 7.4b we show a TEM image of amorphous carbon-coated ruthenium nanoparticles. EDAX analysis shows the presence of ruthenium. The inset in figure 7.4b shows a TEM image of a carbon-coated Ru particle.

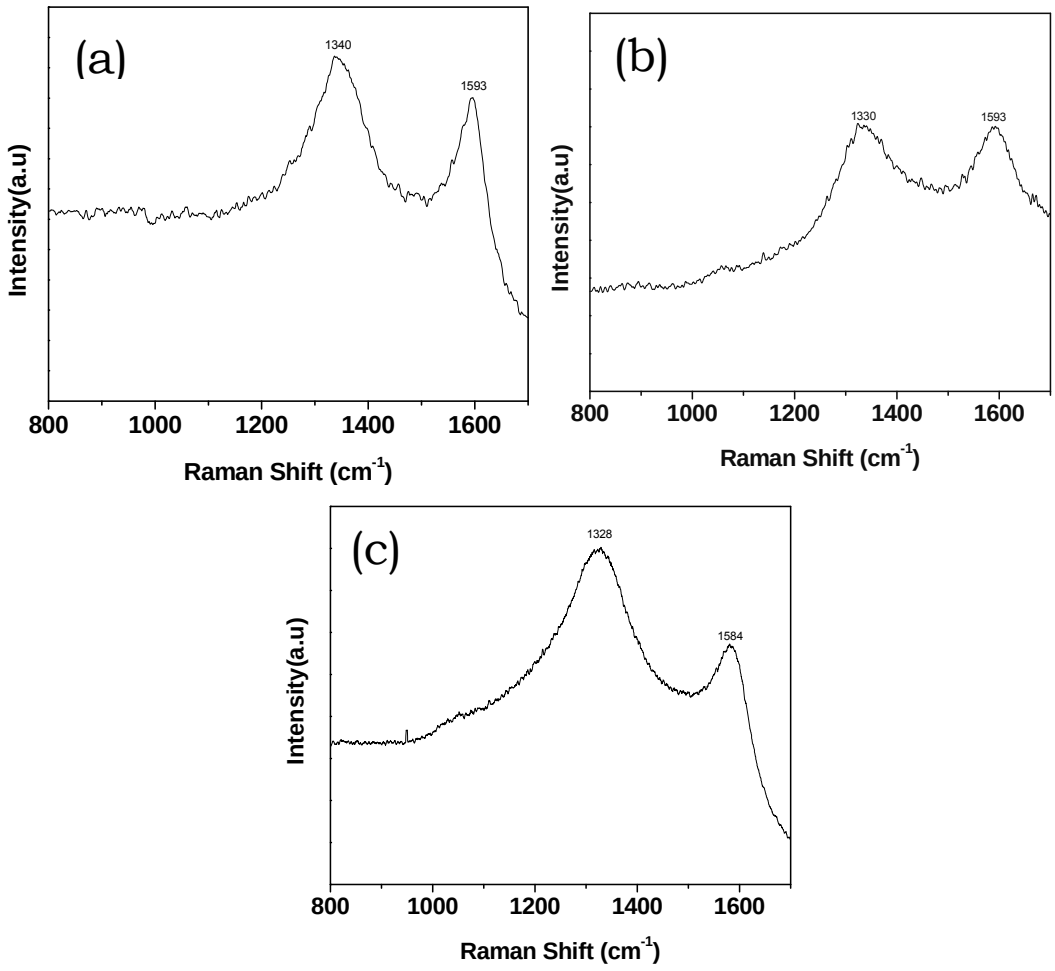

Fig. 7.3. Raman spectra of Ru-supported carbon spheres prepared under different conditions: (a) by pyrolysis of ruthenocene at 1350 °C in a mixture of hydrogen and ethylene gases with flow rates 150 and 50 sccm respectively, (b) by pyrolysis of ruthenocene in argon and ethylene mixturewith flow rates of 150 and 50 sccm respectively at 1100 °C and (c) pyrolysis ofruthenocene in argon (150 sccm) with a mixture of 50 sccm of ethylene bubbled through thiophene at 950 °C.

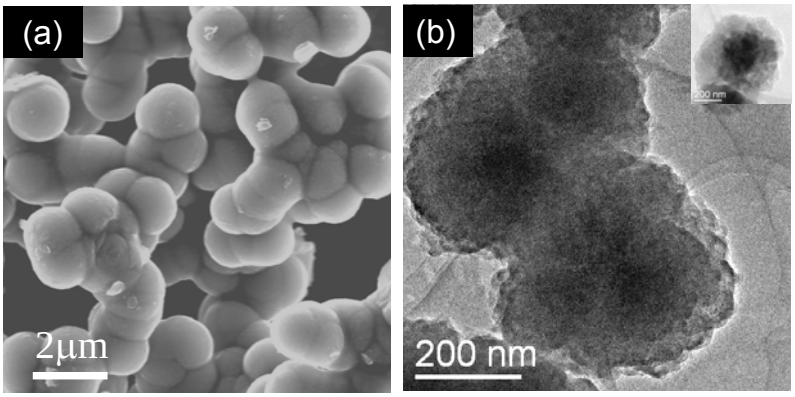

Fig. 7.4. (a) FESEM images of carbon spheres prepared by pyrolysis of ruthenocene at 1100 °C in the presence of argon and ethylene with flow rates 150, 50 sccm respectively, (b) shows a TEM image of the spheres, the inset showing a single sphere of carbon coated ruthenium.

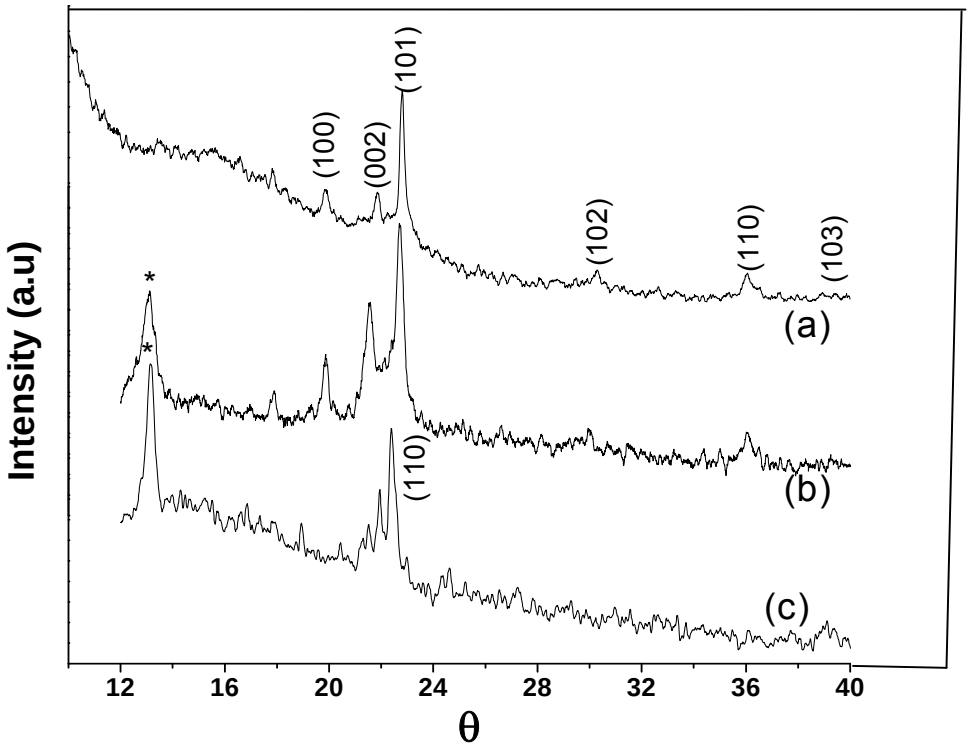

Fig. 7.5. XRD patterns of (a) ruthenium supported carbon spheres (b) FeRu (1:1) binary alloy nanowires inside carbon nanotubes and (c) iron nanowires encapsulated inside carbon nanotubes (asterisk corresponds to carbon nanotube peak).

The electron diffraction pattern as well as the XRD pattern (see figure 7.5a) of these nanospheres confirms the HCP structure of Ru (a= 2.698 Å and c= 4.272 Å, JCPDS file: 02-1258).

Worm-like carbon structures were obtained by the pyrolysis of ruthenocene at 950 °C in the presence of thiophene, argon and ethylene at flow rates of 150 sccm and 50 sccm respectively. In these experiments ethylene was bubbled through thiophene throughout the reaction. SEM and TEM images of the worm-like carbon structures are shown in figure 7.6a and b respectively. The elongated structures have a diameter of around 1 μm. EDAX analysis shows the presence of Ru. The Raman spectrum of these carbon structures (figure 7.3c) shows that sp^3 carbon is in majority rather than sp^2 carbon.

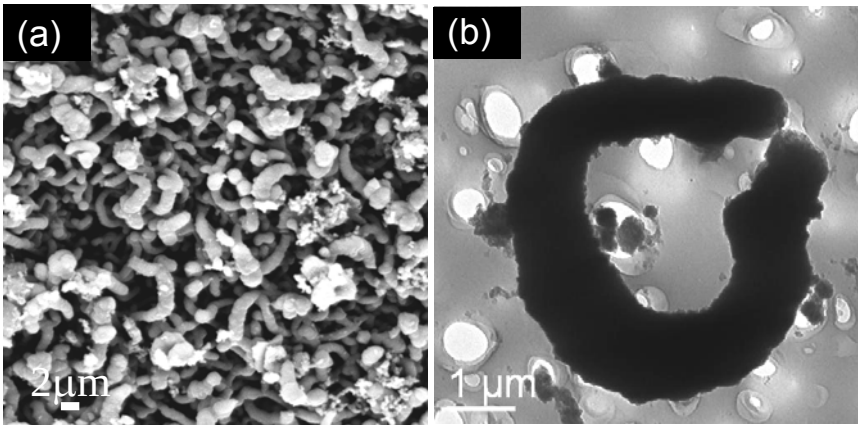

Fig. 7.6. (a) SEM image of carbon structures prepared by pyrolysis of ruthenocene with a mixture of argon (150 sccm) and 50 sccm of ethylene bubbled through thiophene at950 °C and (b) shows the TEM image of these structures

By using ferrocene instead of ruthenocene, under the conditions of procedure 2, we obtained carbon nanotubes rather than carbon spheres as in the case of ruthenocene (*1, 2*). This may be due to the higher stability, diffusion as well as

the solubility of carbon in Fe with a lower eutectic temperature. The Fe-C phase diagram shows a maximum solubility of carbon in Fe to be around 7%. The eutectoid composition is Fe-0.83 wt%C and at this composition the high-temperature austenite phase will undergo the eutectoid reaction at 723 °C and at this temperature γ-Fe, α-Fe and carbon or (Fe_3C) may coexist [13]. Also, the Ru-C phase diagram is a simple eutectic with a eutectic temperature of 1940 °C and eutectic concentration of ~ 18 at% C and maximum solubility of C is ~0.37 wt% C. Since RuC is unstable with decreasing temperature carbon precipitates in the form of graphite on the basal planes. Although Ru does not form carbides at room temperature, soluble carbon (~0.04 wt.% C at room temperature) strongly effect hardness and resistivity, and impairs workability [14]. Thus, the Fe-C phase diagram seems to indicate the formation of Fe catalyzed growth of carbon nanotubes. Since ruthenium itself is not incorporated and forming carbon nanotubes, we thought it interesting to see the effect of addition of ruthenocene to ferrocene on the growth of carbon nanotubes. It was also of interest to see whether Ru particles decorate the carbon nanotube surface or get encapsulated inside the nanotubes. Interestingly, we found bimetallic FeRu nanostructures which get encapsulated inside the nanotubes as seen in the figures 7.7, 7.8 and 7.9. We were able to get FeRu alloy nanorods inside the carbon nanotubes as well as carbon-coated FeRu alloy nanoparticles by the pyrolysis of a mixture of ruthenocene and ferrocene mixtures of different molar ratios (1:1, 1:4, 4:1) in the presence of argon and ethylene (500 and 50 sccm respectively) at 900 °C. Due to relatively

high temperature involved in the synthesis, we are expected to obtain the HCP structure for all the above compositions of FeRu alloy nanostructures [15]. The 1:4 FeRu alloy nanostructure have the lattice constants, a= 2.70 Å and c= 4.27 Å (JCPDS file: 40-1147)) and the 1:1 FeRu alloy nanostructure has the lattice constants, a= 2.60 Å and c= 4.17 Å. A systematic decrease in the d-spacing was also observed in all FeRu alloy nanostructures as compared to pure Ru, confirming the smaller Fe atoms are indeed incorporated in the larger Ru lattice.

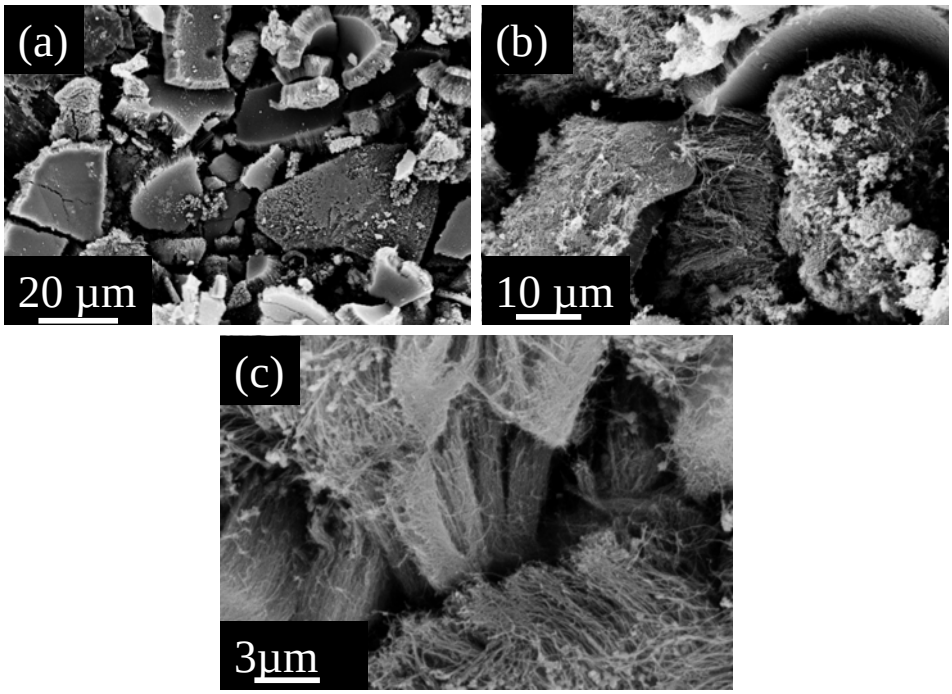

Fig. 7.7 SEM images of RuFe alloy nanorods inside the aligned carbon nanotubes (a) 1:1 (b) 1:4 (c) 4:1 (molar ratios) of ruthenocene-ferrocene mixtures for the pyrolysis.

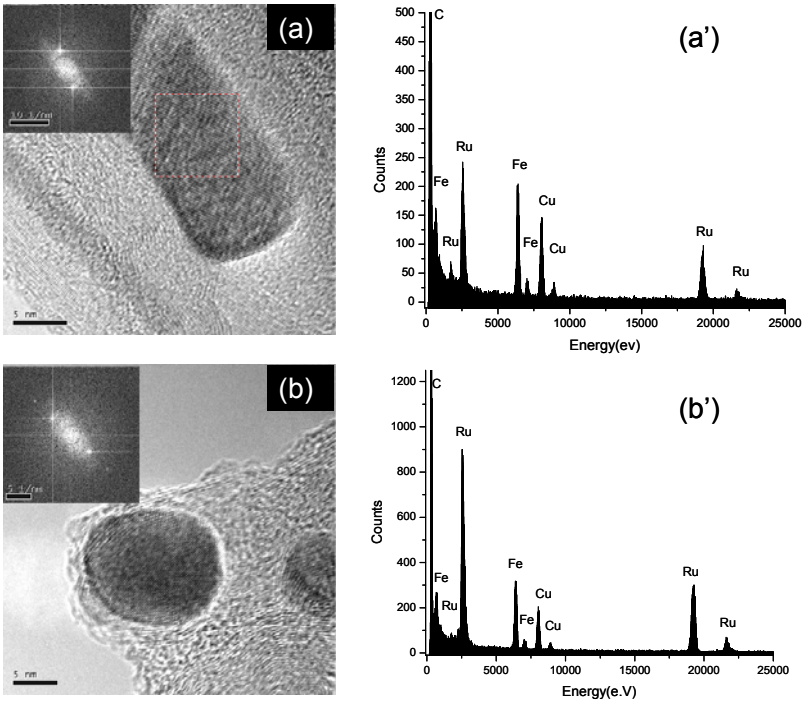

Fig. 7.8. The high magnification TEM images of FeRu alloy nanoparticles and nanorods (inside the carbon nanotubes) obtained by the pyrolysis of a mixture of ruthenocene and ferrocene (1:1) in the presence of Ar and ethylene (500 and 50 sccm respectively) at 900 °C (a) alloy nanorods inside the carbon nanotube (b) alloy nanoparticle. (a′) and (b′) show the corresponding EDAX patterns.

Figure 7.7 shows SEM images of the alloy nanorods inside the aligned carbon nanotubes starting with 1:1 (Fig. 7.7a), 1:4 (Fig. 7.7b) and 4:1 (Fig. 7.7c) molar ratios of ruthenocene-ferrocene mixtures for the pyrolysis. These nanotubes are grown aligned for several micrometers and lengths are in the order of several microns. Figure 7.8a shows a typical high resolution TEM image of the 1:1 alloy nanorod showing a d-spacing of 2.1 Å. Figure 7.8b shows a high resolution TEM image of 1:4 FeRu alloy nanoparticle showing a d-

spacing of 2.4 Å, confirming the single-crystalline nature. From EDAX analysis (figure 7.8), the Ru:Fe ratio was found 1:1 in the case of nanorods formed inside the CNTs and 4:1 in the case of encapsulated nanoparticles. The electron diffraction patterns shown as insets in figures 7.8a and b corresponds to the alloys and indicate the nanostructures to be single crystalline. The carbon coating in the FeRu nanoparticles is graphitic as can be seen from the TEM image. Figures 7.9a and b show the low magnification TEM images of metal alloy (1:1) nanorods formed inside the CNTs.

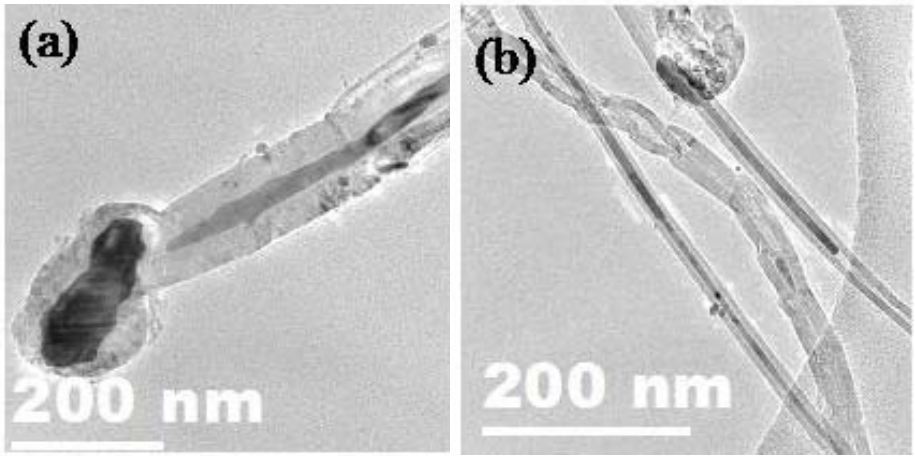

Fig. 7.9. (a-b) Low magnification TEM images of iron-ruthenium alloy nanorods inside carbon nanotubes

Magnetic measurements were carried on the different carbon nanostructures prepared by the pyrolysis of ferrocene, ferrocene-ruthenocene mixtures and ruthenocene in the presence as well as in the absence of hydrocarbons. Magnetic measurements on aligned carbon nanotubes obtained from the pyrolysis of ferrocene-hydrocarbon mixtures have been reported

earlier [16], wherein the M vs H curves showed a smooth S-shaped loop with saturation magnetization of ~24 emu/g, which is smaller than that of bulk iron [16]. In the present measurements a maximum field of ~1 T was applied from the start, swept through zero fields, and the direction of the field reversed to get M Vs H hysteresis loops. Figure 7.10 shows typical hysteresis (M Vs H) curves. It is observed that the saturation magnetization decreases from pure iron nanowire encapsulated in carbon nanotubes (prepared by ferrocene pyrolysis) to carbon coated/encapsulated binary FeRu (4:1, 1:4, 1:1) alloy nanostructures (prepared by ferrocene-ruthenocene pyrolysis) and to carbon-coated Ru particles (prepared by ruthenocene pyrolysis) respectively. The saturation magnetization (M_s) of 26, 7, 1.2, 10.7, 0.007 emu/g for the samples such as iron nanowires encapsulated inside carbon nanotubes, FeRu (4:1, 1:1, 1:4) binary alloy nanowires inside carbon nanotubes and carbon coated Ru nanoparticles respectively, while the corresponding coercivity (H_c) of 507, 205, 157, 194, and 20 Oe. In the case of carbon coated Ru nanoparticles, we have observed very low magnetization. Bulk Ru is nonmagnetic where as in nanosize domains it shows ferromagnetism. Recently universal ferromagnetism has been found in nanoparticles [17]. In nanosize particles, surface magnetism dominates at low fields and shows hysteresis. At high fields, diamagnetism dominates. It is also known that magnetic elements such as Fe, Co and Ni in nanoscale show enhanced moments due to the reduced coordination of atoms and localization of electrons as compared to the case of bulk materials [18]. The spin and orbital contribution to surface magnetism in the 3d elements have

been reported [19]. Several groups have studied magnetism of 4d elements nanoclusters and thin films [20-26]. Hence most of the studies points that magnetism in nanoregime is a surface phenomena.

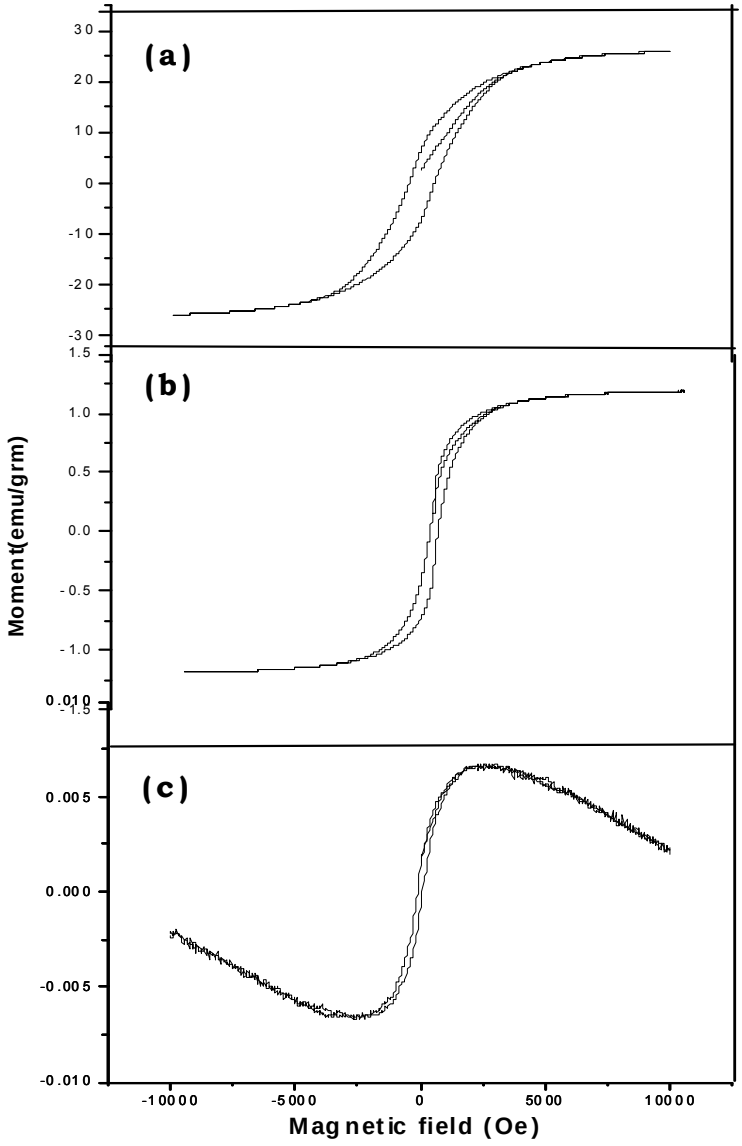

Fig. 7.10. Hysteresis loops (M vs H curves) recorded on samples: (a) iron nanowires encapsulated inside carbon nanotubes (b) FeRu (1:1) binary alloy nanowires inside carbon nanotubes and (c) carbon coated Ru nanoparticles

7.5 Conclusions

Unlike the pyrolysis of ferrocene, cobaltocene and nickelocene where carbon nanotubes are readily obtained, pyrolysis of ruthenocene mainly gives rise to carbon nanospheres. Under certain conditions carbon coated Ru nanoparticles were also obtained. Mixtures of ruthenocene with ferrocene also give rise to FeRu metal nanoparticles and also nanorods covered by carbon, the later being encapsulated inside carbon nanotubes. The pyrolysis method gives rise to useful means to produce nanoparticles of Ru and FeRu alloys. It may be noted that carbon spheres themselves can be obtained by the pyrolysis of hydrocarbon [8]. In view of this it appears as though during the pyrolysis of ruthenocene, cyclopentadienyl radicals undergo decomposition just as in the case of decomposition of pure benzene giving rise to pure carbon structures, with the ruthenium particles forming separate nanoparticles. In the case of Fe, Co and Ni they appear to be better catalysts than Ru to form nanotubes.

References

[1] C. N. R. Rao, B. C. Satishkumar, A. Govindaraj, M. Nath *ChemPhysChem.* . **2001**, 2, 78.

[2] A. Govindaraj, C. N. R. Rao *Pure Appl. Chem.* **2002**, 74, 1571.

[3] R. Andrews, D. Jacques, A. M. Rao, F. Derbyshire, D. Qian, X. Fan, E. C. Dickey, J. Chen *Chem. Phys. Lett.* **1999**, 303, 467.

[4] S. Huang, L. Dai, A. W. H. Mau *J. Phys. Chem. B.* **1999**, 103, 4223.

[5] S. Huang, A. W. H. Mau, T. W. Turney, P. A. White, L. Dai *J. Phys. Chem. B* **2000**, 104, 2193.

[6] C. N. R. Rao, A. Govindaraj, R. Sen, B. C. Satishkumar *Mat. Res. Innovat.* **1998**, 2, 128.

[7] R. Sen, A. Govindaraj, C. N. R. Rao *Chem Phys. Lett.* **1997**, 267, 276.

[8] A. Govindaraj, R. Sen, B. V. N. Raju, C. N. R. Rao *Phil. Mag. Lett.* . **1997**, 76, 363.

[9] J. Garcia, H. T. Gomes, Ph. Serp, Ph. Kalck, J. L. Figueiredo, J. L. Faria *Carbon.* **2006**, 44, 2384.

[10] J. Qiu, H. Zhang, X. Wang, H. Han, C. Liang, C. Li *Reaction Kinetics and Catalysis Lett.* **2006**, 88, 269.

[11] M –C. Tsai, T –K. Yeh, C. H. Tsai *Electrochem. Commum.* **2006**, 8, 1445.

[12] S. Shanmugam, A. Gedanken *J. Phys. Chem. B.* **2006**, 110, 2037.

[13] H. Kim, W. Sigmund *Carbon.* **2005**, 43, 1743.

[14] E. M. Savitskii, V. P. Polyakova, N. B. Gorina in Conference Proceedings written in Russian 90, Vol. (Ed.^Eds.: Editor), City, **1973**.

[15] H –J. Moon, W. Kim, S. J. Oh, J. Park, J- G. Park, E –J. Cho, J. I. Lee, H. C. Ri *J. Kor. Phys. Soc.* **2000**, 36, 49.

[16] B. C. Satishkumar, A. Govindaraj, P. V. Vanitha, A. K. Raychaudhuri, C. N. R. Rao *Chem. Phys. Lett.* **2002**, 362, 301.

[17] A. Sundaresan, R. Bhargavi, N. Rangarajan, U. Siddesh, C. N. R. Rao *Phy. Rev. B.* **2006,**, 74, 161306(R).

[18] I. M. L. Billas, A. Chatelain, W. A. d. Heer *Science.* **1994**, 265, 1682.

[19] O. Eriksson, A. M. Boring, R. C. Albers, G. W. Fernando, B. R. Cooper *Phy. Rev. B.* **1992**, 45, 2868.

[20] W. C. Wang, Y. Kong, X. He, B. X. Liu *App. Phy. Lett.* **2006**, 89, 262511.

[21] A. J. Cox, J. G. Louderback, S. E. Apsel, L. A. Bloomfield *Phy. Rev.***1994**, 49, 12295.

[22] V. L. Moruzzi, P. M. Marcus *Phy. Rev. B* **1990**, 42, 10322.

[23] B. Piveteau, D. M –C, Andrzej, M. Oles, D. Spanjaard *Phy. Rev. B.* **1996**, 53, 9251.

[24] A. E. García, V. González-Robles, R. Baquero *Phy. Rev. B* **1999**, 59, 9392.

[25] I. Cabria, B. Nonas, R. Zeller, P. H. Dederichs *Phy. Rev. B* **2002**, 65, 054414.

[26] Y. C. Bae, H. Osanai, V. Kumar, Y. Kawazoe *Phy. Rev. B.* **2004**, 70, 195413.